Abstract

High carbon bloom steel from the continuous casting shop of Tata Steel at Scunthorpe has been used in order to investigate the variation in secondary dendrite arm spacings (SDAS), and micro-segregation from the surface to centre, and also to assess and develop model capability. The average cooling rate during solidification and associated heat extraction rate were determined for each nodal position of a macro model. However, the thermal conditions for these positions were taken from a macro model of bloom/slab solidification which operated under a simple, equilibrium solidification condition.

A new analytical secondary dendrite arm spacing model has been developed using Matlab software, which takes into account the effects of multicomponent steels on the coarsening dendrite arm factor, geometric factor, local solidification time, and peritectic transformation. The predicted results have shown very good agreement with experimental results from different references. The effect of carbon and other elements on geometric and coarsening dendrite factors are discussed.

A longitudinal section of high carbon steel bloom was cut off in order to measure SDAS; the measured variation from the top surface to centre is discussed, and compared with the SDAS model.

Micro-segregation was calculated according to DICTRA® and an in-house model (QSP) from Tata Steel, from liquidus to solidus and continuing in the fully solid state down to 1000 ℃, employing both measured and calculated SDAS. Example measurements of micro-segregation were conducted using automated line scans from SEM-EDS (on a JEOL6400) through 3 or 4 secondary dendrite arm spacings for each bloom-depth, the results do give a peak in micro-segregation around 46mm, but unlike

the DICTRA or QSP calculations using the thermal data from TTC macro model, the segregation data seem to remain around that peak level from there on into the centre. They are more like the measured SDAS variation than the DICTRA and QSP variation, again suggesting that the models might not be using accurate thermal data for input. The reasons for this and the differences between the model variants are discussed.

A new micro-segregation model was developed in this study based on the Ohnaka model but which extends the limitation of Ohnaka's model for constant length scale of microstructure. In order to satisfy this requirement, the new micro-segregation equation takes into account the coarsening of the dendrite structure. The new micro-segregation equation is shown to work better than would be expected for the predicted peak concentration, solute profile at solidus, and experimental data (Jernkontoret results for carbon and low alloy steels 201-216).

Table of contents

List of Tables

List of Figures

List of Symbols

λ_2	secondary dendrite arm spacing, μm
G	temperature gradient,
V	growth velocity,
C_0	steel composition, wt.%
C_C	carbon content, wt.%
T	temperature, ℃
t_f	local solidification time, s
B	geometrical factor, constant
M	coarsening parameter, $\mu m/s^{1/3}$
α	Fourier number
α^+	Fourier number accounts for coarsening
α_C	extra back-diffusion from coarsening = 0.1
C_R	cooling rate, ℃/s
D	diffusion coefficient, m^2/s
f_s	solid fraction
k	equilibrium partition coefficient, wt.%/wt.%
m	slope of liquidus line, ℃/wt.%
σ	interfacial energy, kj/m^2
Q	heat extraction rate, j/m^3.s^{-1}
H	heat of fusion, kj/mol
β	back diffusion
ΔT	liquidus-solidus temperature interval, K
C_P	heat capacity, kJ/$m^3. k^{-1}$

δ	ferrite phase
γ	austenite phase
L	liquid phase
Ep	peritectic equivalent
C_P	carbon equivalent
A_i	empirical factor

Acknowledgements

I would like to express my deep gratitude to my supervisors, Dr Richard Thackray and Professor Andy Howe, for all of the guidance, encouragement and direction they have given me during the course of my PhD in Sheffield.

I also would like to gratefully acknowledge the IMMPETUS for the financial support for this research project. Specifically, I also wish to thank Tata Steel for their assistance and support.

It has been a pleasure to work in the IMMPETUS research group; I have learn a lot and made some great friends. I also would like to thank many members of technical staff within IMMPETUS, the Department of Materials Science and Engineering in general, and The Sorby Electron Microscopy Centre, have helped during the course of my PhD.

Most importantly, I would like to express my deepest thanks to my dear parents, my dear wife and lovely daughter, my dear Ardeshir Sepehri, my sister and my brother, for their endless support, spiritual encouragement, and love.

Chapter 1: Introduction

1.1 Background

Dendrite arm structures often form during solidification; some of the main factors affecting the development of dendrite arm spacings are the solidification rate or heat extraction rate, and alloyed elements. The secondary dendrite arm spacing is a significant factor that affects the properties of final products, thus it is very important to understand what is controlling dendrite arm spacing during solidification. It is well known that cooling rate is a primary factor that is affecting the final dendrite arms; increasing cooling rate increases productivity and gives faster return investment, but it might lead to poor final properties due to formation of cracks and flaws [1]. Furthermore, it is difficult to impose solidification conditions that have much effect on the cooling rate in the middle of a large cross section of material.

The effect of cooling rate on micro-segregation levels is important regarding the properties of final products. A body of extant literature has studied this effect of cooling rate on micro-segregation. Many simple models have assumed a constant cooling rate, but in real continuous or ingot casting, the cooling rate varies enormously during solidification even at a given position within the casting. The cooling rate will start off slowly at low solid fraction, which is the region where the results are fairly insensitive to cooling rate, but it will finish with a faster cooling rate, in precisely the region where it will affect the results. Also, the simple models in previous studies terminate at the solidus, whereas there can be significant sub-solidus homogenization [2]. The thermal history, rather than a nominal cooling rate, is the important parameter, down to temperatures at which further solute diffusion can be ignored.

In the present study, simulation using DICTRA and QSP software and new SDAS and micro-segregation equations, and experiments with the Scanning Electronic Microscopy- Energy Dispersive X-ray Spectroscopy (SEM-EDS) technique were used to investigate the degree of micro-segregation of Si and Mn, which develops both

during and after solidification. The optical microscopy was also used to measure the secondary dendrite arm spacing.

This thesis focuses on the back-diffusion type models with an assumed simple geometry and ignoring the minor undercooling associated with shape/curvature which plays an important role in determining the formation of dendritic structures. The new micro-segregation equation takes account of the coarsening of the dendrite structure that can improve the predicted degree of segregation at the solidus.

1.2 Aim of research

This research is the first step towards increasing the efficiency and productivity of the steel making process in order to achieve both quality and quantity of slab and bloom as-cast steels by the continuous casting process.

The main aim of this research is to study the effect of cooling rate and the thermal history across a commercial, continuously cast bloom during liquid − solid transformation and sub-solidus homogenisation. Increased solidification rates (at least within the range achievable in large commercial castings) lead to increased micro-segregation and consequently reduced solidus temperatures. However, they also lead to reduced Secondary Dendrite Arm Spacings (SDAS), which will reduce the required diffusion distance for homogenisation during cooling in the solid state. The net result can therefore be a balance between these effects.

This work aims to further develop existing models to improve the capacity to predict SDAS and micro-segregation for continuously cast steels on an industrial level. An analytical model of SDAS will be developed using Matlab code. This model will allow the prediction of SDAS for multi-component steels containing a wide range of carbon content from 0.08 to 1.5% wt%.

The effect of the chemical composition on the SDAS value of multi-component steels has not been extensively investigated in the extant research since this effect is typically difficult to examine due to the effect of the cooling rate. The model developed in the current study is based on literature data, primarily effects of C, Mn, Si, Cr, Ni, Cu, P and N on SDAS value from Jernkontoret (Stockholm) measured SDAS experiments but also other previous studies.

A high carbon bloom has been supplied to this project from the Tata Steel Company to investigate and compare the results of the predicted SDAS and the variation in segregation and model capability from surface to centre. The thermal model conditions for the surface, quarter-thickness and centre positions have been taken from a macro model of slab and bloom solidification which employs a simple, equilibrium condition for micro-segregation. Meanwhile, micro-segregation has been calculated according to DICTRA software and QSP software from Tata Steel, from liquid down to 1000^0 C. The interdendritic micro-segregation has been measured by SEM-EDS from the surface to centre in order to compare with the prediction from the above-mentioned models.

There are many simple models that have been developed to predict solute in the interdendrite region; the Scheil model, Lever-rule model, Clyne-Kurz model and other models. There is still need for an improved simple micro-segregation equation that can estimate the typical degree of micro-segregation and solute profile at the solidus based on the thermal history and which operates far faster than most currently available.

Chapter 2: Literature Review

During the past 60 years much more experience and information has become available on continuous casting. Upon the introduction of continuous casting in the 1850s (at a very small scale of production), liquid steel was poured via the ladle and tundish into a copper mould which is cooled with an external water jacket. In order to avoid sticking of the shell to the mould wall the copper mould is oscillated vertically. The first solidified shell is formed on the mould wall and it increases in the thickness as the steel strand runs through the secondary cooling zone. The solidification ends when the steel temperature in the centre falls to the solidus temperature, allowing for any depression below the equilibrium value due to micro-segregation.

Many different types of continuous casting process are used to cast steels, aluminum and copper alloys. The three widely used casting process are shown in figure 2-1 [3]. Curved machines are used to cast alloyed steels into various shapes and sizes such as slabs, blooms and billets. The fourth, strip casting, is not in large scale production but is the most similar to the original process from the 1850s.
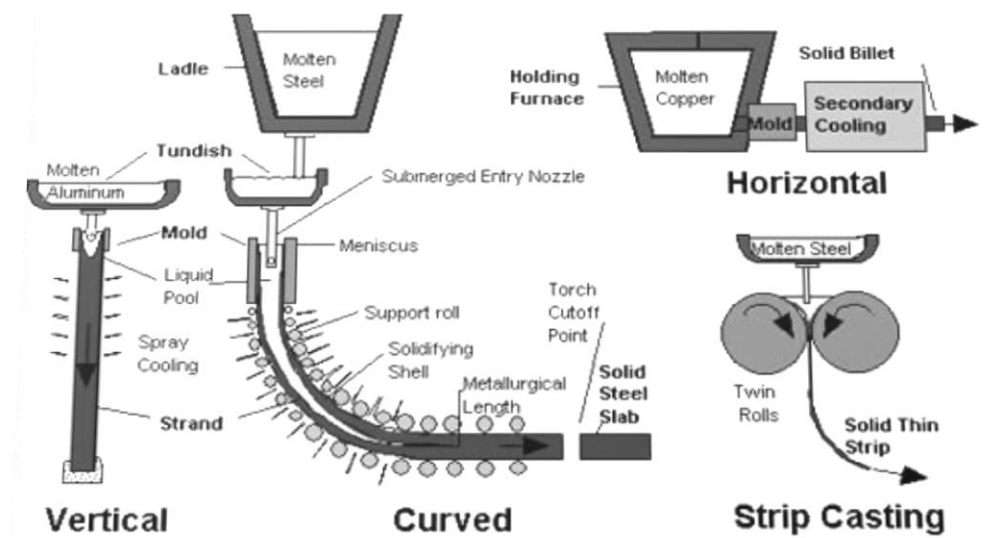
Figure 2-1: Continuous casting methods [3]

There are few studies on the solidification of high carbon steel [4], [5]. Figure 2-2 shows the solidification of high carbon steel bloom using Thermo-Calc. In contrast to delta-ferrite and peritectic transformation whereby low carbon steel undergoes

6

transformation from liquid to delta-ferrite and then it is solidified to austenite, high carbon steel is solidified directly as austenite. Solidification for the depicted, example alloy typically starts around 1475 ℃ and is completed around 1368 ℃. Below the solidus temperature, steel is solidified to austenite. During the solidification process, the quality of solidified steel depends on many solidification parameters such as heat extraction rate or solidification rate, superheat and steel composition.
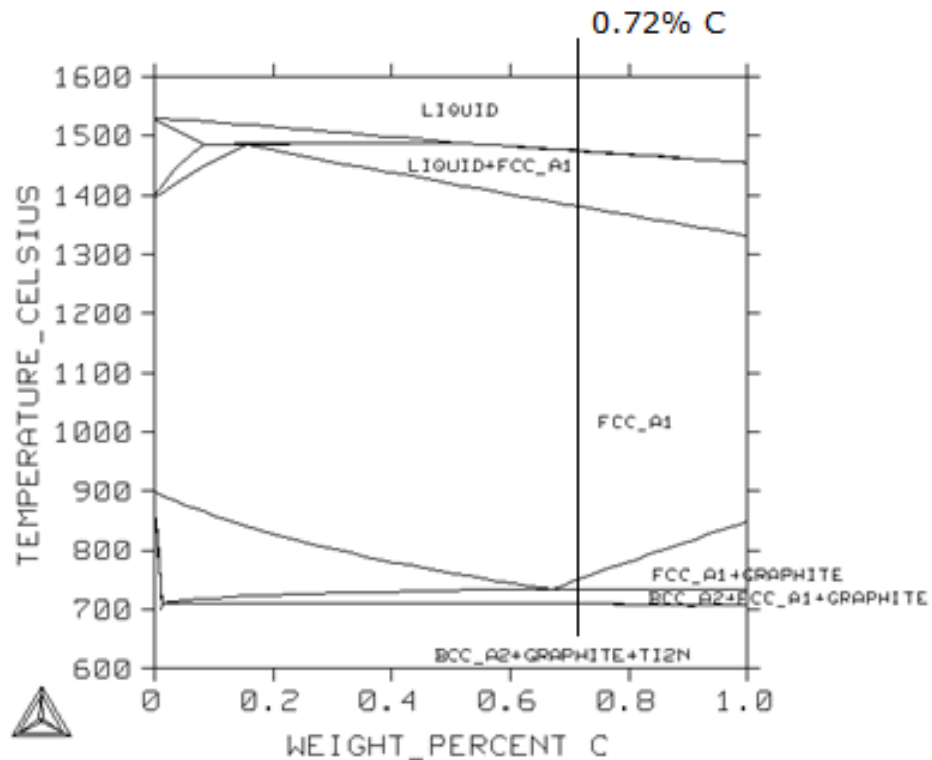
Figure 2-2: Phase diagram of high carbon steel 0.72% C, 0.24% Si, 0.63% Mn

(calculated by Thermol-Calc).

2.1 Previous study on continuous casting of steel

The high carbon bloom steel used in this project was produced by the curved-strand continuous casting method at Tata Steel. Before examining the effect of solidification rate on microstructure evolution and micro-segregation during solidification, it would be very helpful to provide some general background information about the continuous casting process and how the control of solidification can affect the

micro-segregation, maro-segregation and microstructure of the bloom to improve the quality of steel.

By eliminating extra steps involved in the production of steel under the ingot casting process, the continuous casting method leads to higher yield and manpower productivity, more uniform product, better surface condition and internal quality of production. By saving labour time, energy and capital it reduces the cost of production. [1].

The attraction of continuous casting was first recognized by Sellers [6], Laing [7], and Bessemer [8] in the 19th century. Continuous methods introduced by these 19th century pioneers were however mainly applied to non-ferrous materials with low melting points, such as the production of glass. Continuous casting was not applied to steel due to many technical problems associated with high melting point involved and the low thermal conductivity of steel. Thereafter, additional research was carried out to invent and modify continuous casting technology and its application to ferrous and non-ferrous materials. Today, annually 1,432 million tons of crude steel are cast from molten metal [9].

Another signification improvement to continuous casting technology was the introduction of mould oscillation and lubricant addition. Lubrication and oscillation overcome two major problems associated with continuous casting, namely sticking of the solidified shell to the water-cooled mould, and non-uniform surface condition across the strand [10].

The 1950s witnessed rapid technological changes in continuous casting of steel. The major technological developments included the introduction of curved-strand geometry and electromagnetic stirring, and the replacement of vertical cutting of the billet strand by horizontal cutting. Electromagnetic forces were applied to alter the flow

in continuous casting by passing electrical current through coils positioned around the mould. The horizontal plane of the strand is stirred by the electromagnetic forces during cooling [11].

Further improvements in the 1970s and early 1980s included total shrouding of steel streams from the tundish to the mould in the form of a Submerged Entry Nozzle. The amount of argon injected into the nozzle avoids contact with oxygen and controls clogging, resulting in an improvement in the quality of billets, slabs and blooms [11].

Another improvement in the casting was changes to the arc radius in bending and straightening process of a vertical bending type continuous caster.

Since continuously-cast steel is subject to a variety of different surface and subsurface cracks arising from hot tears and micro-segregation, changes from horizontal to vertical bending [12] minimizes the occurrence of the cracks and increases the quality of the billets, slabs and blooms.

The type of secondary cooling mechanisms have been subjected to many investigations [1]. Dynamic control of continuous casters and dynamic spray cooling methods are used to control the temperature of the strand in continuous casting (the heat extraction rate of the high carbon bloom steel is recorded during continuous casting). In contrast to solidification, in spray cooling, water droplets impinge onto the very hot steel surface and vaporize instantaneously which prevents the water from wetting the surface [13]. Higher cooling rate increases micro-segregation and increases the risk of formation of precipitation leading to the poor quality of steel products.

The type of microstructure developed during the solidification of casting is determined by three main factors: (i) The temperature gradient (G), (ii) growth velocity (V), and (iii) The steel composition (C_0). Depending on the G/V ratio, three zones in the macrostructure of a continuously cast steel semi can be recognized: the microstructure is

planar as the G/V ratio gets larger, cellular and then to dendritic, as *G/V* gets smaller [1].

New technological developments combined with production of steel on large scale led to a lower cost of production, improvements in quality and higher return on investment. Liquid iron making from larger capacity blast furnaces was transported to steelmaking shops where a basic oxygen furnace was used to reduce carbon content and after pre-treatment to remove undesired elements like sulphur, silicon or phosphorous. Liquid steel was then transferred to the continuous casting machine for casting billets, slabs and bloom steel. Various techniques, such as increasing the average sequence length, the casting speed, the average section size cast and the strand width were used to improve the productivity [1].

However, these productivity enhancing methods had their own drawbacks, adversely affecting the life of equipment used in the process, production costs and desirable properties of the steel. For example while slitting of the width of a wide strand was an effective method to increase productivity compared to casting a small width section, this method is suitable for the conventional cold-charge process but not for hot charging. Billets, slabs and bloom steel usually cools down to room temperature before being reheated again to around 1250 ℃ for hot rolling process which increases energy consumption and production cost [1] compared to hot charging directly to rolling.

After solidification in the mould, the strand undergoes the secondary cooling process until its temperature is lowered enough for the steel to be solid and ready for cutting with a torch. Finding the critical cooling rate has been subject to extensive research. High cooling rate can result in many technical problems for both the caster and the quality of billets, slabs and blooms such as higher degrees of micro-segregation and surface cracks. Depending on the product size the cooling rate could be adjusted to minimize these problems [1].

2.2 Segregation during Solidification of Steels

All castings are segregated to some extent because of the way in which the solutes in the alloys partition between the solid and the liquid during freezing.

Some variation in composition occurs in alloy castings on a microscopic scale between dendrite arms, known as micro-segregation, and some variation occurs on a scale larger than that of the dendrite arm spacings [14].The various types of segregation, which are often encountered in longitudinal sections of actual steel continuous casting slabs are: interdendritic segregation or micro-segregation, V segregation, centreline segregation or macro-segregation, and white bands [15].

Micro-segregation results from solute redistribution during the solidification of an intercellular or interdendritic liquid during casting (or welding). Interdendritic micro-segregation can be clearly observed in the columnar zones close to both upper and lower surfaces. It is small in size though not necessarily in intensity. Usually, it does not result in severe problems by itself alone. Micro-segregation is basically the consequence of many factors including the growth and morphology of the dendrites, the nature of the solidification phases and precipitation reactions, 'mushy zone' (i.e., the ranges of temperature and position within the casting over which solidification occurs) and the fractional solidification within that range [16], [17], [5].

Macro-segregation refers to non-uniformity of chemical composition over larger sections of steel ranging from several millimeters to centimeters or even meters. Most macro-segregation is caused by the flow of liquid through the interdendritic spaces in the liquid-solid zone and is considered more harmful than micro-segregation which by itself generally does not constitute a major quality problem, since micro-segregation can be alleviated during subsequent soaking and hot working operations. However, without the micro-segregation, its associated solidification microstructure, macro-segregation would not develop.

White band segregation occurs when the content of solute elements is less than average (negative segregation)and is often followed by a larger than average, positive segregation, due to sudden and intense liquid flow parallel to the solidification front [15]. The negative segregation is usually the more obvious such band but is not as harmful as positive segregation.

The next section provides a more detailed account of micro-segregation and macro-segregation.

2.2.1 Micro-segregation during solidification

The effects of micro-segregation on the mechanical properties of the final product during solidification of steels have extensively been studied during the past 3 decades. Solute segregation during continuous casting leads to non equilibrium phases, cracks, columnar dendrites and coarsening, lowering the mechanical properties of the final product [2], as well as being a pre-requisite for macro-segregation [18].

Micro-segregation refers to differences in concentration between the core of a dendrite and the interdendrite arm position, often called coring [19], as shown in the following figure 2-3;
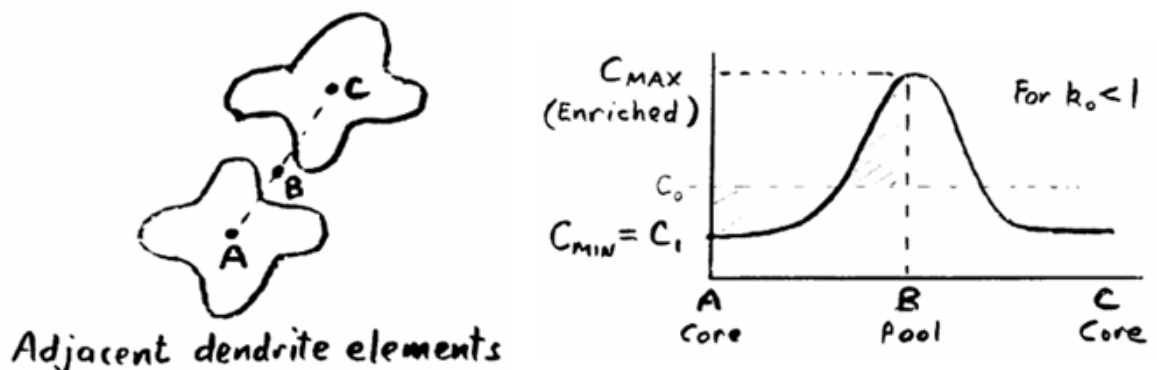
Figure 2-3: Schematic phase diagram of micro-segregation [19]
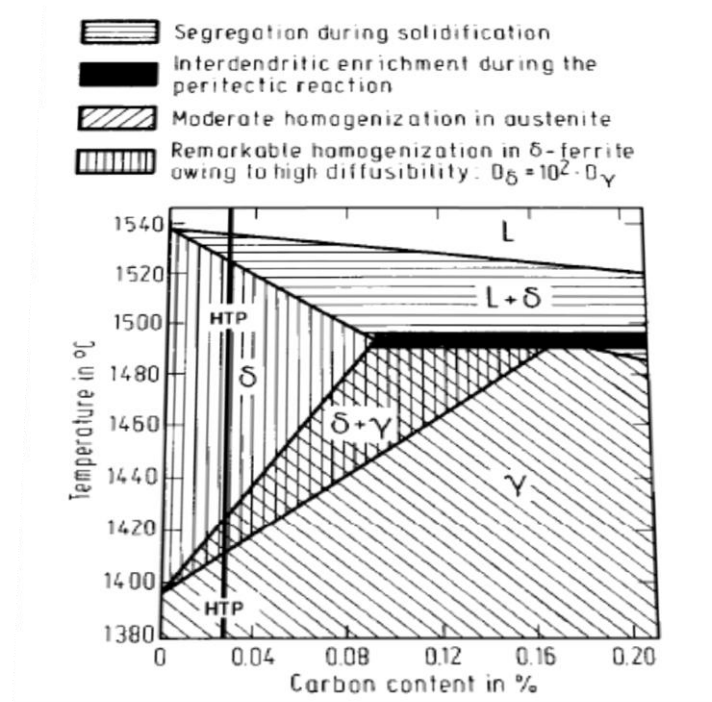
Figure 2-4: Part of the Fe-C diagram with classification of the segregation

severity [20].

If the carbon content is below 0.09%C (and other elements are present only in very small amounts), the solidification goes directly through the δ phase without the peritectic reaction, effectively avoiding interdendritic segregation because of the very high solute diffusivity in the ferrite phase. If carbon content is 0.09% and higher, the interdendritic enrichment during the peritectic reaction increases with increasing extent of austenitic solidification, with additional micro-segregation effects possible around the ferrite/austenite interface. The reaction causes an additional shrinkage due to the transformation from delta ferrite to austenite. It is well known that a lower carbon content reduces the tendency for segregation [20] and improves several properties of the final product, such as the impact energy, the ductility and formability and the ductile-brittle transition temperature.

Turkeli and Kirkwood [21] studied manganese micro-segregation in ternary Fe-1.6%Mn - 0.1 to 0.8%C steels. They measured micro-segregation between secondary

arms, primary arms and spot regions. Micro-segregation of carbon increased with increasing cooling rate and with higher initial carbon content. The segregation ratio of carbon was found to be higher both between secondary arms and primary arms with higher carbon content. There were no effects of cooling rate found on segregation of manganese in secondary dendrite arms, but it was found to increase slightly the segregation of manganese in the primary dendrite arm when the cooling rate increased.

Many researchers believe that the peritectic reaction is important for the degree of micro-segregation and can also result in unexpected solute distributions in the solidified steels [16], [22]. Howe and Kirkwood [23] examined the computer prediction of micro-segregation in peritectic alloy systems and calculated peritectic equivalent coefficients E_p using partition coefficient k and m liquidus slope with ferrite and austenite phase, respectively. These can help judge whether a particular composition is likely to undergo the peritectic transformation.

2.2.2 Macro-segregation during solidification

Most steel elements have a higher solubility in the liquid than in the solid phase, known as the solute partition. During solidification, the solutes are generally rejected into the liquid phase resulting in lower solute concentrations in the primary solid and a continual enrichment of solute concentrations in the liquid steel. This is not usually serious if the partitioning remains at the micro-scale of the dendrite arms. However, it can easily lead to macro-segregation given enough time and driving force for relative movement of segregated liquid. The movement or flow of segregated solid and liquid during solidification can occur over large distances, whereupon the casting becomes macroscopically segregated. In contrast to positive macro-segregation, negative macro-segregation is caused by solute concentration below the average steel concentration. All macro-segregation must add to zero over the entire casting. Liquid flow and solid

movement in casting processes are caused by many factors: (i) Flow that feeds the solidification shrinkage and the contractions of the liquid and solid during cooling; (ii) buoyancy induced flows due to thermal and solutal gradients in the liquid; (iii) Flows due to capillary forces at liquid-gas interfaces; (iv) Residual flows from pouring; (v) Flows induced by gas bubbles; (vi) Forced flows due to applied electromagnetic fields, stirring, rotation, vibration, etc (vii) Movement of small (equiaxed) grains or solid fragments that have heterogeneously nucleated in the melt, separated from a mold wall or free surface, or melted off dendrites; (vii) Deformation of the solid network in the mushy zone due to thermal and shrinkage stresses, head pressures, or external forces on the solid shell [24].

Macro-segregation occurs during solidification due to relative movement or flow of segregated liquid and solid. There are numerous causes of fluid flow and solid movement in casting processes. One reason for this movement of segregated liquid may be density differences of the metal due to temperature or variations in composition [25].
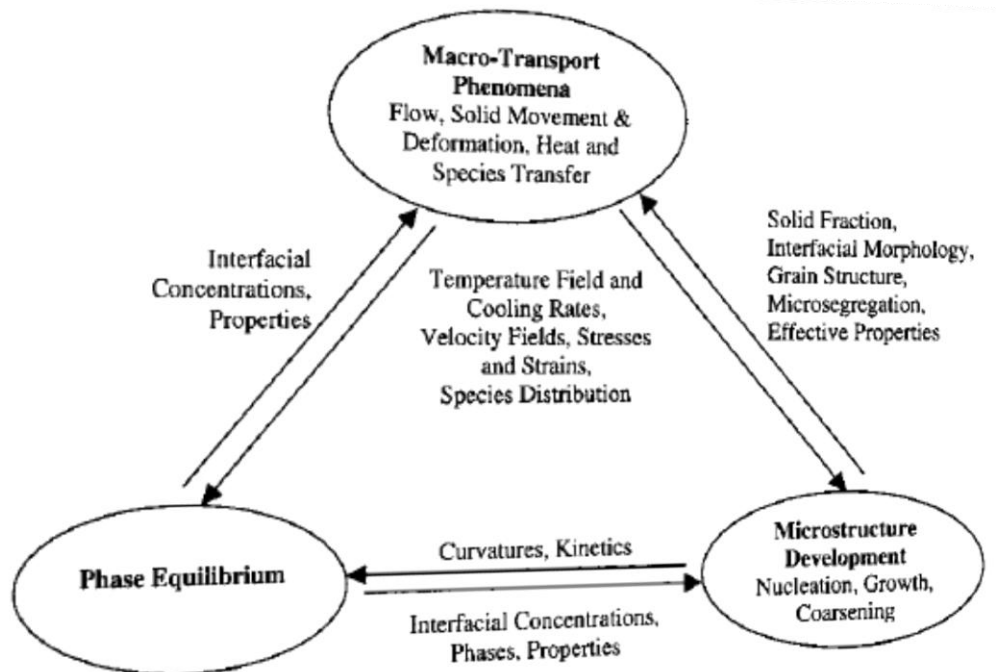
Figure 2-5: Potentially important interactions in modelling macro-segregation in castings [24]

Macro-segregation occurs over similar distances to the size of the casting. This can be caused by a number of complex processes involving shrinkage effects as the casting solidifies, and a variation in the density of the liquid as solute is partitioned. We will not discuss these processes further because it is not the subject of this thesis.

These compositional variations have a detrimental impact on the subsequent processing behaviour and properties of cast materials and can lead to rejection of cast components or processed products. Macro-segregation is present in virtually all casting processes, including continuous, ingot, and shape casting of steel and aluminum alloys, iron casting, casting of single-crystal super alloys, semisolid casting, and even growth of semiconductor crystals [25].

2.3 Previous studies on the effect of cooling rate on micro-segregation

Continuous Casting is the process whereby molten metal is solidified into ''semi-finished'' billet, bloom, or slab before undergoing the rolling process. The process is utilized very often to cast steel and other metals such as copper and aluminium. This production process has three main advantages: (i) The near-net shape formation of steel during continuous casting and subsequent saving in energy, time and labour; (ii) The development of new functional properties brought about by microstructure evolution, such as the formation of non-equilibrium phases; and (iii) An improvement of mechanical properties resulting from decreased segregation and the refinement of grain size [26].

Variations in the cooling rate and its influence on microstructure of the final product and therefore mechanical and physical properties of casting has been observed at three ranges of cooling rate: the low cooling rates (10^{-1} to 10^{1} K/s), the high cooling rates (10^{3} to 10^{7} K/s), and the medium cooling rates (10^{1} to 10^{3} K/s). Variations in the

cooling rate for different solidification processes are summarized in table 2-1. At the low cooling rates which occur in large ingot castings or directional solidification, variations in the cooling rate is observed to lead only to small changes in microstructure at such low cooling rates and with micro-segregation close to equilibrium partitioning. By contrast, the most dramatic changes in microstructure occur at the high cooling rates produced by rapid solidification processing or welding techniques [27]. The cooling rates in the latter case are far away from the equilibrium rate. At the medium cooling rates changes in the cooling rate leads to complex microstructure changes and it is these which occur during continuous casting of billets, slab and bloom steel [27].

Table 2-1: Estimated cooling rate ranges of various solidification processing techniques [28]

Process	Cooling rate (K/s)
Directional solidification	$10^{-1} - 10^{1}$
Continuous casting	$10^{-0} - 10^{2}$
Arc welding	$10^{1} - 10^{3}$
Electron beam welding	$10^{2} - 10^{4}$
Laser beam welding	$10^{2} - 10^{6}$
Rapid solidification Processing	$10^{3} - 10^{7}$
Electron bean or Laser beam surface modification	$10^{5} - 10^{7}$
Single laser pulse	$10^{7} - 10^{8}$

Two types of techniques are often employed to examine the effect of cooling rate on micro-segregation. The first technique uses relatively small isothermal samples weighing less than 100 g, which frequently solidified at a constant cooling rate. Using this technique, Michael and Bever [29] and Kohn and Philibert [30] studied Al-Cu

alloys, Hammar and Grumbaum [31]and Doherty and Melford [32] investigated low-alloy steels, while Liu and Kang [33] studied Al-Mg alloys. The cooling rate prevailing in all these experiments varied from 0.01 K/s to 160 K/s. In this range, a decreasing cooling rate was found to be associated with a decrease in micro-segregation. However, some studies found that micro-segregation levels might decrease by increasing the cooling rate above a certain threshold value (for medium cooling rates) [34]. In contrast to the concentration homogenization, increased solidification rates also lead to reduced Secondary Dendrite Arm Spacings (SDAS), which then reduces the required diffusion distance for homogenisation during cooling in the solid state. The net result can therefore be a balance between these two effects [35]. Faster cooling leads to finer dendrite arm spacings: of themselves the shorter distances between the arms (and hence positive and negative regions of the coring profile) should encourage homogenisation, and this is indeed what is observed during solid state heat treatment. However, just at the end of solidification, faster cooling and finer SDAS is associated with increased micro-segregation, with the reduced time for homogenisation outweighing the reduced distances during solidification.

The second technique used to study the cooling rate effect on micro-segregation uses directionally solidified samples weighing from a few kilograms to 100 kilograms. A different cooling rate is found to have a different heat extraction rate depending on the location from the surface to centre. It was found that micro-segregation severity decreases toward the surface as the cooling rate increases. However, it should be noted that the cooling rate for the reported studies is usually less than 200 K/s, which falls below the rate associated with a maximum in the micro-segregation severity [34].

2.4 Previous studies on the effect of cooling rate on microstructure (or previous studies on microstructure)

The effect of steel microstructure and cracks on mechanical properties of steel and its machinability have become a central issue for many researchers since the middle of the 20th century. Previous studies have attempted to explain: (i) how the steel microstructure is formed during the solidification process; (ii) how the steel microstructure affects its mechanical and machinability properties [1].

The rapid solidification processing is remarkable in terms of the refinement of solidified microstructure, the scale of segregation, formation of metal stable phases and morphological changes [36]. In contrast to rapid solidification, conventional solidification of billets or blooms as cast usually contains a coarse or non-uniform microstructure, more degree of segregation depending on the steel grades and the solidification process parameters. Various methods have been used to refine and homogenize the as-cast steel microstructures: (i) increasing the heat extraction rate (or cooling rate), (ii) applying electromagnetic stirring (EMS) fields, (iii) addition of grain refining elements, (iv) applying liquid core reduction to break the dendrite arms and homogenize the solidification microstructure [37].

A considerable amount of literature has examined the relationship between additive elements in steel microstructure and its mechanical properties and machinability. Adding additive elements to liquid steel can generate inclusions in the solidified structure, and change the defect density during secondary cooling process [1]. Howe [38] has developed a model of micro-segregation and inclusion development during the casting of steel, in which the enrichment of element in the residual liquid during solidification is identified as a major contributing factor to the fitness of the steel and as a major influence on the precipitates and oxide inclusions. This model allows

prediction of the maximum inclusion size forming in the mushy zone across the thickness of the billet or bloom section.

The formation of microcracks and cracks are more serious than other defects occurring during solidification. The origin of cracks has been classified by Brimacombe and Sorimachi [39] into internal and surface cracks. Uneven heating may cause surface cracks leading to longitudinal and transverse facial cracks [40].

Among the potential defects occurring during solidification, microcracks and cracks are more serious. The underlying causes of cracks are classified into two main categories: internal and external forces. Internal and surface cracks debase the steel quality during solidification, these cracks are formed by combination of tensile stress and metallurgical embrittlement [1].

Surface cracks initiated in the mould can appear near both the corner regions and midface [13]. There are various types of surface cracks, such as transverse corner or transverse surface, longitudinal midface or longitudinal corner and star cracks, as shown in figure [1]. Brimacombe et al., [41] show that transverse surface and corner cracks are formed when the surface temperature is within the low ductility range of 700-900 ℃. These cracks are formed initially in the mould where axial tensile stresses are induced by spray cooling during continuous casting slab. Pelak et al [42] show that longitudinal cracks are formed in the mould and they are propagated and elongated in the slab surface as a result of thermal and mechanical stress. The contributing factor to longitudinal cracks includes the chemical composition and purity of steel, the casting flux quality, the mould oscillation frequency and the secondary cooling intensity.

Internal cracks initiated at the solidification front often appear near the corners, at the centreline or diagonally between opposite corners. There are various types of internal cracks, such as midway, centreline cracks and centre segregation, as shown in

figure 2-6. Brimacombe et al [41] show that midway cracks can be caused by excessive spray cooling or insufficient spray length which lead to the heat to transfer backward to the surface, generating tensile stresses beneath the surface and in the solidification front. The small cracks which are formed in the mould can be caused by insufficient spray cooling below the mould leading to several defects such as midface cracks, triple point cracks, centreline cracks and centre segregation. Triple point cracks occur due to the rapid cooling or too low cooling of side surfaces and poor equipment conditions [43].The increase in temperature of the tundish causes an increase in the length of cracks. Cracks in the microstructure of steel can also be caused by different phase transformations during the cooling process [1].

Surface Cracks (initiated in the mold)

Transverse corner
Transverse surface
Longitudinal midface
Longitudinal corner
Star

Internal cracks
(initiated at solidification front)

Midway
Straightening
Pinch roll

Off corner

Radial streaks

Diagonal

Triple point

Centerline
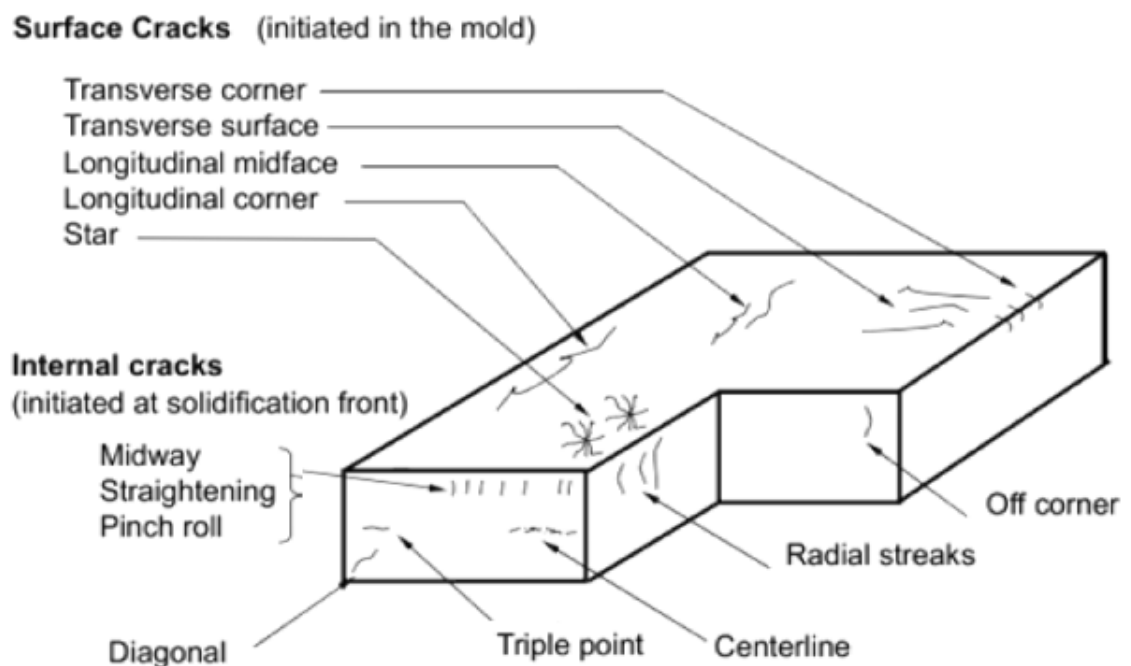
Figure 2-6: Surface cracks and internal cracks detect in continuous cast steels [1]

Many studies have shown that the solidification parameters play an important role in the characterization of defects. The tundish temperature controls axial porosity of the steel [1], where using a low casting speed, gravity accumulates the inclusions unevenly making the microstructure vulnerable to fracture by decreasing the energy absorbed in the microstructure [44], [45]. The electromagnetic stirring method has

widely used during continuous casting of steels, in the mould [46], [47] or in the secondary cooling zone [48], [49]. This technique creates a narrow negative segregation zone (white band) and temporarily eliminates constitutional supercooling [50].

Various parameters affect the cooling rate, including quenchant type, quenchant temperature, agitation velocity, viscosity, agitation type, polymer foaming, polymer degradation, grain nature, grain size, geometry, and carbon content [51]. For the purpose of this study, it would be helpful to review the previous work on the several important features of cast steel that affect the properties of the product. These features include secondary dendrite arm spacing, grain size, inclusions and segregation. The single most important feature of the casting process is solidification rate and the determination of optimum cooling rate [52] during and after the solidification process.

The subject of optimum cooling rate is related to the topic of quenching. Quenching allows for the most rapid cooling rate with a quenchant such as water, air, oil, salt and other chemical compounds [53]. Liquid quenchants are often used in the industry which supplies the quenching process with homogeneous and easily controllable heat transfer from the hot cast body [52]. Much of this technology is not appropriate to large scale continuous casting. Also, even if the surface is quenched at a high rate, the centre of a large cross-section will still only cool slowly.

During the cooling process, the austenite temperature may result in different phase transformation sequences such as ferrite, pearlite, bainite and martensite [54]. A large body of literature has discussed various aspects of the solid-solid phase transformation. For example, austenite transforms to ferrite at a slow cooling rate and ferrite or martensite under high cooling rate [1]. And Miller [55] found that the amount of martensite in the final microstructure depends not only on the carbon content but also on intercritical phase transformation temperature and the cooling rate.

The desired solidification structure has been the subject of many previous works. Many mathematical models have been developed to simulate solidification structure formation in a casting and an ingot. However, the application of the models to steel is problematic for two main reasons; First, the continuous casting process often applies the electromagnetic stirring, which makes it difficult to model solidification structure formation in steel. Second, the complex phase transformation occuring during the solidification process, such as peritectic reaction and subsequent peritectic transformation, make it difficult to model the solidification structure formation in steel [1]. In order to avoid the difficulty in modelling peritectic transformation, Yamazaki et al., [56] chose an Fe-0.7%C binary alloy without the peritectic reaction. They carried out the simulation of solidification structure formation during the continuous casting process with and without electromagnetic stirring. In the case without EMS, the columnar crystals were grown from the chill zone to the centre of the billet, and a small region of equiaxed grains was observed. In the case involving EMS, a solidification structure similar to the one observed in a larger equiaxed zone could be simulated.

It is well known that rapid solidification (cooling rate in the range of $10^3 - 10^7$ K/s) can produce more uniform and refined microstructure as compared to conventional solidification. Pryds et al., [57] examined the effect of cooling rate on a low carbon steel Fe-Cr alloy. According their experimental results, they found that columnar ferrite grains form in the matrix structure over a larger cooling rate variation range. Increasing cooling rate resulted in a decrease in the size.

Choudhary et al., [5] investigated the morphology and segregation in continuously cast high carbon steel. A chill zone was found in the macrostructure of billet samples, which is a characteristic of rapid solidification of liquid steel at the meniscus. Beyond a short distance from the surface, they also observed a rapid coarsening of the columnar structure which occurs as a result of a reduced heat

23

extraction. Moreover, they observed a fully equiaxed structure toward the centre due to a reduced cooling rate toward the centre. They also found that carbon enrichment of liquid may have an influence on the size distribution of the dendrite zone, reducing SDAS in the equiaxed zone.

2.5 Previous studies on secondary dendrite arm spacing (SDAS).

The quality and properties of the as-cast steels are mainly related to the microstructure developed during solidification process [58]. Some of the main factors affecting the development of the grain size and grain morphology (i.e. columnar, equiaxed) are now well known. These include solidification rate or heat extraction rate, the amount of alloying elements and solidification conditions. The secondary dendrite arm spacing is a significant factor that affects the microstructure. For ingots or castings, improvements in mechanical properties of alloys are made by refined SDAS. The SDAS affects the industrial semisolid structure during solidification and how to predict the SDAS of the alloyed steels could be very useful for optimizing the properties of the alloyed steels and for designing new steels [59].

There are many models that could be used to predict the SDAS which consider the effect of coarsening parameter M and local solidification time t_f on binary steels [60] and multicomponents steels [16], some of which include a geometric factor B [61].While there has been a growing literature on peritectic transformation during solidification [18], there are few models which allow researchers to predict SDAS with larger range of carbon content and alloy addition [62], [2]. However, these models are based on an empirical relationship with a best fit for range of carbon content and they do not take into account variation in coarsening parameter M and geometric factor B. This study aims at developing a new model that takes into account the effect of a

varying coarsening parameter M, geometric factor B on SDAS and peritectic transformation during solidification with a large range of carbon content of 0.08-1.4 %.

The following λ_2 can be expressed as a function of a geometrical factor B, the coarsening parameter M and the local solidification time t_f for binary steels.

$$\lambda_2 = B*M*t_f^{1/3} \qquad\qquad (2\text{-}1)$$

The growth of the dendrite morphology or arm spacings depends on the growth of the tip region as shown in figure 2-7.
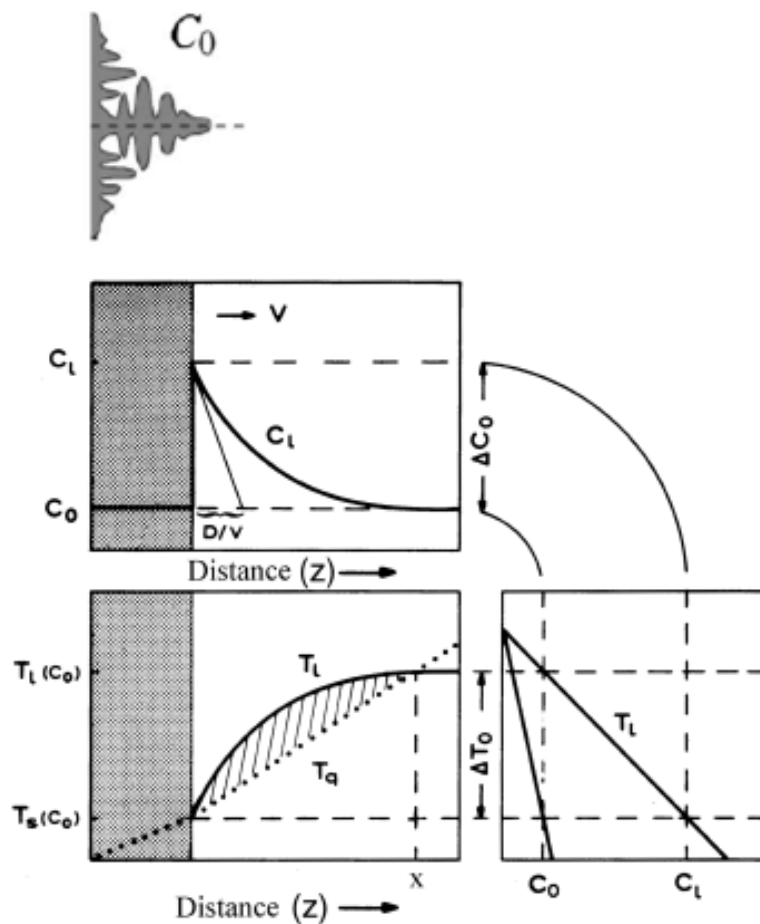
Figure 2-7: Grow of the tip of dendrite [63]

The planar growth front is unstable. The effects of curvature would be a major factor in the final, actual dendritic shape, but minor regarding whether it actually goes dendritic or not. If we imagine a pure metal growing into liquid, being at the liquidus temperature at the interface but then with a positive temperature gradient, any random perturbation

of the growth front will find itself in hotter liquid and melt back; the planar front is therefore stable. However, if it is growing into supercooled liquid (but remembering the interface is still at the liquidus / local equilibrium, i.e. with a negative temperature gradient into the liquid), any perturbation ahead of the otherwise planar growth front would find itself in cooler/sub-liquidus liquid, and would therefore be able to grow faster than the rest of the growth front. Therefore the planar front is unstable, and will break down into "fingers" of solid shooting out into the liquid and, eventually, dendrites will form.

In the case of an alloy; normally, there will be a positive temperature gradient, so how can dendrites form? Why would a planar interface be unstable? As in figure 2-7 we can see that, not only is there a temperature gradient but there is also a composition gradient. This varying composition will have a varying liquidus temperature accordingly. If a random perturbation is in a local liquid which has a liquidus temperature above the local temperature, despite the positive temperature gradient ahead of the otherwise planar front, i.e. so-called "constitutional supercooling", it will grow and hence the planar front will break down, then dendrites will form.

Suppose steel of composition C_0 is directionally solidified from temperature T_1 and T_2, the decreasing liquid composition influences the equilibrium melting temperature, T_l, which is shown by the solid line in the lower, left diagram of figure 2-7. If the actual temperature, T_q, shown by the dotted line, is less than T_l, therefore the liquid will be undercooled, and possibly dendrites will be formed [63] (the dendrites are very hard to avoid during continuous casting of steel due to significant levels of impurities).

In the case of steel, the possibility of kinetic undercooling has not been included as steel always exhibits a low entropy of melting, i.e. negligible driving force is needed to rearrange the liquid's atoms into the simple ferrite or austenite crystal structures. The

formation of secondary dendrite arm spacing depends on solidification rate or local solidification time [63], dendrite arm coarsening [64] and geometric factor [61] for both columnar and equiaxed zone. The local solidification time is defined as t_f, the time taken at a given location /depth in a steel bloom, billet and slab, for the temperature to drop from the liquidus to the non-equilibrium solidus [60]. The local solidification time is the main parameter controlling the SDAS in alloy steels. Many SDAS models assume a constant solidus temperature. However, in real continuous or ingot casting, the solidus temperature varies between the surface, mid way and centre during solidification, with differences in solidus temperature varying with the casting size, and casting conditions. SDAS should influence the extent of micro-segregation, and hence change the solidus temperature. In this research, we calculate the solidus temperature across the thickness using DICTRA software and QSP software.
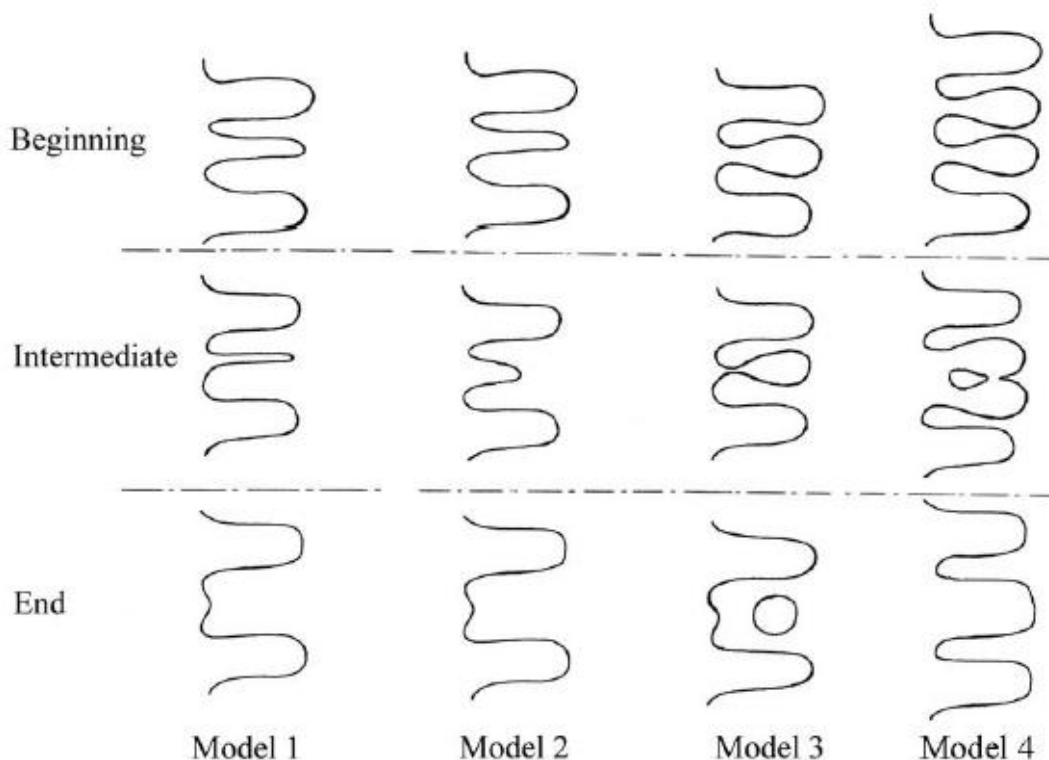
Figure 2-8: Four different models for isothermal coarsening: (1) radial remelting, (2) axial remelting, (3) arm detachment, (4) arm coalescence [65]

Figure 2-8 shows four different models for isothermal coarsening at different stages of solidification, beginning, intermediate and final stages: (i) model 1 shows radial remelting of a small arm and thickening of larger ones [66], (ii) model 2 shows remelting from tip to root of small arms [66], (iii) model 3 shows remelting of roots of small, tear-shaped arms [67], (iv) model 4 shows coalescence between arms [68]. The four models are undergoing the same process to minimize the interfacial energy of the dendritic microstructures. These models illustrate the overall complexity of dendritic microstructures [65, 69].

Rather than model a comprehensive theory of coarsening of dendrites, studies focus on measuring the secondary dendrite arm spacing, λ2, as it is easier to measure in the laboratory [65]. A relationship exists between the secondary dendrite arm spacing and the time evolution of the secondary arm spacing during coarsening [70], [63] commonly expressed as:

$$\lambda_2 \sim t_f^{1/3} \qquad\qquad (2\text{-}3)$$

Factors governing dendrite arm spacing, including competitive growth and ripening mechanisms are considered dominant at low solid fractions [71], [72]. Arm coalescence may become more effective at higher solid fractions if a coarsening mechanism continues to occur [73], [59], [74]. Some studies suggest that thinner secondary arms would melt, and the primary mechanism for the coarsening process is increasing in the diameter of thicker branches [5], [75]. At the theoretical level, Voller and Beckermann [76] showed that coarsening could be included in any micro-segregation models by adding an additional term to the Fourier number α_i (where α_i is a Fourier number for solute element i, $\alpha_i = \frac{D_{S,i} t_f}{X^2}$) in a one-dimensional micro-segregation model $\alpha_c = 0.1$ (where $\alpha_i^+ = \alpha_i + \alpha_c$), the smaller secondary arm spacing actually exists during solidification before the coarsening process [2]. The shape of the

cooling curve is shown to have an effect on micro-segregation level, with the effect of coarsening at the final stage of solidification [77]. Some models have extended the coarsening process to the case of peritectic transformation [78].

The effect of coarsening process during solidification on the final as-cast structure and the amount of undercooling has been studied by Kattamis and Flemings [79]. Using iron and nickel base alloys they concluded that the dendrite structure coarsened with time and that the secondary dendrite arm spacing decreased with increasing the amount of undercooling, and that λ_2 also increased with increasing the distance toward the centre (and hence time for coarsening). The dendrite shapes were considered to be either cylindrical or spherical in their study, depending on the amount of undercooling. The authors also conducted similar experiments on the effect of coarsening mechanism on secondary dendrite arm spacing using magnesium-zinc alloys [80], and aluminium-copper alloys The authors proposed two idealized models for coarsening during solidification: (i) A dendritic arm is thinner than the surrounding thicker arms, and suggests that the melting of the thinner arm occurs by means of solute transport to the thicker arms, which leads to increasing the secondary dendrite arm spacing, (ii) a tear-shaped dendritic arm situated between cylindrical arms, which suggests the tear-shaped arm is melting off at its roots, by transport of material to its tip, and eventually pinches off [65] as shown as figure 2-9.
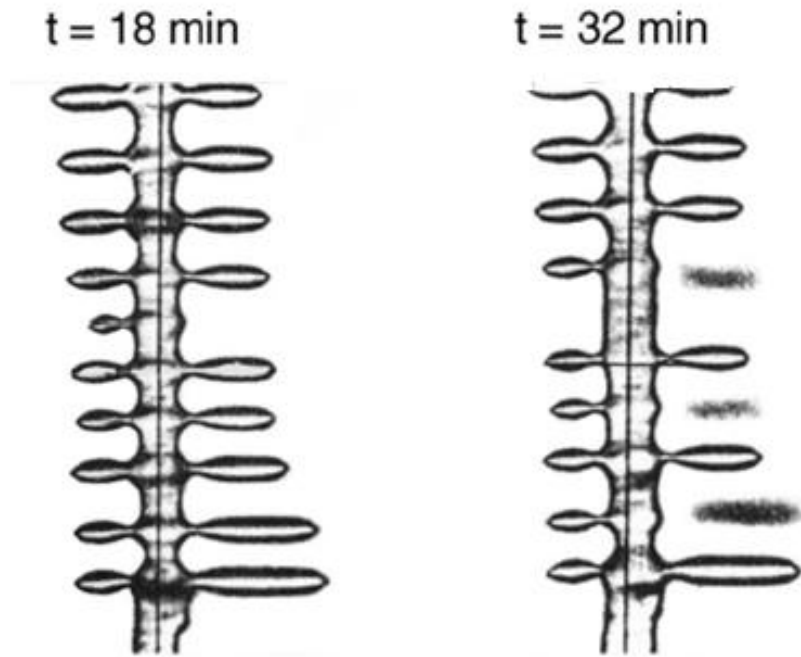
Figure 2-9: Separation of dendrite arm in NH$_4$Cl [65]

The type of dendritic microstructure is either columnar or equaxed zone, depending on how heat is extracted [69]. Equiaxed grains have a tendency to grow dendritically for two reasons; (i) the thermal profile of the equiaxed grains melt at a higher temperature than the surrounding melt causing perturbations to grow preferentially, (ii) addition of alloying elements help the formation of perturbations which grow and form dendrites [59].

2.6 Modelling dendrite arm growth in multicomponent alloys

While the prediction of secondary arm dendrite spacing has been much studied for binaries using experimental measured data [62], [81], there are fewer studies on multicomponent steels. The expression of secondary dendrite arm spacing is a function of local solidification time and dendrite arm coarsening parameter [64], [60], [82]. Few studies have examined the effect of multicomponents on micro-segregation and dendrite arm coarsening in solidified steels that contain elements that cause secondary dendrite arm spacing to be different from surface to centre (for big sections).

Kirkwood [60] investigated a simple model for dendrite arm coarsening. He proposed the following equation of secondary arm spacing in the case of short times:

$$\lambda_0{}^3 = -\frac{128D\sigma T}{Hm\,C_1(1-k)}t_0 = Mt_0 \qquad (2\text{-}4)$$

When the eutectic reaction occurs at the end of solidification, and liquid of composition C_0 is in the interdendrite at t_f, the proposed equation of secondary arm spacing can be written as [60].

$$\lambda_f{}^3 = -\frac{128D\sigma T\ln(C_e/C_o)}{Hm\,C_1(1-k)(C_e-C_0)}t_f = Mt_f \qquad (2\text{-}5)$$

From figure 2-10, we can see that λ_2 is a function of local solidification time plotted versus secondary arm spacing in Al-4.5%C alloys. The theoretical prediction of equation (3) follows closely empirical predictions based on the experimental data.
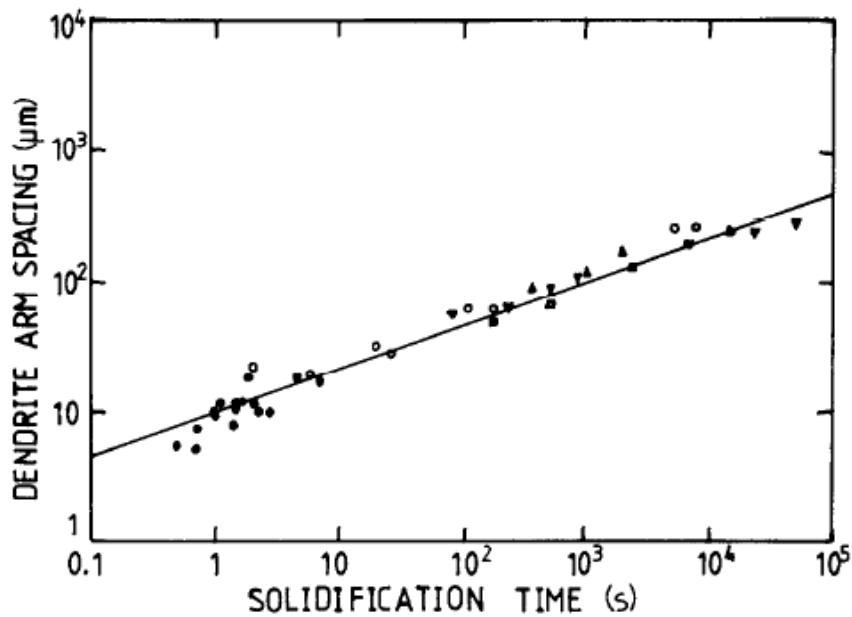
Figure 2-10: Secondary dendrite arm spacings plotted against local solidification time [60]

Beaverstock [64] was first to consider the effect of multicomponents on secondary dendrite arm coarsening and micro-segregation, extending the binary model

of Kirkwood. Based on the Gibbs-Thomson relationship (dT = KσT/H), the superheating of the shrinking tip decreases by solute levels (dt = $\sum m_i dC_{li}$). He obtained an equation for multicomponent secondary arm coarsening.

$$\lambda_2^2 d\lambda_2 = B \sum M_i \, dt \tag{2-6}$$

where M_i is an isothermal coarsening parameter for solute i

B is a geometric factor which is function of fraction solid

t is time

$$M_i = \frac{\sigma T D_{li}}{H(k_i - 1)m_i C_{li}} \qquad B = \frac{4}{f_s^2(1 - f_s)}$$

Beaverstock [64] also found that dendrite arm coarsening was controlled by elements having a partition coefficient around unity. In steels, major alloying elements are manganese, chromium, and nickel. Other studies also found that carbon has significant effect on secondary dendrite arm spacing [2], [62].

Beaverstock's model and Kirkwood's model have the same expression for dendrite arm coarsening. The main difference between these two models is the geometric factor B in Beaverstock's model which is a function of solid fraction and it has been less studied.

Pierer and Bernhard [62] studied the influence of carbon on secondary dendrite arm spacing in steel. Their model has the expression of $\lambda_2 = K * t_f^{1/3}$ for steels having a larger range of carbon content (0.08-0.7%). Finally, they proposed the following empirical relation:

$$\lambda_2(\mu m) = (23.7 - 13.1 \text{wt.%C}^{1/3}) t_f^{1/3} \tag{2-7}$$

The expression of K is made a function of carbon content; equation (2-7) shows that increasing carbon content decreases the value of λ_2, shown as figure 2-11.
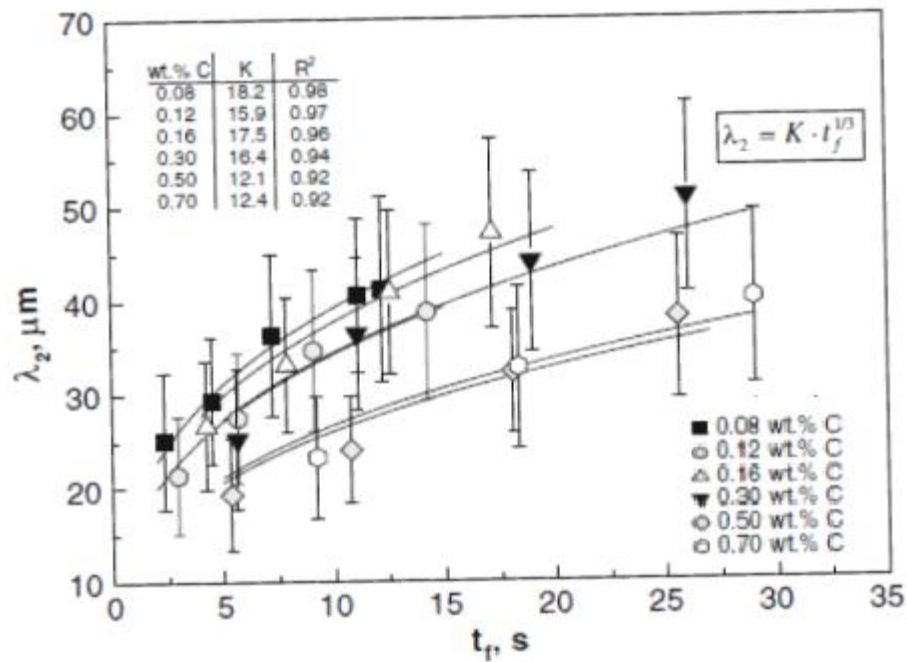
Figure 2-11: Secondary dendrite arm spacing is function of local solidification

time [62]

A comparison of predicted λ_2 with the measured experimental data indicates a high R-squared (0.92-0.98) for a large range of carbon content of 0.08-0.7%. K values decrease from 18.2 to 12.4 when carbon content increases.

2.7 Previous studies on solute diffusion during solidification and cooling

Several attempts have been made to predict the transformation occurring during alloy solidification, for example as in the continuous casting process. The modelling of micro-segregation has emerged as a major field in prediction assuming finite or complete diffusion in the liquid, incomplete diffusion in the solid phase, dendrite arm coarsening and multi-components [83]. Micro-segregation of an alloy during solidification is described as the mass diffusion or convection controlled redistribution of rejected solute elements at the scale of the solid-liquid interface [83]. Beckermann et al. [84] investigated the complex interactions taking place among various physical phenomena which occur on different length scales. The microscopic mechanisms to be

33

incorporated in the dendritic solidification include nucleation, back diffusion, growth kinetics and the dendrite morphology [85].

Such models assume a representative volume element or cell between a secondary dendrite arm. This model arises from the conservation of solute at the interface advancing: it means that the amount of solute which is rejected from the interface must equal the extra solute accommodated between the residual liquid and the solid shown as figure 2-12.

Fraction or distance across representative cell or dendrite
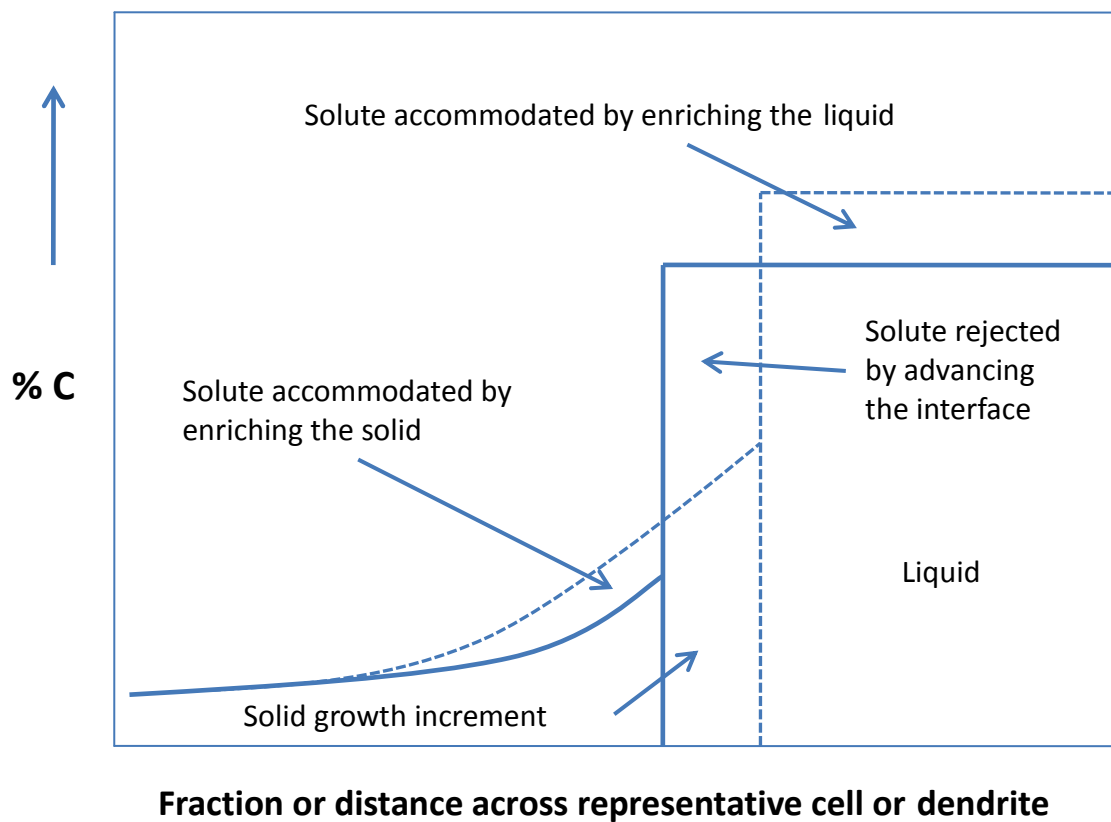
Figure 2-12: Schematic concentration/fraction plot showing the key components for the solute balance equation [86].

The existing solute diffusion models for dendritic solidification are classified into three distinctive groups [87]: (i) local-equilibrium models which do not incorporate nucleation and undercooling; (ii) solute diffusion models for columnar growth which incorporate dendrite tip undercooling; (iii) solute diffusion models for equiaxed growth

which focus on coupling the growth kinetic of dendrite tips to the evolution of an equiaxed grain.

Spittle et al. [88] used a Monte Carlo method to develop a computer model for simulating dendrite solidification. A cellular automata (CA) coupled with a macroscopic calculation of temperature were used by Rappaz and Grandin [89] in order to simulate grain structure formation during solidification. Yang et al. [90] investigated the measured composition profile by a Monte Carlo simulation approach; in their study, two aspects of the method was examined. The first method were associated with the random sampling, such as the effect of the random distribution of a limited number of sampling points, and the second was the scatter in composition measurement.

Solute diffusion was studied for the direct simulation of solidification by phase-field methods and other diffuse interface approaches [91]. By introducing an order parameter φ (phase field), that may assign a value of $\varphi = 0$ for the solid phase and $\varphi = 1$ for a liquid phase. A continuous variation of the order parameter between the equilibrium values represents the transition between the solid and liquid phase. Caginalp [92] applied a phase field model which is considered useful to treat macroscopic aspects of phase transformation for solidification of pure material [93] and later, extended for multi-phase and multicomponent steel by Sakai [93].

Beckermann et al [94] proposed a novel diffuse interface model which is presented for the direct numerical simulation of microstructure evolution in solidification processes. This model involved convection in the liquid phase. Phase-field theories are the solidification front treated as a moving interface in the diffuse approximation. He investigated two examples which involve solid/liquid phase-change: (i) both the interface curvature and the flow permeability evolve the time for coarsening

of mush of a binary alloy, and (ii) dendrite growth in the presence of melt convection with emphasis on the operating point of the dendrite tip.

In the case of local equilibrium solidification models (i.e. at the interface), the primary objective of modelling is to investigate the effect of back diffusion in the solid while assuming that the liquid is solutally well mixed [95], [96], [97]. Depending on the extent of solute diffusion in the solid, three basic analytical equations have been obtained; (1) the Lever rule model where complete diffusion to equilibrium of all alloying elements in both the liquid and solid phases is assumed; (2) The Scheil equation which assumes no solute diffusion in the solid phase, complete solid diffusion in the liquid phase, and local equilibrium at the solid-liquid interface; and (3) the Brody-Flemings model which assumes complete diffusion in the liquid phase and incomplete back diffusion in the solid phase as well as a fixed dendrite arm spacing as a plate dendrite.

More specifically, the Lever rule model can be written as:

$$C_{L,i} = \frac{C_{0,i}}{1-(1-k_i)f_s} \qquad (2\text{-}8)$$

Where

$C_{L,i}$ denotes the liquid concentration of a given solute element at the solid-liquid interface, wt.%

$C_{0,i}$ is the initial liquid concentration, wt.%

k_i is the equilibrium partition coefficient for element i, wt.%/wt.%

f_s is the solid fraction.

The Lever rule underestimates the degree of micro-segregation, especially for the interfacial / slower diffusing elements. The underestimation becomes progressively more marked towards the end of solidification [2].

Under the Scheil equation, $C_{L,i}$ is expressed as:

$$C_{L,i} = \frac{C_{0,i}}{(1-f_S)^{1-k_i}}$$
(2-9)

However, this overestimates the degree of micro-segregation, and the estimation of the final solute concentration under this category of models is problematic since $C_{L,i}$ becomes infinite at $f_s = 1$. Sarreal et al., [98] found that the Scheil model [99] is only applicable under very rapid solidification processes such as laser welding with the cooling rate exceeding 10^2 k/s [2].

Under the Brody-Flemings model $C_{L,i}$ is expressed as:

$$C_{L,i} = C_{0,i}(1 + f_S(\beta_i k_i - 1))^{(1-k_i)/(\beta_i k_i - 1)}$$
(2-10)

Where β_i is known as a back diffusion parameter, which should be restricted to values between zero and one depending on the nature of mass diffusion in the solid phase [6]. In the Brody-Flemings model [100] β_i is expressed a function of Fourier number of solute element i (α_i):

$$\beta_i = 2\alpha_i$$
(2-11)

Where α_i is in turn specified as:

$$\alpha_i = \frac{D_{S,i} t_f}{X^2}$$
(2-12)

where $D_{S,i}$ (m^2/s) denotes the diffusion coefficient of solute element i in the solid phase, t_f (s) the local solidification time from liquidus to solidus temperature and X (µm) the half of the secondary dendrite arm spacing or the length scale of the micro-segregation domain.

The key feature in the micro-segregation models is the back diffusion parameter, which depends on the nature of mass diffusion in the solid phase, this parameter takes values between 0 as no mass diffusion in the solid phase and equal 1 as complete mass

diffusion in the solid phase [83].The problem with Brody-Flemings model is that for large values of α, $β_i$ exceeds one.

When discussing the balancing factors for increasing/decreasing micro-segregation, Brody and Flemings showed that for calculations with a fixed dendrite arm spacing, if that spacing was proportional to the square root of time then the degree of micro-segregation at the solidus would be the same. More recently, Howe showed that with inclusion of dendrite arm coarsening, if the coarsening law was with the square root of time, then likewise the degree of micro-segregation would stay the same regardless of the heat extraction (cooling) rate. Moreover, the observed increase of micro-segregation with increasing cooling rate meant that the coarsening law exponent had to be below a half (the typically quoted value of one third) [101].

More recently, Ohnaka [102] has modified the Brody-Flemings model by rewriting the expression for the back diffusion parameter as follows:

$$β_i = 2α_i /(1+2α_i) \qquad\qquad (2\text{-}13)$$

The Ohnaka model uses approximate solutions of the diffusion equation applying for plate dendrites, which assumes a quadratic solute concentration profile in the solid phase [2].

Clyne and Kurz's [103] modifies the back diffusion parameter as follows:

$$β_i = 2α_i[1\text{-}exp(\text{-}1/α_i)] – exp(\text{-}1/2α_i) \qquad\qquad (2\text{-}14)$$

The above models make simplifying assumptions for the back-diffusion term. Kobayashi [104] obtained a true solution for micro-segregation which assumes incomplete back diffusion in the solid phase, complete diffusion in the liquid phase, constant diffusivity, constant partition coefficient, and a parabolic solidification rate.

The Kobayashi and Clyne-Kurz or Ohnaka models all assume parabolic growth and constant diffusivity. When the value of k_i and α_i are low, the Kobayashi model shows significantly more segregation, implying that the Clyne-Kurz and Ohnaka models are seriously wrong. When the values of k and α are high, Kobayashis' results are similar to those of the Clyne-Kurz or Ohnaka model [86].
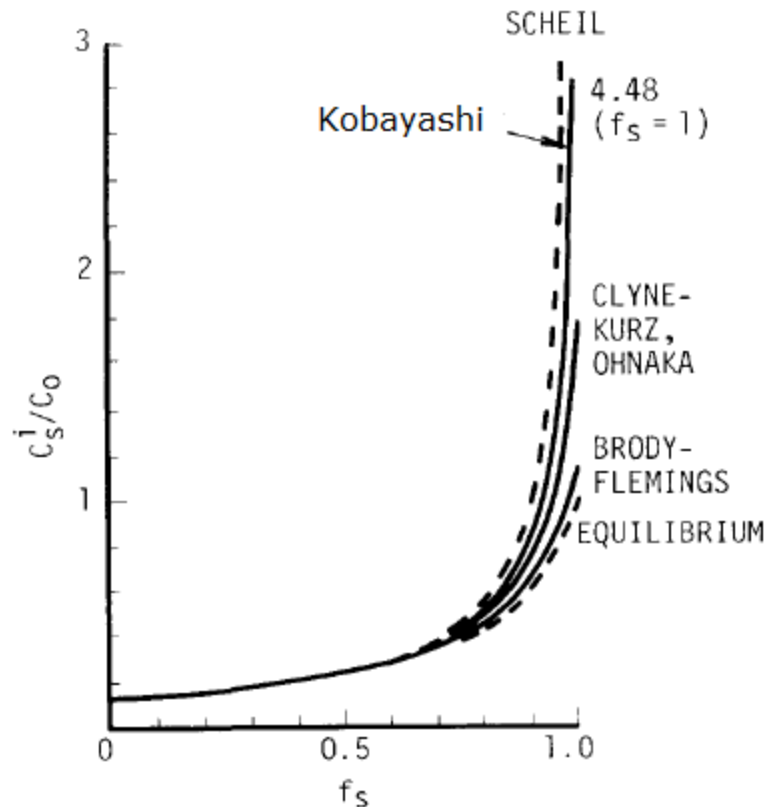
Figure 2-13 : Comparison of Kobayashi's result with other equations for the evolution of the segregation ratio with fraction solid: phosphorus in ferritic iron, k = 0.13, α = 0.4 and D = 4x10^{-11} m2/s [86]

Figure 2-13 provides a comparison of Kobayashi's results with other equations for the evolution of the segregation ratio. The Clyne and Kurz's results are almost the same as the results of Ohnaka. Kobayashi' true solution comes close to the Clyne and Kurz's result up to about 90% fraction solid, but it rises rapidly to a C_s/C_0 ratio of 4.48 at fraction of solid equal to 1, as compared to 1.8 in the Clyne and Kurz model [104]. Also, regarding the Clyne-Kurz and Ohnaka -v- Kobayashi, debate Howe [86] has

shown that if the restriction to parabolic growth is removed, then a simple model based on a back-diffusion parameter can then be much closer to the Kobayashi solution. However, this does require an iterative solution rather than being represented by a single equation.

Howe [78] has developed a solidification and micro-segregation model that operates far faster than others available, which is a fully numerical models but with a more accurate basis than the other models available, which use analytical approximations.

Chapter 3: Experimental Procedure

3.1 Materials

The continuously cast high carbon bloom steel used in this study was supplied by Tata Steel Europe from the Scunthorpe steel plant. The bloom steel sample had dimensions of 283x230 mm and was cast at a target casting speed of 1.3 m/min. The nominal compositions of the as-cast material are given in table 3-1.

Table 3-1. Chemical composition of high carbon bloom steel (wt.%)

C	Si	Mn	P	S	Cr	Ni	Al	Cu	N
0.72	0.24	0.63	0.016	0.018	0.02	0.02	0.001	0.033	0.004

3.2 Secondary dendrite arm spacing measurements

A longitudinal section from the surface to centre was cut off in order to measure secondary dendrite arm spacing. After cutting samples of 10 mm thick from the surface toward the centre following the nodal positions of the macro-model results, all samples were mounted using a mounting press and were prepared using standard grinding procedures beginning with180 grade silicon carbide paper and finishing with 1200 grade silicon carbide paper.

Once all the samples were ground, the samples were washed in water followed by alcohol and dried before being polished. The polishing process used first 3 and then 1 micron diamond paste in order to produce a mirror-like finish on the sample without any scratches.

Once all the samples were polished, the samples were washed in alcohol, dried and then the samples were left to sit in air for 24 h before being etched..All samples were etched with Oberhoffer's reagent which had a composition of 500 ml H_2O, 500 ml Ethanol, 1g $CuCl_2$, 30g $FeCl_3$, 50 ml HCl, 0.5g $SnCl_2$. Oberhoffer's reagent was used because of the excellent results that can be obtained.
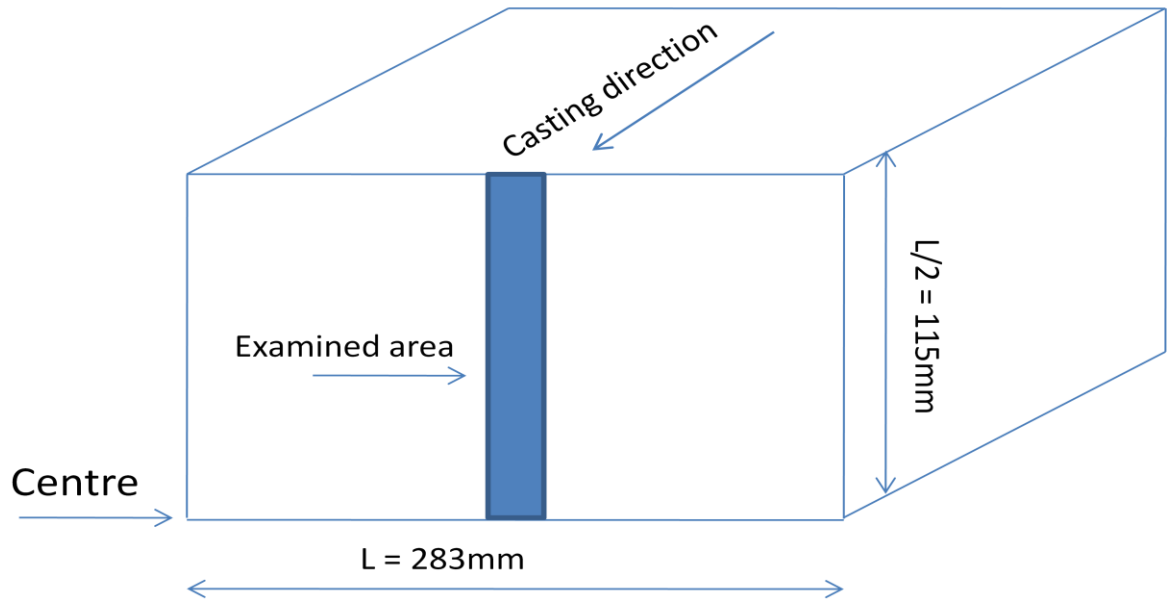
Figure 3-1: High carbon bloom steel Dimension of 0.72%C, 283x230 mm

The microstructure of the high carbon steel was then examined and photographed with an optical microscope (POLYVAR) in order to measure the secondary dendrite arm spacing values at different bloom depths. For the secondary dendrite arm spacing standard measurements, the measurements were made close to and parallel with the primary dendrite branches. At least four or five secondary arms per primary arm were counted within each bloom depth, and at least eight or nine measurements were recorded in order to get the average and standard deviation SDAS of each position [64] as shown in figure 5-2. The results of the secondary dendrite arm spacing measurements are reported in table 5-1.

3.3 Modelling method

3.3.1 QSP Introduction

QSP software was developed by Howe [105], and is a simple computer model of solidification at the micro-scale and the accompanying micro-segregation; this model is expected to be operated much more quickly than the available numerical models [105]. QSP software is now readily available and is free for Universities collaborating with

Tata Steel. QSP software allows prediction of the residual liquid composition and temperature as solidification proceeds. It is used for carbon and low alloy steels containing C, Si, Mn, P, Cr, Mo, Ni, Nb, V, Ti, O and N. The software has been validated up to 1%C and other major alloying elements totalling up to 5% [105]. The QSP software is a more user-friendly window version which is now available for use as a tool for various calculations such as [105].

1. Solidification pathways, notably with respect to peritectic transformation

2. Temperature range and fraction solid profile across the mushy zone

3. Extent of micro-segregation during and at the completion of solidification

4. Solute homogenisation and segregation during cooling

5. Propensity for TiN inclusion from the residual liquid

6. Propensity for NbCN precipitation from the enriched solid

The software assumes a 1-D representative cell of half the dendrite arm spacing (assuming planes of symmetry on either side of this region) for interdendritic solidification, as illustrated in figure 2-12) for the case of single phase solidification. The key equation for the micro-segregation model is given by the following solute balance [106]:

$$C_L (1-k)\dot{r} = D.\left\langle \frac{dC_S}{dr} \right\rangle_{Int.} + (r_0 - r)\dot{C_L} .$$ (3-1)

where C_L is the liquid concentration at a given time, k is the partition coefficient (solid concentration/ liquid concentration), r is distance solidified across the cell, the cell width being r_0, D is the solute diffusivity, dC_S/dr is the concentration gradient in the solid; a raised dot signifies the time derivative and the subscript Int. signifies at the solid/liquid interface.

In equation 3-1, the three terms represent: (i) the rate of solute rejection as the interface advances, (ii) the rate of solute acceptance by "back diffusion" and (iii) enrichment of the residual liquid.

In QSP software, if a solution is required, it does not require the actual calculation of the solute profiles across the solid. Especially, the gradient at the interface can be found by re-writing the solute balance as follows:

$$D.\left\langle \frac{dC_S}{dr} \right\rangle_{Int.} \rightarrow D.\frac{dC_{S,Int.}}{dr_{Int.}} = Dk\frac{\dot{C}_L}{\dot{r}} \rightarrow \frac{D/r\dot{r}}{1 + D/r\dot{r}}.rk\dot{C}_L = \frac{D}{(D + r\dot{r})}.rk\dot{C}_L = Ark\dot{C}_L \quad (3\text{-}2)$$

The first term $D.< \frac{dC_S}{dr} >_{Int}$ is often approximated (Brody/Flemings et al) by the

second term $D.\frac{dC_{S,Int.}}{dr_{Int.}}$ (D times the change in interface concentration with distance).

This becomes progressively poorer an approximation the more "back diffusion" there is: it is correct for Scheil behaviour, but it is not good for equilibrium behaviour. However, where it is good enough, it allows us to progress with an analytical formulation and thus to a solution to the solute balance equation. It equals the third term in the string of terms covered by equation 3- 2. The third term equals the fourth term, if the fourth term didn't have the $(1 + D/r\dot{r})$ underneath. However, by approximating it by what is actually written as the fourth term in equation 3-2 (hence the arrow), we avoid the big problem caused by the first approximation: with this second approximation, when D gets very large as for approaching equilibrium, this part of the solute balance now tends to the correct term again. So, with this second approximation, it is still accurate enough for near-Scheil / low D cases ~ $(1 + D/r\dot{r})$ is essentially 1, and for very high D cases, (

$\dfrac{D/_{r\dot r}}{1+D/_{r\dot r}}$) tends to 1, which is correct for equilibrium. The remaining two terms are

straight algebra, i.e. equations, not further approximations, with the definition of A. This term is correct for use within the solute balance for both very low and very high D solutes, and pending experimental verification, therefore might well be reasonable for in-between D cases also.

For the case of a single phase solidification, the solute balance becomes (by substituting equation 3-2 to equation 3-1):

$$C_L(1-k)\dot r = Ark\dot C_L + (r_0 - r)\dot C_L = (r_0 - (1-Ak)r)\dot C_L \qquad (3\text{-}3)$$

Where A is back diffusion parameter varying from 0 for Scheil, to 1 for the Lever Rule behaviour.

$$A = \frac{D+0.1}{D+r\dot r+0.1} \qquad (3\text{-}4)$$

In equation 3-4, the value D is $10^{-9}m^2/s$, for convenience within the QSP software, these are multiplied by 10^{12} to be in units of $\mu m^2/s$ for calculation of the A parameters, because λ_2 is similarly in µm units (see appendix 7).

For multicomponent steels, each solute has its specific solute balance equation as above, but its growth rate is the same, and is controlled by simultaneous solution with the thermal balance equation:

$$\dot Q = H\dot f_s + \theta\dot T \qquad \text{where } \dot T = \sum m_{L,i}\dot C_{L,i} \qquad (3\text{-}5)$$

The heat extraction rate, $\dot Q$, is imposed by the user, H is the latent heat of solidification, f_s is the fraction solid, θ is the heat capacity, T is the temperature in K, and m_{Li} is the liquidus slope for the solute i.

46

The major benefit of this software is its ability to predict micro-segregation in peritectic alloy systems [23]. The three phase peritectic reaction is encountered with carbon and low alloy steels. The assumption for the rapid solution scheme was that carbon dominated the relative velocity between austenite / ferrite and austenite / liquid interfaces shown in figures 3 -2 and 3.
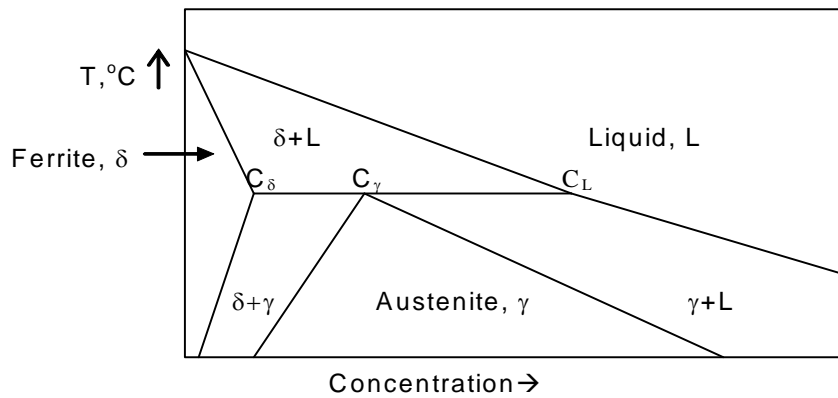
Figure 3-2: Schematic section of a peritectic phase diagram

Fraction or distance across representative cell
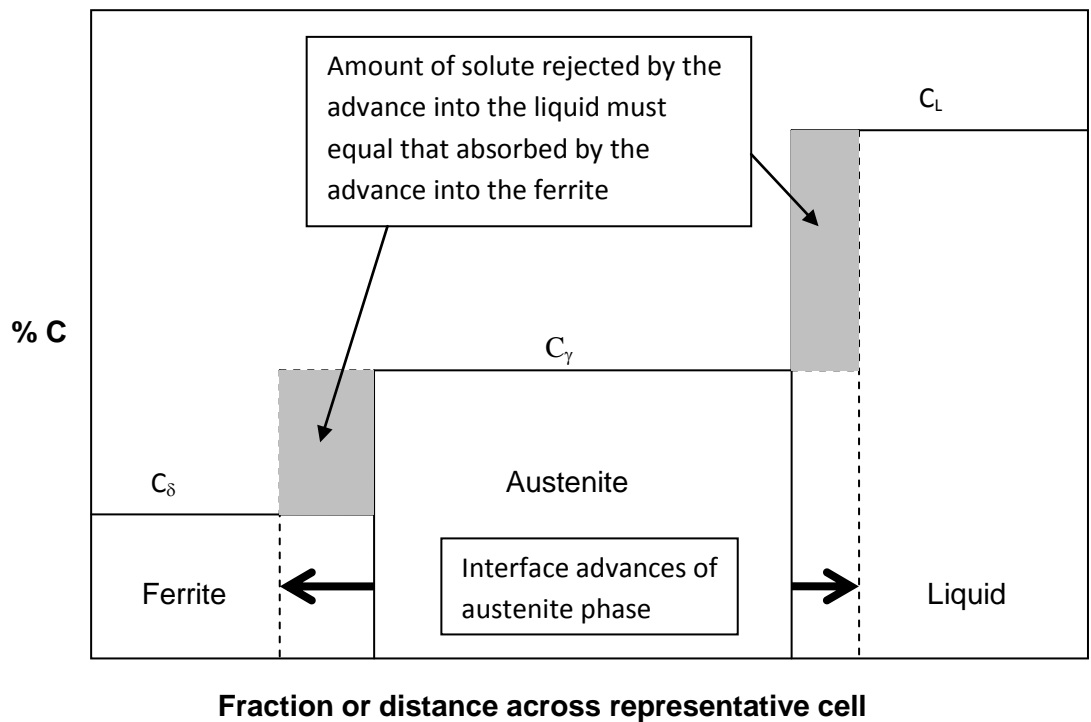
Figure 3-3: Schematic solute balance for carbon during the peritectic,

maintaining constant concentrations in each phase.

The QSP model has the ability to handle steels which deal with all or part of the peritectic transformation [106]:

$$L \to L + \delta \to L + \delta + \gamma \to L + \gamma \to \gamma, \qquad (3\text{-}6)$$
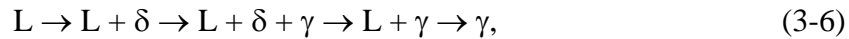
where L is liquid, δ is ferrite (bbc) and γ is austenite (fcc).

Howe's model [106] considers the equilibrium (complete mixing) cases for carbon and a "passenger" element, upon a step advance of the austenite phase based on both the liquid and ferrite. The solid lines in figure 3-4 represent "before" and the dotted lines represents "after". The detail for the solute balance was described in Howe's paper [106].
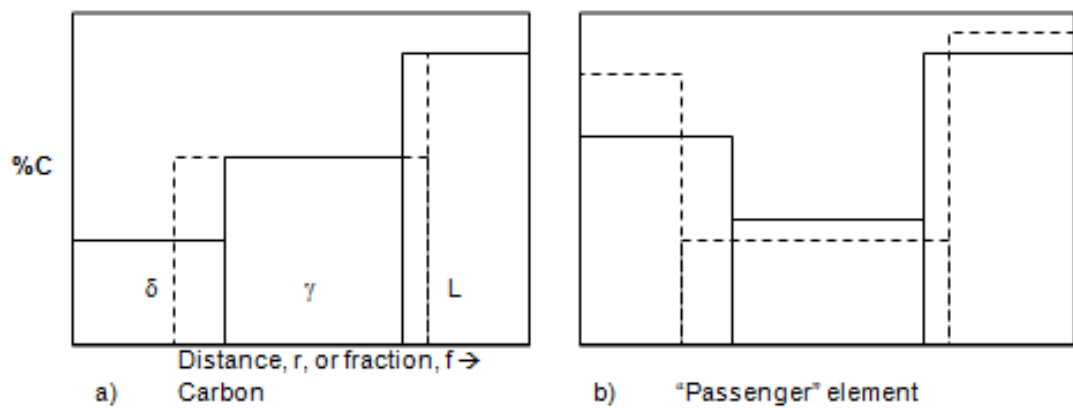
Figure 3-4: Schematic solute balances with complete mixing / infinite diffusivity

In the course of the peritectic reaction (the essence is that carbon is dictating what the phase proportions are during the peritectic reaction, and the slow-diffusing elements just react to this), the passenger element cannot also keep constant phase concentrations with the relative interface advance being dictated by another element. Indeed, in the "passenger" element case with this element exhibiting lower concentrations in the austenite than the ferrite, i.e. being a ferrite stabiliser, it would not of itself exhibit the three phase reaction at all [106].

Once composition and heat extraction rate is entered, the calculation is performed, and assumed to start when the liquidus temperature has been reached. Two cases will be run with secondary dendrite arm spacing; the first case runs the program with a constant dendrite arm spacing, a zero should be entered in the data / text box for the arm coarsening coefficient, and final value of secondary dendrite arm spacing in the data / text box. The second case runs the program with a coarsening dendrite, and a coarsening coefficient M_0 ($\mu m/s^{1/3}$) is entered in the data / text box.

The expression of secondary dendrite arm spacing is as follows:

$$\frac{\lambda}{2} = M_0 . t^{1/3} \tag{3-7}$$

Micro-segregation calculation:

Figure 3-5: User interface of the QuikSeg Peritectic (QSP) program

In this example, high carbon bloom steel was calculated at the 11.5mm depth. The solidus has just been reached, the calculated element concentrations in the liquid, core gamma and max solid are displayed in the element concentrations frame.

Once the concentration of the steel, secondary dendrite arm spacing and heat extraction rate are entered into the general "input" frame, clicking the **Start** button results in the software calculating the initial solidification phase as bbc (ferrite) or fcc (austenite), the liquidus temperature, equilibrium solidus temperature, and the final dendrite arm spacing. The results appear in the data boxes in the general input field.

Once the results appear in the white data boxes in the general input field, by clicking the **solidification increment** button, each click corresponds an increase in the solid fraction of 0.1. The calculated element concentrations in the liquid, core delta, core gamma and max solid are displayed in the "Element Concentration" frame. General system data including time for solidification, liquidus, current temperature, fractions of phase present, and the "Peritectic Equivalent" are displayed to the right of the solidification increment button.

Calculation of sub-solidus homogenisation

If the user wants to calculate sub-solidus homogenisation which is determining the residual micro-segregation after cooling in the solid, the program can continue sub-solidus which is assuming a single solid phase. Once the software reaches a fraction solid of one (completion of solidification at solidus), the user can enter a lower temperature, and a modified heat extraction rate in the solid phase that is based on cooling curve. Clicking the **Homogenise** button results in the program calculating the corresponding decrease in peak and rise in core concentration and the results are displayed in the element concentrations frame. For the carbon and low alloy steels of interest, it transforms quite quickly to austenite on further cooling. The program

undergoes purely the homogenisation of single phase austenite with the power law solute profile [105].
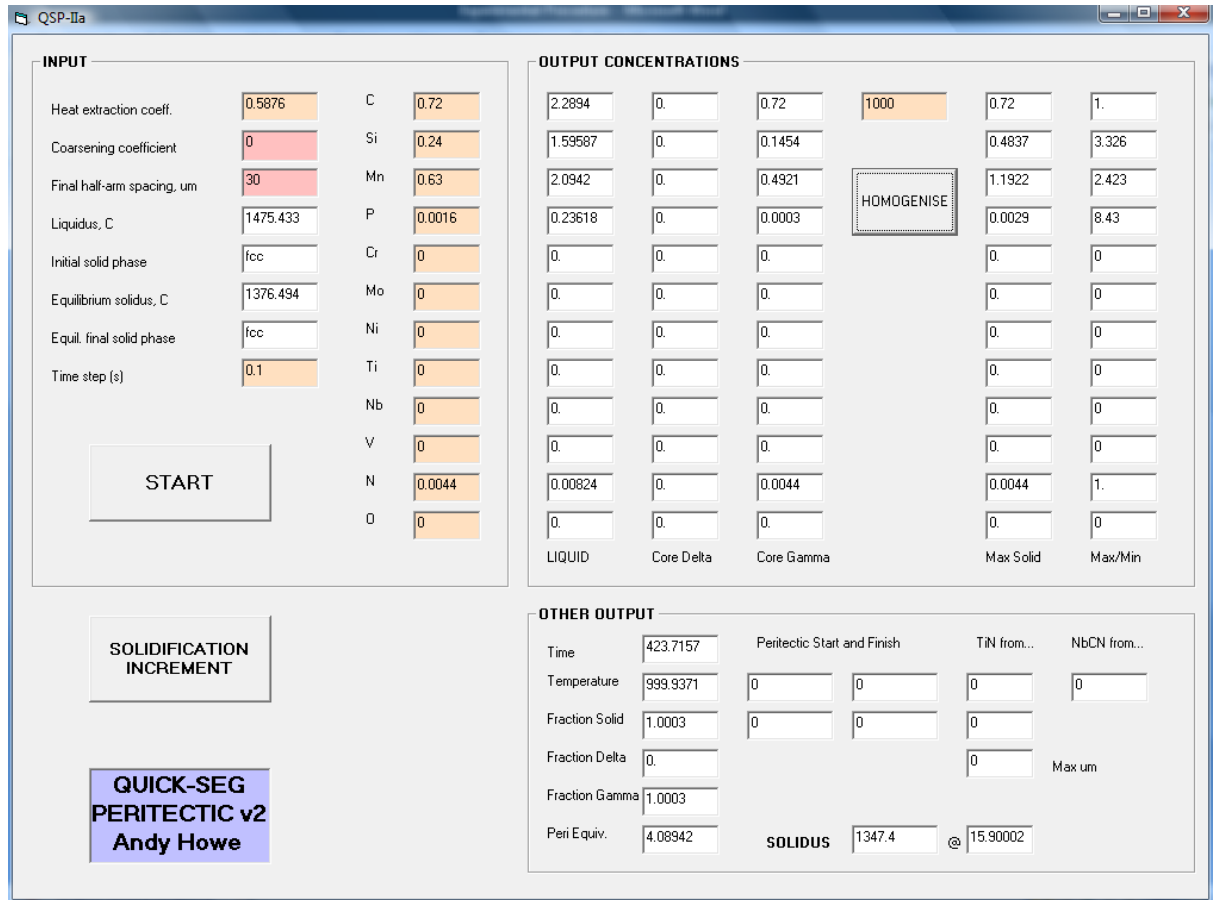
Figure 3-6: User interface of the QuikSeg Peritectic (QSP) program

In this example, high carbon bloom steel was calculated at the 11.5mm depth. The solidus has just been reached, the calculation sub-solidus homogenisation at 1000 ℃ has begun. The program calculates the corresponding degree in peak, and rise in core, and the results are displayed in the element concentrations frame.

3.3.2 DICTRA introduction

DICTRA (Diffusion controlled TRAnsformation) is widely used for simulation of diffusion controlled transformation in multicomponent steels. It works linked with the Thermo-Calc software, which supplies all the necessary thermodynamic calculations [107]. It has been used successfully to simulate complex system, for example, micro-segregation during solidification and homogenization of AerMet 100 steel [108].

However, the DICTRA software can only handle one dimensional (planar, cylindrical and spherical) geometries [107].

The DICTRA calculation scheme is described in figure 3-7 and it consists of two steps. The diffusion step is called the first step, which is simply a one phase problem since all diffusion occurs in a matrix phase. However, the composition change in the matrix during the diffusion step and the new equilibrium is then calculated from the new average composition using Themo-Calc. The diffusion step is then repeated and this provides the new composition profile in the matrix phase, etc. [107].
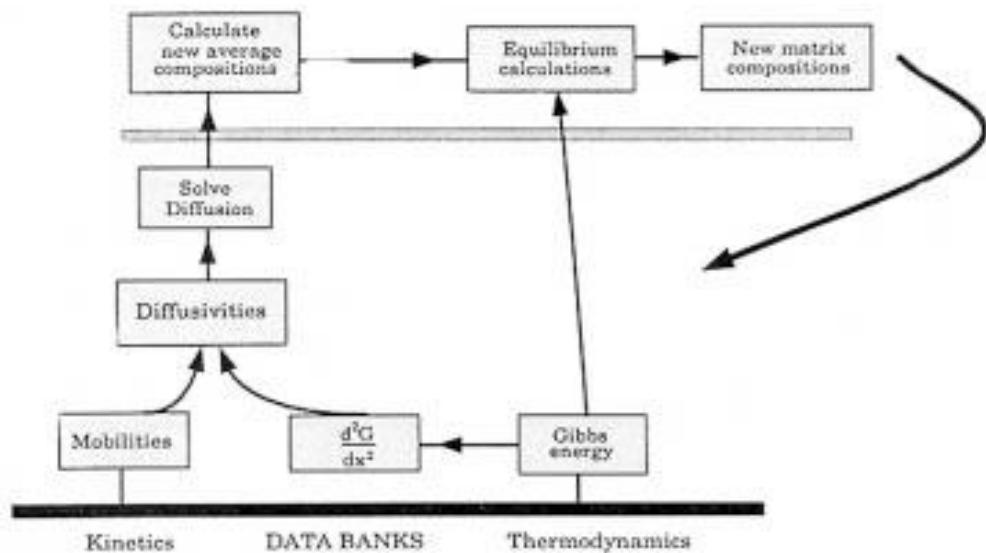
..Figure 3-7: The calculation scheme used in the model for diffusion in dispersed systems [109].

3.4. Micro-segregation measurements

Once the SDAS structure had been revealed by the etching process as described in section 3-2, the same samples were used to investigate the micro-segregation of silicon and manganese using the EDS-SEM technique on a JEOL6400 Scanning Electron Microscope

Example measurements of micro-segregation were conducted using automated line scans using EDS-SEM through between 2 and 4 secondary dendrite arm spacings

for each bloom-depth. The working conditions of the EDS-SEM setup were an accelerating voltage of 20 kV, a working distance of 15mm, a live time of 50 (s) and a process time of 3 (s). The dead time was adjusted to around 26% during the automated line scan. All EDS-SEM measurements were carried out using these parameters which were found to yield more accurate results for this Si and Mn micro-segregation investigation.

Chapter 4: Secondary Dendrite Arm Spacing Models

A strong relationship between the secondary dendrite arm spacing and the properties of the final products has been reported in the literature [62], [96], [110], [5]. During the solidification, the secondary dendrite arms tend to increase their spacing (in order to reduce the curvature and interfacial energy), this increasing spacing is strongly dependent on the solidification rate and the time spent in the liquid-solid region called the local solidification time. The other important factor to control the secondary dendrite arm spacing is the nature of the alloys, but this effect is typically difficult to examine due to the effect of the cooling rate.

4.1 Description of current work

There are many secondary dendrite models for binary steels; some models have been extended for the prediction of dendrite arm coarsening in multicomponent steels. So far, however, there has been little discussion about peritectic transformations during solidification.

The expression of λ_2 is as follows;

$$\lambda_2 = M_0.t_f^{1/3} \tag{4-1}$$

Where: M_0 is the coarsening parameter; t_f is the local solidification time.

Kirkwood and other researchers [60], [111], [72], [112] have extended the secondary dendrite models based on the concept of Fick's law and the Gibbs-Thompson equation. The following λ_2 can be expressed as a function of a geometrical factor B, the remaining coarsening parameter M and the local solidification time t_f for binary steels.

$$\lambda_2 = B_0.M.t_f^{1/3} \tag{4-2}$$

$$M = \frac{\sigma T D_{Li}}{H(k_i-1)m_i C_{Li}} \quad , B_0 = \frac{4}{f_S^2(1-f_S)}$$

Where: M is coarsening parameter for solute i

k is the partition coefficient for solute i, wt.%/wt.%

55

m_i is the liquidus slope, K/wt.%

B_0 is the geometrical factor

H is the heat of fusion, kj/mol

σ is the interfacial energy, kj/m^2

D is the diffusivity, m^2/s

However, a major problem with the above equation is that it is developed for binary steels, but it is not applicable or valid for multicomponent steels. Commercial steels, contain more than one solute element which influences the secondary arm coarsening during solidification, especially regarding to the solidus temperature, liquid-solid diffusion and micro-segregation effects to the secondary dendrite arms.

The original work of Beaverstock [64] considered the effect of secondary arm coarsening on the level of micro-segregation in binary alloys in the manner of Kirkwood. However, the model has been extended to multicomponent alloys under the assumptions of a constant cooling rate and no solid-state diffusion.

Based on Beaverstock' model for one element (using a differentiated version of equation 4-2, with modified constant B and M);

$$\lambda_2^2 d\lambda_2 = B_0.Mdt = B_o \frac{\sigma T D}{H(k_i-1)mC_{Li}} dt \tag{4-3}$$

Where: $mC_{L,i}$ is the liquidus depression

k_i is the partition coefficient

The model has been extended to multicomponet steels as follows;

$$\lambda_2^2 d\lambda_2 = B_o \frac{1}{\sum \frac{H(k_i-1)mC_{Li}}{\sigma T D}} dt \tag{4-4}$$

From the equation 4-4, alternatively this may be written

$$\lambda_2^2 d\lambda_2 \approx B \frac{1}{\sum A(k_i-1)mC_0} dt \qquad\qquad (4\text{-}5)$$

where $= \frac{H}{\sigma TD}$, and is considered approximately constant.

Of note, for a single solute which does not segregate (k = 1), the SDAS would be infinite (i.e dendrites would not form). The SDAS prediction will be dominated by the terms in the summation for those elements which segregate most.

In order to understand how B (constant) and M affect secondary dendrite arm spacing λ_2, the integrated equation of 4-5 (with modified constant) for multicomponent steels is suggested based on their theory as follows.

$$\lambda_2 = B * M * \tau^{1/3} = B \frac{1}{\sum A_i(k_i-1)m_iC_{0i}} \tau^{1/3} \qquad\qquad (4\text{-}6)$$

Different authors have studied B and M in a variety of ways to extend the model to muticomponent steels. The semi-model approach was chosen because we could fit the geometrical factor as a function of carbon content or for ferritic to austenitic solidification for the multicomponent steels undergoing peritectic. Where B could be function of carbon content, and multicomponent depending on liquid/δ, liquid/γ, and δ/γ transformation.

The A_i factor is called the empirical factor of element i in multicomponent steels, using the extra A_i factor we were able to extend the theory from the binary steels to the multicomponent steels.

4.2 Jernkontoret's Measured SDAS Experiments

The Jernkontoret institute has measured the secondary dendrite arm spacing of the most common commercial steels under production solidification conditions, they have given a suitable experimental technique to determine the following [113]:

- The liquidus, solidus temperature and the formation of austenite temperature.

- A controlled cooling rate which could be varied within wide limits.

The experiments were set up and carried out on small ingots (35 g) solidified in a ceramic crucible. The temperature and cooling rate of the furnace was controlled by the power input. The heat of the furnace was controlled by a programmable temperature-time regulator. The temperature of the steel sample was measured at its centre by means of a thermocouple (Pt/Pt-10% Rh). The output temperature of the steel sample was recorded by a digital microvoltmeter. The liquidus, solidus temperature and cooling rate were then evaluated from the cooling curve (Fig 6-2).

Table 4-1: Carbon and low steels, composition (wt, %) [113].

Steel	C	Mn	Si	Ni	Cr	P	Mo	Al	N
Carbon steel									
201	0.11	1.25	0.12	0.03	0.06	0.04	0.07	0.038	0.012
202	0.12	1.53	0.27	0.03	0.02	0.01	0.03	0.029	0.011
203	0.18	1.26	0.44	0.02	0.01	0.016	0.06	0.004	0.007
204	0.19	1.42	0.4	0.13	0.07	0.012	0.02	0.006	0.005
205	0.36	0.58	0.27	0.05	0.08	0.015	0.02	0.004	0.007
206	0.69	0.72	0.23	0.02	0.02	0.02	0.01	0.006	0.002
207	1.01	0.46	0.25	0.03	0.02	0.012	0.02	0.004	0.002
Low allow steel									
208	0.1	0.57	0.28	3.3	1.14	0.008	0.14	0.013	0.009
209	0.2	0.9	0.25	1.05	0.81	0.014	0.06	0.036	0.009
210	0.27	0.32	0.02	3.5	1.66	0.006	0.42	0.044	0.007
211	0.29	0.62	0.21	0.15	1.11	0.012	0.21	0.011	0.004

212	0.29	0.52	0.22	3.2	1.02	0.009	0.25	0.01	0.005
213	0.35	0.67	0.24	0.05	0.92	0.01	0.19	0.004	0.008
214	0.52	0.85	0.22	0.07	1.07	0.01	0.07	0.004	0.008
215	0.55	0.5	0.27	3	0.99	0.019	0.31	0.011	0.008
216	1.01	0.33	0.23	0.02	1.55	0.021	0.01	0.011	0.003

The secondary dendrite arm spacings have been measured at a low magnification. For each steel specimen, at least four or five secondary arms per primary arm were counted and at least ten such measurements were taken with a good statistical significance of the mean values.

Table 4-2: Carbon and low alloy steel, Liquidus, equilibrium solidus, average cooling rate, calculated local solidification time and measured SDAS

Steel No	type analyses	Liquidus	Equilibrium Solidus	Average Cooling.rate	Local Solidi.time	Measured SDAS
Carbon:						
201	0.1%C	1517.6	1459.8	2	28.9	80
		1517.6	1459.8	0.5	115.6	130
		1517.6	1459.8	0.1	578	300
202	0.12%C	1515.3	1472.5	2	21.4	85
		1515.3	1472.5	0.5	85.6	200
		1515.3	1472.5	0.1	428	390
203	0.18%C	1510.1	1463.9	2	23.1	80
		1510.1	1463.9	0.5	92.4	190
		1510.1	1463.9	0.1	462	250
204	0.2%C	1508.5	1465.5	2	21.5	75
		1508.5	1465.5	0.5	86	120
		1508.5	1465.5	0.1	430	230
205	0.4%C	1499.8	1437.8	2	31	85
		1499.8	1437.8	0.5	124	90
		1499.8	1437.8	0.1	620	280
	0.7%C	1476.2	1370.6	2	52.8	75

206		1476.2	1370.6	0.5	211.2	130
		1476.2	1370.6	0.1	1056	160
207	1.0%C	1457.4	1314.8	2	71.3	70
		1457.4	1314.8	0.5	285.2	80
		1457.4	1314.8	0.1	1426	210
Low alloy:						
208	0.1%C Cr Ni	1503.9	1464.6	2	19.65	75
		1503.9	1464.6	0.5	78.6	110
		1503.9	1464.6	0.1	393	250
209	0.2%C Cr Ni	1505.9	1462.9	2	21.5	85
		1505.9	1462.9	0.5	86	110
		1505.9	1462.9	0.1	430	180
210	0.3%C Cr Ni Mo	1491.8	1449.2	2	21.3	70
		1491.8	1449.2	0.5	85.2	90
		1491.8	1449.2	0.1	426	160
211	0.3%C Cr Mo	1504.5	1450.4	2	27.05	70
		1504.5	1450.4	0.5	108.2	90
		1504.5	1450.4	0.1	541	150
212	0.3%C Cr Ni Mo	1490.2	1442.6	2	23.8	75
		1490.2	1442.6	0.5	95.2	110
		1490.2	1442.6	0.1	476	180
213	0.35%C Cr Mo	1499.5	1439.7	2	29.9	80
		1499.5	1439.7	0.5	119.6	100
		1499.5	1439.7	0.1	598	190
214	0.5%C Cr	1484.4	1405.3	2	39.55	75
		1484.4	1405.3	0.5	158.2	90
		1484.4	1405.3	0.1	791	140
215	0.55%C Cr Ni Mo	1473.2	1385.2	2	44	70
		1473.2	1385.2	0.5	176	90
		1473.2	1385.2	0.1	880	130
216	1.0%C Cr	1454.9	1307	2	73.95	75
		1454.9	1307	0.5	295.8	90
		1454.9	1307	0.1	1479	140

4.3 Other Previous Measured SDAS Experiments

Table 4-3 shows the measured SDAS that were collected from other literature research studies on steels containing a wide range of carbon content up to 1.48 wt%. Steel used by Taha contained very high manganese content (27.7%), which is much higher than generally used, but was useful for this study.

Table 4-3: Other Literature Measured SDAS Experiments [62], [114], [115], [81].

Steel	% C	% Mn	% Si	% P	% Al	λ_2, µm	τ, s
Jacobi steel A	0.59	1.1	0.03	0.009	0.04	340	1380
						280	690
						280	690
						220	376
						220	376
						210	355
						180	309
						160	181
						120	97
						100	65
Jacobi steel B	1.48	1.14	0.03	0.01	0.2	350	2846
						330	1879
						280	1423
						210	940
						190	711
						150	451
						130	341
						110	225

						100	159
						80	91
						70	158
Imagumbai steel A	0.62	0.58	0.12	0.006	0.049	316	1173
						301	659
						257	484
						172	189
Taha steel	0.64	27.7	0.042	0.007	0.075	152	1440
						121	900
						114	840
						78	285
						60	299
						52	163
						32	46
						32	53
						52	258
Robert steel	0.08	1.32	0.28	0.007		25	3
						29	4
						36	8
						40	12
						40	13
	0.12	1.32	0.28	0.007		22	3
						27	6
						34	9

					38	14
0.16	1.32	0.28	0.007		26	9
					34	8
					40	13
					46	16
0.3	1.32	0.28	0.007		25	6
					36	12
					44	19
					51	26
0.5	1.32	0.28	0.007		19	6
					24	11
					31	18
					39	26
0.7	1.32	0.28	0.007		24	9
					32	19
					39	28

4.4 Effect of Carbon Content or Carbon Equivalent on Geometric factor

The expression of SDAS for multicomponent alloys can be written as:

$$\lambda_2 = B * M * \tau^{1/3} = B \frac{1}{A_C(k_C-1)m_C C_C + A_{Mn}(k_{Mn}-1)m_{Mn}C_{Mn} + .. + A_N(k_N-1)m_N C_N}\tau^{1/3}$$

$$(4\text{-}7)$$

where; B is the geometric factor

M is the coarsening dendrite arm for multicomponent i.

$$M = \frac{1}{A_C(k_C-1)m_C C_C + A_{Mn}(k_{Mn}-1)m_{Mn}C_{Mn} + .. + A_N(k_N-1)m_N C_N} \qquad (4\text{-}8)$$

Where; A_i factor is an empirical factor of element of C, Mn, Si, Cr, Ni, Mo, P and N in multicomponent steels. These parameters will be solved using Matlab software by experimental data from the literature. Aluminium and sulphur are not used because dilute aluminium shows no segregation during the ferritic solidification process, and sulphur form as MnS at the end of solidification.

Matlab software is shown to be an appropriate tool to obtain the solutions. The expression for SDAS with more experimental data can be rewritten as:

$$\begin{bmatrix} \lambda_{21} \\ \cdot \\ \lambda_{2m} \end{bmatrix} = B \begin{bmatrix} \dfrac{1}{A_C(k_C-1)m_C C_C + A_{Mn}(k_{Mn}-1)m_{Mn} C_{Mn} + .. + A_N(k_N-1)m_N C_N} \\ \cdot \\ \dfrac{1}{A_C(k_C-1)m_C C_C + A_{Mn}(k_{Mn}-1)m_{Mn} C_{Mn} + .. + A_N(k_N-1)m_N C_N} \end{bmatrix} \begin{bmatrix} \tau_1 \\ \cdot \\ \tau_m \end{bmatrix} \quad (4\text{-}9)$$

It can be seem from equation 4-2 that the geometric factor, B, is a variable, depending on the fraction solid, and is therefore difficult to use in simple equations. It has therefore tended to be used as a constant "effective" geometric factor.

Few researchers have considered the geometric factor B. Kirkwood [60] found B to be equal to 5.04 while Feurer and Feurer [111] found the value B be 5.48. Kattamis and Flemings [79] also found B to be equal to 5.5 using the expression of $\lambda_2 = 5.5 * (M*t)^{1/3}$. Ma et al. [82] amended the expression $\lambda_2 = 7.5 * (M*t)^{1/3}$. These researchers mostly use alloys with low carbon content. In our mode, we allow for a large variation in carbon content (0.08%-1.48%) and consequently different paths through the peritectic, figure 4-1.

Based on the solidification model of figure 4-1, the following values for geometric factor B are used:

If carbon content $< 0.16\%$ then B = 5.05

Else if carbon content $0.16\% \le C < 0.53\%$ then B = 7.25

Else if carbon content $0.53\% \le C < 0.72\%$ then B = 12.8

Else if carbon content $C \ge 0.72\%$ then B = 17.8

Of note, the changes of geometric factor at ~0.16 and 0.53 could reflect the way in which the steel is solidifying, but it might just be a statistical anomaly. The results obtained using this methodology were found to be more accurate than using a varying function of carbon.

Table 4-4: Data used in modelling from Howe and Kirkwood [23]

Solute	m delta/liquid	m gamma/liquid	k delta/liquid	k gamma/liquid
C	-83	-62.3	0.17	0.32
Si	-9	-11.9	0.7	0.6
Mn	-5.1	-4.2	0.74	0.78
P	-34	-33.4	0.13	0.06
Cr	-1	-1.8	0.95	0.8
Mo	-2.4	-3.83	0.81	0.67
Ni	-5	-2.9	0.79	0.9
N	-59	-35.4	0.28	0.54

Solvus slopes m, in degrees Kelvin per weight percent

Partition coefficient k, in wt-%/wt-%
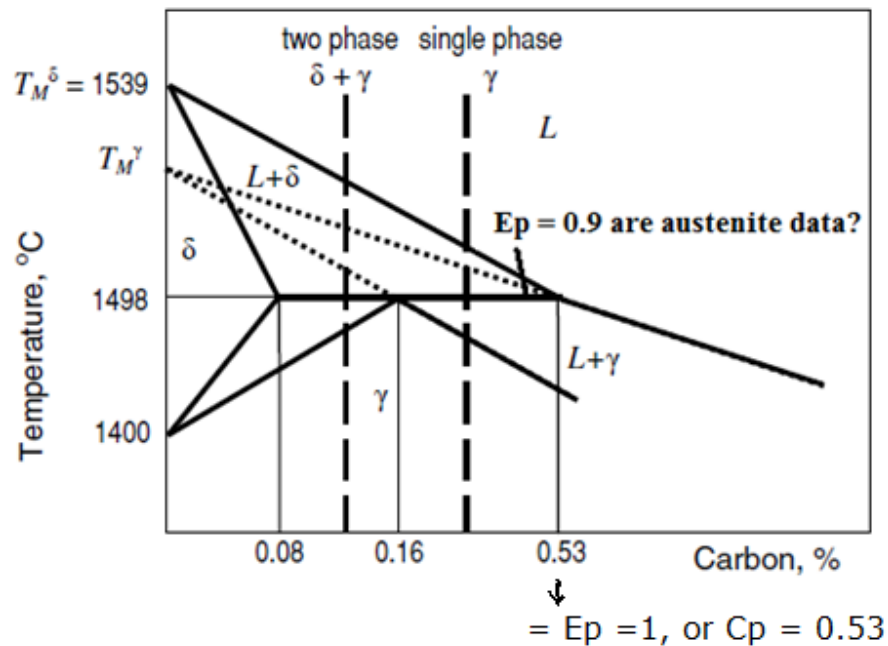
Figure 4-1: Schematic phase diagram of the peritectic region of carbon steel [116] and the key carbon (or carbon equivalent) values.

Peritectic reaction and transformation

Two kind of steels used in this model are the carbon steel and low alloy steel, both encompassing the peritectic transformation range. The peritectic reaction affects local solidification time and the formation of cracks during continuous casting of steels [117], along with 'a high degree of micro-segregation and unexpected solute distributions in the solidified alloy' [23]

In the case of carbon steels, the solidification path depending on carbon content is illustratable in figure 4-1 [116], at carbon content less than 0.16% C, both δ ferrite and γ phase coexist after the end of peritectic solidification. At carbon content higher than 0.53% C, only primary austenite form from the liquid. These values are affected by the other elements, reflected by their "carbon equivalent" [18]

A major question for this work is how the peritectic transformation affects secondary dendrite arm spacing (SDAS). For this study, we need a simple but adequate procedure for characterising a steel composition in relation to the peritectic, either through a "carbon equivalent" or a "peritectic equivalent". The effect of multicomponent alloys on the peritectic reaction from ferrite to austenitic during solidification has been examined by Howe [16] [23], using QSP (Quick Seg Peritectic) software to calculate E_p (peritectic equivalent as described in the Appendix) for all multicomponent steels of experimental data. QSP has been used to calculate E_p of steels 201-216, the results are listed in table 4-5, where $E_p \geq 1$ suggests austenitic solidification.

Table 4-5: Calculation of Peritectic equivalent coefficient; E_p

Steel number	Ep	Steel number	Ep
201	0.3	209	0.54
202	0.3	210	1
203	0.34	211	0.46
204	0.4	212	1
205	0.67	213	0.58
206	1.3	214	0.9
207	1.88	215	1.46
208	0.7	216	1.75
Jaco steel with 0.59wt.% C			1.19
Jaco steel with 1.48wt.% C			2.87
Imagumbai steel with 0.62wt.% C			1.18
Taha steel with 0.64wt.% C			3.36
Robert steel with 0.08wt.% C			0.18
Robert steel with 0.12wt.% C			0.26
Robert steel with 0.16wt.% C			0.34
Robert steel with 0.30wt.% C			0.60
Robert steel with 0.50wt.% C			0.98
Robert steel with 0.70wt.% C			1.35

This study considers three cases. For E_p approaching 1, very little of the solidification would be ferritic and the peritectic can probably be ignored. It starts with ferritic data if:

- $k_{\delta/l}$ and $m_{\delta/l}$ for $E_p < 1$, and $k_{\gamma/l}$ and $m_{\gamma/l}$ for $E_p \geq 1$ or

- $k_{\delta/l}$ and $m_{\delta/l}$ for $E_p < 0.97$, and $k_{\gamma/l}$ and $m_{\gamma/l}$ for $E_p \geq 0.97$ or

- $k_{\delta/l}$ and $m_{\delta/l}$ for $E_p < 0.9$, and $k_{\gamma/l}$ and $m_{\gamma/l}$ for $E_p \geq 0.9$

4.4.1. Case 1: $k_{\delta/l}$ and $m_{\delta/l}$ for $E_p < 1$, and $k_{\gamma/l}$ and $m_{\gamma/l}$ for $E_p \geq 1$

Figure 4-2: Comparison of SDAS from predicted and measured data

Table 4-6: Results from modelling of the empirical factor A_i

Elements	results	Elements	results
C	$A_C = 0.0118$	Cr	$A_{Cr} = 0.7353$
Mn	$A_{Mn} = 0.0324$	P	$A_P = 0.3062$
Si	$A_{Si} = 0.2240$	Mo	$A_{Mo} = -0.4579$
Ni	$A_{Ni} = 0.0182$	N	$A_N = -0.4648$

From figure 4-2 we can see that the predicted values follow closely the experimental values with high R-squared of 0.938. This suggests that the effect of geometric factor B on secondary dendrite arm spacing is more important for multicomponent steels with larger range of carbon content. The geometric factor depends on the solidification model or carbon content, ranging from 5.05 for carbon content below 0.16% to 7.27 for carbon between 0.16 and 0.53%, 12.8 for carbon content between 0.54 and less than 0.80%, and 17.8 for carbon content above 0.8%. (Matlab code and results are described in appendix 1)

A significant positive correlation was found between the SDAS predictions and SDAS measurements and following the ideal line up to 230 μm. Some of the scatter was found to belong to steels with a higher peritectic equivalent a bit higher that the value of steel number 210, the predicted λ_2 values are lower than their λ_2 measured values approximately by 1.2 times. From higher values 230 μm, the results show more scatter, this scatter belong to high carbon steels. This result may be explained by the fact that measured local solidification time is lower than the real local solidification time at the equiaxed zone, and will be explained in chapter 5.

From table 4-6 we can see the effect of multicomponent alloys on the coarsening dendrite arm mechanism. C, Mn, Si, Ni and Cr with positive values cause melting back

of the tips of the dendrite arm, while Mo and N with negative values might prevent the melting back of the tips of dendrite arm during solidification process, although there is no obvious reason for such an effect.

4.4.2. Case 2: $k_{\delta/l}$ and $m_{\delta/l}$ for $E_p < 0.97$, and $k_{\gamma/l}$ and $m_{\gamma/l}$ for $E_p \geq 0.97$
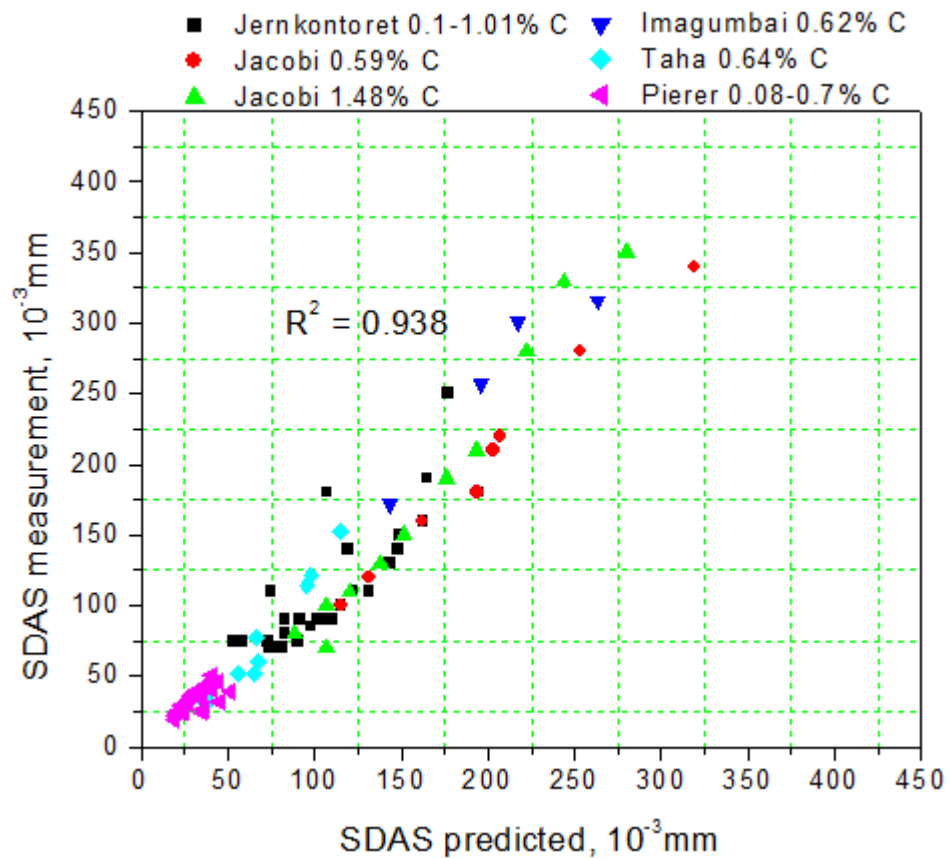

Figure 4-3: Comparision of SDAS from predicted and measured data

Table 4-7: Results from modelling of the empirical factor A_i

Elements	Results	Elements	results
C	$A_C = 0.0121$	Cr	$A_{Cr} = 0.7382$
Mn	$A_{Mn} = 0.0323$	P	$A_P = 0.2815$
Si	$A_{Si} = 0.2280$	Mo	$A_{Mo} = -0.4575$
Ni	$A_{Ni} = 0.0187$	N	$A_N = -0.4645$

Similar results (figure 4-3) are obtained with slightly decreasing R-squared of 0.934 when the value of Ep is reduced from 1 to 0.97 which allow us to use $k_{\gamma/L}$ and $m_{\gamma/L}$. The results (table 4-7) again show that Mo and N with negative values might increase secondary dendrite arm spacings while other elements with positive values show decreasing λ_2 during solidification. (Matlab code and results are described in appendix 2).

4.4.3. Case 3: $k_{\delta/l}$ and $m_{\delta/l}$ for Ep < 0.9, and $k_{\gamma/l}$ and $m_{\gamma/l}$ for Ep ≥ 0.9
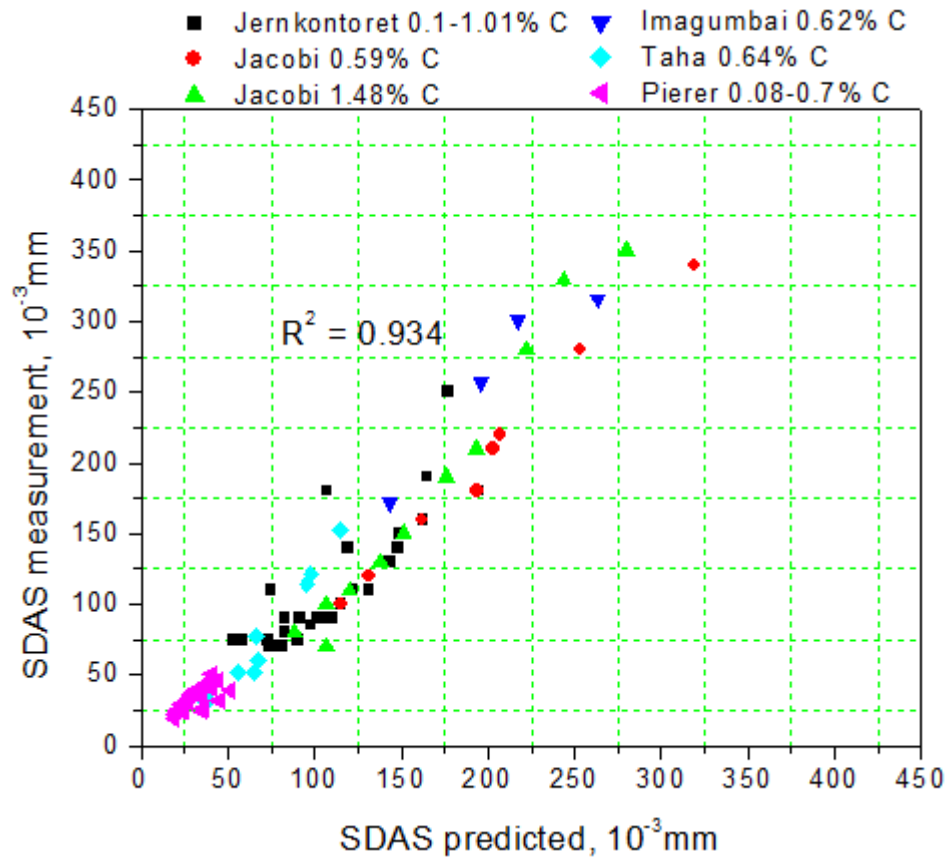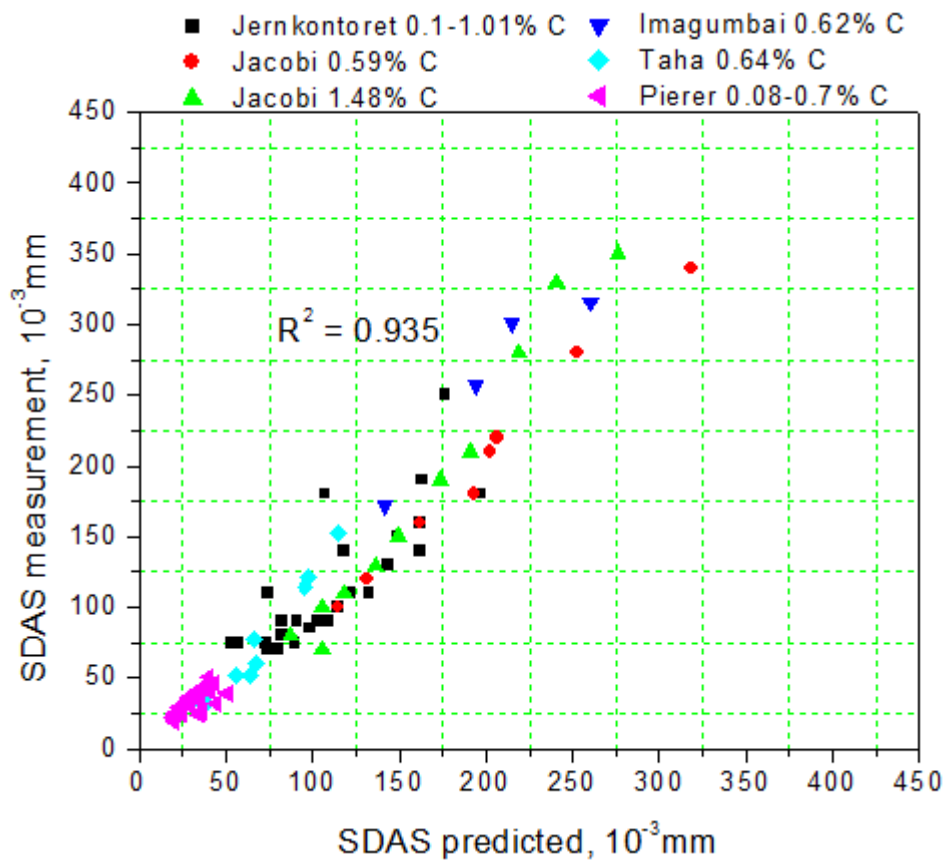

Figure 4-4: Comparision of SDAS from predicted and measured data

Table 4-8: Results from modelling of the empirical factor A_i

Elements	results	Elements	results
C	$A_C = 0.0115$	Cr	$A_{Cr} = 0.4556$
Mn	$A_{Mn} = 0.0318$	P	$A_P = 0.4408$
Si	$A_{Si} = 0.1917$	Mo	$A_{Mo} = -0.2386$
Ni	$A_{Ni} = 0.0283$	N	$A_N = -0.5378$

When the value of E_p is reduced to 0.9 which allow us to use $k_{\gamma/L}$ and $m_{\gamma/L}$. R-squared also slightly drops to 0.935 in figure 4-4. From table 4-8, we can see that the coarsening dendrite parameter is most strongly controlled by those elements with large values of the empirical factor A_i such as Si, Cr, Mo and N. When the value of E_p is reduced from 1 to 0.9 this allows us to use $k_{\gamma/L}$ and $m_{\gamma/L}$. It is interesting to note that, there were no significant differences in the values of the empirical factor of C, Mn, and Ni that is those elements with expanded austenite field, but significant differences were found in those elements with expanded ferrite field like Si, Cr and Mo. The value of Cr decreases from 0.735 to 0.455, while Mo increases from 0.457 to 0.238. (Matlab code and results are described in appendix 3).

It appears that even a temporary appearance of ferrite early on in solidification should not be ignored, and seems to control the secondary dendrite arm spacing. The choice of E_p value upon which to change from ferritic to austenitic data does not appear to be critical.

4.5 Effect of carbon equivalent on full multicomponent behaviour

The term carbon equivalent content determines various properties of the alloys when more than one alloying elements are used, similarly to E_p. Figure 4-1 shows a Fe-C phase diagram, when other alloying elements are added, the temperature and shape are different is a pseudo-binary manner. Several attempts have been made to study carbon and low alloy steels with the ferrite and austenite peritectic reaction during solidification. Howe [118], [16] conducted a series of carbon and low alloy steels in which he generated the carbon equivalent on full multicomponent steels that is used in this chapter.

Howe' carbon equivalent for carbon and low alloy steels with major Si and Mn contents [118].

$$C_p = C_C - 0.14C_{Si} + 0.04C_{Mn} \qquad (4\text{-}10)$$

Of note, similar terms can be obtained from QSP [105], once once the factors (k and m) were changed from ferritic to austenitic solidification at $C_p = 0.53$ (as in the Fe-C binary) rather than at $E_p = 1$. Not surprisingly, very similar results were obtained, but R-squared showed a very minor improvement (0.941 v 0.938) with C_p rather than E_p.

Table 4-9: Results from modelling of the empirical factor A_i

Elements	results	Elements	results
C	$A_C = 0.0117$	Cr	$A_{Cr} = 0.8009$
Mn	$A_{Mn} = 0.0522$	P	$A_P = 0.2758$
Si	$A_{Si} = 0.2049$	Mo	$A_{Mo} = -0.4882$
Ni	$A_{Ni} = 0.0184$	N	$A_N = -0.4511$
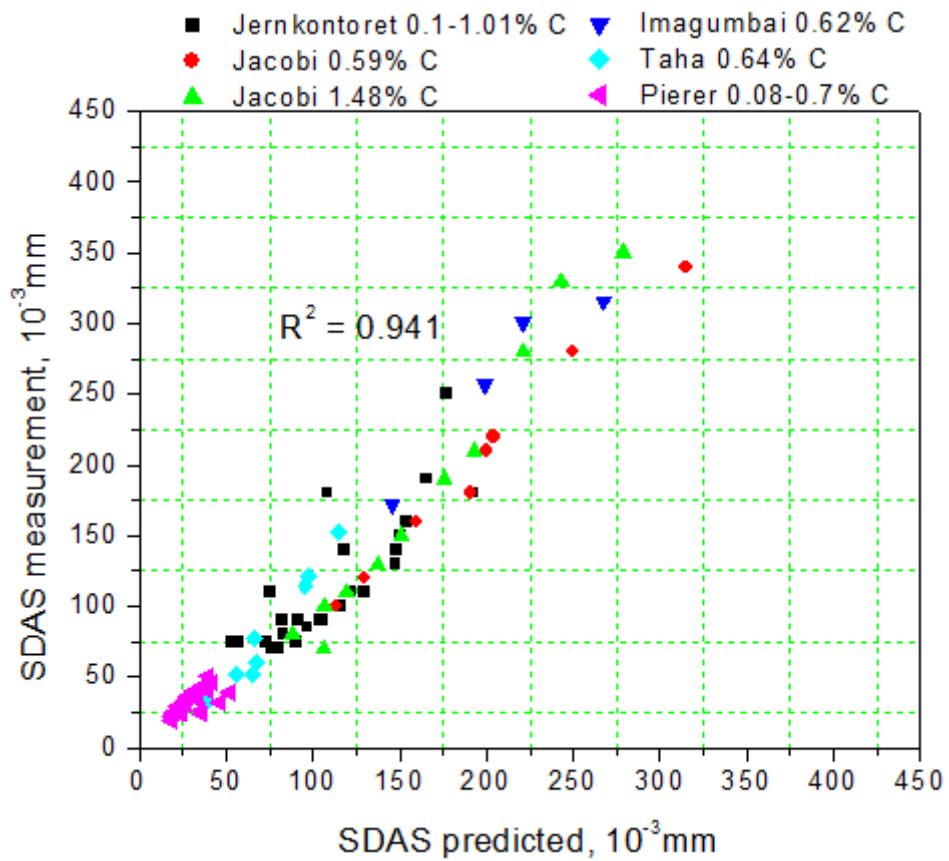
Figure 4-5: Comparision of SDAS from predicted and measured data

As can be seen from figure 4-5 the result with the use of carbon equivalents showed slightly increasing R-squared of 0.941 compared with the use of E_p R-squared of 0.938 in figure 4-2. The results show that carbon is the main element controlling the pseudo-binary manner in these steel, carbon is the only element needed to affect to the geometric factor B. Other elements are more strongly affected by the coarsening parameter A compared to C content only. So we have a balance of the effect of C content and other elements for multicomponent steels on the secondary dendrite arm spacing. It is apparent from table 4-9 that very few different results of empirical factors A_i compare with table 4-4. (Matlab code and results are described in appendix 4)

Howe' carbon equivalent [18] for carbon and low alloy steels with full multicomponent including Ni and Cr elements is as shown below.

$$C_p = C_C - 0.123C_{Si} + 0.04C_{Mn} + 0.06C_S - 0.018C_{Cr} - 0.05C_{Mo} + 0.08C_{Ni}$$

(4-11)
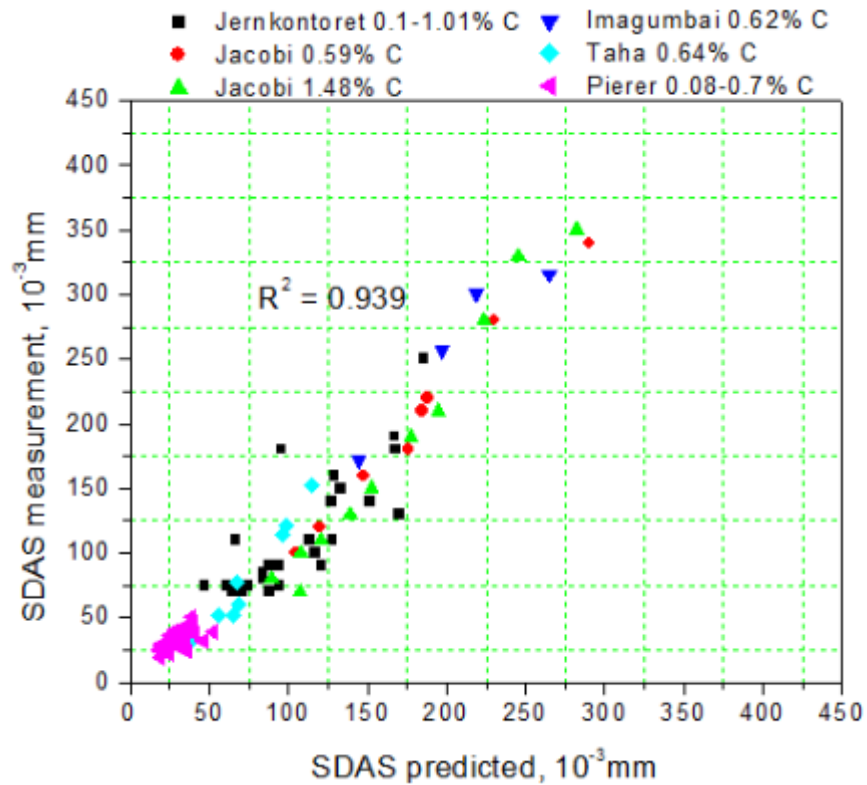
Figure 4-6: Comparision of SDAS from predicted and measured data

Figure 4-6 shows the result with the use of full multicomponent steels, the result is slightly decreasing R-squared of 0.939 compared with the use of the Fe-C-Si-Mn system which gives R-squared of 0.941 in figure 4-6. The extension to full multicomponent steels gives a slightly decreasing R-squared but is the extension to allow applying the low alloy steels containing other elements such as Cr, Ni and Mo. We also can see that in steels studied by Jacobi, Imagumbai, Taha and Pierer the correlation between the SDAS measurement and SDAS prediction follows the ideal line. Some of the SDAS scatter was found in Jernkontoret' steel for those steels containing high levels of Cr and Ni (contents higher than 3wt.%) such as numbers 210, 212 and 215. The reason for this could be that these steels which undergoes ferrite followed by interdendritic precipitation of austenite that dendritic structure could result

from either a divorced eutectic or peritectic reaction [118]. (Matlab code and results are described in appendix 5).

Table 4-10: Results from modelling of the empirical factor A_i

Elements	results	Elements	results
C	$A_C = 0.0102$	Cr	$A_{Cr} = 0.5715$
Mn	$A_{Mn} = 0.0512$	P	$A_P = 0.5538$
Si	$A_{Si} = 0.1921$	Mo	$A_{Mo} = -0.1668$
Ni	$A_{Ni} = 0.0493$	N	$A_N = -0.6290$

It is apparent from table 4-10 that we obtain very different results of empirical factors of Ni, Cr and Mo compared with table 4-9, so these are rather sensitive to the choice of E_p or C_p factors. The results again show that Mo and N with negative values might increase secondary dendrite arm spacing while other elements with positive values show decreasing λ_2 during solidification.

Chapter 5: Secondary Dendrite Arm Spacing Measurements

5.1 Results on Secondary dendrite arm spacing measurements

The microstructure of the high carbon steel was examined and photographed with an optical microscope in order to measure the secondary dendrite arm spacing values at different bloom depths. For the secondary dendrite arm spacing standard measurements, the measurements must be made close to and parallel with the primary dendrite branches. At least four or five secondary arms per primary arm were counted within each bloom depth, and at least eight or nine measurements have been recorded in order to get the average and standard deviation SDAS of each position [64] shown in figure 5-2. The results of the secondary dendrite arm spacing measurements were then reported in table 5-1.

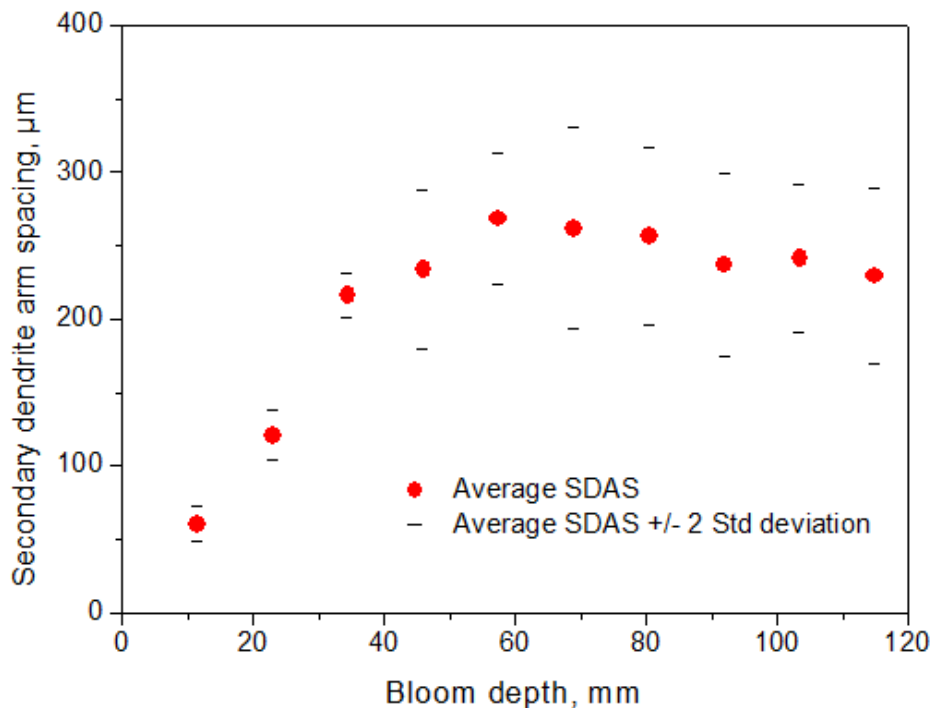Figure 5-1: Average SDAS and +/- 2 standard deviation measurements

Figure 5-1 shows a typical variation of the average secondary dendrite arm spacing measurement and standard deviation from top surface to centre. It shows low values of dendrite arm spacing at the surface, increasing toward the centre; a maximum value has been recorded at the quarter-thickness, and approximately constant toward the

centre, but possibly decreasing again. Simple statistical analysis was used to get confidence intervals. The 95% confidence intervals show significant scatter beyond 40mm depth.

Generally, it was expected that decreasing the cooling rate with the depth would lead to increasing the secondary dendrite arm spacing because of the longer solidification time in comparison to the surface [119]. From 57 mm depth toward the centre, the secondary dendrite arm spacing decreases about 30 μm from 268 μm to 229 μm at the centre. It shows a half "seagull" λ_2 profile, The finding of the current research are consistent with those of Ganguly [5] and Howe [120] as shown in figures 5-2 and 5-3.

Secondary dendrite arm spacing in Figure 5-1 exhibits scatter beyond 40mm depth and a dip at the centre, this scatter and dip in the SDAS corresponds to the equiaxed zone. This finding was seen by Howe [120] in examination of previous high carbon bloom steel in figure 5-3.

The expectation from theory is that the SDAS should increase with local solidification time, t_f(s), so it would not see the dip of SDAS in figure 5-1. If $\lambda_2 = M_0.t_f^{1/3}$, then the dip would suggest that the local solidification time goes down in the middle.

Ganguly's explanation for this result may be, besides the change in solidification rate, carbon enrichment of liquid and change in mobility of dendrites having an impact of the dendrite size distribution in the equiaxed zone. This possible explanation for the decrease of secondary dendrite arm spacing in the equiaxed zone may be inadequate, however [5].
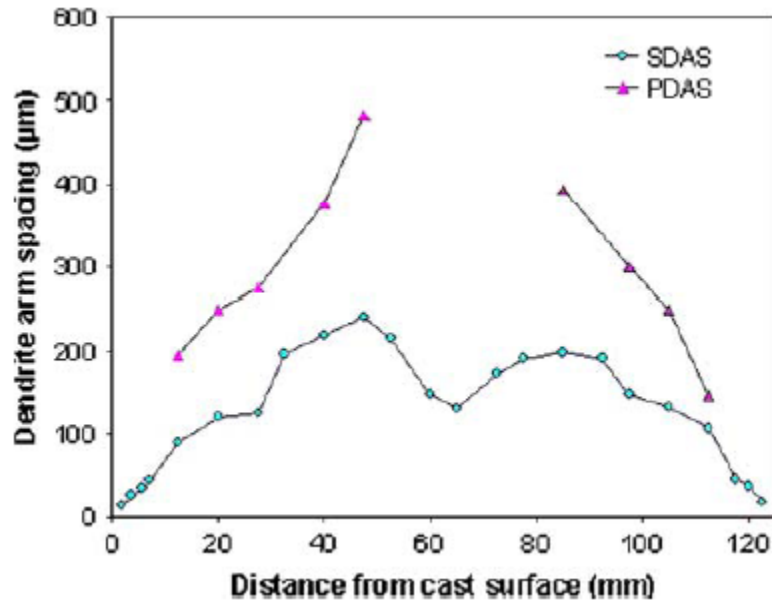
Figure 5-2: Variation of measured value of average DAS from surface to centre

of a high carbon steel billet [5].

Howe has a possible explanation for the decrease of SDAS in the equiaxed zone; an acceleration in the cooling rate at the centre of the bloom is suggested by this seagull λ_2 profile. The evidence of the macro-model results indeed show this tendency, for both the thickness of bloom to the liquidus isotherm and to the solidus isotherm shown in figure 5-4 [120].

Figure 5-4 exhibits the curl round of the bottom of the sump / solidus isotherm, the results from Tata Steel / TTC macro-model still have the local solidification time t_f (s) that still increases right up to the central region (table 5-2), and therefore would not explain the apparent dip / "seagull profile" in figure 5-1.

However, the TTC model only assumes heat extraction transverse to the casting direction (macro model does not include longitudinal heat extraction). For most of the cast length, this should be a good approximation: The temperature gradient (and thus heat flow rate) will be much steeper through the shell thickness than down in the casting direction. But around the sump, heat flow down in the casting direction could become

significant, and could maybe reduce the local solidification t_f (s) in the central region which results in a "seagull profile".
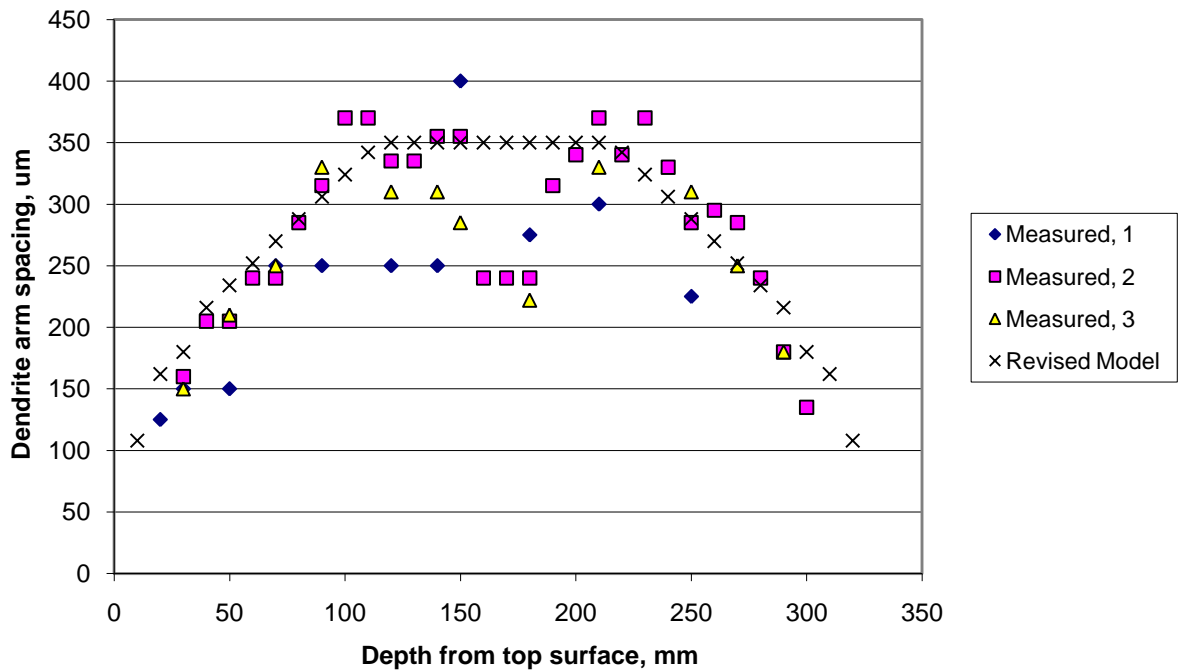
Figure 5-3: Measured secondary dendrite arm spacing across Bloom 750 and

revised model data [120].

Another possible explanation for this is that the submerged entry pouring configuration and the effect of argon on the flow pattern lead the hottest region in the midway of billets or blooms and the coldest region in the centre near the SEN [121] This finding seems to be consistent with the solidus predictions across the thickness presented in figure 6-5, the calculated solidus temperatures showed a typical difference of about 5K between them. It also might push the liquidus isotherm further down the strand than the macro-model predicts [120], increasing the tendency for an accelerated solidification in the centre, figure 5-4.
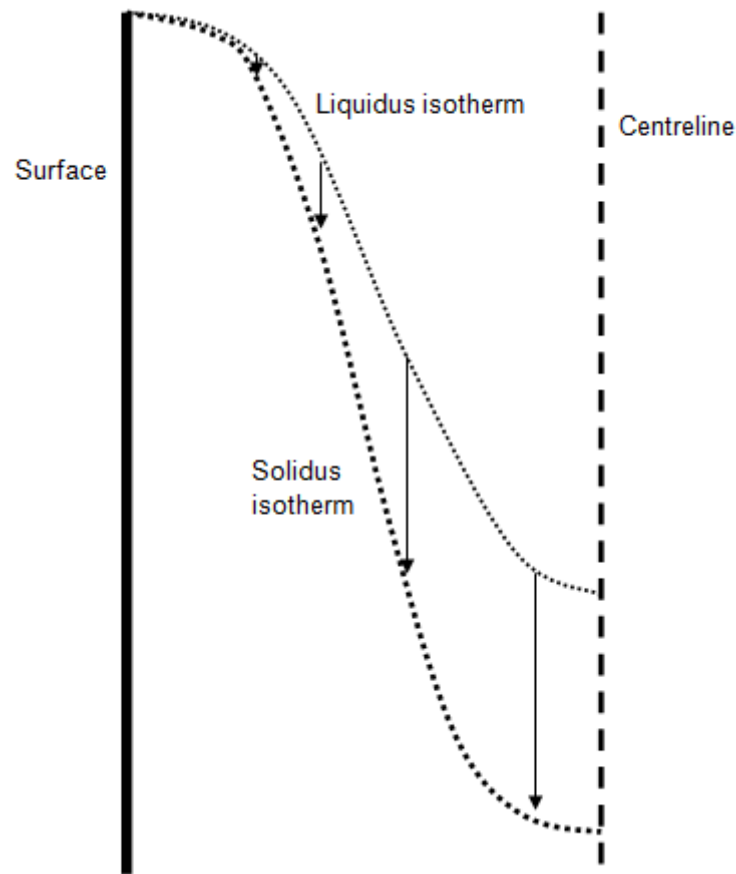
Figure 5-4: Schematic solidification profile, showing the curving-round of the liquidus and solidus isotherms: an acceleration at the centre of actual solidification time for the "double-hump" profile requires the distance between these isotherms to reduce [120].

From data in figure 5-1, it is apparent that the depth below 40 mm shows the average secondary dendrite arm spacing with low standard deviation. Strong evidence of this was found in figures 5-5 to 5-8. We can see many secondary dendrite arms in the long primary dendrite trunk. The secondary dendrite arm spacing looks to be the same. In this columnar structure, the primary dendrite trunks grow parallel to each other. Unlike in the equiaxed structure, the spacing between the secondary dendrite arm spacing is not the same distance; we can see the evidence from figure 5-9 to 5-14.

It is worth mentioning at this point the possible sources of error associated with measurement of this type. A longitudinal section from the surface to centre was cut off

in order to measure secondary dendrite arm spacing. For most steels, we are looking for traces of low levels of elements in a structure which is completely different from that with which it solidified. In Al alloys for example, you might have the heavily segregated, one phase to look at, and maybe the interdenditic positions also marked by eutectic; likewise many Ni alloys or high-alloy stainless steels. But we have a rather dilute composition, which undergoes a further, solid-state transformation after solidification, so we are looking for relatively small changes in composition in a different structure. Therefore the solidification structure is not very clear, which makes quantification of SDAS quite difficult. In dilute steels, you are often looking at a poor image, with the etch affected by all sorts of other extraneous factors, and not just the interdendritic segregation.

SDAS measurements on metallographic images are never perfectly accurate. Hence, it is important make a good estimation of the error. There are several errors in the secondary dendrite arm spacing measurements;

- The error could come from optical measurements of secondary dendrite arm spacing. To avoid this error, more measurements should be carried out to minimise the errors. In this project, we followed the Beaverstock' technique whereby a minimum of eight measurements were taken in order to obtain the sample mean and standard deviation SDAS of each depth.

- The error could also be introduced during specimen sampling. Misalignment of the primary dendritic arm can be introduced during the cutting stage of the sample preparation. The specimen should be in the right direction of a primary arm branch. However, this is not always possible, especially due to some of the structures introduced during casting as well as naturally heterogeneity of the bloom. This can lead to some errors in the SDAS measurement.

- The error could come from sample grinding and polishing. Keeping the sample flat can be a problem especially with manual grinding. This can lead to misalignment of the primary arm branch and this can result in some errors.

Figure 5-5: Secondary dendrite arm spacing measurement at 11.5 mm depth.

Figure 5-6: Secondary dendrite arm spacing measurement at 23 mm depth.

Figure 5-7: Secondary dendrite arm spacing measurement at 34.5 mm depth.

Figure 5-8: Secondary dendrite arm spacing measurement at 46 mm depth.

Figure 5-9: Secondary dendrite arm spacing measurement at 57 mm depth.

Figure 5-10: Secondary dendrite arm spacing measurement at 69 mm depth.
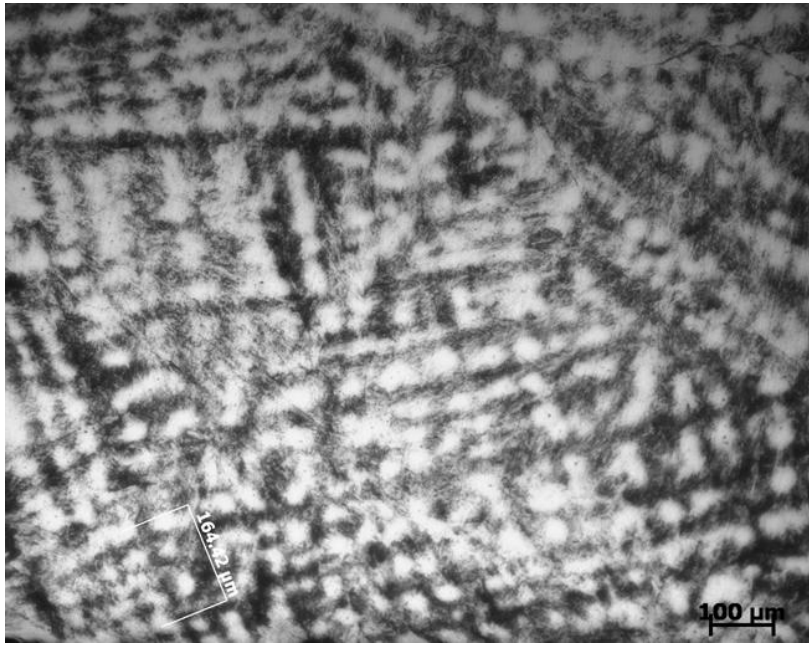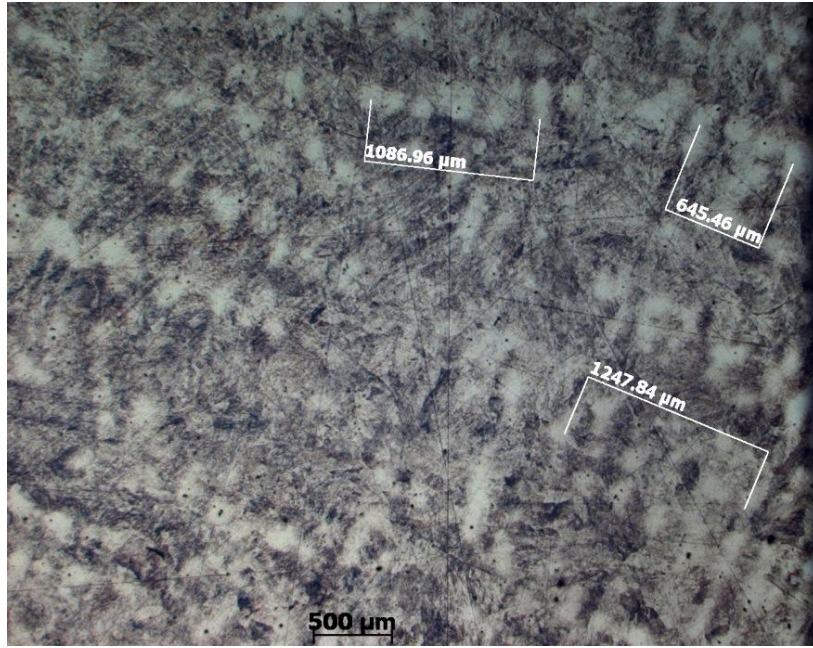
Figure 5-11: Secondary dendrite arm spacing measurement at 80.5 mm depth.

Figure 5-12: Secondary dendrite arm spacing measurement at 92 mm depth.

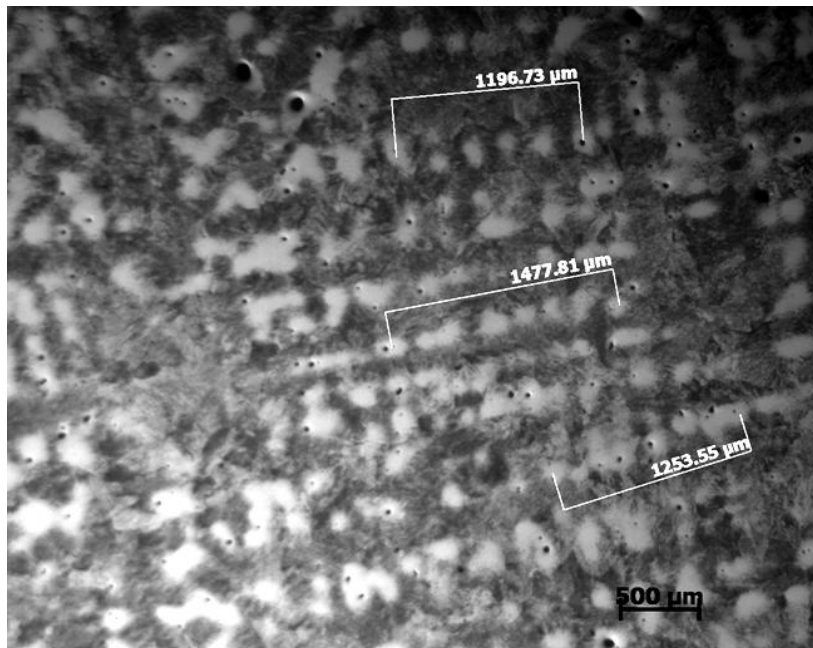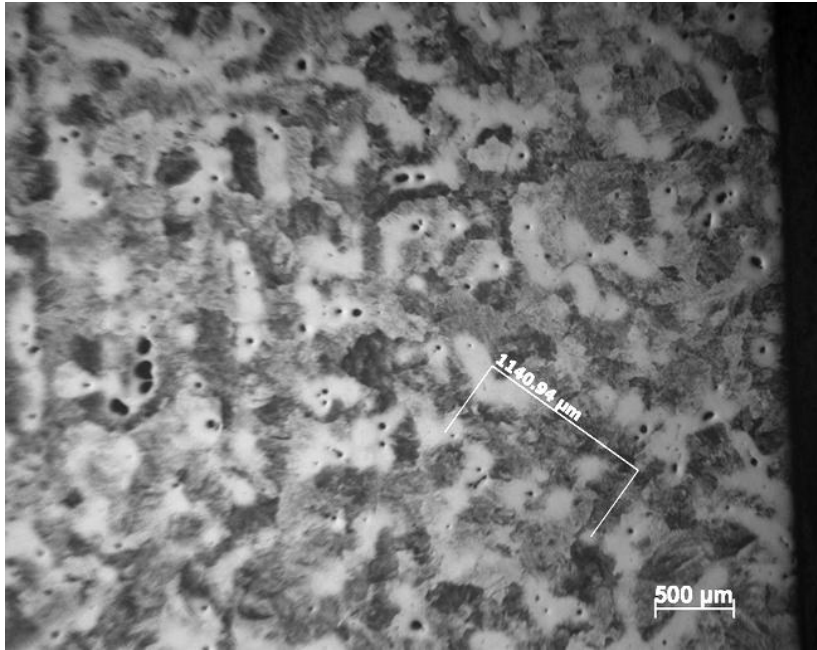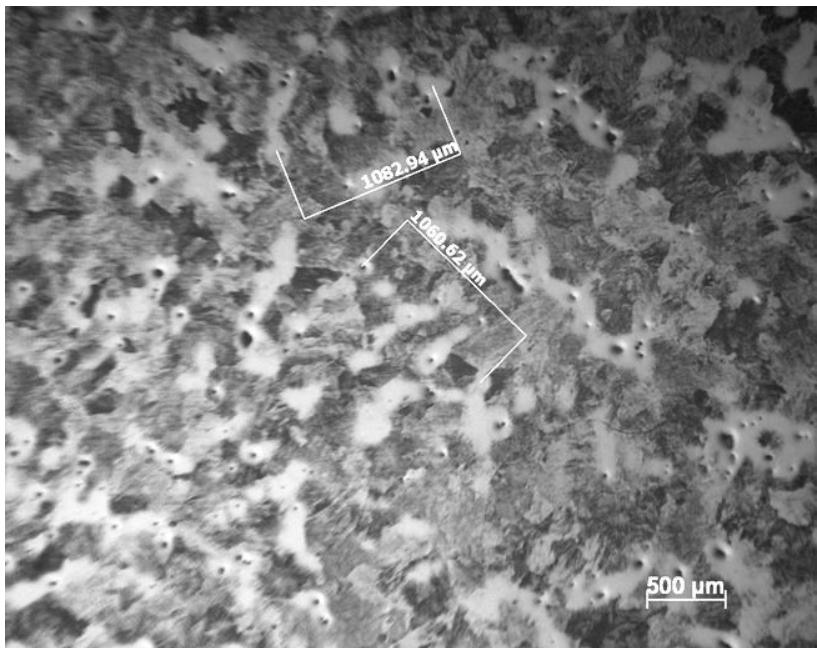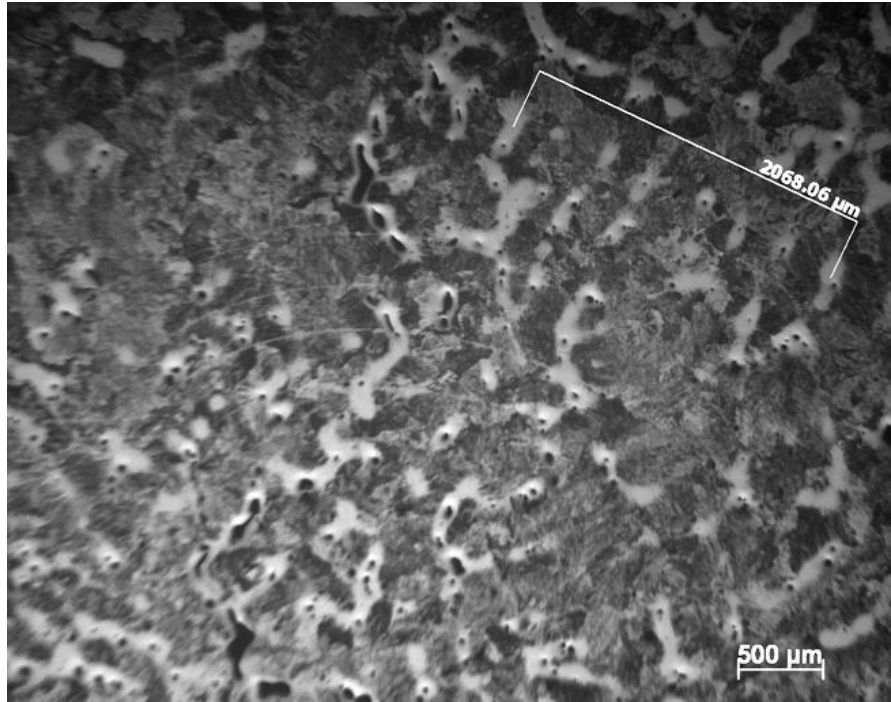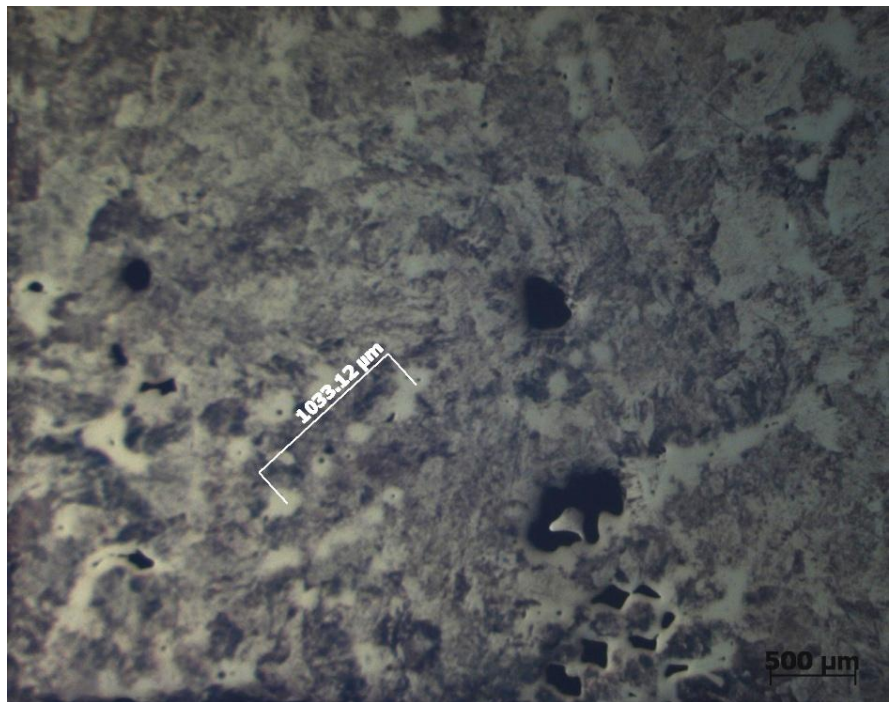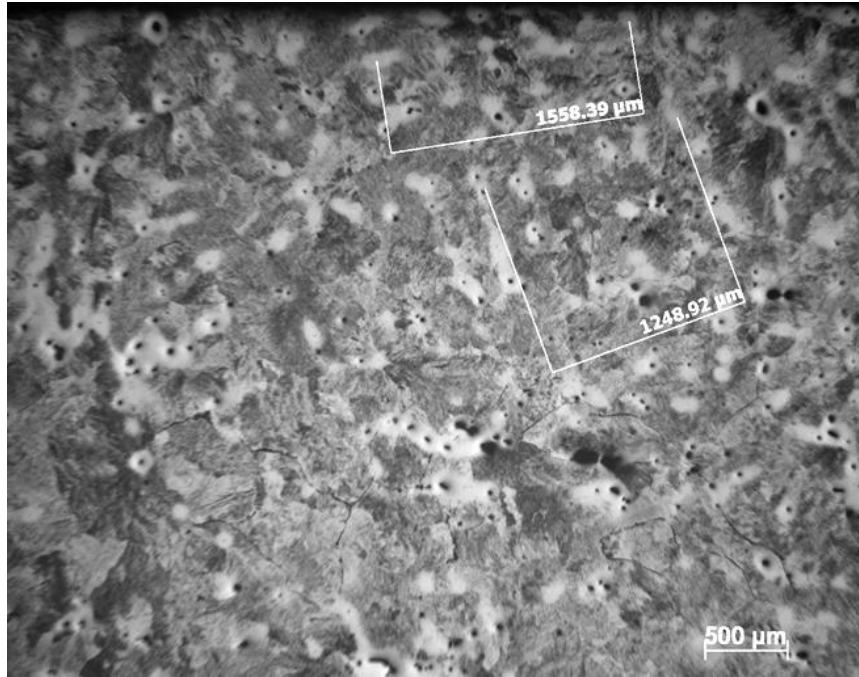Figure 5-13: Secondary dendrite arm spacing measurement at 103.5 mm depth.

Figure 5-14: Secondary dendrite arm spacing measurement at 115 mm depth.

5.2 Measured and predicted secondary dendrite arm spacing comparison

Tata Steel has developed a model for continuous casting, which employs thermal data across the mushy zone corresponding to equilibrium solidification. The solidification time was extracted from the TTC model for each node across the cast thickness and represented as an average heat extraction rate for use in QSP model. The heat extraction rates have been recorded as high at the surface with a significant decrease to the centre. From the heat extraction rate, we can calculate the local solidification time and average cooling rate as shown in table 5-2.

The derived heat extraction rates of high carbon bloom steel of CC5 caster (283x230mm) are presented in table 5-2. The solidification rates have been recorded highest at the surface with a significant decrease to the midway of bloom, from 57mm depth it can be seen that the heat extraction rates become rather similar. From 92mm depth, the smaller section size of the bloom becomes evident, and a minimum of the heat extraction rate during solidification has been recorded at the centre (115mm) of 0.43 kj/Kg.s.

Table 5-1: Thermodynamic data of high carbon bloom steel [120]

Latent heat, Liquid-to-Austenite, kJ/Kg	235.9	
Specific heat capacity: kJ/KgK:	Liquid	Austenite
	0.8	0.69
Reference temperature, pure Fe austenite, deg.C	1526	
Reference diffusivity, Fe in austenite $D(Fe)=Do.exp(-Q/RT)$ m^2/s	**Do** /m^2/s	**Q** /kJ/mol
	0.7x10-4	286,000
Element	**Partition coefficient**, k, wt%/wt% (γ/L)	**Solvus slope**, m, K/wt%	**Diffusivity factor** (xD(Fe))
C	0.32	-62.3	10000
Si	0.6	-11.9	2
Mn	0.78	-4.2	2
O	0.045	-57	10000

Composition of; 0.72%C, 0.63%Mn, 0.24%Si, 0.016%P and 0.0004%N

Liquidus temperature = 1475 ^{0}C and Solidus temperature = 1368.7 ^{0}C

The heat extraction rate is given by Ogilvy [122] who studied the heat extraction rate, and extended this to a multicomponent system. Howe [118] changed the assumption of a constant cooling rate to one of a constant rate of volumetric heat extraction, the equation of heat extraction rate is as follows:

$$Q = H\frac{df_s}{dt} + C_p \frac{dT}{dt} \qquad (5\text{-}1)$$

where Q is the heat extraction rate, J/m3.s-1

H is latent heat, kj/Kg

C_P is heat capacity, kJ/m^3.k^{-1}

T is temperature, k

t is time, s

f_s is fraction of solid

We then could calculate the local solidification time thought the heat extraction equation as follows:

$$\dot{Q} = \frac{(H + C_p \Delta T)}{t_f} \qquad (5\text{-}2)$$

Where ∆T is the different temperature between liquidus and solidus

Table 5-2: Thermal data for heat extracted from Tata Steel macro-model and SDAS measurements of 0.7% carbon bloom steel.

Depth (mm)	Thermal Rate (KJ/Kg s)	Local time (s)	Cooling Rate (^{O}C/s)	Predicted SDAS (µm)	Measured SDAS (µm)
11.5	20.67	15.27	6.96	68.47	60.056
23	7.75	40.73	2.61	94.96	120.62
34.5	3.26	96.82	1.09	126.74	216.35
46	1.77	178.33	0.59	155.35	233.93
57.5	1.11	284.36	0.37	181.49	268.82
69	0.74	426.54	0.25	207.76	261.63
80.5	0.58	544.21	0.20	225.34	256.71
92	0.5	631.28	0.17	236.76	237.15
103.5	0.45	701.42	0.15	245.23	241.48
115	0.43	734	0.14	248.00	229.20

The analytical secondary dendrite arm spacing models have been introduced in the chapter 4. In order to assess these models, high carbon bloom steel has been sectioned and the secondary dendrite arm spacing measured, as shown in table 5-2.

Figure 5-15 shows that the analytical model introduced in chapter 4 (applied case 1, SDAS equation 4-7, and A_i is listed in table 4-6) approximately agrees, even though there has been no empirical tuning of the model to the high carbon steel bloom data. However, the predicted results continue to increase towards the centre whereas the measured results stop doing so from the quarter-depth position. There might be two reasons for this difference between the SDAS measured and predicted; First, it could be a difference in the thermal conditions during solidification, most of the data used in this model are from lab scale, which results in experiments attempting to maintain a constant cooling rate, but in commercial casting, the thermal conditions do not lead to constant cooling rate and are variable from the surface to centre. This can explain why

the secondary arms are shorter then typical of commercial casts of similar compositions: Second, during the coarsening process, it might be melting of the thinner secondary arms which have studied been by several researchers in the past [75].
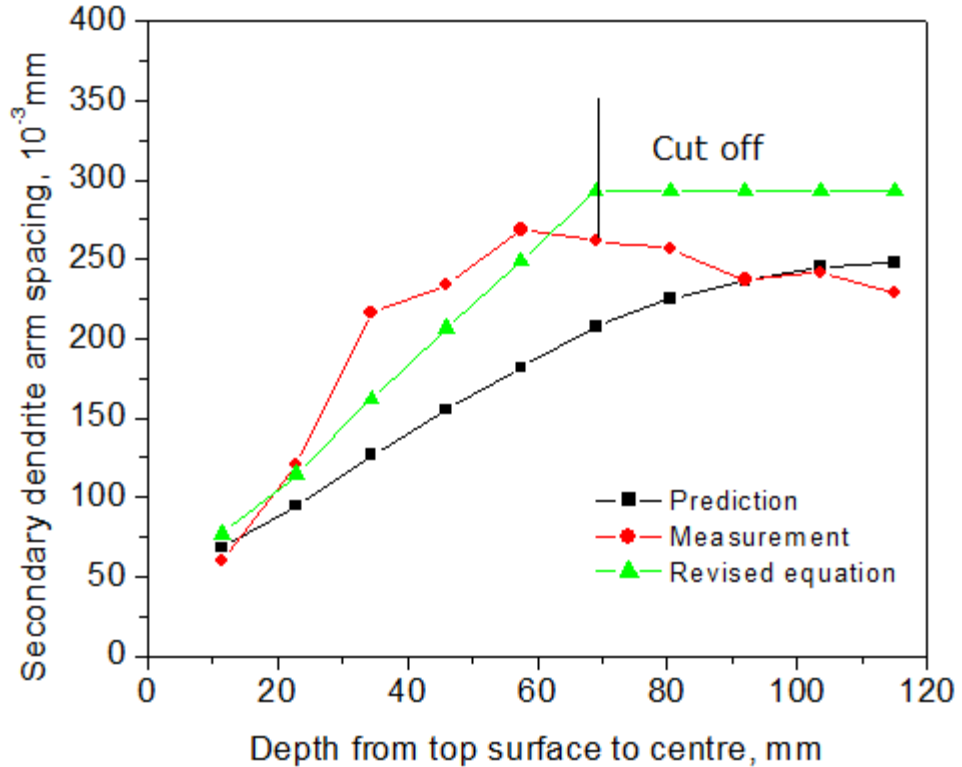
Figure 5-15: Comparison of SDAS from predicted and measured data

The secondary dendrite arm spacing was employed, $\lambda_2 = G t^{1/3}$ [64], [61], [16], [60], A revised equation λ_2 was used in order to compare between λ_2 predicted and measured. G was fixed so as to yield ~ 77 μm near the surface, the local solidification time was used from table 5-1. The results of the revised equation λ_2 show good agreement with results from the measured λ_2 up to the depth of 70 mm; this looks linear with results from the measured λ_2. The revised equation λ_2 is cut off from the depth of 70mm toward the centre. It shows a half "seagull" λ_2 profile like the measured λ_2.
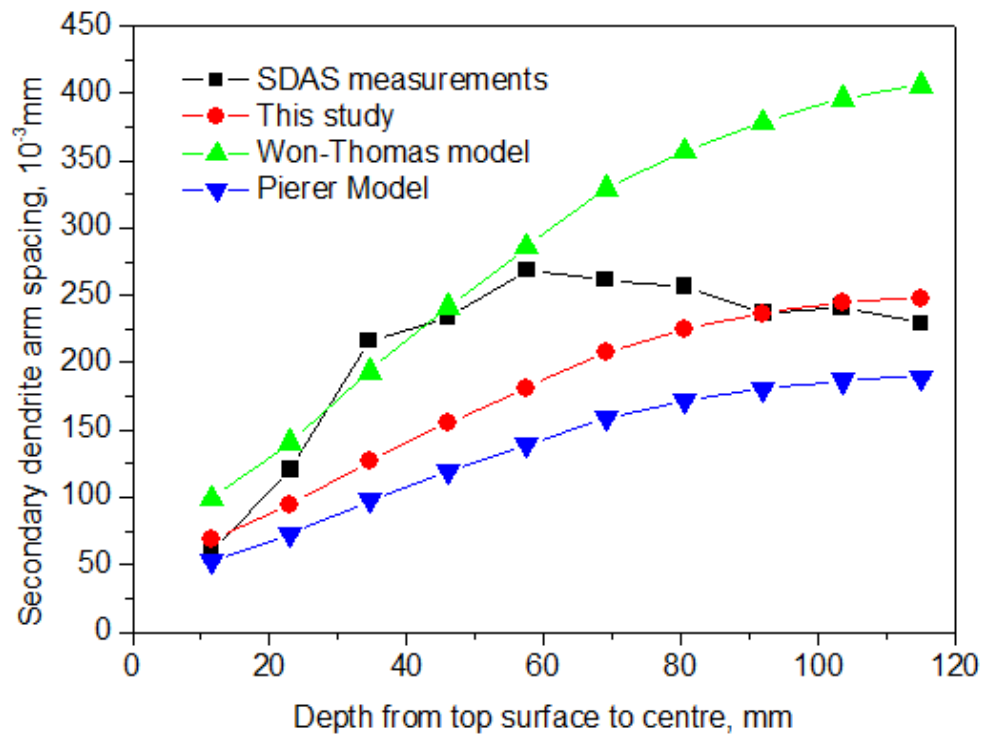
Figure 5-16: Comparison of SDAS for high carbon bloom steel with various

SDAS models.

Won-Thomas' SDAS model [2] is described as follows:

$$\lambda_{2SDAS}(\mu m) = (169.1 - 702.9 * C_c) * C_R^{-0.4935}$$

for $0 < C_c \leq 0.15$

$$143.9 * C_R^{0.3616} * C_c^{(0.5501 - 1.996C_c)}$$ \hfill (5-3)

for $015 < C_c$

where C_R is cooling rate (k/s), and C_c is carbon content (wt%)

Pierer' SDAS model was mentioned in chapter 2 (see equation 2-6)

The comparison of SDAS from this study and other SDAS models is shown in figure 5-16. The Won-Thomas model shows good agreement at 23 mm to 57.5 mm, predicted SDAS results beyond quarter-thickness are much higher compared to the SDAS measurements. The Pierer model is much lower compared to both the predicted results of SDAS for this study and SDAS measurements. This model has been shown to

be more accurate than other existing models found in the literature, when applied to this

particular example.

Chapter 6: Solidification and Segregation Modelling From QSP and DICTRA Software

6.1 QSP and DICTRA simulation method

The high carbon steel used in the study was supplied from Tata Steel with the dimension 283x230 mm & casting speed of 1.3 m/min. For simplicity, only the three major elements were considered (Fe-0.72 wt.%C-0.24wt.%Si-0.63 wt.%Mn) as the others were at residual levels unlikely to materially affect the results. The thermal histories were determined from an in-house Tata Steel macro-model, Figure 6-1.
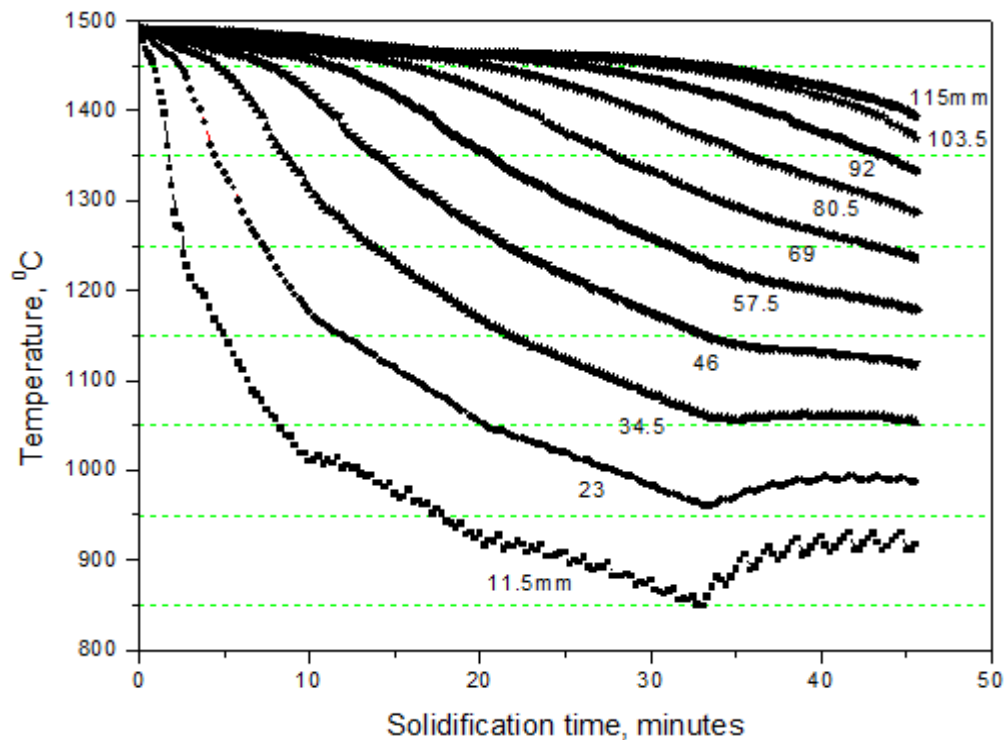
Figure 6-1: Cooling curves of high carbon steel from top surface to centre.

The solidification time for each nodal position across the bloom was determined from this and presented as an average heat extraction rate for use as presented in Table 5-2 and Figure 6-2. The thermal conditions during solidification were based on the macro-model, although this employed equilibrium solidification assumption. Key variables are the liquidus-solidus temperature interval, ΔT (K) and the local solidification time, t_f (s), the latter varying with depth. From these, the cooling rate for DICTRA, and the heat extraction rate for QSP were derived, accepting there will be

some discrepancies owing to the macro-model's equilibrium assumption. The average

cooling rate ($\frac{\Delta T}{t_f}$) is related to the heat extraction rate by the following equation:

$$\dot{Q} = \frac{H_L + C_p * \Delta T}{t_f} \qquad (6\text{-}1)$$

where $\dot{Q}$ is the average heat extraction rate (kJ/Kg.s), H_L is the latent heat

(kJ/Kg), C_P is the specific heat capacity (kJ/KgK), t_f is the local solidification time (s)

and ΔT is the difference in temperature between liquidus and solidus temperature (K).

The commercial code, DICTRA (calculation of Diffusion Controlled

TRAnsformations) with the mobility database MOB2 [123], [124] was employed, for

which assumptions had to be made of a constant SDAS and cooling rate. The cooling

rate was changed below the solidus based on the cooling curves in figure 6-1, down to

900 °C. During solidification, the equilibrium data applied at the interface are free to

vary according to the associated thermodynamic database, and there is diffusion in both
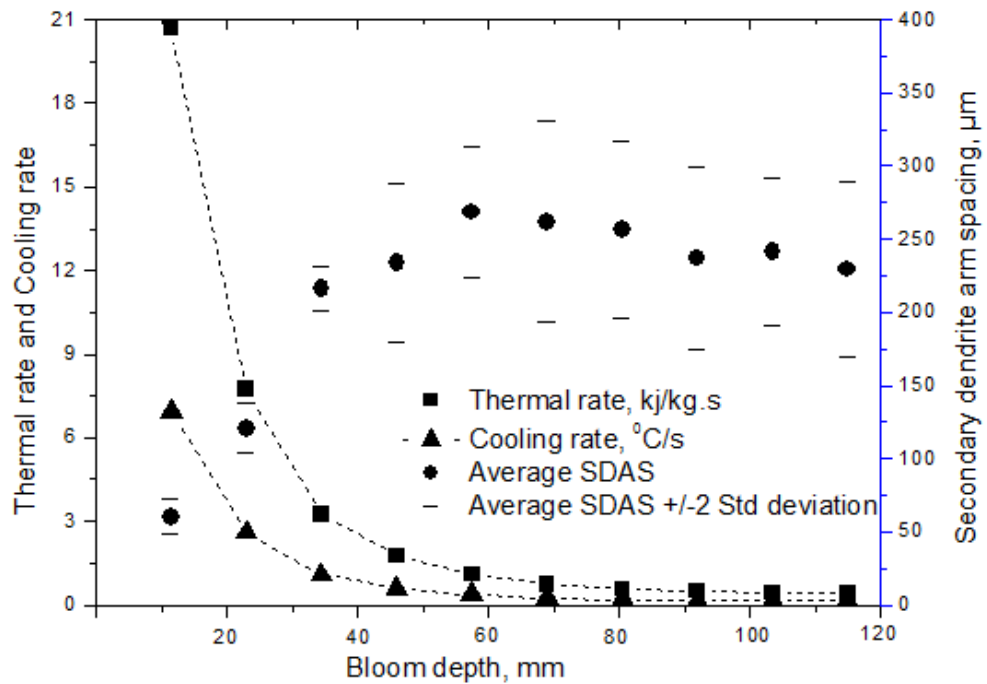
the liquid and solid phase.

Figure 6-2: Thermal data, cooling rate and SDAS measured of 0.72%C bloom,

282x230 mm

QSP is a simplified, rapid in-house model from Tata Steel [105] which is used to simulate the solidification and subsequent cooling below the solidus controlled by the heat extraction rate. This rate can be changed during a run, notably to follow the sub-solidus cooling curves as in this work. It employs linear multicomponent phase diagram data, with finite diffusion in the solid phases, only. This software allows for secondary dendrite arm coarsening but in this study, we run with the constant SDAS in order to compare with DICTRA simulation.

6.2 Microsegregation modelling results

Effect of cooling rate on micro-segregation levels is important to final properties. Many attempts have studied the effect of cooling rate on micro-segregation employed. Many models have assumed a constant cooling rate, but in real continuous or ingot casting, the cooling rate varies enormously during solidification from the liquid to solidus temperature. Below the solidus temperature, the solidification rates show significant decreases, and by 1100 °C to room temperature it can be seen that the cooling rate has become rather similar shown in table 6-1, and this could lead to sub-solidus homogenization.

Using the terminology from [125] where:

$(\frac{dT}{d\tau})_m$ is the measured cooling rate

$$(\frac{dT}{d\tau})_c = \frac{1}{C_p}\frac{dQ}{d\tau}$$

The difference between the measured cooling rate $(\frac{dT}{d\tau})_m$ and $(\frac{dT}{d\tau})_c$ is due to the evolution of latent heat in the sample

$$\frac{dL}{d\tau} = C_p[\left(\frac{dT}{d\tau}\right)_m - (\frac{dT}{d\tau})_c]$$
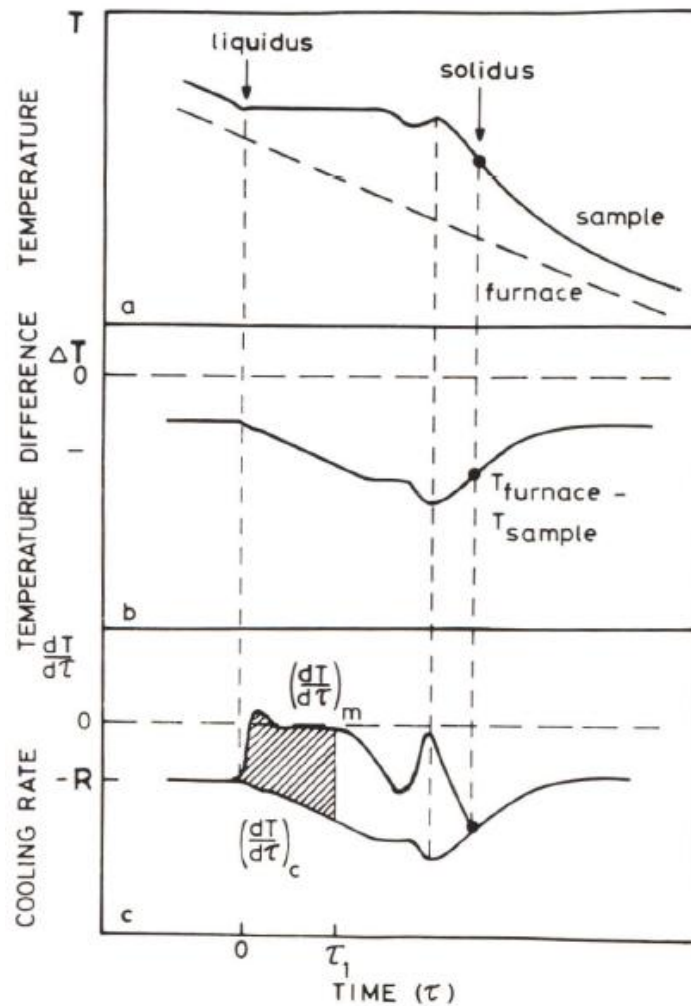
Figure 6-3: Derivation of fraction solid phase; a is temperature, b is temperature

difference, and c is cooling rate profiles [125]

Figure 6-3c shows the change of cooling rate during solidification and below the solidus temperature. At the early stages of solidification, the measured cooling rate varies enormously, and is then constant; it starts increasing at the growth temperature of dendrites, decreases at the secondary phase precipitation, and then decreases at the solidification.

The cooling rate is the same as that of the furnace (-R) until solidification starts. The rate measured in the centre of the sample then decreases to zero as solidification proceeds at the liquidus temperature until the solidification front reaches the thermocouple. Development of a new solid phase and loss of the liquid phase also affect the cooling rate.

Solidification simulations were performed with both models at each nodal position, an example being presented in Fig 6-4. This traces the Si and Mn liquid concentration with increasing solid fraction during solidification. The Si and Mn profiles agree reasonably for both the QSP and DICTRA simulation, although the DICTRA results can be difficult to read precisely on such a sharp rise at the end of solidification. The QSP results show less segregation at 115 than 11.5mm, but DICTRA gave more similar results at these positions.

At 11.5mm, the QSP and DICTRA peak, Mn concentrations are similar, but the Si results are not. However, at 115mm, the Si peak values are equal. The discrepancies between the models cannot therefore be related to a single cause such as different values of partition coefficient k.
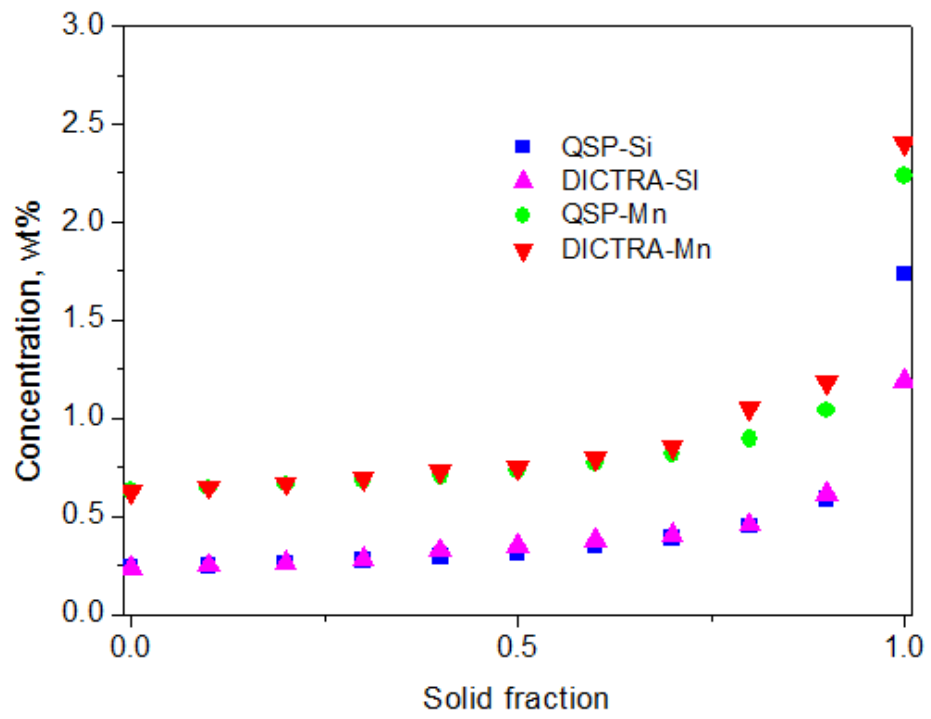
a)
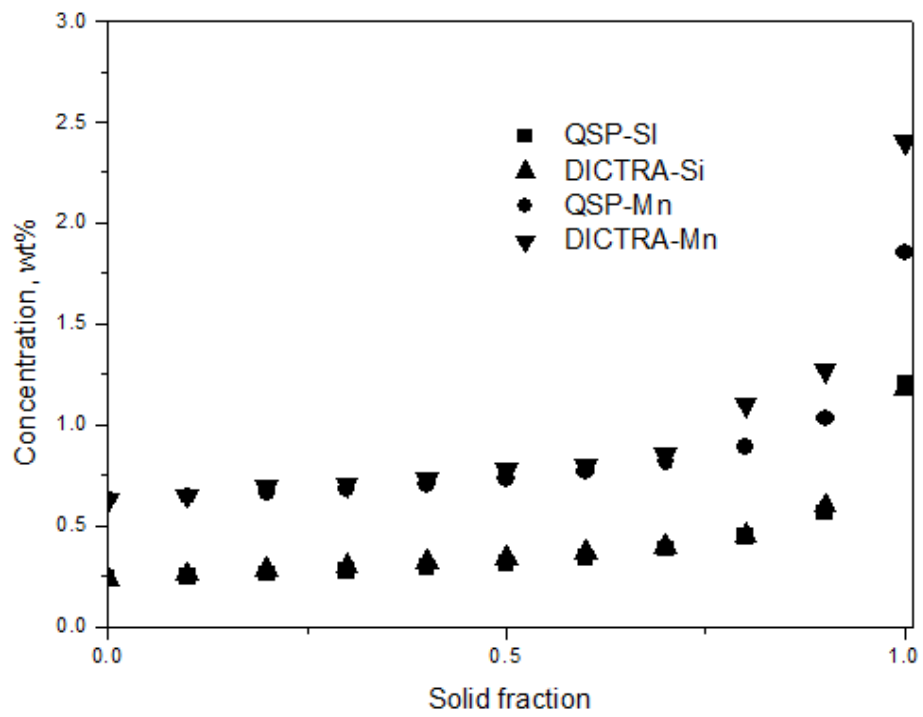
b)

Figure 6-4: QSP and DICTRA predictions for trace of liquid composition with

increasing solid fraction: (a) 11.5 mm and (b) 115 mm depth.
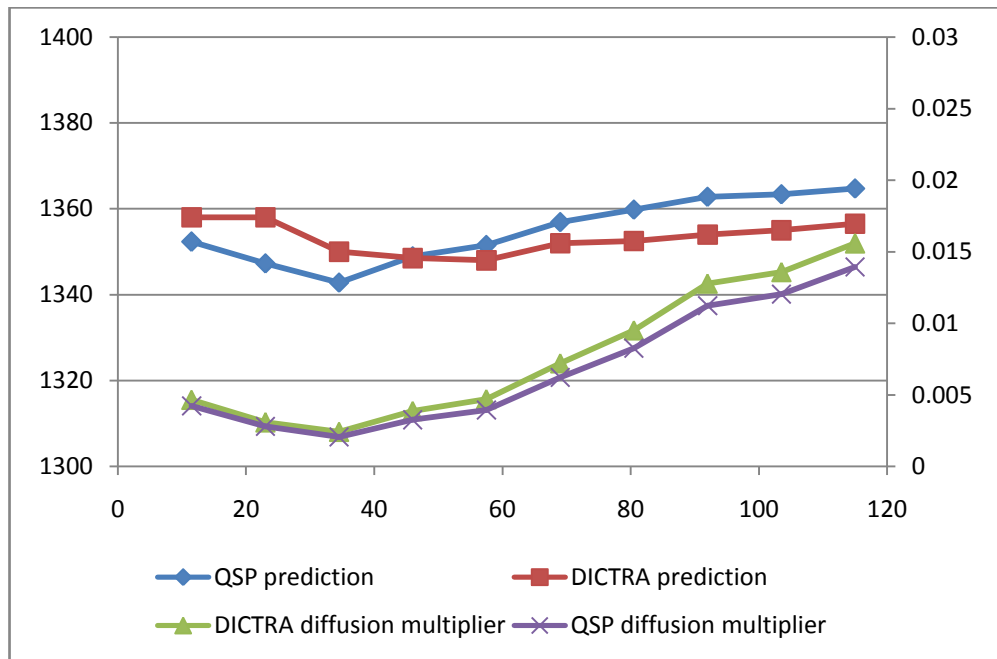
6.3 Solidus temperature results

Figure 6-5: Solidus temperature and diffusion multiplier t_f/λ_2^2 profiles

The solidus predictions across the thickness are presented in Figure 6-5. The calculated solidus temperatures showed a typical difference of about 5K between them, though not through a simple off-set. The usual expectation would be that the solidus should decrease from the centre to surface, reflecting increasing solidification rate. The QSP results show a stronger effect than DICTRA, but qualitatively, both proceed in this manner at first, but closer to the surface the trend is reversed, exhibiting a solidus trough (and consequent micro-segregation peak) at 34.5 mm for QSP and 46 or 57.5 mm depth for DICTRA. The relative extents of micro-segregation at 11.5 and 115mm depth in Figure 6-4 are consistent with QSP still having the solidus at 11.5 lower than at 115mm depth, whereas DICTRA has them as very similar.

In an attempt to understand this behaviour, the results were compared with qualitative expectation from diffusion controlled behaviour. A given degree of diffusive homogenisation occurs for the same parameter, Dt_f/X^2 where D is the solute diffusivity, t is the time and x is the distance (known as half secondary dendrite arm

spacing). D is primarily an exponential function of temperature, but there is little variation in the current case with all positions undergoing very similar liquidus-solidus intervals. Therefore, comparison of the relevant multiplier, f_f/λ_2^2 in this case, should be sufficient for comparative purposes. This parameter is included in Figure 6-5 and shows a very good agreement between them, but with the minimum value in both corresponding to the QSP solidus trough rather than the DICTRA one.

6.4 Sub-solidus homogenization results

The effect of cooling below the solidus temperature on micro-segregation has been investigated; the results show a significant degree of diffusive homogenization, which is a function of the diffusion modulus Dt_f/X^2. (X here is half of the secondary dendrite arm spacing, and the solute diffusivity D is a function of temperature.)

QSP and DICTRA used the cooling curves in Figure 6-1. The cooling curves extend down to 850 ℃ for those bloom-depths. An approximation of a sequence of constant cooling rates has been calculated from the cooling curves for the 11.5 mm , 23 mm, 35.5 mm and 46 mm positions for the temperature ranges down to 1000 ℃. For the case of 11.5mm depth, the cooling rate is 3.8 ℃/s from the solidus down to 1250 ℃, 0.85 ℃/s down to 1000 ^{0}C, and 0.258 ℃/s down to 900 ℃. For the 46 mm depth, the cooling curve just goes to around 1100 ℃ with a cooling rate of 0.092 ℃/s, an extrapolation has been made down to 1000 ℃ with cooling rate of 0.055 ℃ which is good enough for our purpose to run the DICTRA simulation. From the above constant cooling rates, the heat extraction rates are then calculated (multiplying them by C_P, where C_P is the specific heat capacity = 0.69 (kj/KgK for austenite), those heat extraction rates are used for the QSP simulation in order to compare the results with DICTRA (table 1).
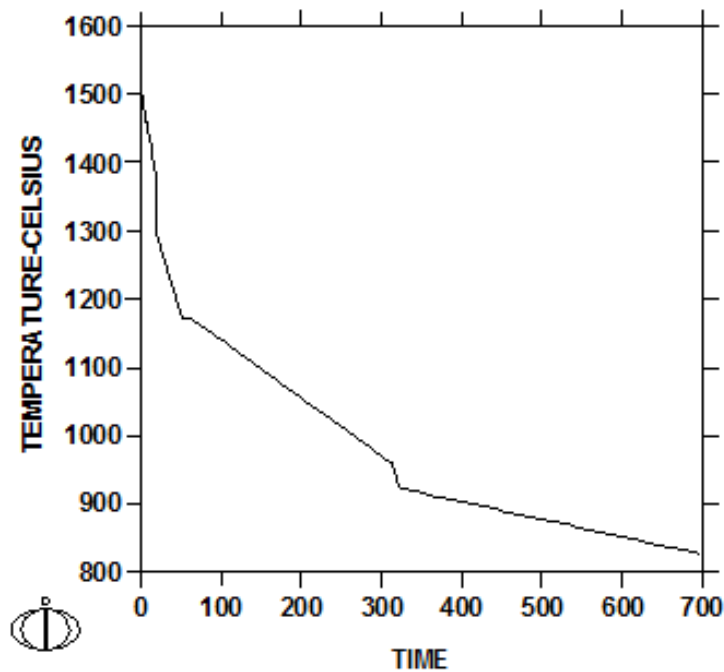
Figure 6-6: DICTRA simulation with different cooling rate based on cooling

curve at bloom depth of 11.5 mm.

Figure 6-6 shows the case of bloom depth of 11.5 mm, the cooling conditions are used in DICTRA based on cooling rate of 6.96 ℃/s from 1507 ℃ down to solidus, 3.81 ℃/s from the solidus of 1368.7 ℃ down to 1250 ℃, 0.85 ℃/s down to 1000 ℃, and 0.258 ℃/s down to 900 ℃.

The micro-segregation of elements decreases as the temperature decreases during continuous cooling; this decrease depends on the cooling conditions. For the continuous casting of large cross-sections of steel, this is more complicated, not only there being an effect of cooling rate, but also of multicomponent and multiphase alloys [22]. Figure 6-7 shows the sub-solidus homogenisation of C, Si and Mn. The micro-segregation of Si and Mn shows significant decrease during cooling. Carbon diffuses sufficiently rapidly to equalise, but interactions with the Si and Mn peaks are evident.
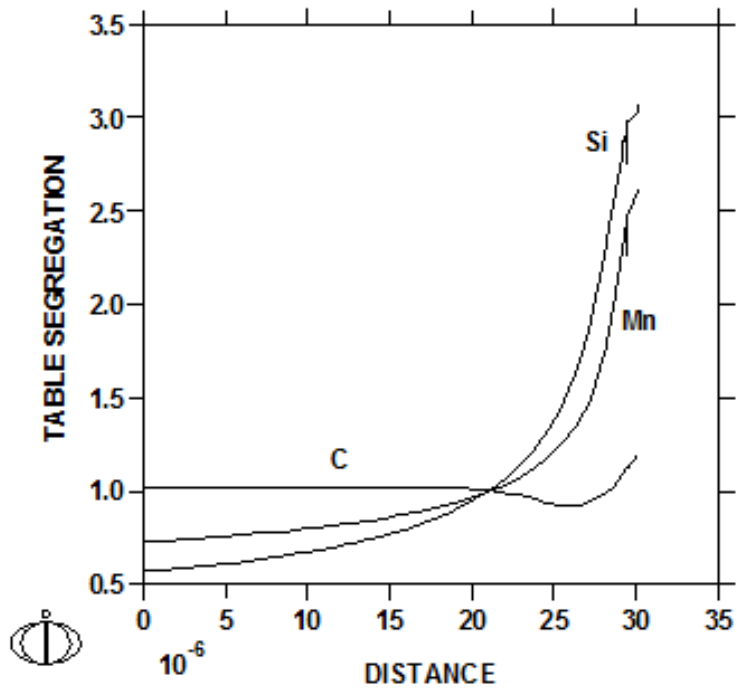
a) 1250 ℃
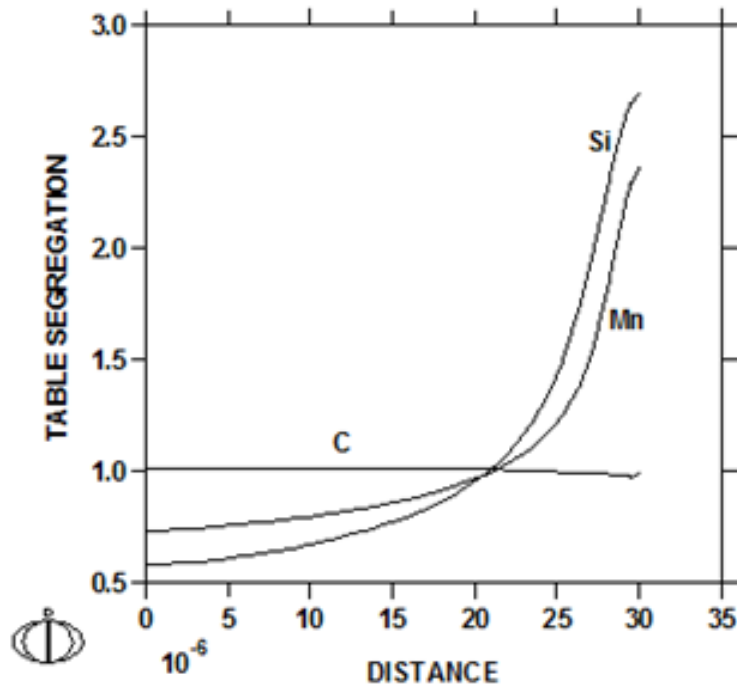
b) 900 ℃

Figure 6-7: Sub-solidus homogenization simulation using DICTRA of a 0.72C-0.24Si-0.63%Mn at 11.5 mm: (a) temperature down to 1250 ℃, (b) temperature down to 900 ℃.

Table 1 shows from simulation how Si and Mn solute profiles (Cmax) homogenise during cooling below the solidus based on the cooling curve in Fig. 1. At the 23 mm position, Si and Mn solutes show higher micro-segregation than the 11.5 mm position for both models, despite their different location of the solidus troughs, Figure 6-5. The 35.5mm position is less segregated than the 23mm position, and the 46 mm position is less segregated that the 35.5mm position. Toward the centre, it shows homogenization sub-solidus.

The movement of the peak position away from the solidus trough must reflect relative thermal histories during and after solidification, but can be explained through the 23 mm position having a SDAS of 120 µm, twice at the 11.5mm position of 60 µm. The faster cooling rate nearer the surface itself leads to more micro-segregation / depressed solidus temperature, but the smaller length-scale allows more homogenization sub-solidus. So the absolute segregation is a balance, this finding will be discussed in chapter 7.

QSP has generally shown more silicon micro-segregation than DICTRA, manganese micro-segregation varies from rather similar (near surface) to very different (near centre).

Table 6-1: Comparison between QSP and DICTRA sub-solidus homogenisation

simulation

| 11.5 mm position		QSP, Solidus T = 1352.3 ℃		DICTRA, Solidus T = 1358 ℃	
Temperature (℃)	Cooling rate (℃/s)	Si Cmax	Mn Cmax	Si Cmax	Mn Cmax
Solidus	6.96	1.041	1.744	0.714	1.872
1250	3.81	0.728	1.484	0.4836	1.343
1000	0.852	0.486	1.222	0.4104	1.209
900	0.258	0.333	0.981	0.3996	1.200
23 mm position		QSP, Solidus T =1347.3 ℃		DICTRA, Solidus T = 1358 ℃	
Temperature (℃)	Cooling rate (℃/s)	Si Cmax	Mn Cmax	Si Cmax	Mn Cmax
Solidus	2.61	1.170	1.855	0.702	1.833
1200	1.56	0.845	1.609	0.499	1.343
1100	0.49	0.656	1.436	0.474	1.310
1000	0.25	0.537	1.306	0.460	1.255
35.5 mm position		QSP, Solidus T =1342.8 ℃		DICTRA, Solidus T = 1350 ℃	
Temperature (℃)	Cooling rate (℃/s)	Si Cmax	Mn Cmax	Si Cmax	Mn Cmax
Solidus	1.09	1.259	1.919	0.840	2.262
1250	0.326	0.866	1.635	0.468	1.267
1150	0.282	0.806	1.584	0.448	1.249
1000	0.06	0.515	1.291	0.420	1.210
46 mm position		QSP, Solidus T =1348.9 ℃		DICTRA, Solidus T = 1348.5℃	
Temperature (℃)	Cooling rate (℃/s)	Si Cmax	Mn Cmax	Si Cmax	Mn Cmax
Solidus	0.59	1.127	1.823	0.870	2.550
1250	0.22	0.757	1.528	0.462	1.278
1100	0.092	0.571	1.336	0.416	1.185
1000	0.055	0.500	1.256	0.405	1.178
57.5 mm position		QSP, Solidus T =1351.5 ℃		DICTRA, Solidus T = 1348 ℃	
Temperature (℃)	Cooling rate (℃/s)	Si Cmax	Mn Cmax	Si Cmax	Mn Cmax
solidus	0.37	1.065	1.769	0.864	2.535
1250	0.16	0.719	1.482	0.449	1.217
1150	0.098	0.565	1.323	0.410	1.159
1000	0.061	0.487	1.228	0.396	1.150
69 mm position		QSP, Solidus T =1356.9 ℃		DICTRA, Solidus T = 1352 ℃	
Temperature (℃)	Cooling rate (℃/s)	Si Cmax	Mn Cmax	Si Cmax	Mn Cmax
solidus	0.249	0.936	1.657	0.810	2.418
1250	0.115	0.611	1.355	0.349	0.994
1150	0.048	0.481	1.202	0.331	0.993
1000	0.030	0.417	1.113	0.318	0.970

Chapter 7: Si and Mn Micro-segregation Measurements In The High Carbon Steel

7.1 SEM-EDS experimental results

Micro-segregation is the chemical inhomogeneity, which develop both during and after solidification at the scale of the solidification microstructure, generally that between the secondary dendrite arms [105], [108], [126], [127], over a length-scale of the order 60 μm. The extent of this segregation depends on the balance between the thermodynamics and kinetics, between the cooling rate and length-scale (typically half the secondary dendrite arm spacing) [2], [128], [129]. Most of the research in micro-segregation has been carried out in a small section at a laboratory scale rather than an industrial scale.

The research to date has tended to focus on Si and Mn micro-segregation both during solidification and sub-solidus rather than only during solidification at each bloom depth (the comparison with experiment requires account of the development below solidus).

Figures 7-1 to 7-40 show EDS-SEM line scans going through 2, 3 or 4 secondary dendrite arm spacings. The Si and Mn concentration profiles are the rolling averages of 3 data points to afford some smoothing. The Si and Mn concentration profiles are approximately proportional. The interdendritic peaks are clearer for Mn than for Si.
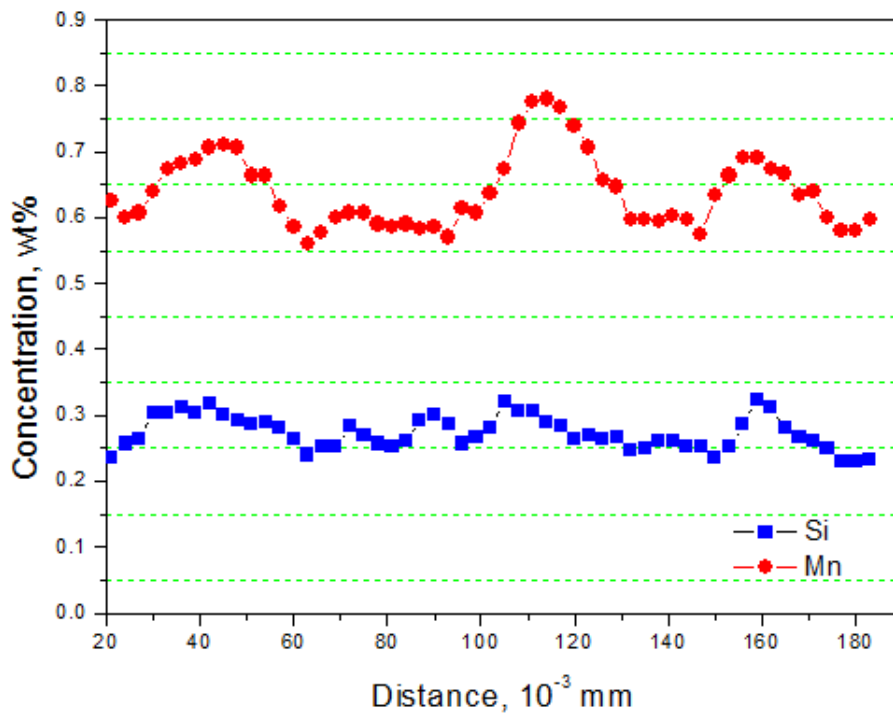
a)
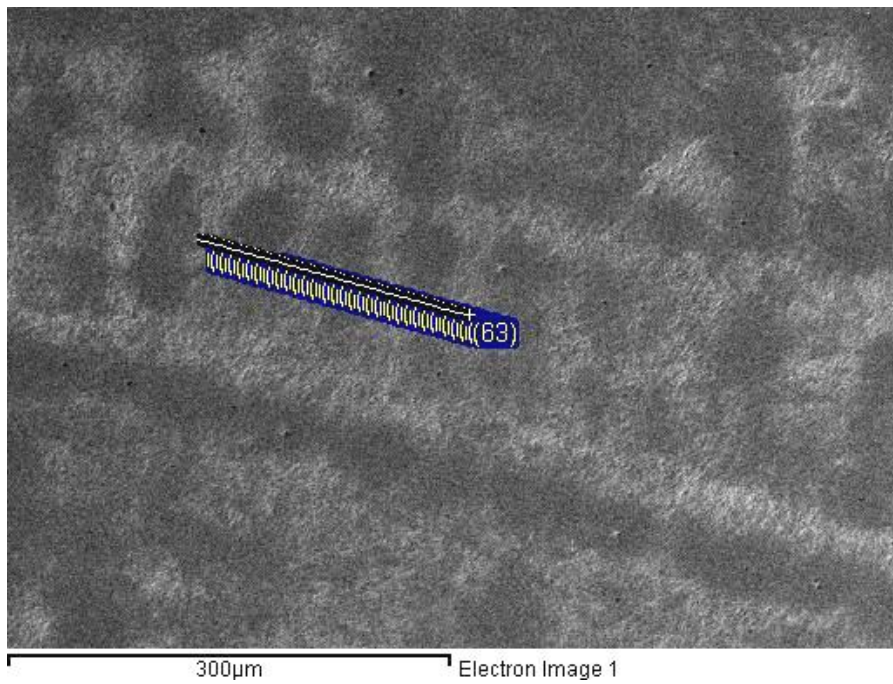
b)

Figure 7-1: EDS-SEM line-scan which through 3 SDAS at the 11.5 mm depth.

(a) Si and Mn concentration profiles, (b) Dendrite structure

Figure 7-1 shows the Si and Mn micro-segregation profiles through 3 SDAS at 11.5mm, from measurements taken every 3 µm. From the Mn concentration profile we can see that the Mn peaks have recorded as 0.8wt% at interdendritic regions; a minimum concentration of the Mn was recorded as 0.55wt% at dendrite cores. The Mn peaks are variable depending on the distance between the adjacent dendrites. A short distance of the dendrite arms results in a lower level of concentration at the same solidification conditions and cooling rate. The Mn profile goes around the average concentration of 0.64wt%. For the Si concentration profile, the Si peaks has recorded as 0.34wt%, the minimum concentration of Si has recorded of 0.23wt% at the dendrite cores. The Si concentration profile goes around the average concentration of 0.24wt%.
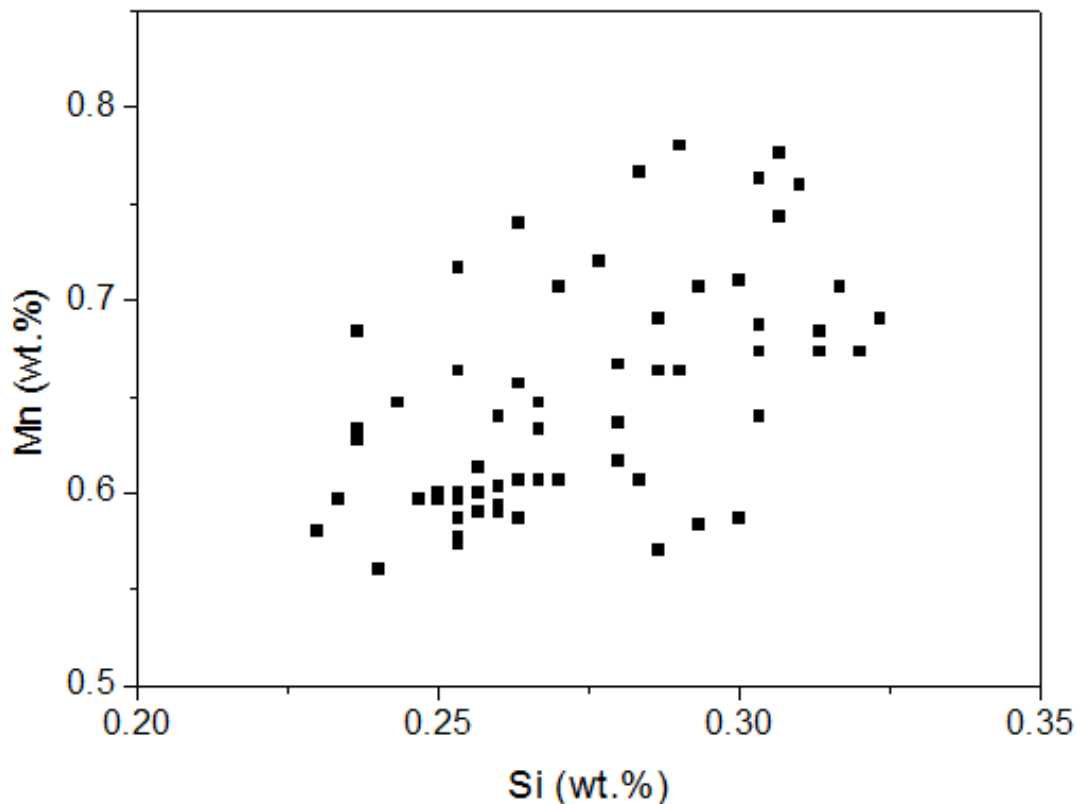

Figure 7-2: Correlation between silicon and manganese at the 11.5mm depth

Study of the correlation between silicon and manganese can be used as a tool to sort the micro-segregation with different depths. If the solidification proceeded with a single-phase, the correlation between silicon and manganese should be monotonic. If a

second phase forms in the interdendritic regions in the course of the solidification as in the peritectic reaction, there can be peaks or troughs at the dendrite cores to interdendritic [126], [75], and the correlation between silicon and manganese is less simple. The scatter not only depends on the thermal rate and solute diffusivity but also on the secondary dendrite arm spacing, details of the 3D morphology, and measurement error.

Figure 7-2 shows the correlation between silicon and manganese at the 11.5 mm position. Some of the EDS scatter for Si and Mn concentrations was smoothed using the 3 rolling average technique. The correlation follows the ideal line but shows big scatter. We can see that, increasing the Mn concentration resulted in an increase of the Si concentration. There are some reasons for the scatter; the faster cooling rate near the surface itself leads to more micro-segregation, and the tendency for precipitate formation could play a role. The different length-scales also lead to variable micro-segregation at the same thermal rate. The strong evidence of this was found in figure 7-1b, the spacing of the secondary arm in the middle is longer than at both sides, and it resulted in higher micro-segregation.
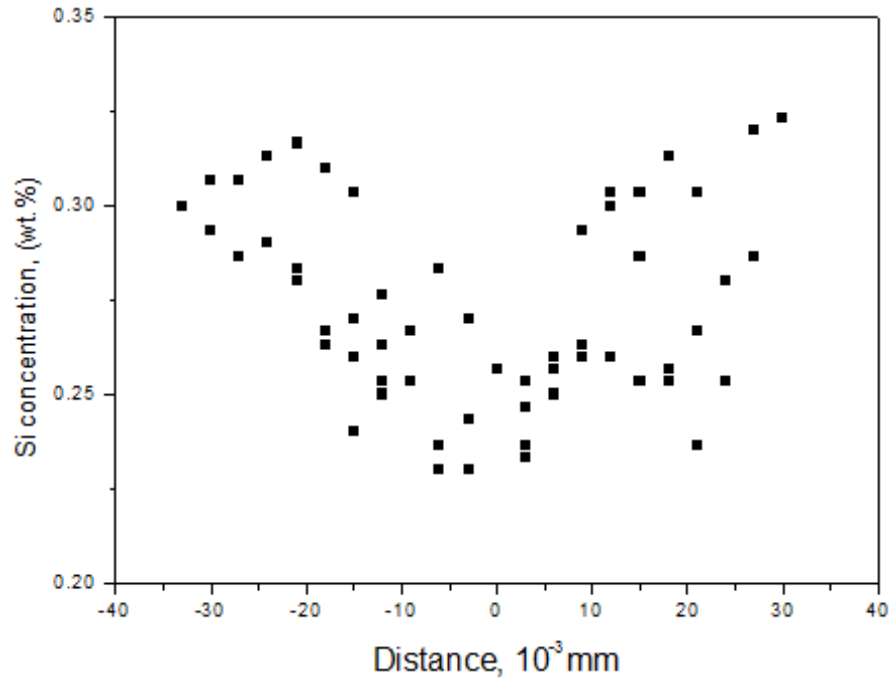
a)
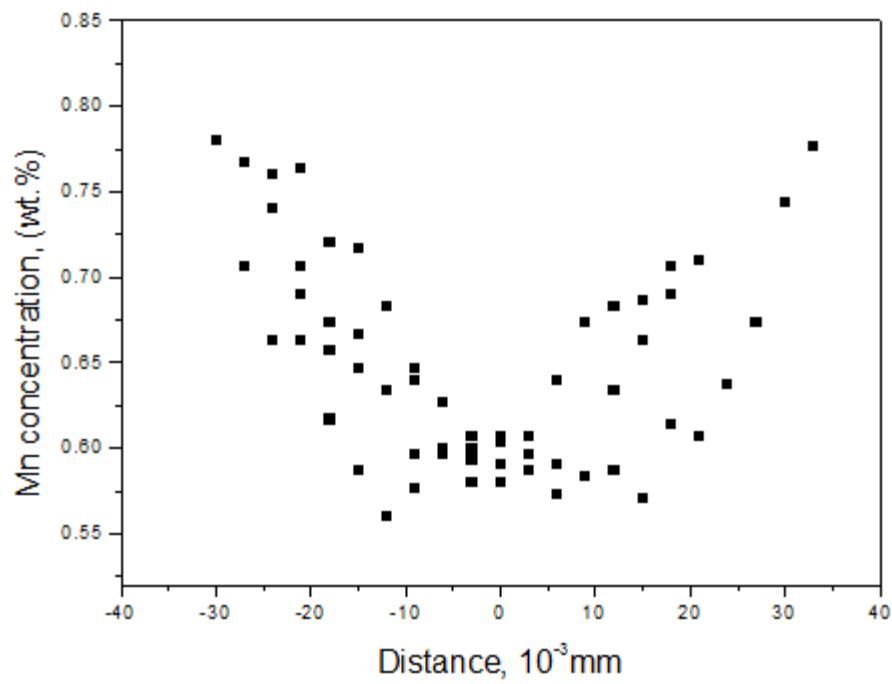
b)

Figure 7-3: Experimental profile compositions at the 11.5mm depth across a 60

μm secondary dendrite arm for (a) silicon and (b) manganese.

It was not easy to investigate the significant relationships of the micro-segregation of solutes and each bloom-depth further because the secondary dendrite arm spacing was variable. Figure 7-3 shows the silicon and manganese against distance from the dendrite core to the interdendrite region by reordering the EDS line scan experimental data at the 11.5mm depth position for all the dendrites in figure 7-1 a. The 3-rolling average technique was again applied to the experimental data in order to remove some of the EDS scatters. This alternative method for making the length-scale homogenous is used to measure exact micro-segregation of silicon and manganese. Silicon goes around the average composition of 0.24 wt.% and tends to segregate to the interdendrite region. Manganese also goes around the average composition of 0.63 wt.% and tends to segregate to the interdendrite region.

Figure 7-4 shows the Si and Mn micro-segregation profiles through 4 SDAS at 23mm, from measurements taken every 6 µm. From the Mn concentration profile we can see that the Mn peaks have recorded as 0.82wt% at interdendritic regions, a minimum concentration of Mn was recorded as 0.55wt% at the dendrite cores. Experimental data from this figure can be compared with the experimental data in figure 7-1 which shows a slight increasing from 0.8wt% to 0.82wt% toward 23mm. The appears to be some misalignment of the Si and Mn peaks and troughs, which will lead to scatter on their correlation, figure 7-6.
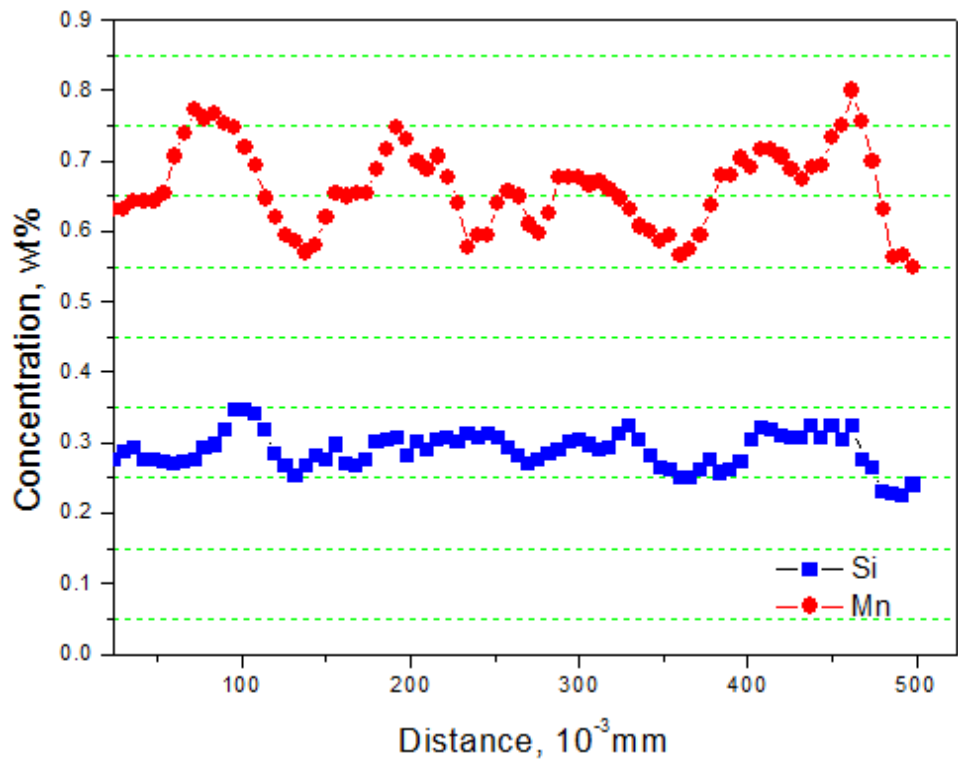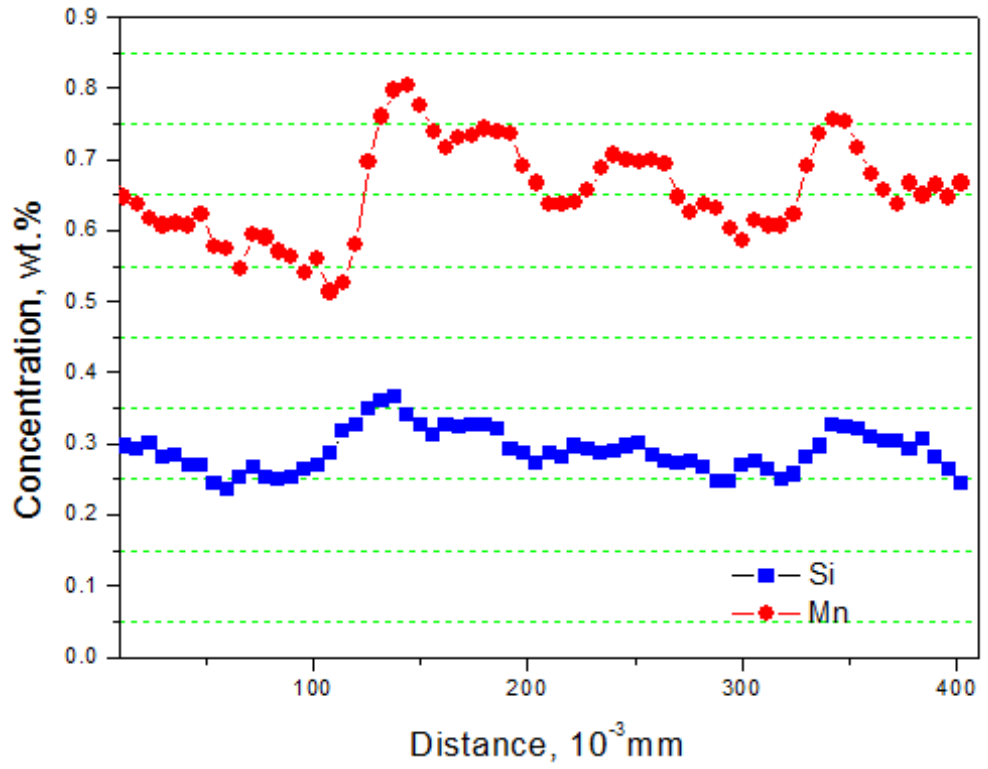
a)
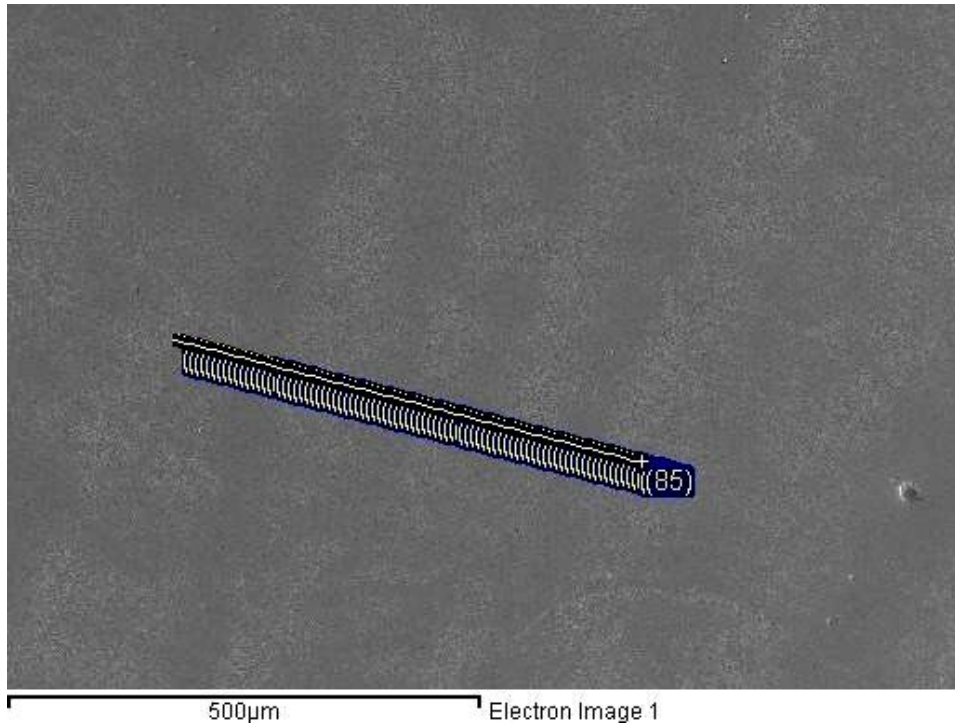
b)

Figure 7-4: EDS-SEM line-scan which goes through 4 SDAS at the 23 mm

depth. (a) Si and Mn concentration profiles, (b) Dendrite structure

a)

b)

Figure 7-5: Another EDS-SEM line-scan which goes through 4 SDAS at the 23

mm depth. (a) Si and Mn concentration profiles, (b) Dendrite structure
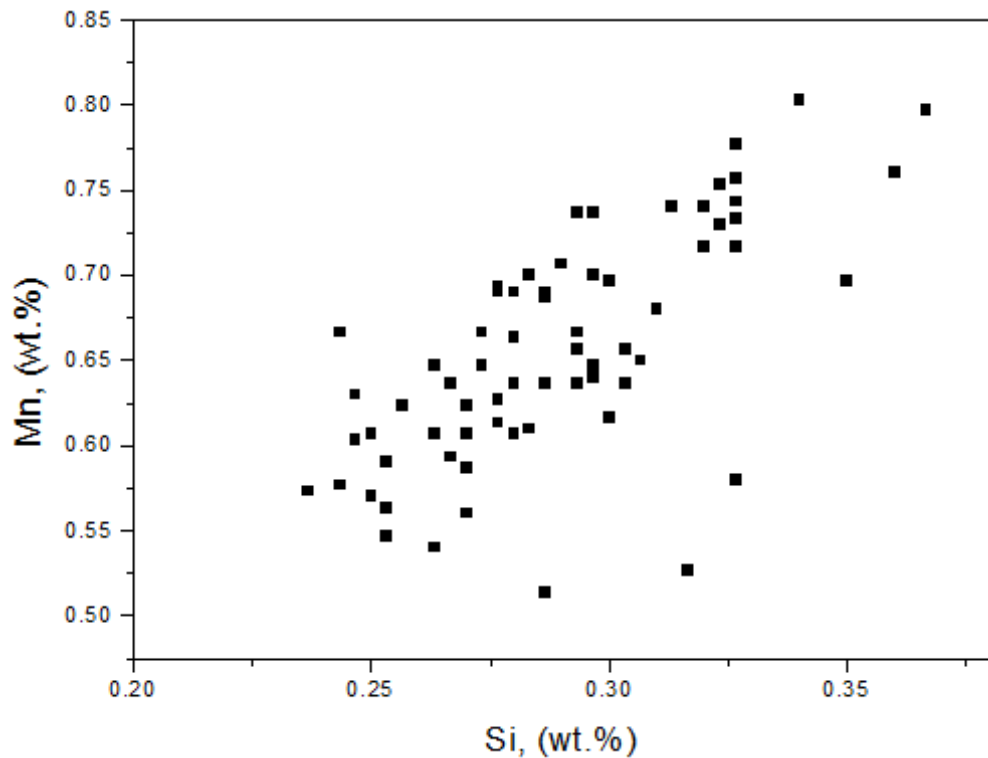
Figure 7-6: Correlation between silicon and manganese at the 23 mm depth.

Figure 7-6 shows the correlation between silicon and manganese at the 23 mm position of figure 7-5. A positive correlation was found between silicon and manganese, following the ideal line, with much less scatter than at 11.5 mm. Some of the scatter was found at the dendrite core; ie, low manganese with high silicon.

Figure 7-7 shows the silicon and manganese wt.% against distance from the dendrite core to the interdendrite region by reordering the EDS line scan experimental data at the 23 mm depth position of figure 7-5. The position with low manganese and high silicon as seen in figure 7-5, could be explained by the fact that there might be a hole or MnS inclusion which leads to lower manganese concentration than in other positions.

a)

b)

Figure 7-7: Experimental profile compositions at the 23 mm depth across a 120 μm secondary dendrite arm for (a) silicon and (b) manganese.
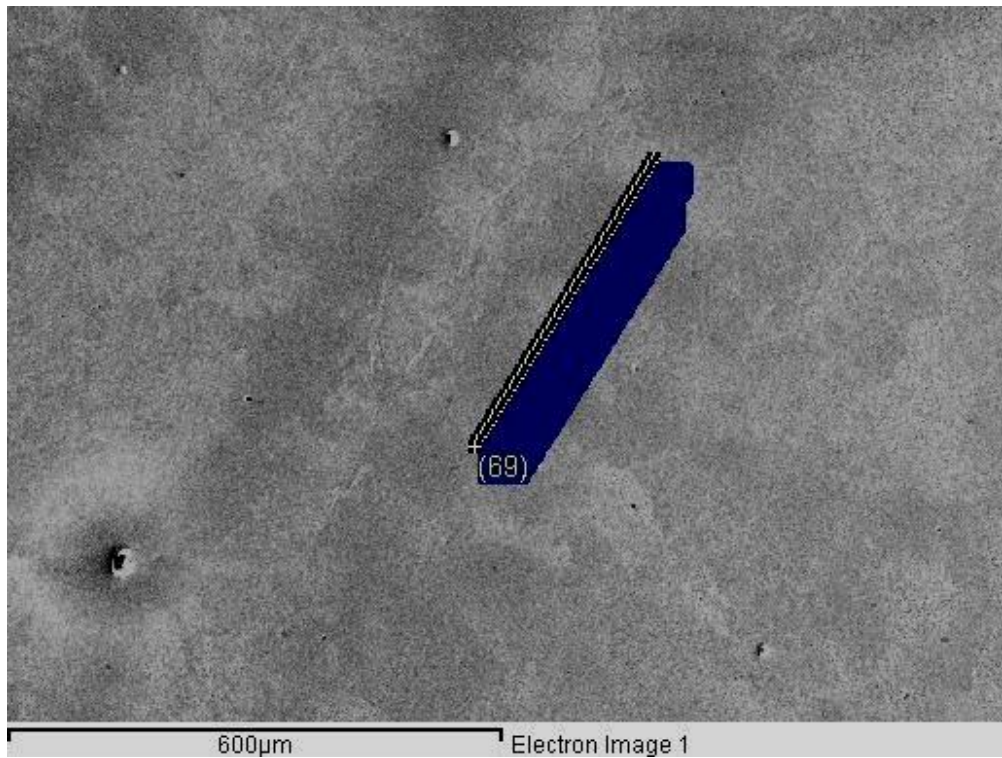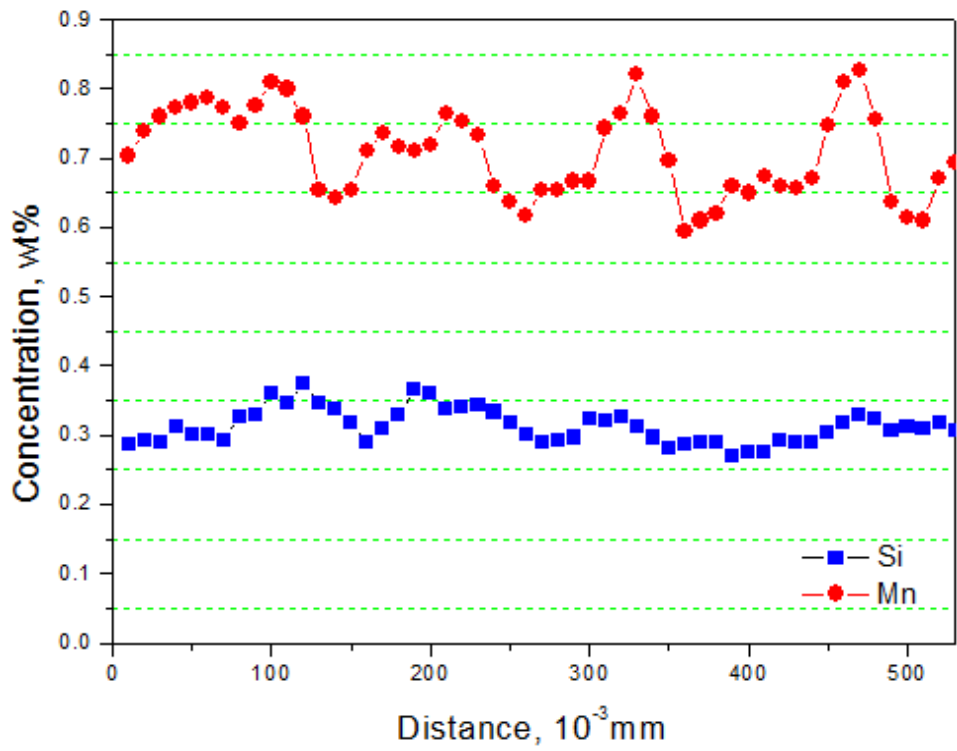
a)
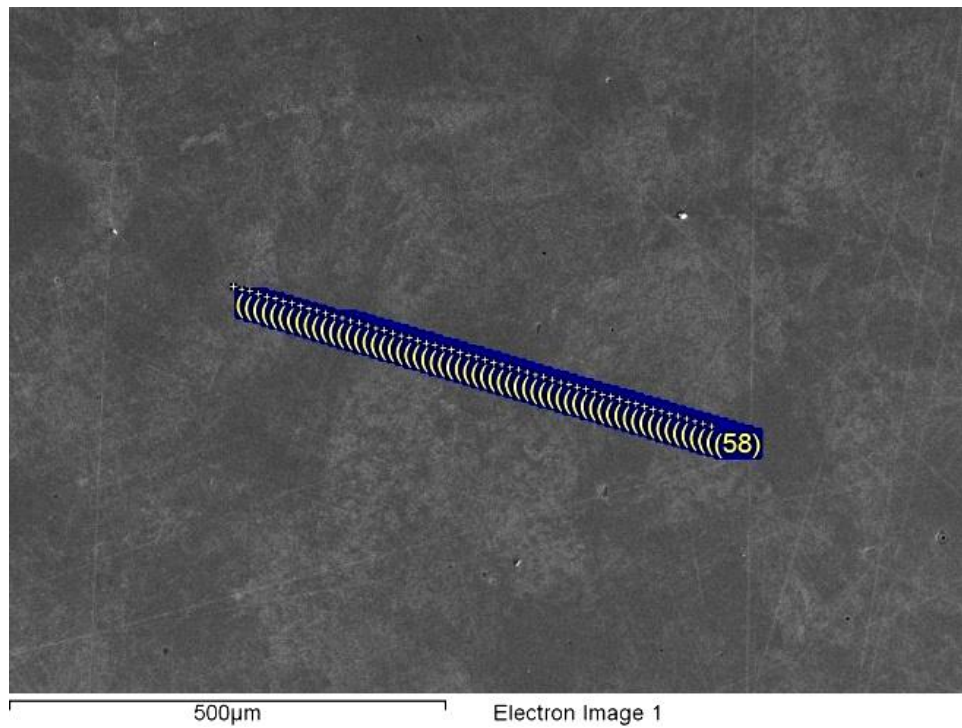
b)

Figure 7-8: EDS-SEM line-scan which goes through 3 SDAS at the 34.5 mm

depth. (a) Si and Mn concentration profiles, (b) Dendrite structure
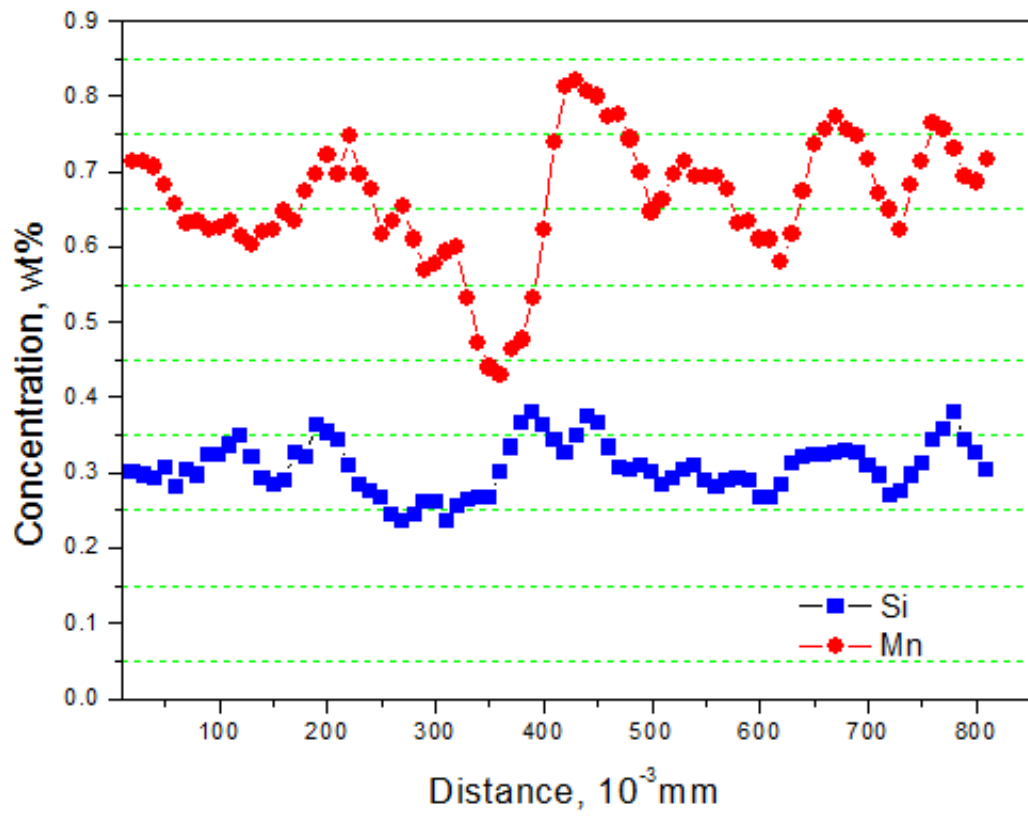
a)
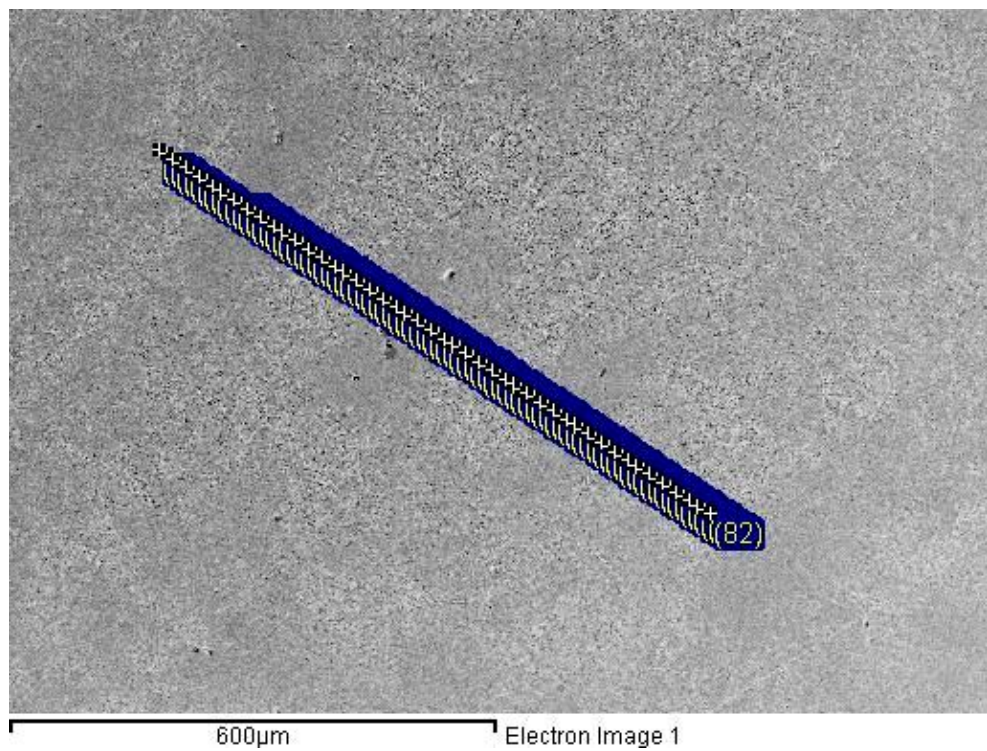
b)

Figure 7-9: Another EDS-SEM line-scan which goes through 4 SDAS at the 34.5 mm depth. (a) Si and Mn concentration profiles, (b) Dendrite structure
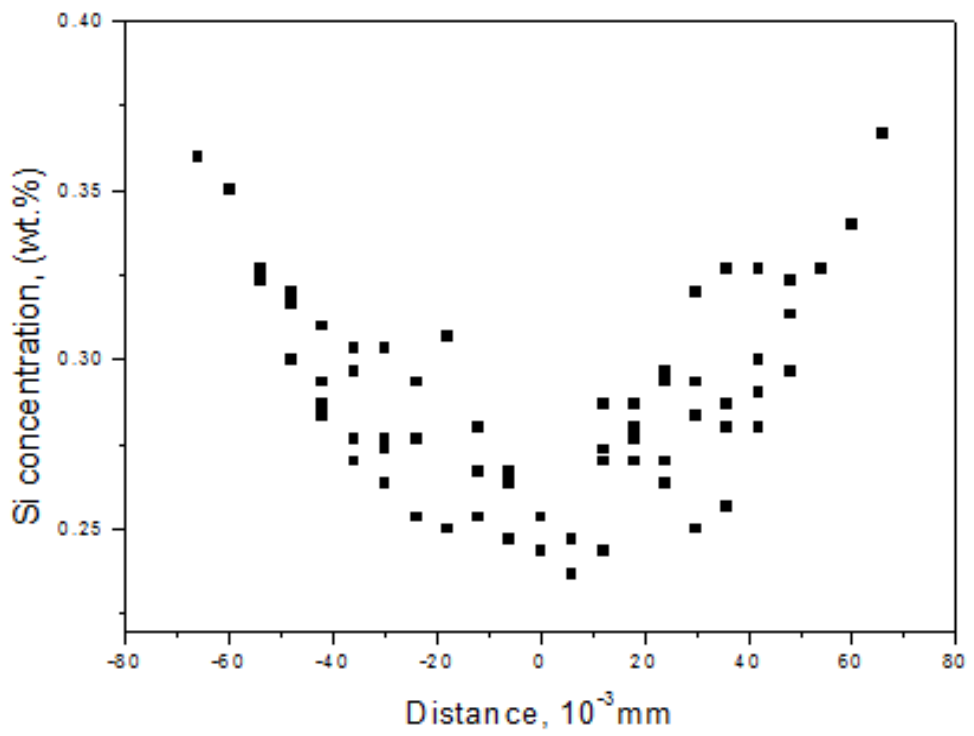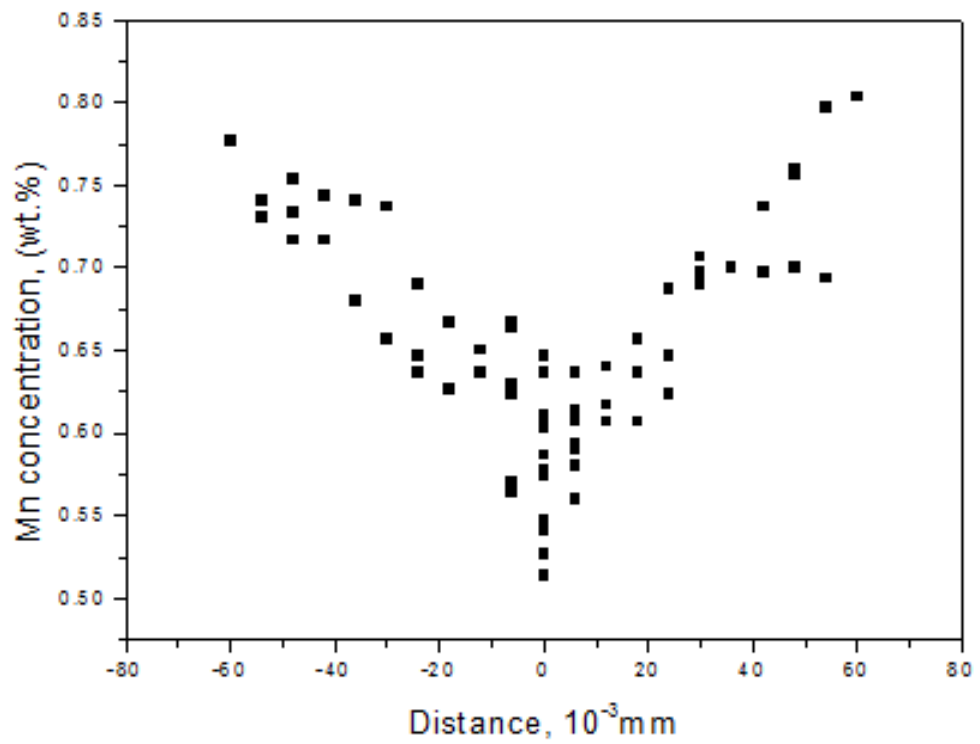
Figure 7-8 shows the Si and Mn micro-segregation profiles through 3 SDAS at 23mm, from measurements taken every 10 µm. From the Mn concentration profile, we can see that the Mn peaks have recorded 0.84wt% at the interdendritic regions, a minimum concentration of Mn was recorded of 0.6wt% at the dendrite cores. Comparison of Mn peaks between the two depth positions of 23mm and 34.5mm shows a slight increase from 0.82wt% to 0.84wt% toward 34.5mm.

Figure 7-9 shows another Si and Mn concentration profile at the same depth of 34.5 mm, The Si and Mn experimental data are smoother than the results in figure 7-8. Si peaks have significantly increased compared to close to the surface. The mean Si concentration has increased to 0.3wt% compared with average Si concentration of 0.24wt%. The position with low manganese and high silicon as seem in figure 7-9, could be explained by the fact that there might be a hole or MnS inclusion which leads lower manganese concentration than other positions, this is an unexpected experimental result. Mn concentration profiles show good agreement; Mn peaks have slightly increased compare to back towards the surface. Mn experimental results go around the average concentration.
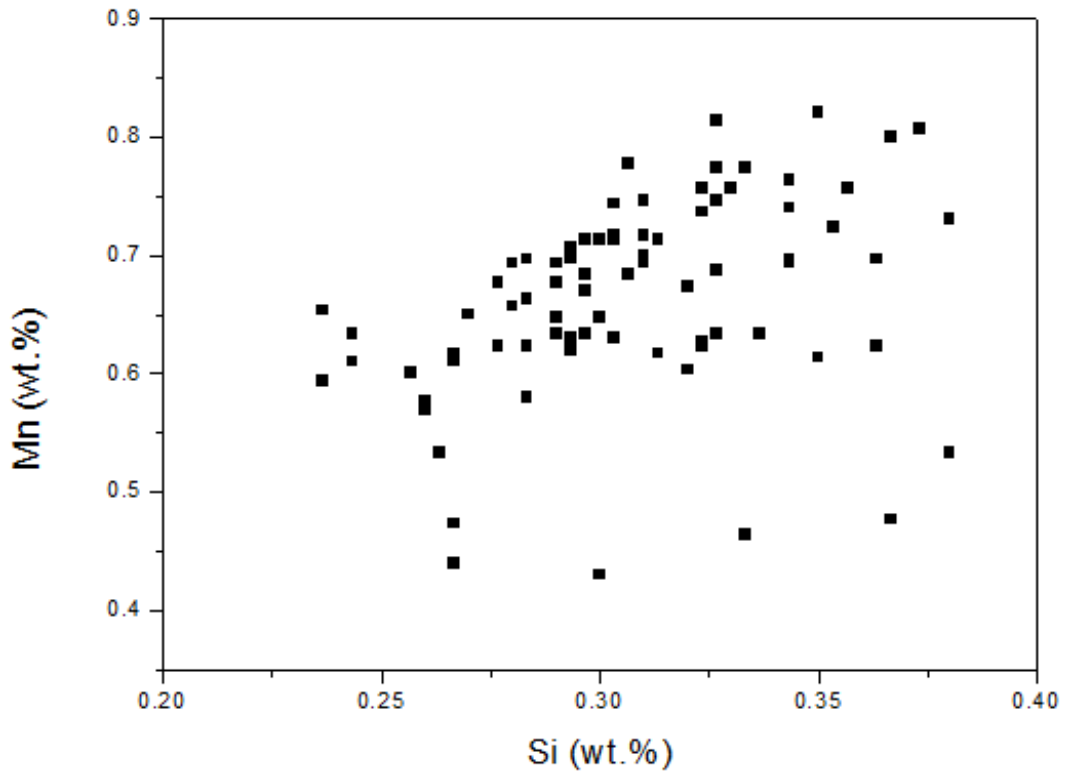
Figure 7-10: Correlation between silicon and manganese at the 34.5mm depth

(extracted from figure 7-9).

Figure 7-10 exhibits odd behaviour in the Si-Mn correlation. Notably, there are several results of very low Mn content that are below the theoretical minimum of $k_{Mn} * C_{0,Mn} = 0.49\%$ (where $k_{Mn} = 0.78$, $C_{0,Mn} = 0.63$). Figure 7-11 exhibit the silicon and manganese against distance of the dendrite core to the interdendrite region (some manganese scatters below the minimum concentration have been removed).

Figure 7-12 shows the Si and Mn micro-segregation profiles through 2 SDAS at 46mm, from measurements taken every 10 μm. Both Si and Mn profiles are proportional; smooth and increase from the dendrite cores to the interdendritic position; Mn peaks have slightly increased compared with the depth of 34.5mm. Again Si mean concentration is higher than the average concentration.
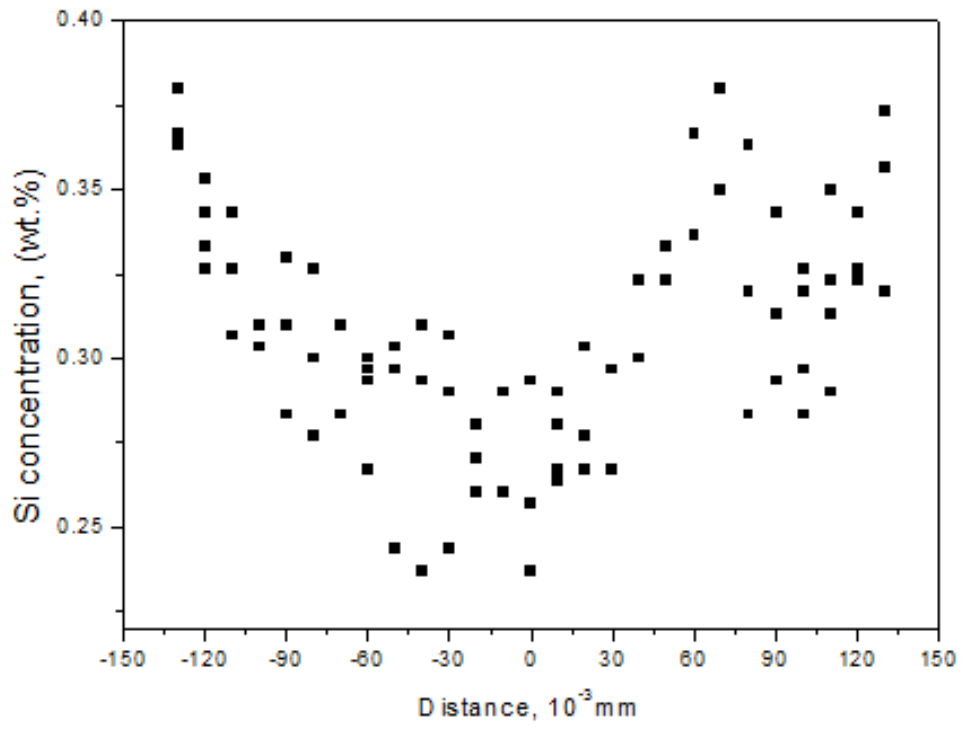
a)
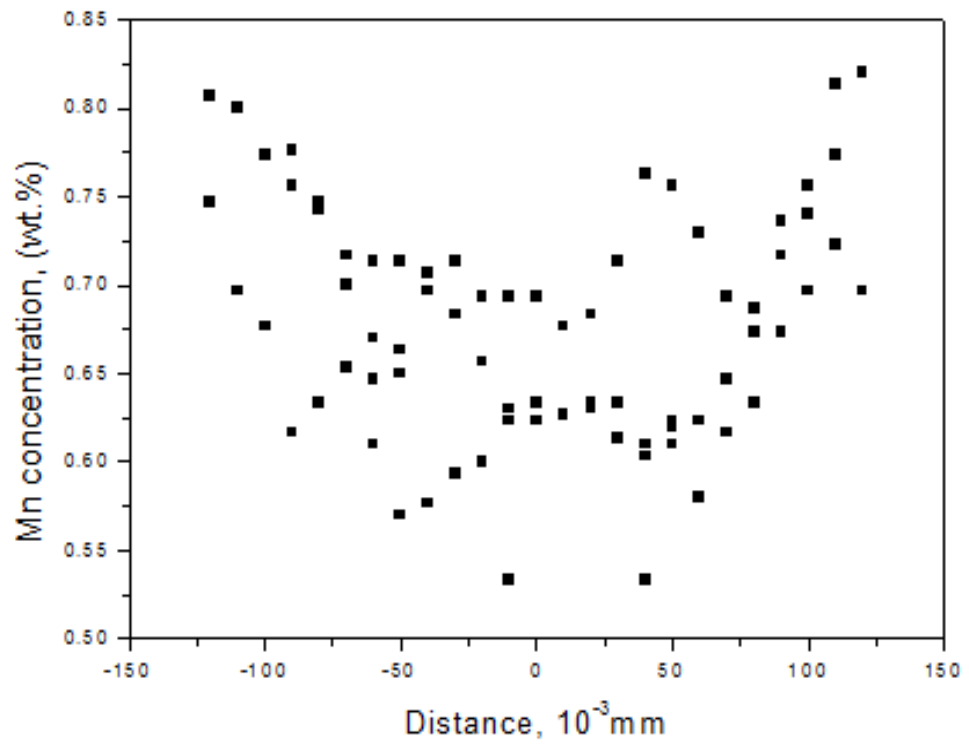
b)

Figure 7-11: Experimental profile compositions at the 34.5mm depth across a

216 μm secondary dendrite arm for (a) silicon and (b) manganese.
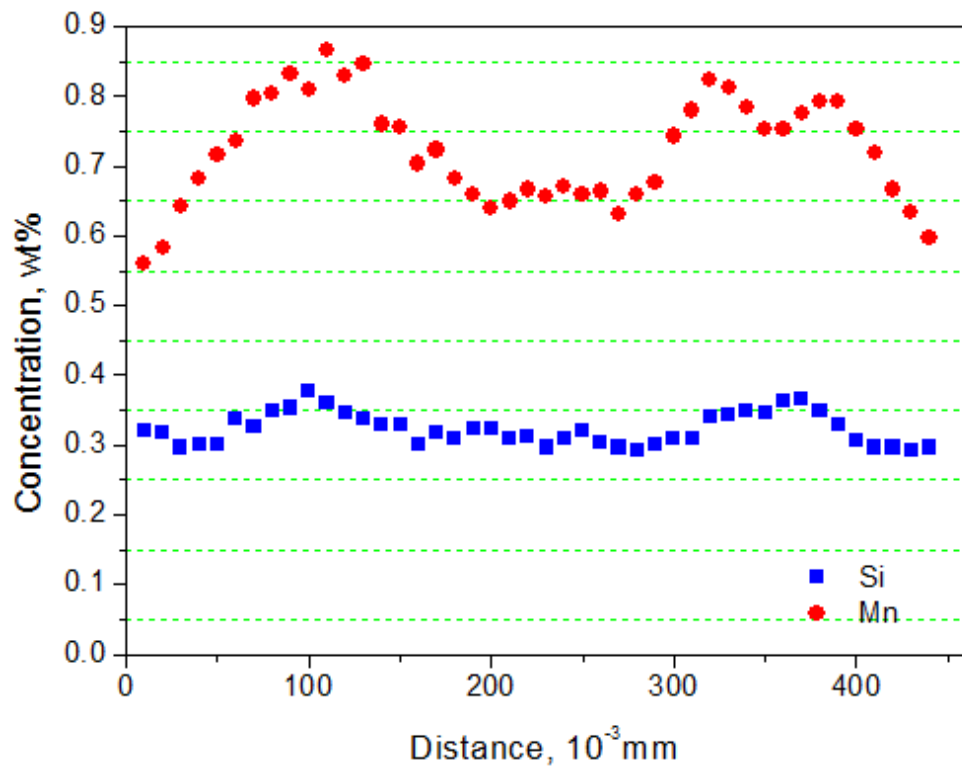
a)
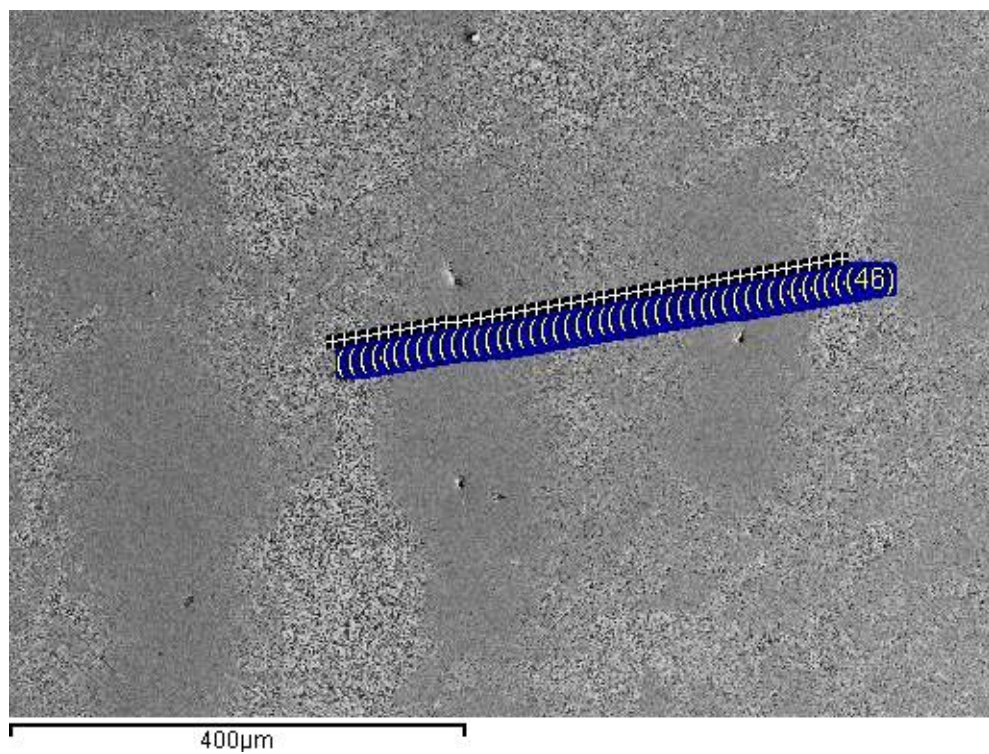
b)

Figure 7-12: EDS-SEM line-scan which goes through 2 SDAS at the 46 mm

depth. (a) Si and Mn concentration profiles, (b) Dendrite structure
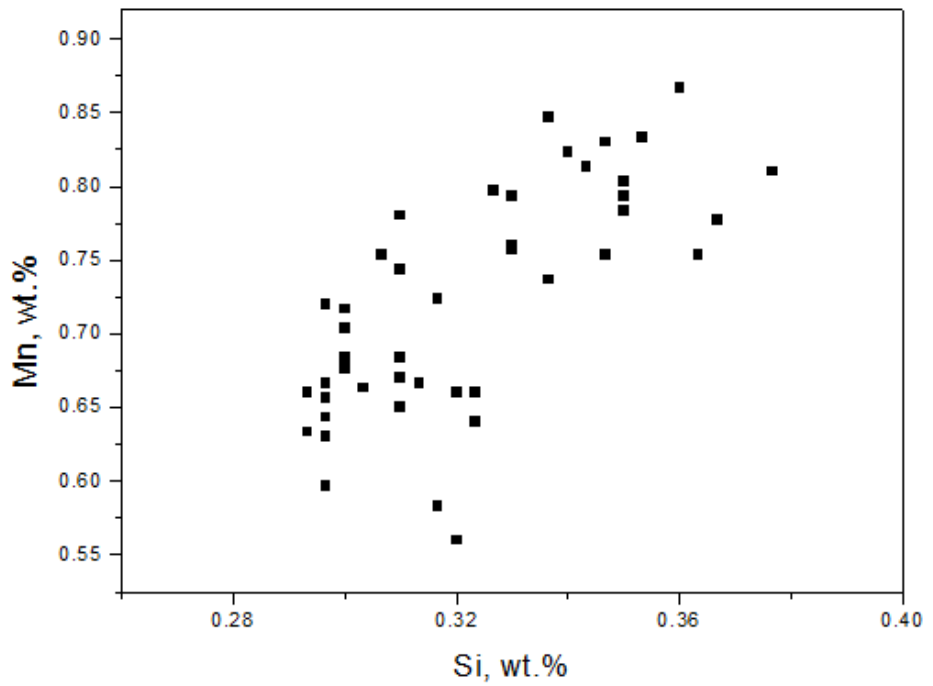
Figure 7-13: Correlation between silicon and manganese at the 46mm depth.

Figure 7-14 exhibits the silicon and manganese concentrations against distance of the dendrite core to the interdendrite region. The silicon curve exhibits a very good U shape slope with less scatter with the minimum point being the dendrite core and the highest at the interdendritic position. Manganese exhibits a very good V shaped curve with the lowest manganese points at 0.56 wt,% (dendrite core) and increasing to the highest point at the interdendritic position. The different Si and Mn profiles caused the correlation in figure 7-13.

a)

b)

Figure 7-14: Experimental profile compositions at the 46mm depth across a 233 μm secondary dendrite arm for (a) silicon and (b) manganese.
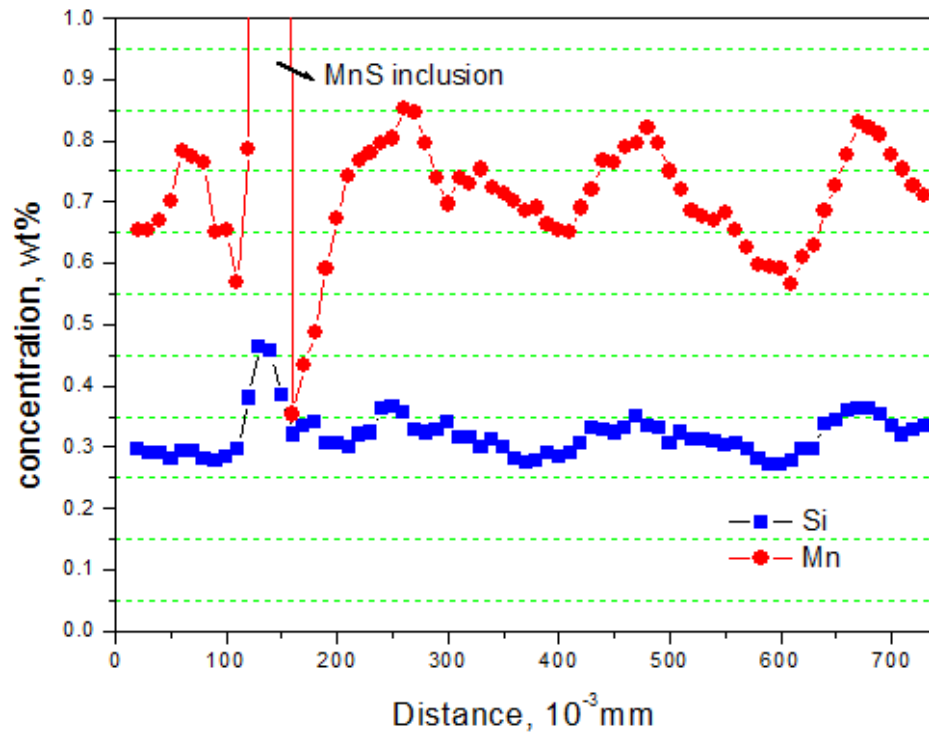
a)
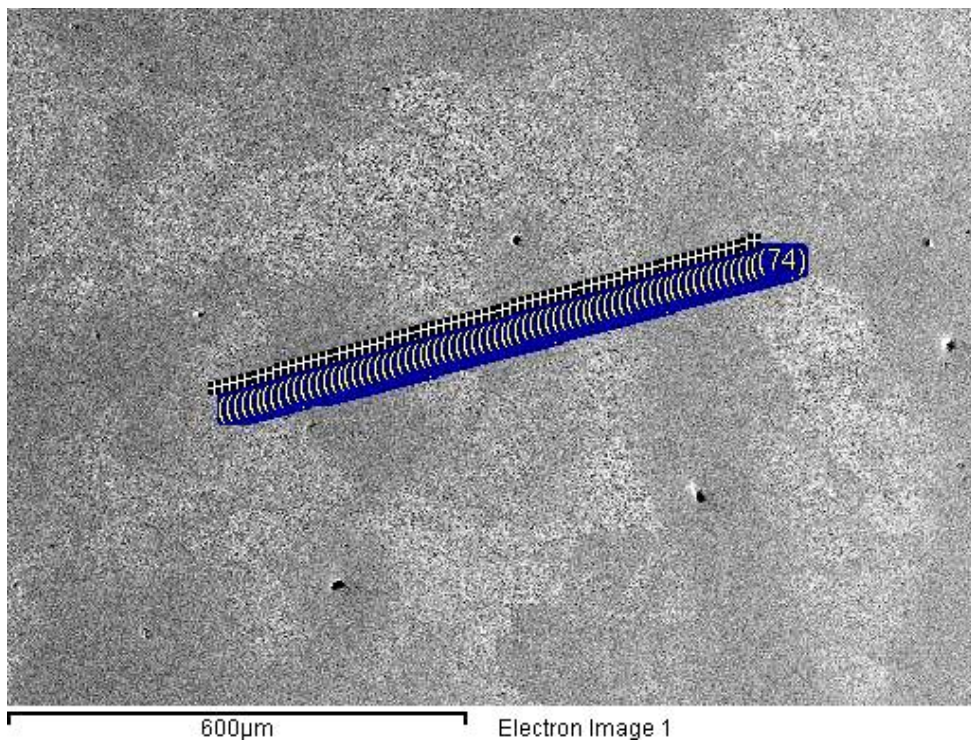
b)

Figure 7-15: EDS-SEM line-scan which goes through 3 SDAS at the 57.5 mm

depth. (a) Si and Mn concentration profiles, (b) Dendrite structure

Figure 7-15 shows the Si and Mn micro-segregation profiles through 2 SDAS at 57.5mm, from measurements taken every 10 μm. The highest Mn peak was recorded at position 14, it was a MnS inclusion within the chosen line scan; the strong evidence of this MnS was found in figure 7-16, a strong peak of S was found at point 14.
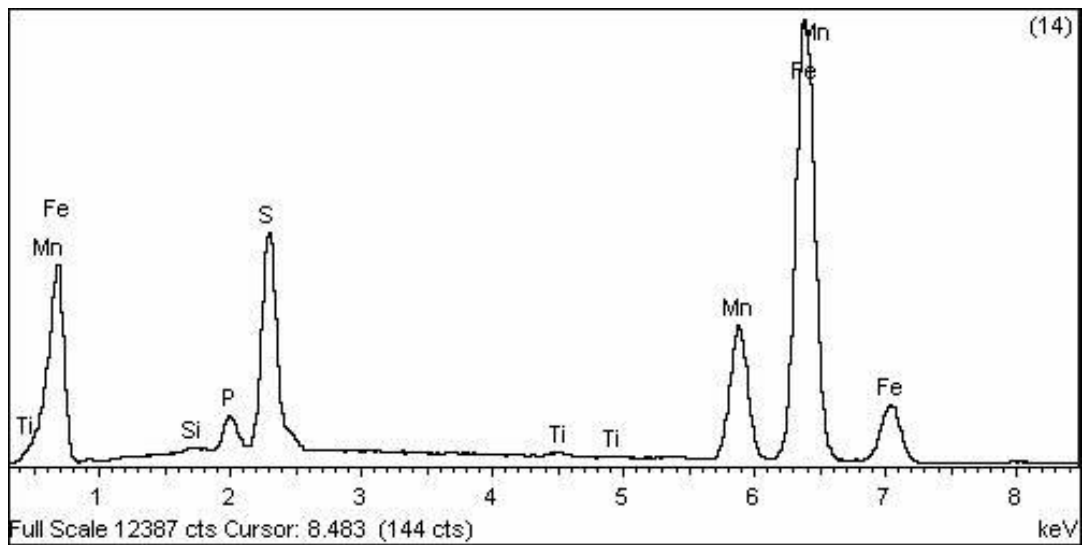
Figure 7-16: Evidence of MnS on a chosen EDS-SEM line-scan at the 57.5 mm depth.
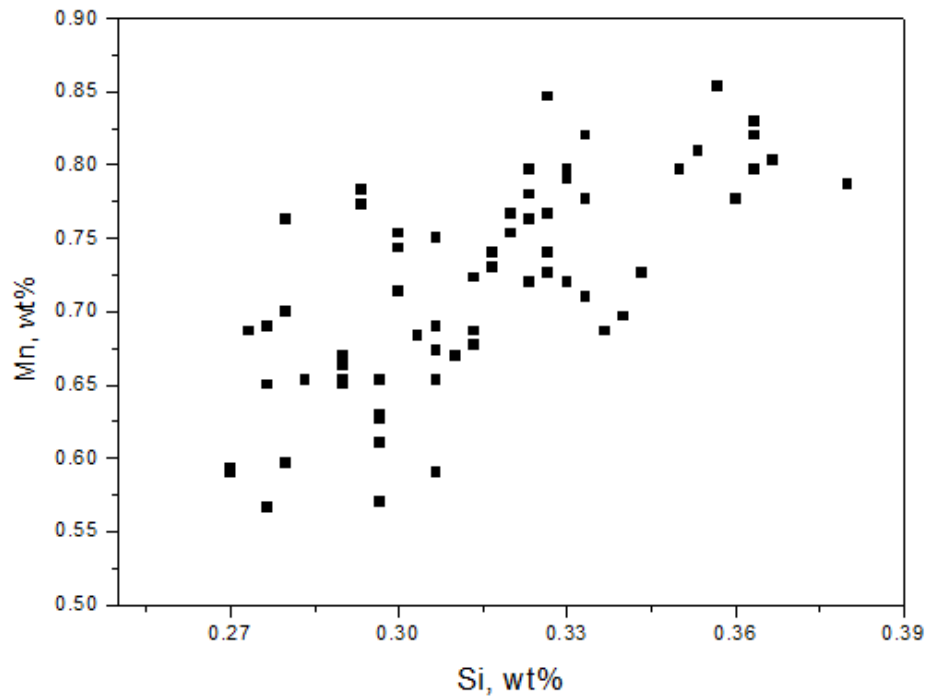
Figure 7-17: Correlation between silicon and manganese at the 57.5mm depth.

Figure 7-18 shows the silicon and manganese against distance of the dendrite core to the interdendrite region. Silicon exhibits a very good U shaped curve with the lowest point at the dendrite core and increasing to the highest point at the interdendritic position. Manganese exhibits a very good V shaped curve with the lowest manganese points at 0.56 wt,% and increasing to the highest point at the interdendritic postion. The different Si and Mn profiles caused the correlation in figure 7-17.
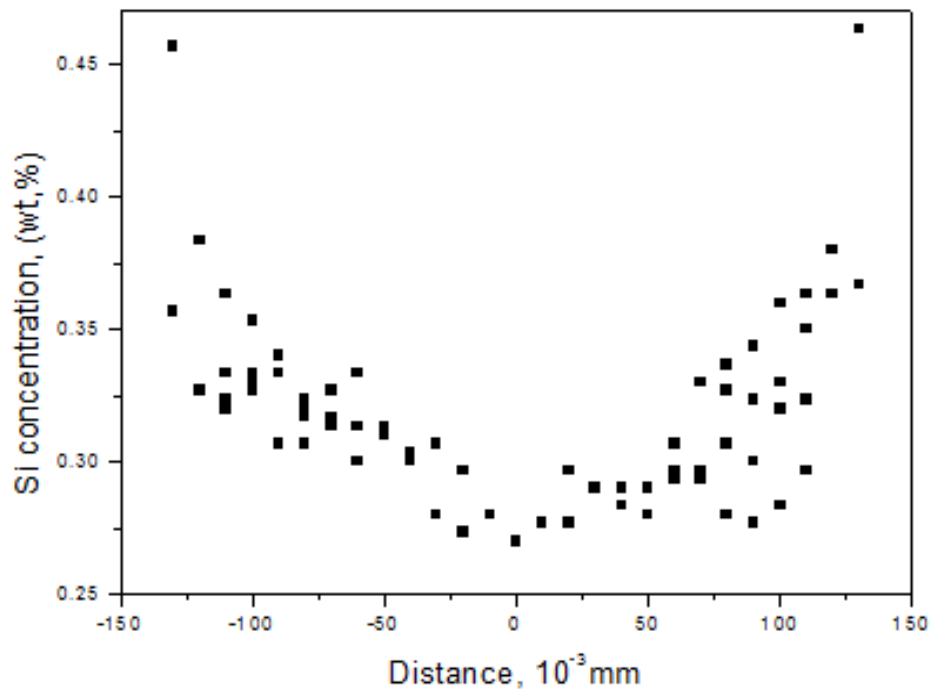
a)
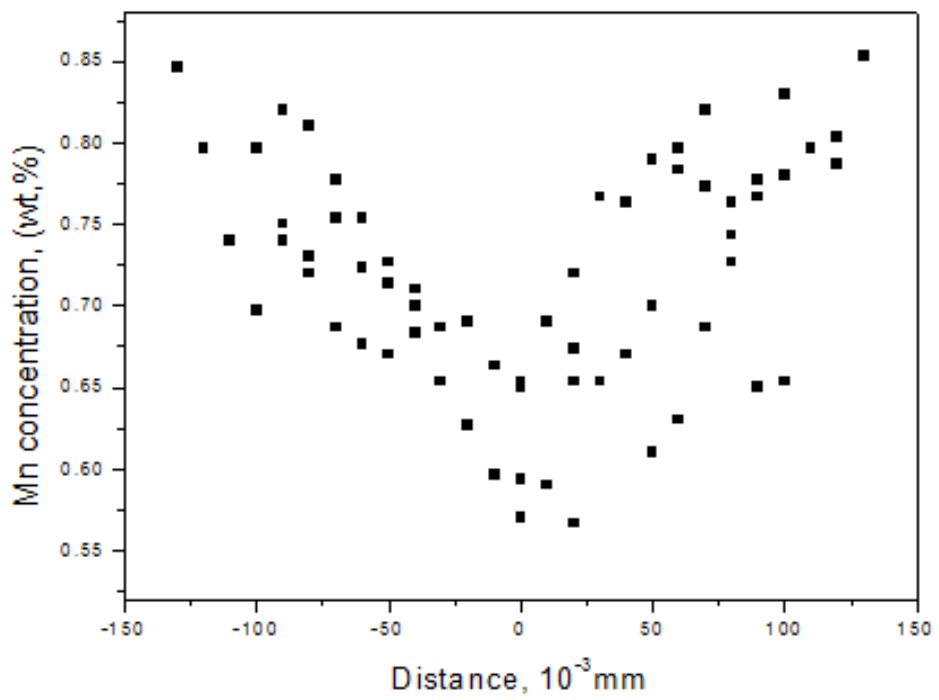
b)

Figure 7-18: Experimental profile compositions at the 57.5mm depth across a
268 μm secondary dendrite arm for (a) silicon and (b) manganese.
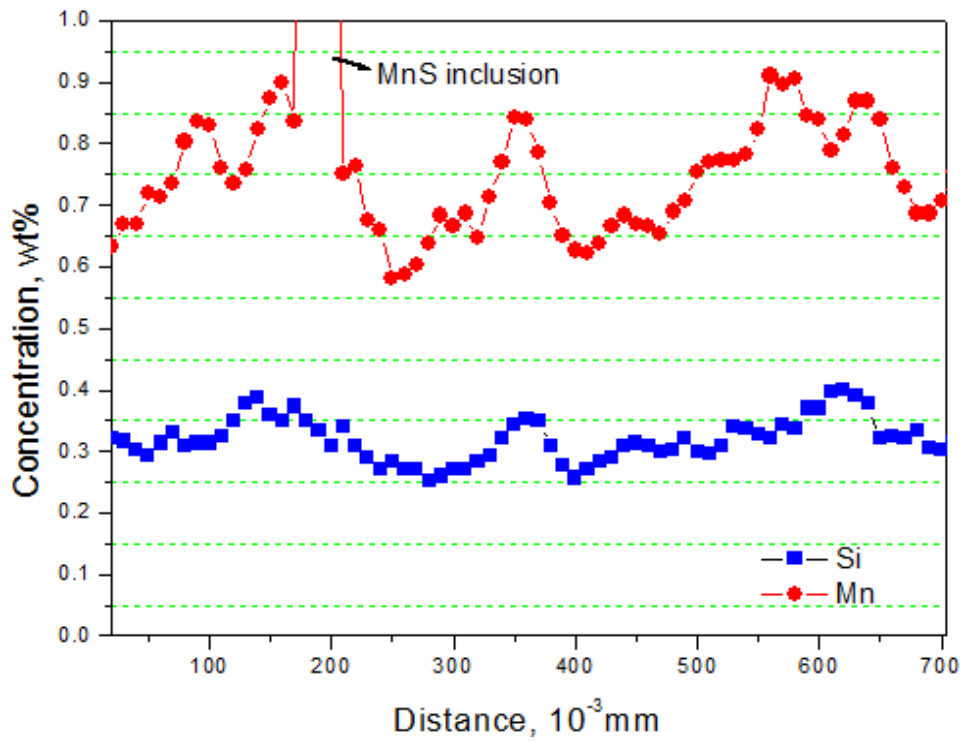
a)
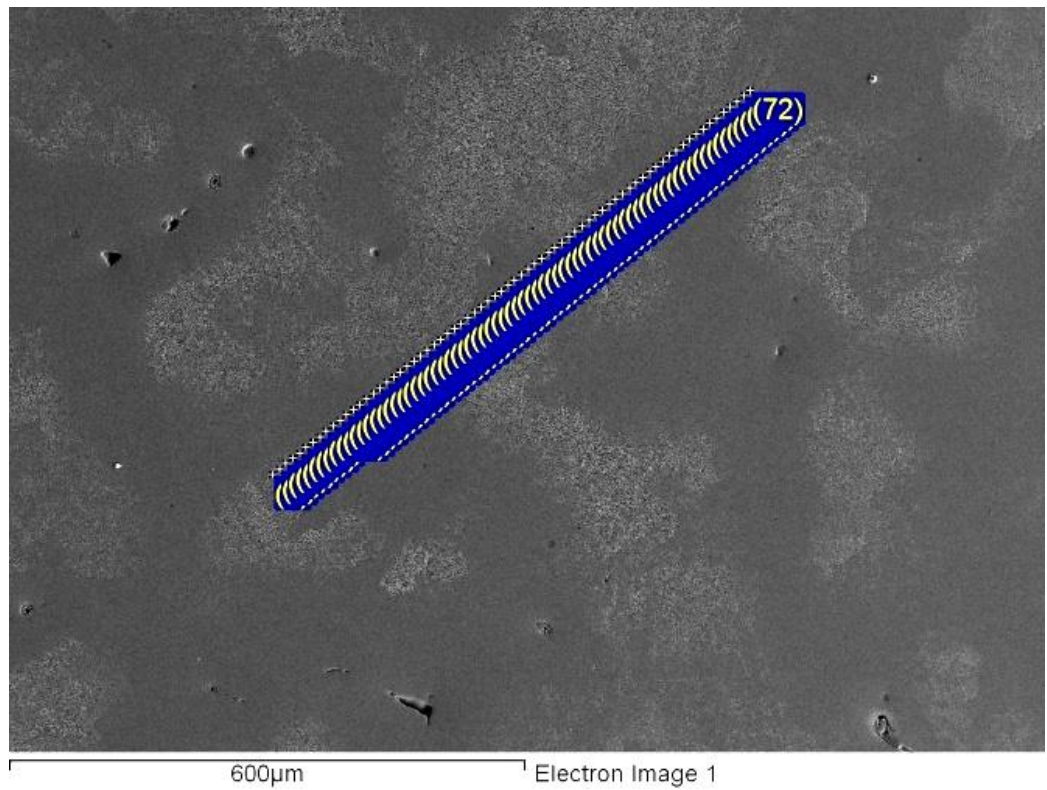
b)

Figure 7-19: EDS-SEM line-scan which goes through 3 SDAS at the 69 mm

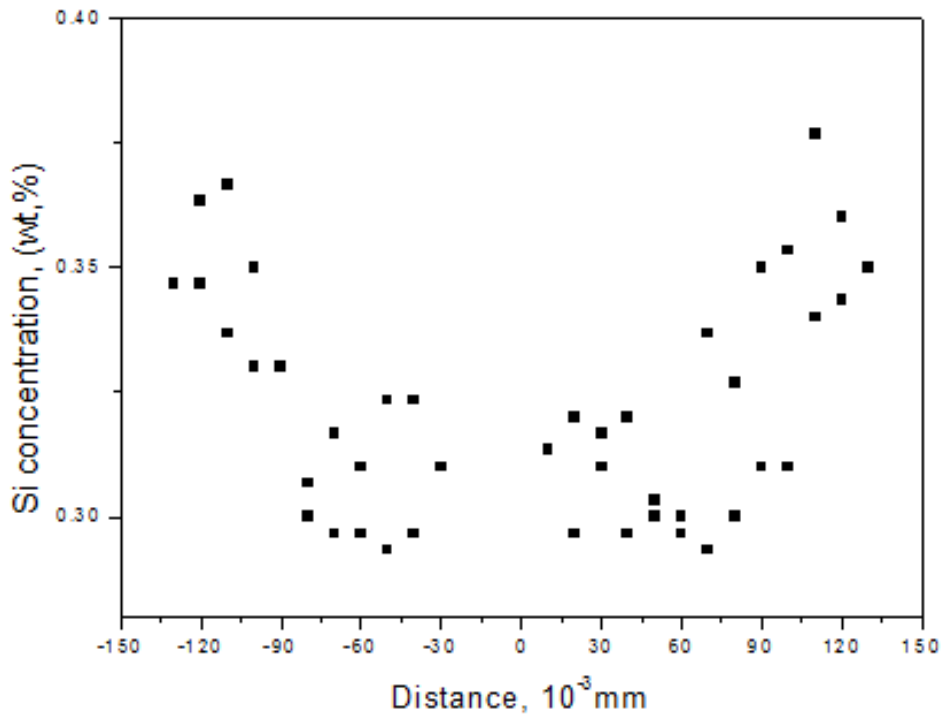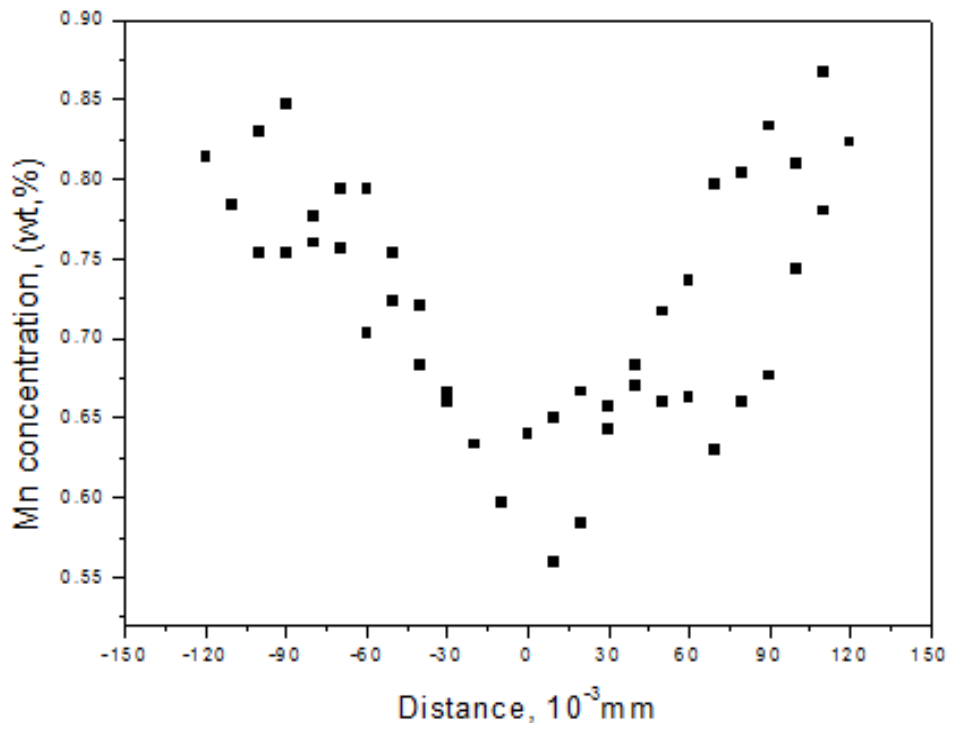depth. (a) Si and Mn concentration profiles, (b) Dendrite structure
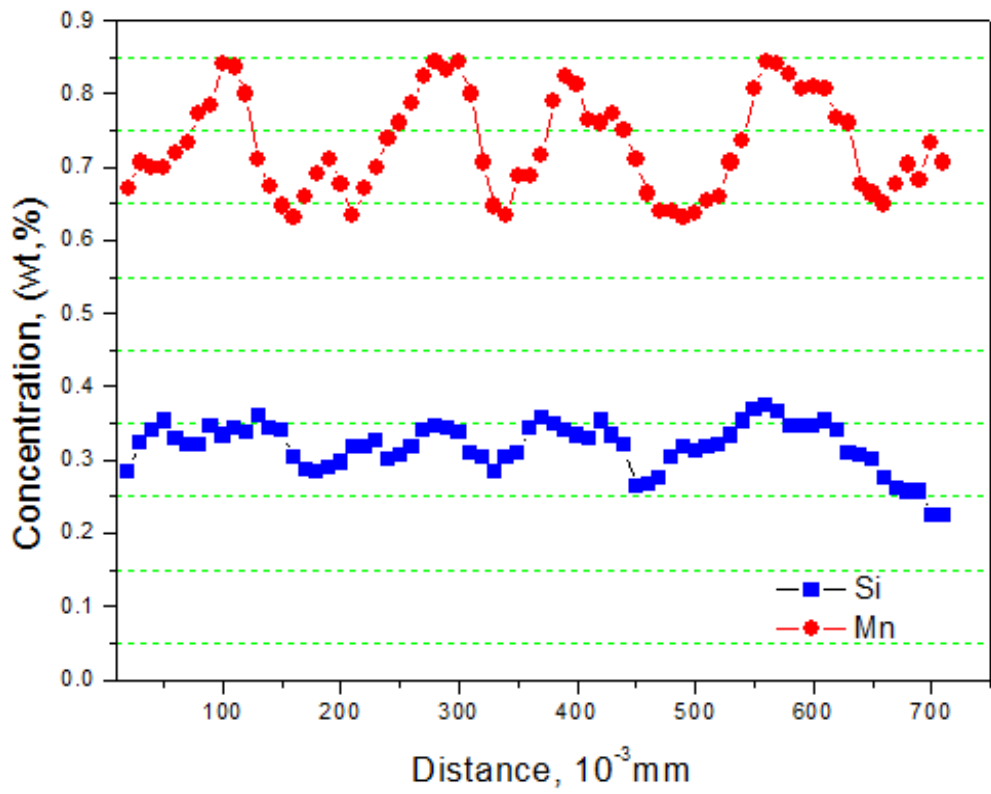
a)

b)

Figure 7-20: Another EDS-SEM line-scan which goes through 3 SDAS at the 69

mm depth. (a) Si and Mn concentration profiles, (b) Dendrite structure

Figure 7-21: Correlation between silicon and manganese at the 69mm depth

(extracted from figure 7-20).

Figure 7-19 shows the Si and Mn micro-segregation profiles through 3 SDAS at 69 mm, from measurements taken every 10 μm. Si and Mn concentration profiles are not smooth, but it still shows the Si and Mn peaks at the interdendritic positions. At this depth, both Si and Mn peaks show higher values than back towards the surface and toward the centre. The experimental work was repeated at this depth at another position in order to get a smoother Si and Mn concentration profile shown as figure 7-20. Si mean concentration was again confirmed higher than the average concentration.

Figure 7-21 exhibits odd behaviour in the Si-Mn correlation as compared to figure 7-20. It shows a "tail" on the correction plot. Figure 7-22 shows the silicon and manganese against distance of the dendrite core to the interdendrite region. The Mn profile was less scattered as compared to the Si profile. The latter included two suspect points of very low Si content, and possibly a "tail" on the correction plot heading towards them; suggesting an unexpected trough in Si at the dendrite core.
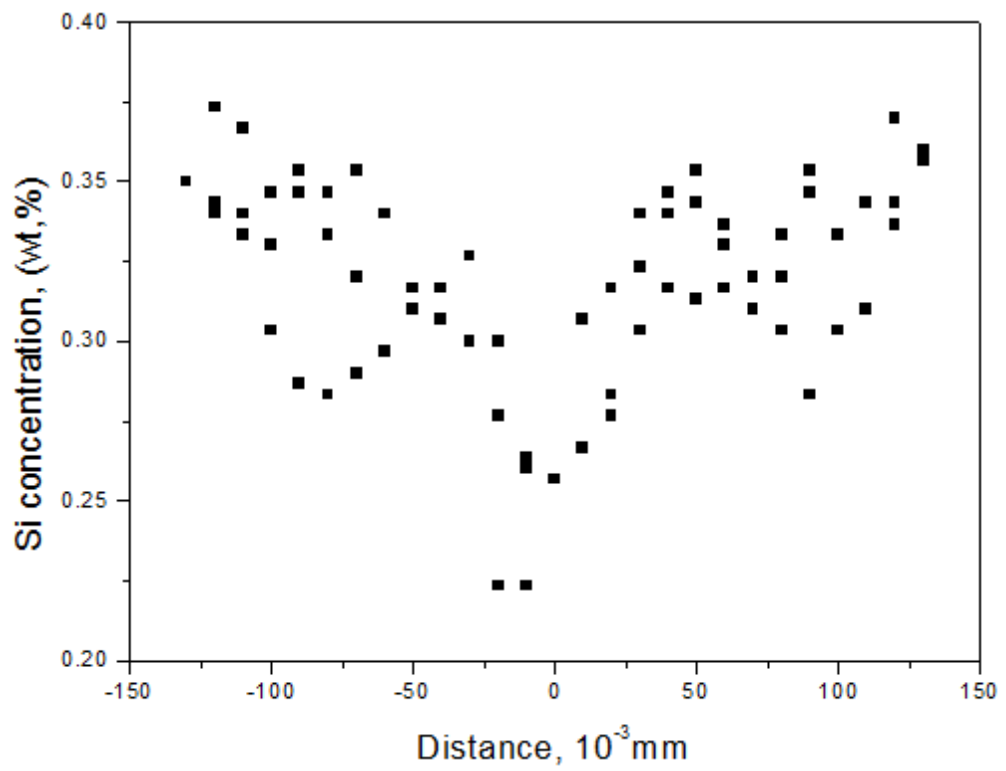
a)
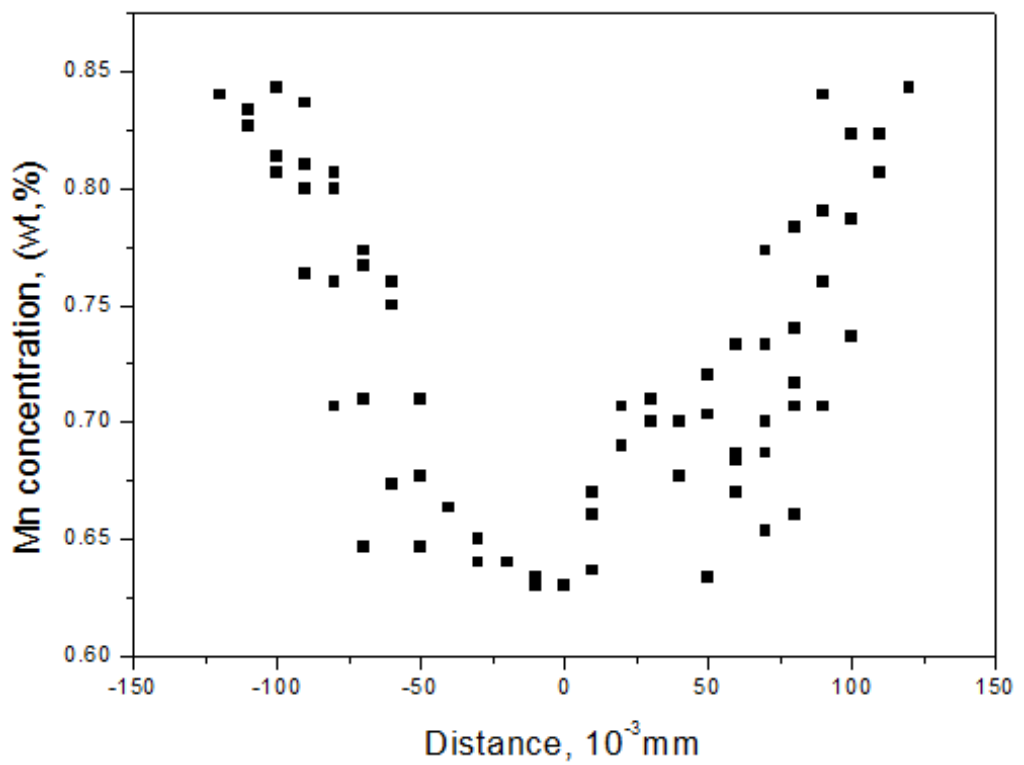
b)

Figure 7-22: Experimental profile compositions at the 69mm depth (extracted from figure 7-20) across a 261 μm secondary dendrite arm for (a) silicon and (b) manganese.
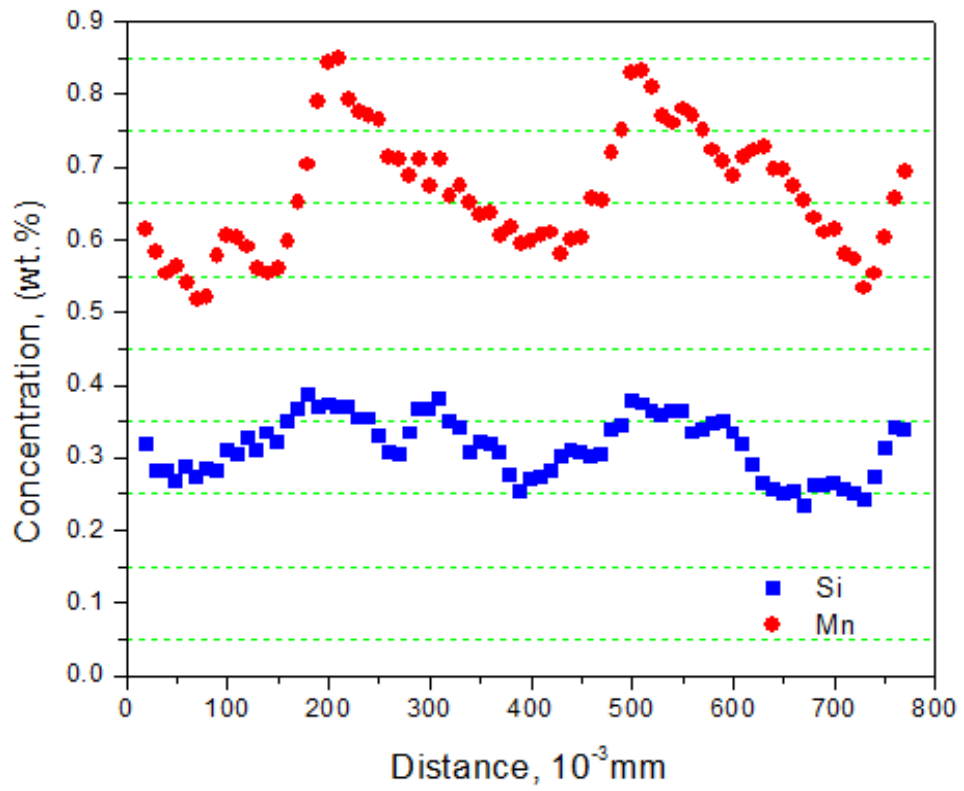
a)


b)

Figure 7-23: Experimental profile compositions at the 69mm depth across a 261

μm secondary dendrite arm for (a) silicon and (b) manganese.
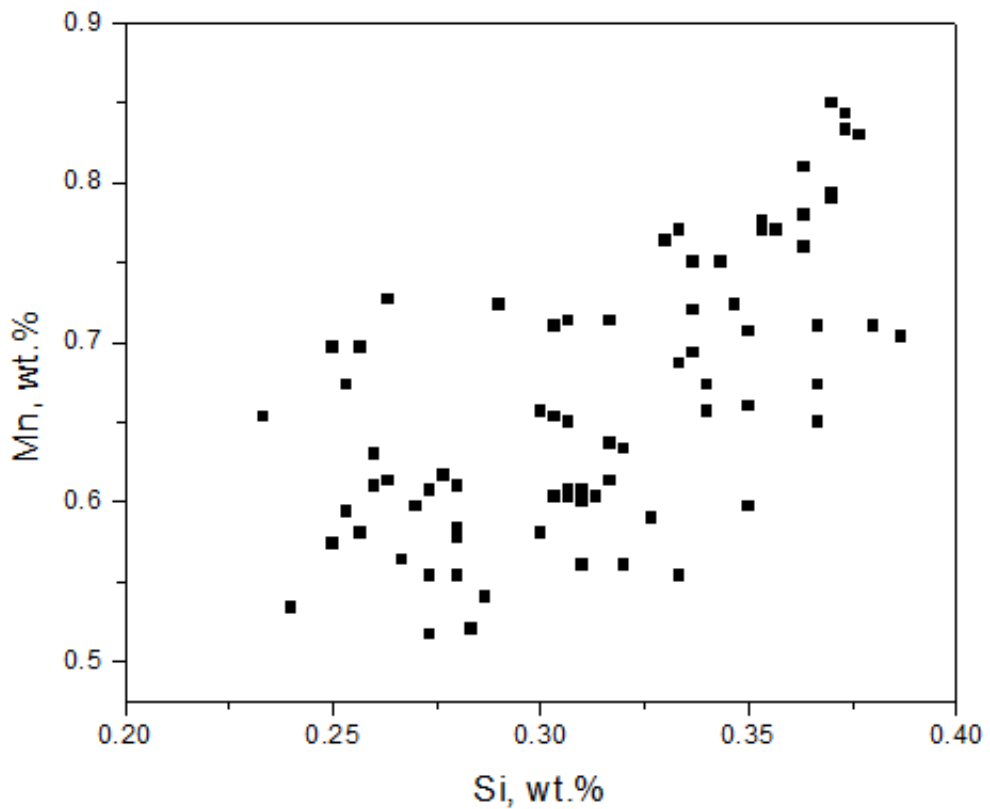
Figure 7-24: Correlation between silicon and manganese at the 69mm depth.

Figure 7-23 shows the Si and Mn micro-segregation profiles through 2 SDAS at 69mm, from measurements taken every 10 μm. The Mn profile is smooth and exhibits a "saw-tooth". Figure 7-23 exhibits the peak drifting between silicon and manganese profiles, where the silicon peak is not ideally aligned with the manganese and it is believed that the solute peaks slightly displace apart after solidification [126]. The Si concentration profile exhibits encompasses two separate peaks, and not aligned with the manganese concentration. This is caused by some scatter shown as figure 7-24 as well as lower silicon and higher manganese.

Figure 7-25 exhibits the silicon and manganese against distance of the dendrite core to the interdendrite region. The silicon and manganese exhibit a very good U shaped profile with the lowest point at the dendrite core and the highest point at the interdendritic position. The silicon profile exhibits the steeper initial slope of the Si profile.

a)

b)

Figure 7-25: Experimental profile compositions at the 69mm depth across a 261

μm secondary dendrite arm for (a) silicon and (b) manganese.

From observation under the microscope, the depths of 57.5mm and 69mm show more inclusion particles than other depth positions. From the experimental results, Si and Mn showed the highest micro-segregation levels at the interdendrite region at the depths of 57.5mm and 69mm.

It is interesting to examine Si and Mn micro-segregation at the depths of 57.5mm and 69mm, the secondary dendrite arm spacing were reported highest at the depth of 57.5mm and decreased toward the centre as shown in figure 5-1. From figure 7-18 and 7-25 we can see that, both Si and Mn micro-segregation degree at the depth 57.5mm show the same as the depth 69mm.
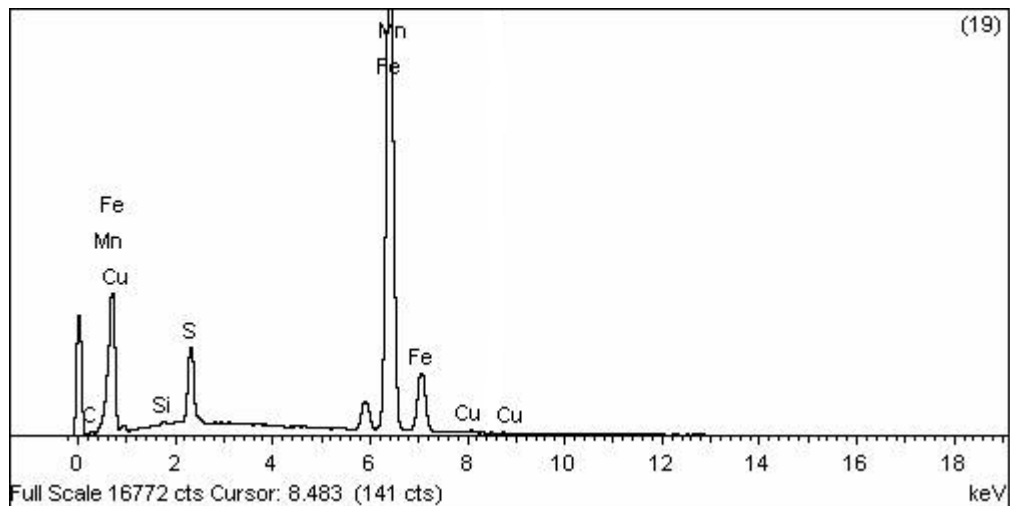
Figure 7-26: Evidence of MnS on a chosen EDS-SEM line-scan at the 69 mm depth (extracted from figure 7-19).
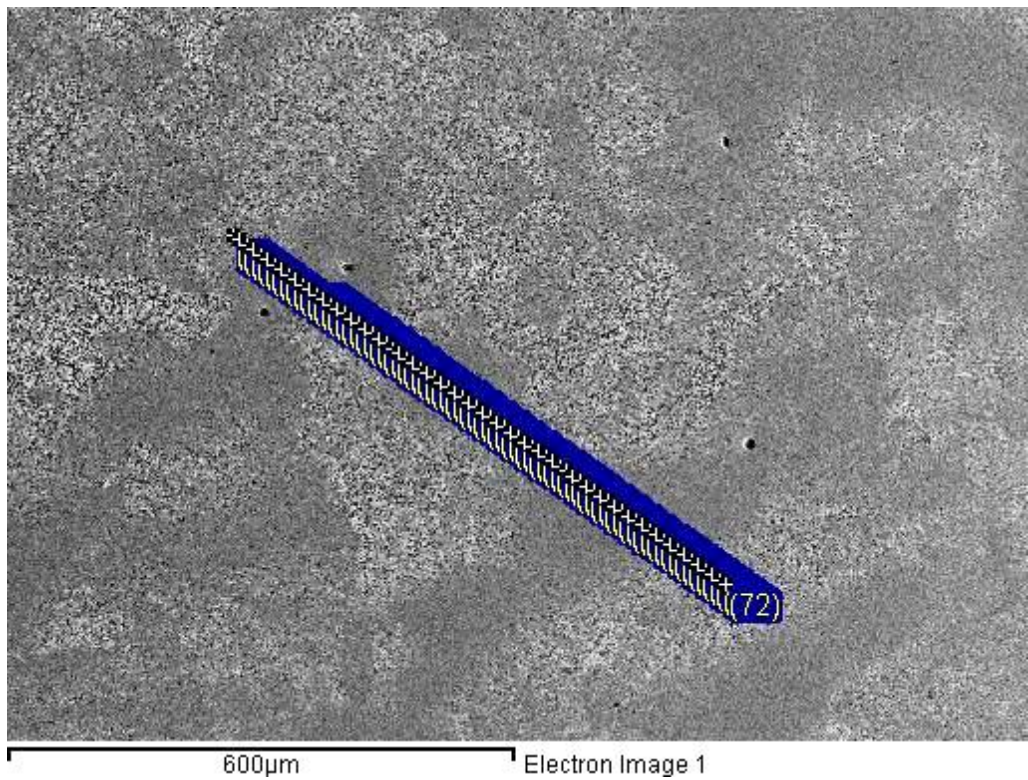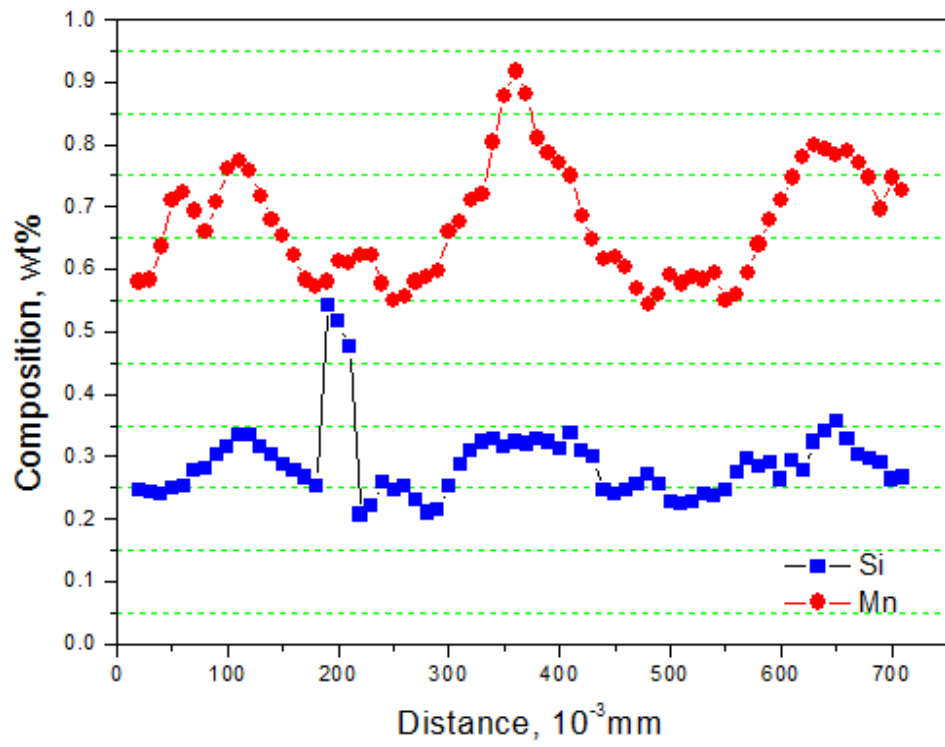
a)
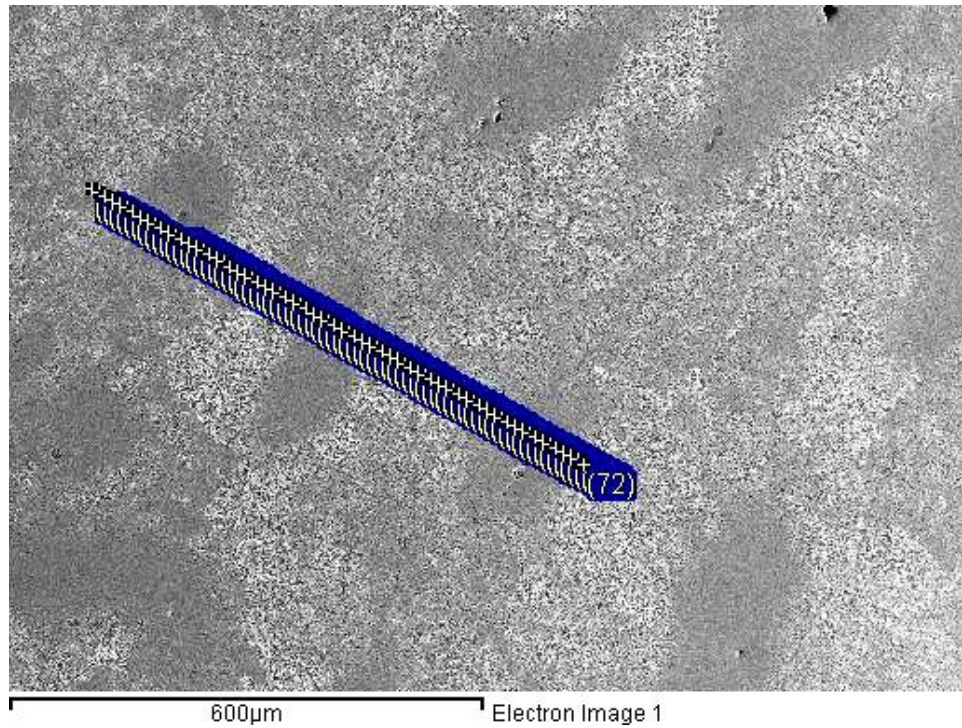
b)

Figure 7-27: EDS-SEM line-scan which goes through 3 SDAS at the 80.5 mm

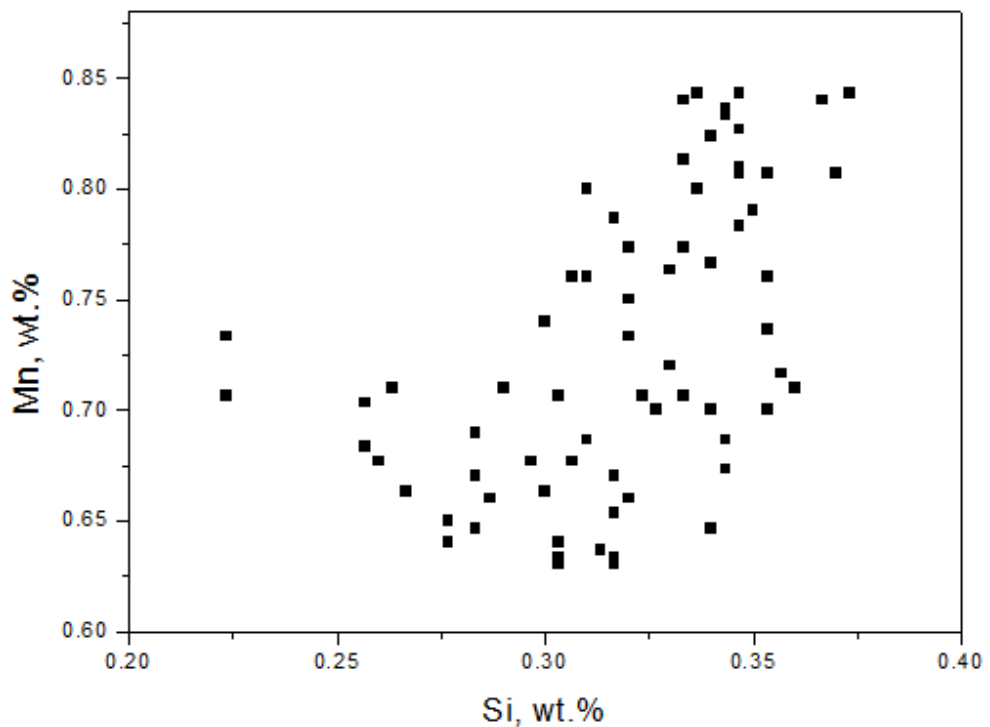depth. (a) Si and Mn concentration profiles, (b) Dendrite structure

Figure 7-27 shows the Si and Mn micro-segregation profiles through 3 SDAS at 80.5mm, from measurements taken every 10 μm. Si and Mn concentration profiles are smooth and proportional. Both Si and Mn concentration profiles were slightly depressed in comparison to the 69mm depth. The Mn peak at the centre dendrite is higher compared to either side. From figure 7-27b, we can see that, the dendrite distance at the centre is longer than the other. The correlation between segregation and dendrite arm distance was mentioned; the longer dendrite distance results in high levels of segregation at the same thermal rate conditions.
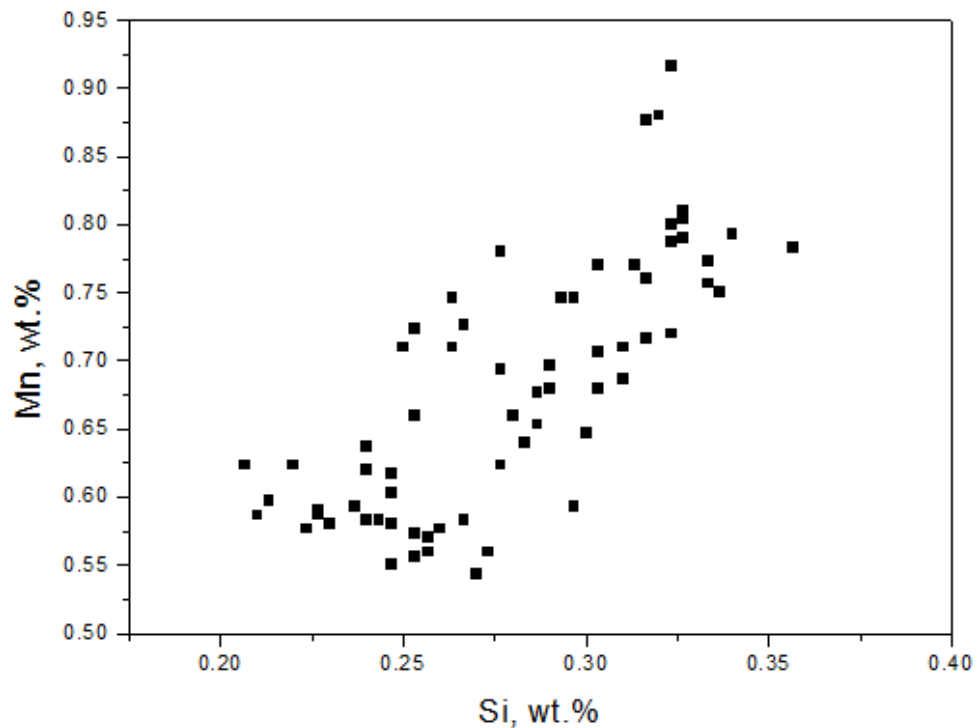
Figure 7-28: Correlation between silicon and manganese at the 80.5mm depth.

Figure 7-28 shows very good positive correlation between Si and Mn. Both Si and Mn profiles was less scattered than those back towards the surface as shown as figure 7-29.
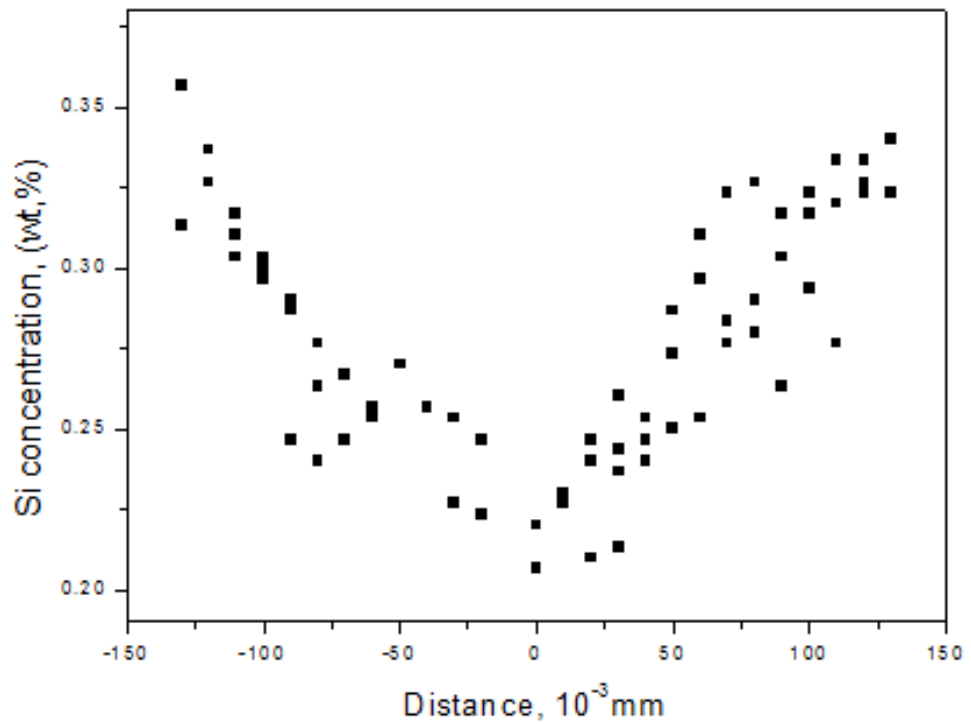
a)
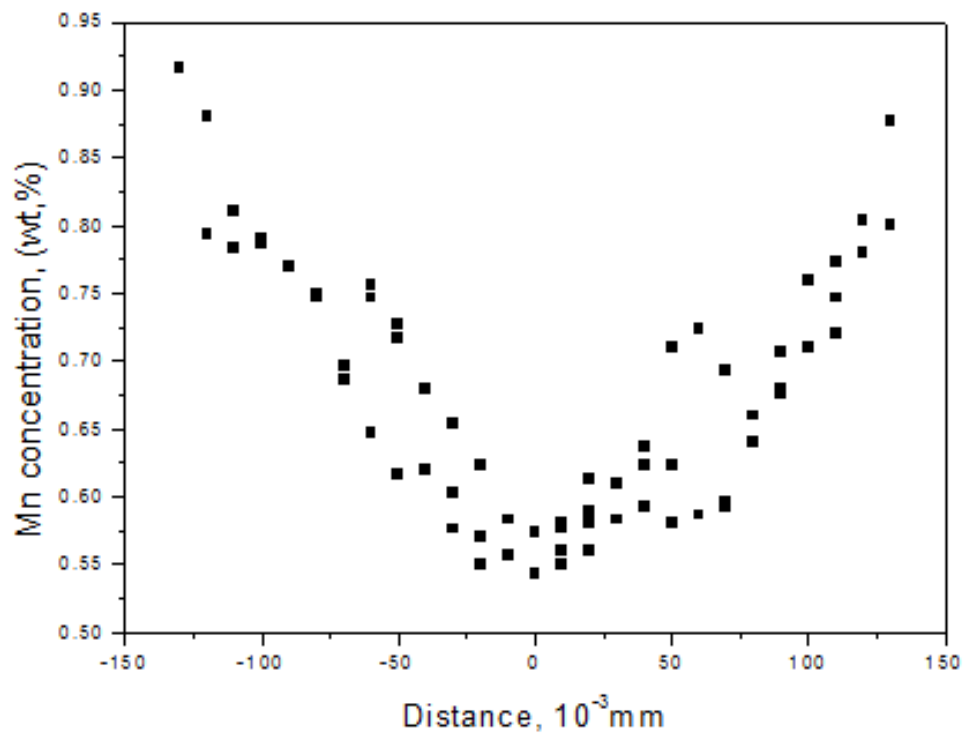
b)

Figure 7-29: Experimental profile compositions at the 80.5mm depth across a
256 μm secondary dendrite arm for (a) silicon and (b) manganese.
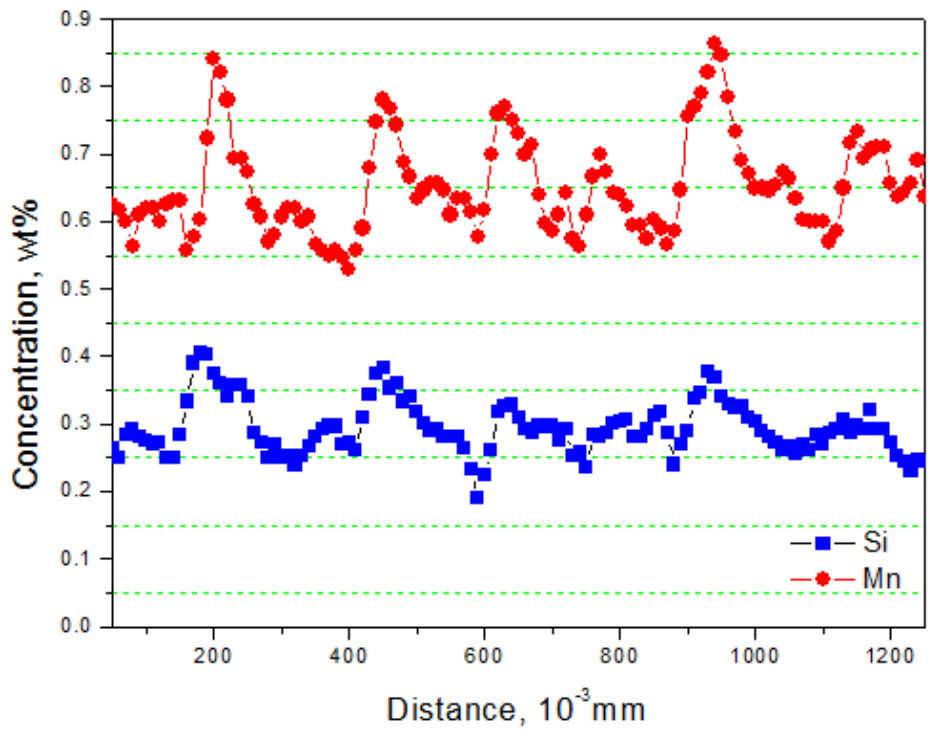
a)
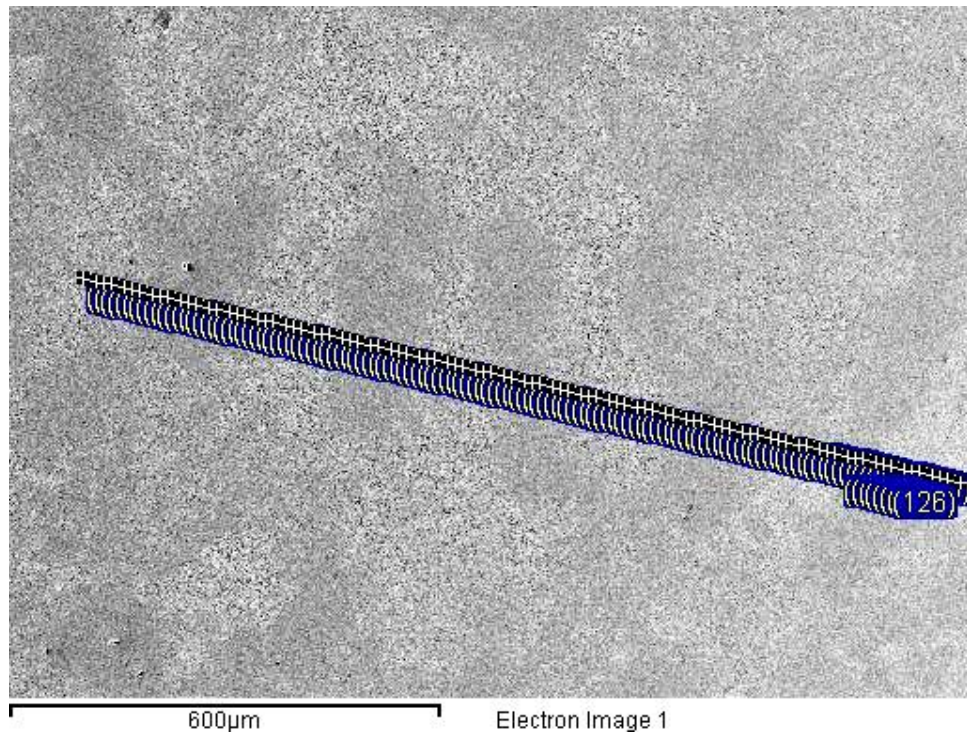
b)

Figure 7-30: EDS-SEM line-scan which goes through 5 SDAS at the 92 mm

depth. (a) Si and Mn concentration profiles, (b) Dendrite structure

The standard expectation is for silicon and manganese solutes to exhibit peaks of concentration at the same position at the final solidification. However, in some cases, silicon and manganese solute peaks are not coincident, and appear to slightly drift apart as sub-solidus homogenization occurred [126]. Figure 7-30 exhibits the peak drifting between silicon and manganese profiles, where the silicon peak is not ideally aligned with the manganese and it is believed that the solute peaks slightly drifted apart after solidification [126]. The slightly silicon drifting apart is caused by some suspected point of very low manganese content and high silicon content shown in figure 7-31.

In alloyed steels, solutes have a widely differing diffusivity, a rapid diffuser could exhibit a single, merged peak, and a sluggish diffuser could exhibits encompasses two separate peaks. Silicon and manganese diffuse much less than carbon, however, silicon diffuses less than manganese [126]. It also caused two unexpected troughs in silicon, shown in figure 7-32a. The manganese profile shows good agreement with the lowest value at the dendrite core and the highest value at the interdendritic positions as shown in figure 7-32b.
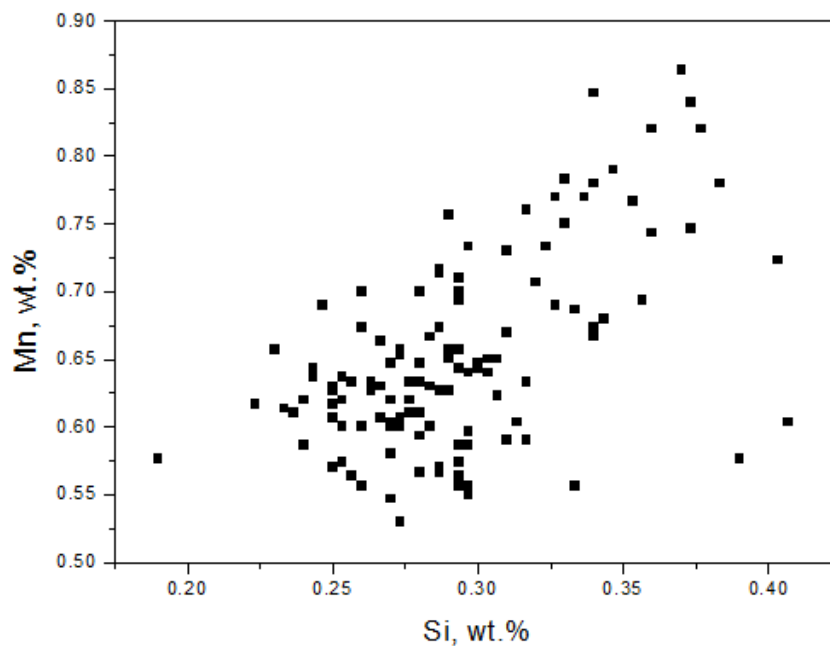
Figure 7-31: Correlation between silicon and manganese at the 92mm depth

(extracted from figure 7-30)

144
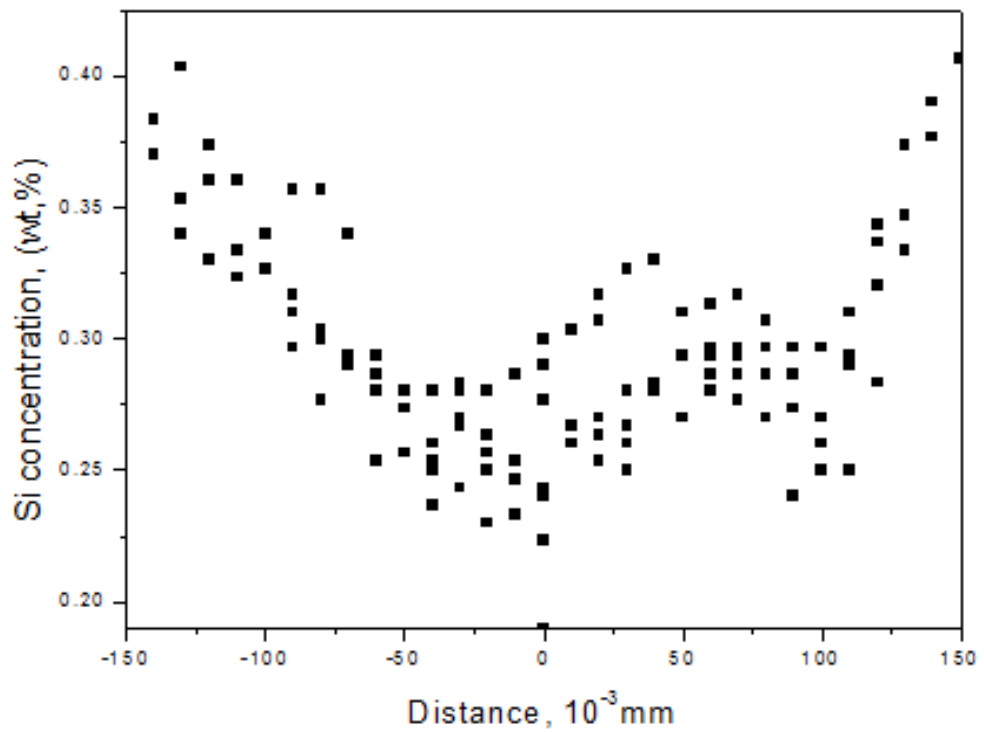
a)
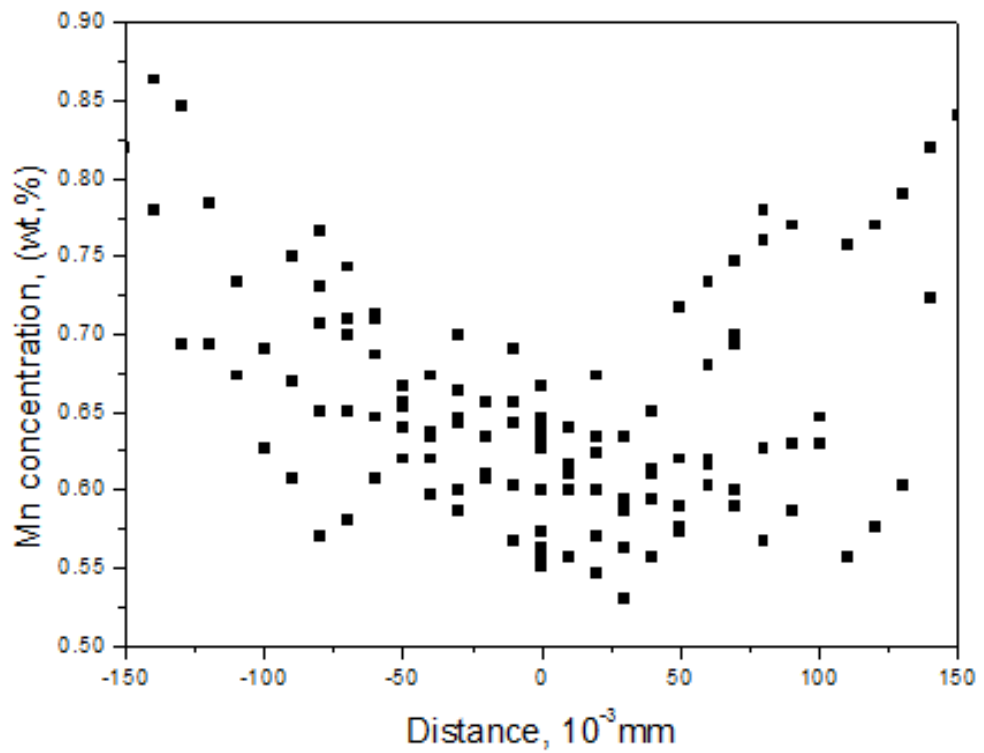
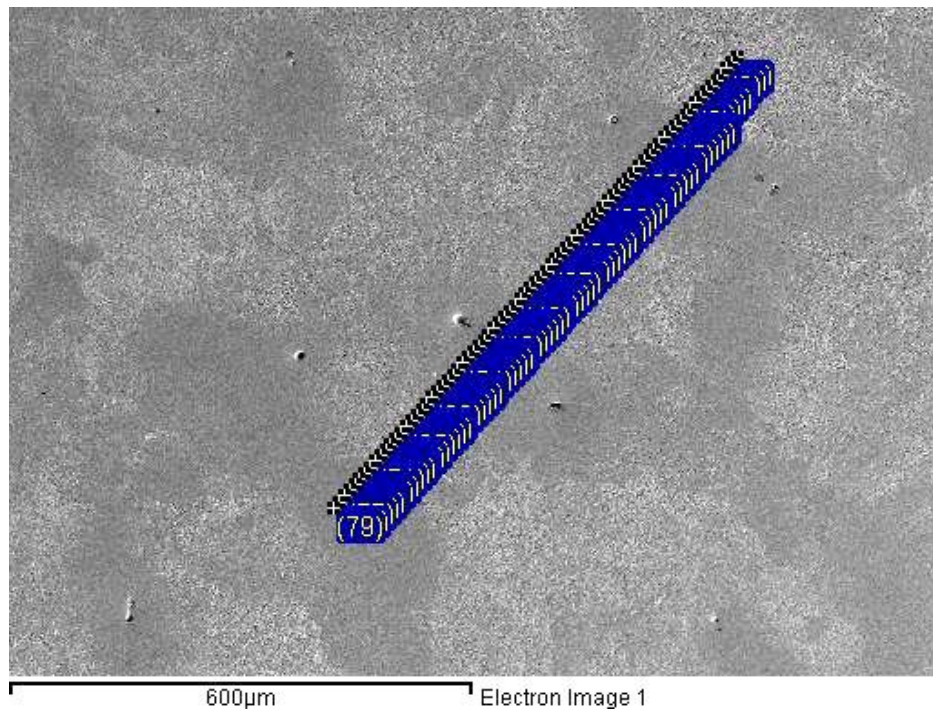
b)

Figure 7-32: Experimental profile compositions at the 92mm depth across a 237

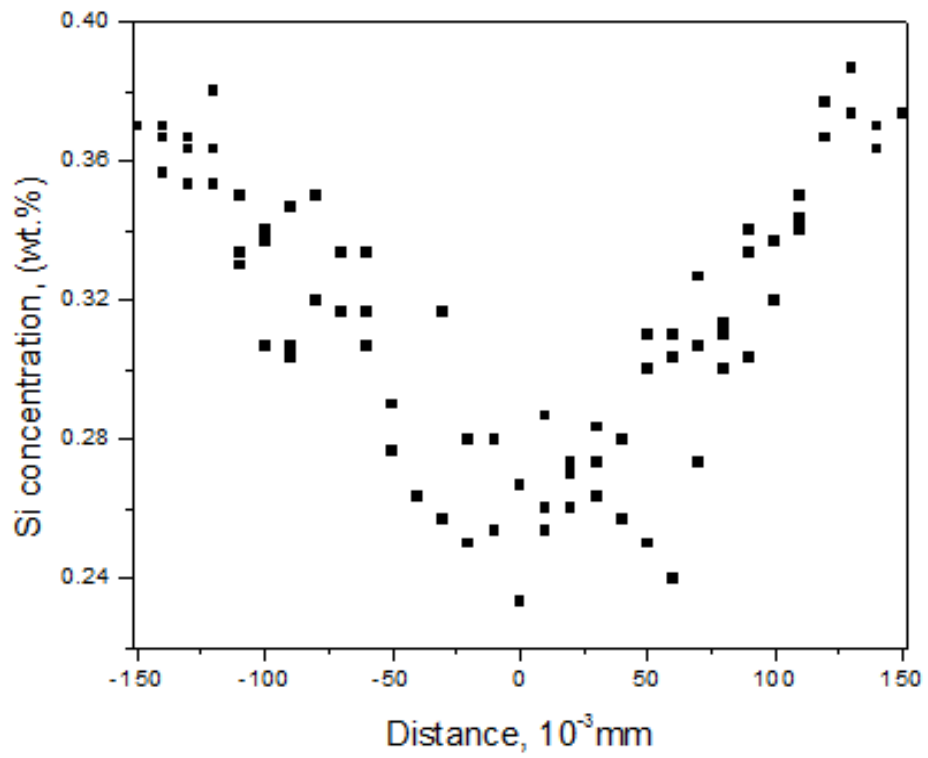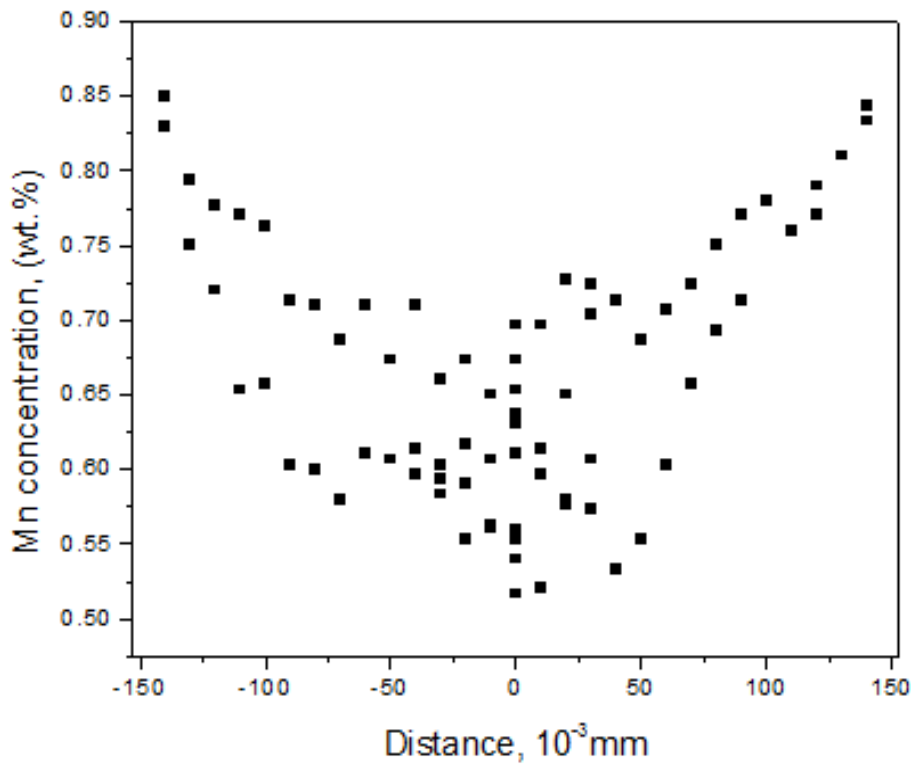µm secondary dendrite arm for (a) silicon and (b) manganese.
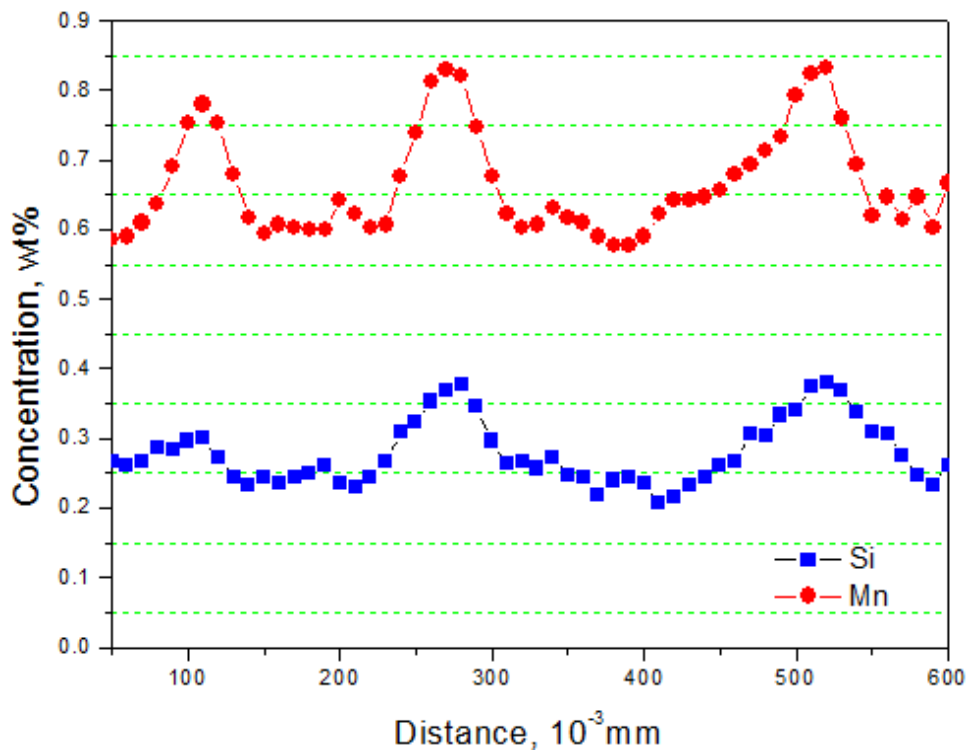
a)
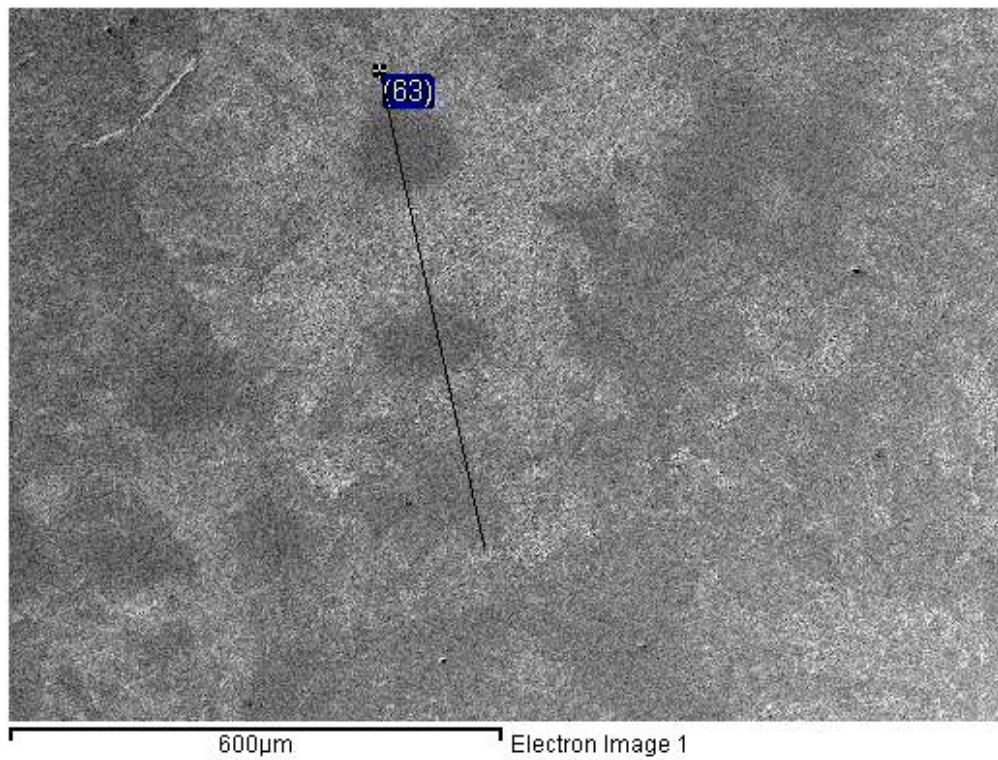
b)

Figure 7-33: EDS-SEM line-scan goes through 3 SDAS at the 103.5 mm depth.

(a) Si and Mn concentration profiles, (b) Dendrite structure

Figure 7-33 shows the Si and Mn micro-segregation profiles through 3 SDAS at 103mm, from measurements taken every 10 μm. Both Si and Mn profiles are proportional; smooth and increase from the dendrite cores to the interdendritic positions. Both Mn and Si concentration profiles oscillate around the average concentration.
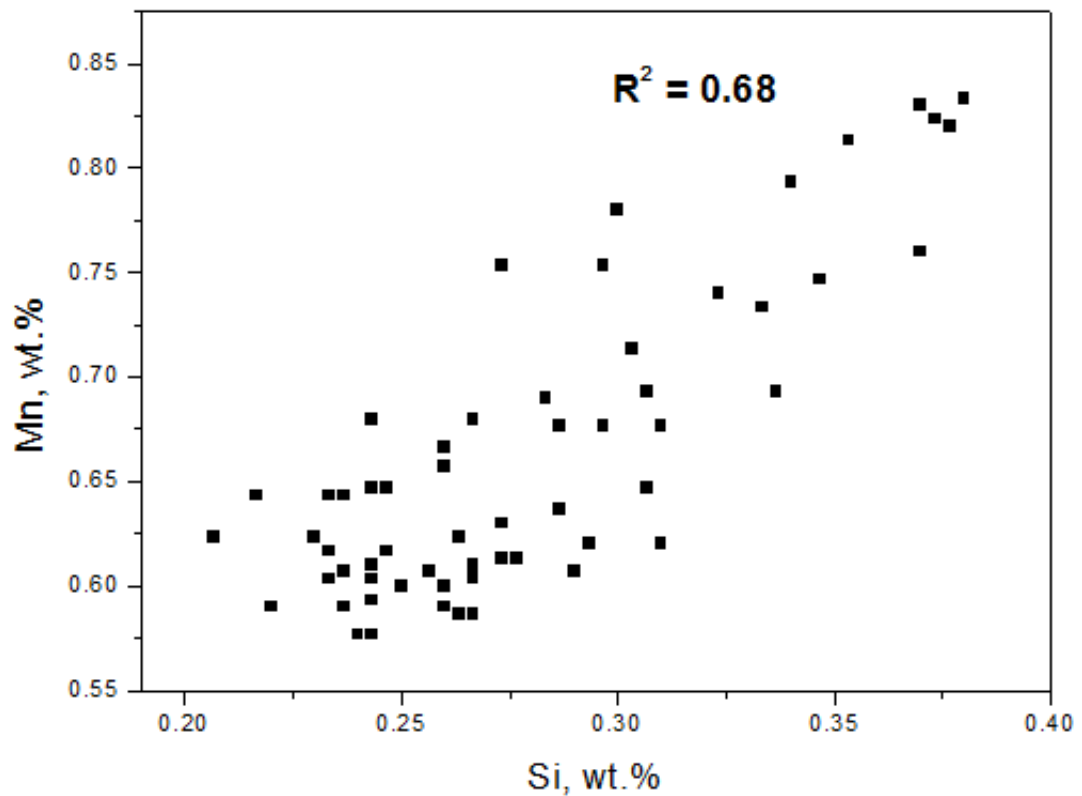
Figure 7-34: Correlation between silicon and manganese at the 103.5mm depth.

Figure 7-34 shows the correlation between silicon and manganese at the 103 mm position. A positive correlation was found between silicon and manganese which followed the ideal line with high R-squared of 0.68. The correlation between silicon and manganese is better than at the other positions. Both silicon and manganese profiles were less scattered, the manganese profile exhibits a better shape compared with the silicon profile as shown in figure 7-35.
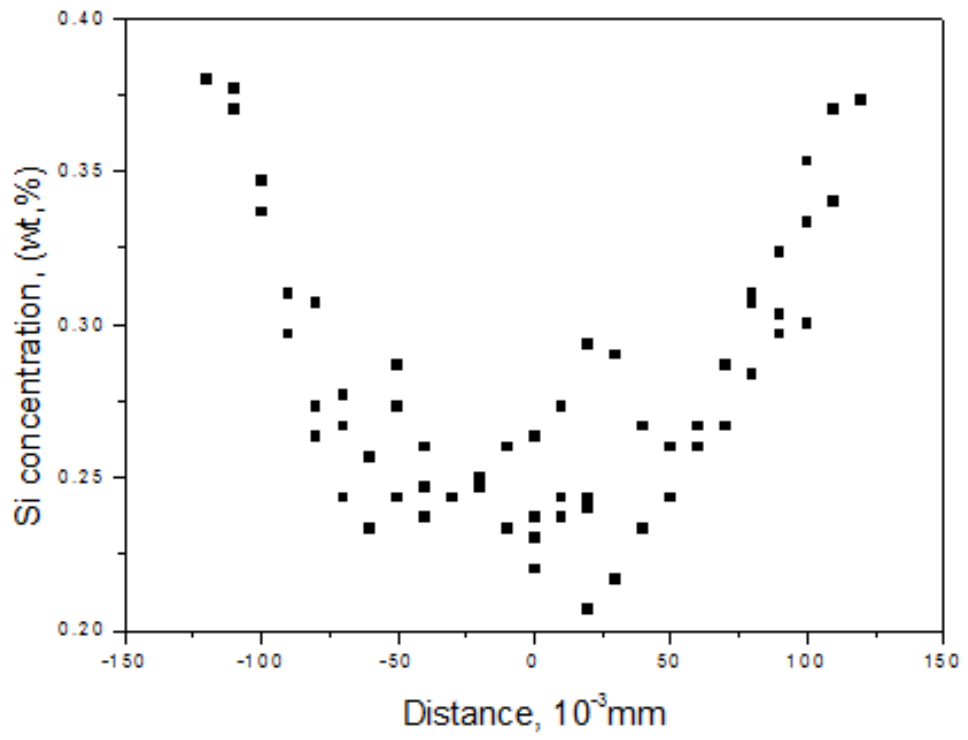
a)
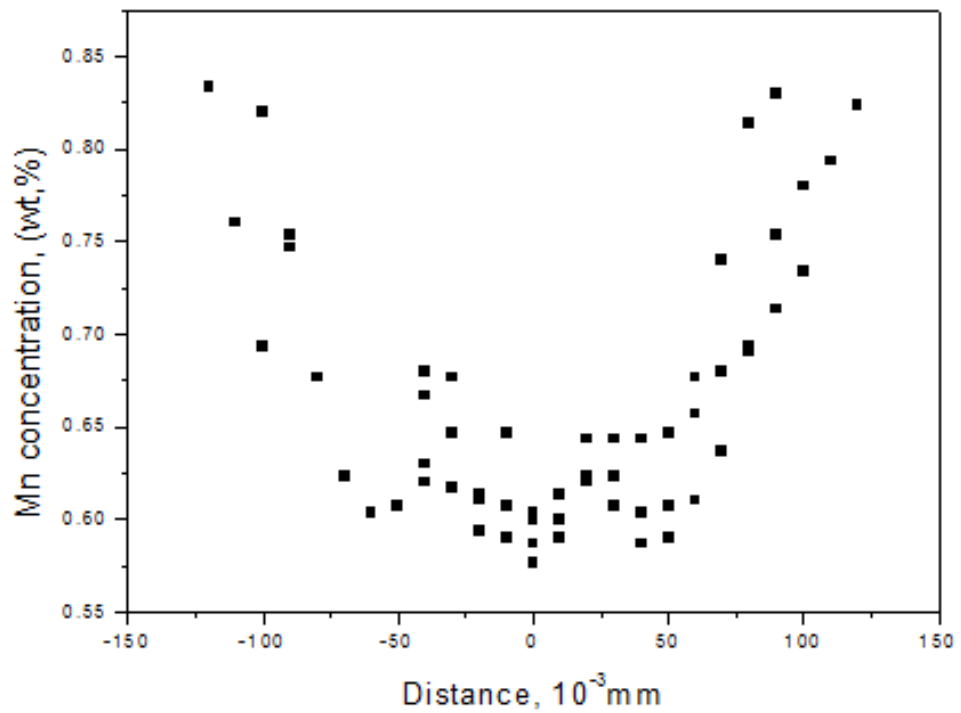
b)

Figure 7-35: Experimental profile compositions at the 103.5mm depth across a

241 μm secondary dendrite arm for (a) silicon and (b) manganese.
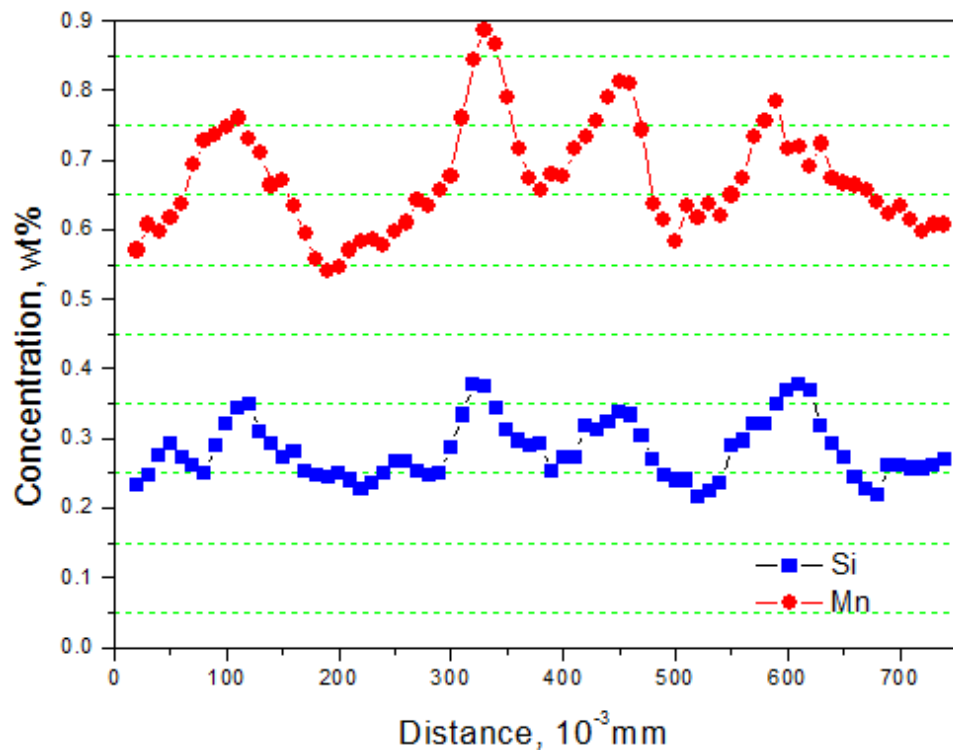
a)
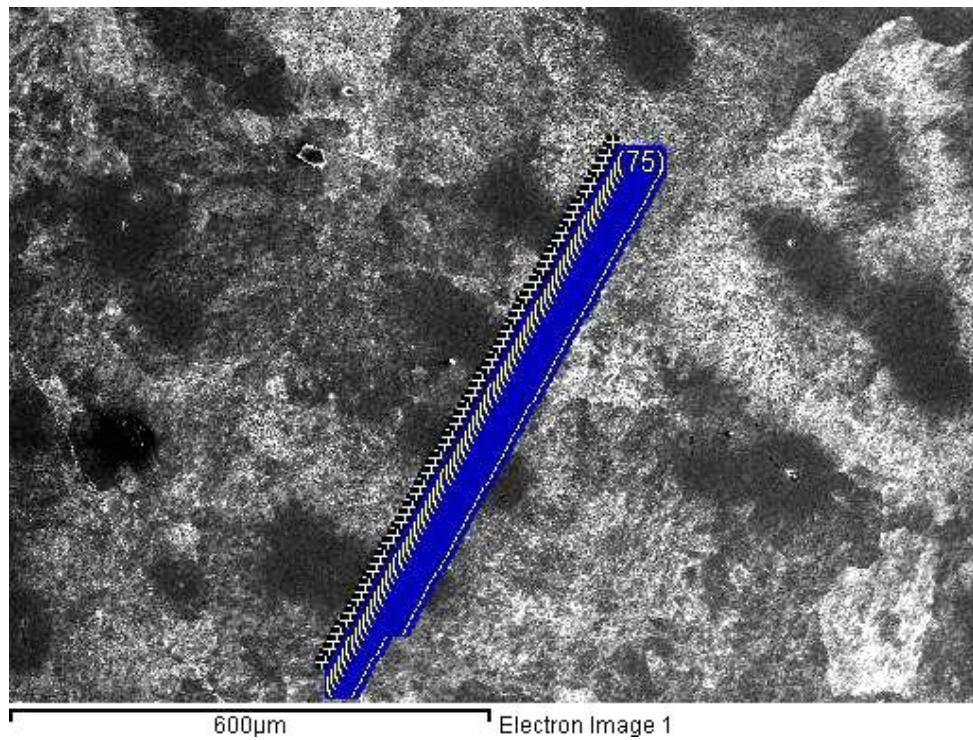
b)

Figure 7-36: EDS-SEM line-scan which goes through 4 SDAS at the 115 mm

depth. (a) Si and Mn concentration profiles, (b) Dendrite structure

Figure 7-36 shows the Si and Mn micro-segregation profiles through 4 SDAS at 115mm, from measurements taken every 10 μm. Both Si and Mn profiles are proportional, and increase from the dendrite cores to the interdendritic positions. Silicon concentration profile was better than that of manganese. It is also better than the other depths. Both Mn and Si concentration profiles go around the average concentration.
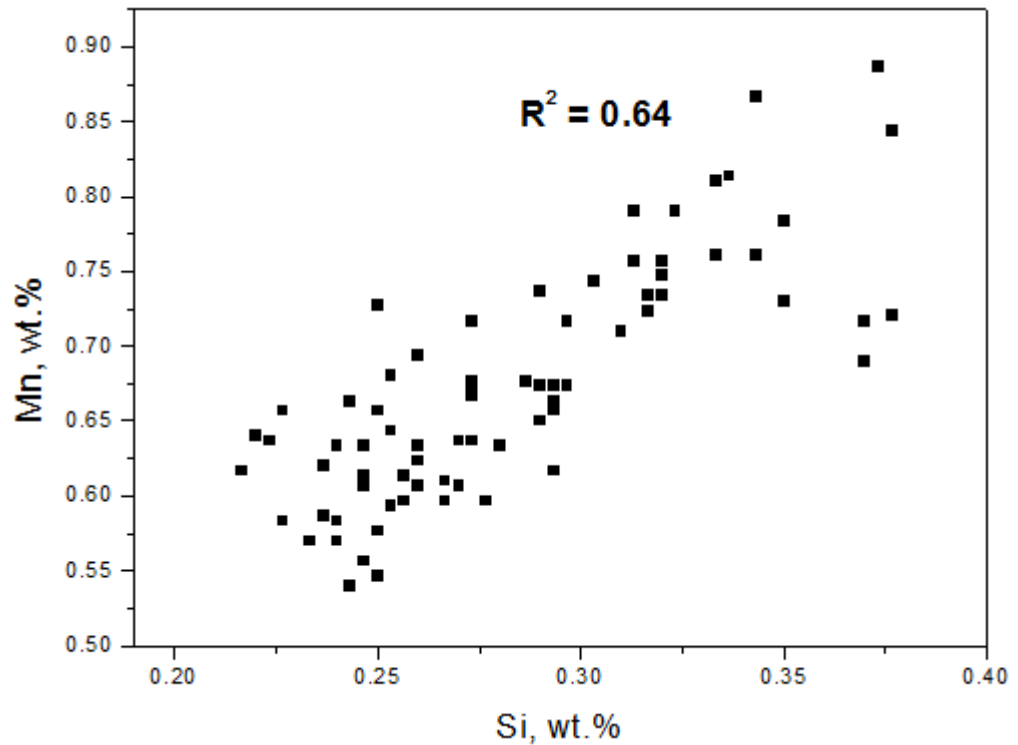
Figure 7-37: Correlation between silicon and manganese at the 115mm depth.

Figure 7-37 shows the correlation between silicon and manganese at the 115 mm position. A positive correlation was found between silicon and manganese and they were both close to the ideal line with a high R-squared value of 0.64. The correlation between silicon and manganese was better than at other depths, slightly decreasing as compared to the 103mm position. There are three points of high Si content with medium Mn content, this is caused by silicon slightly drifting apart, and is not ideally aligned with the manganese (last silicon peak in figure 7-36a).
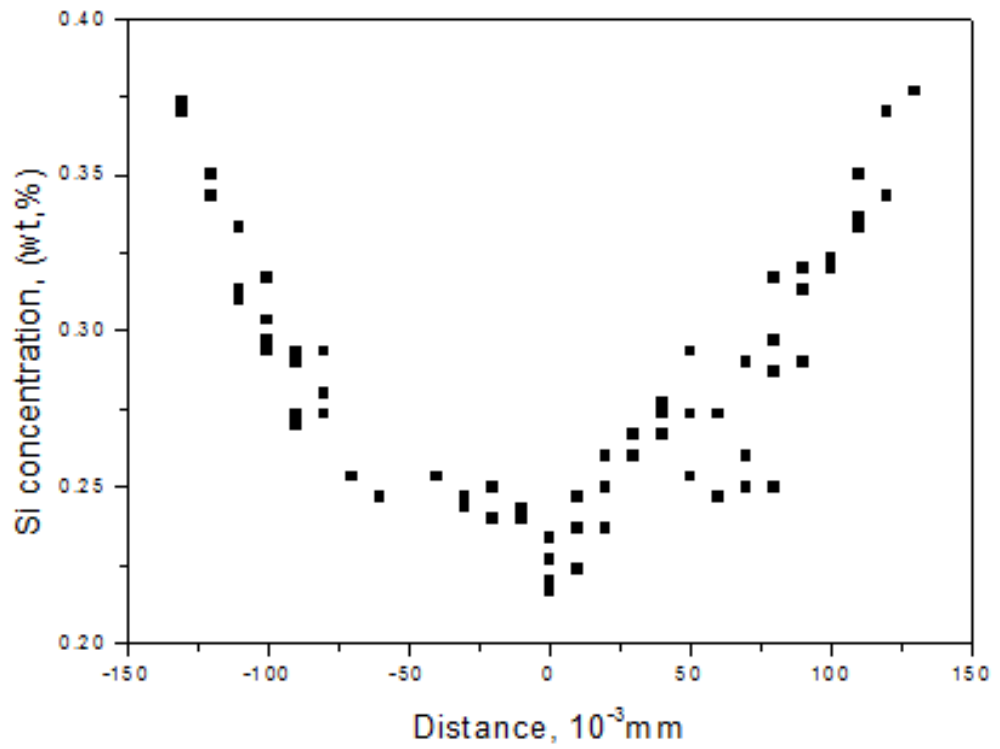
a)
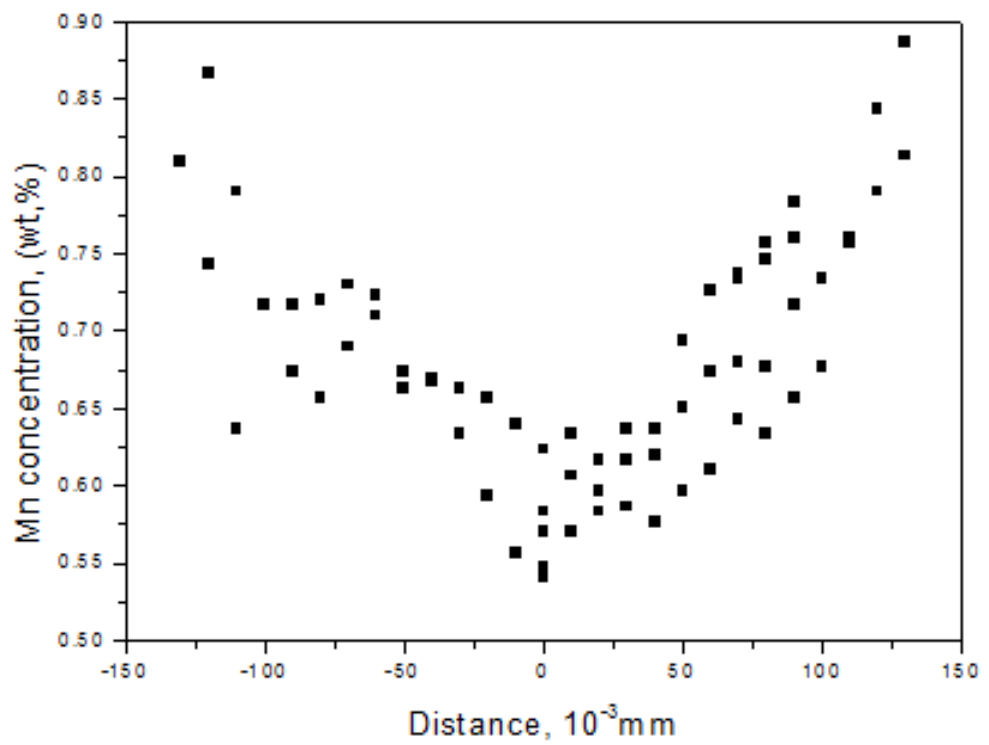
b)

Figure 7-38: Experimental profile compositions at the 115mm depth across a 230 μm secondary dendrite arm for (a) silicon and (b) manganese.

Figure 7-39 shows the silicon and manganese wt.% against proportion of the dendrite cores to the interdendrite regions. Both Si and Mn concentration profiles follow the ideal line and oscillate around the average composition.

Figure 7-29 to 7-38 show that from the depth of 57.5mm toward the centre, the Si and Mn concentration profiles are smooth and approximately proportional; the Si concentration profiles look smoother than back towards to the surface, both Si and Mn peaks are clearer. This finding has important implications for developing the micro-segregation model for industrial scale which could predict the micro-segregation degree for big sections such as slab and bloom steels. The experiments were successful as it was able to identify the Si and Mn micro-segregation degree from the surface, mid-way and toward the centre. The present results are significant in that at least it could identify the effect of cooling rate or heat extraction rate, solidification microstructure and solute diffusion on micro-segregation both during and after solidification.

However, some EDS scatter was found at around the dendrite cores, a possible explanation for this was given by other researchers as discussed above, but it is still difficult to explain in these ways, further studies on the EDS scatter is therefore recommended.

7.2 Summary of Si and Mn concentrations at the dendrite core and interdendritic positions

Table 7-1: Si and Mn concentrations at the dendrite core and interdendritic

positions from EDS-SEM measurements

Depth, mm	Min Si, wt.%	Max Si, wt.%	Min Mn, wt.%	Max Mn, wt.%
11.5	0.23	0.32	0.57	0.77
23	0.24	0.35	0.58	0.78
34.5	0.24	0.37	0.57	0.81
46	0.29	0.37	0.59	0.85
57.5	0.27	0.37	0.58	0.84
69	0.26	0.37	0.63	0.84
80.5	0.22	0.35	0.55	0.83
92	0.23	0.38	0.55	0.84
103.5	0.22	0.37	0.58	0.82
115	0.23	0.37	0.57	0.85

Micro-segregation of Si and Mn were measured by EDS-SEM line scan going through 2-4 SDAS from the surface to centre. Table 7-1 shows summarized Si and Mn concentrations at the dendritic cores and Si and Mn peaks at the interdendrite positions. The minimum concentration of Si averages 0.24 wt%. At quarter-thickness, the minimum concentration of Si is generally higher than the average concentration of 0.24 wt%. Further toward the centre, the minimum concentration of Si gets lower compared to the average concentration. The minimum concentration of Mn is lower compared to the average concentration of 0.63 wt% with the exception of the depth of 69mm.

The experimental results of manganese peak profile increases from the surface to the depth of 46 mm, but scatter around that level to the centre as shown in figure 7-39. The manganese peak profile did not conform to the local solidification time which was extracted from the TTC model. This profile conformed to the measured results of

SDAS (figure 5 -1). The experimental results of the silicon peak profile increased from the surface to the depth of 35.5 mm, and reached a constant value of 0.37 wt.% further toward the centre. Silicon peaks alternates between two depths of 80.5 and 92 mm around the constant value of 0.37 wt.% as shown in figure 7-40.
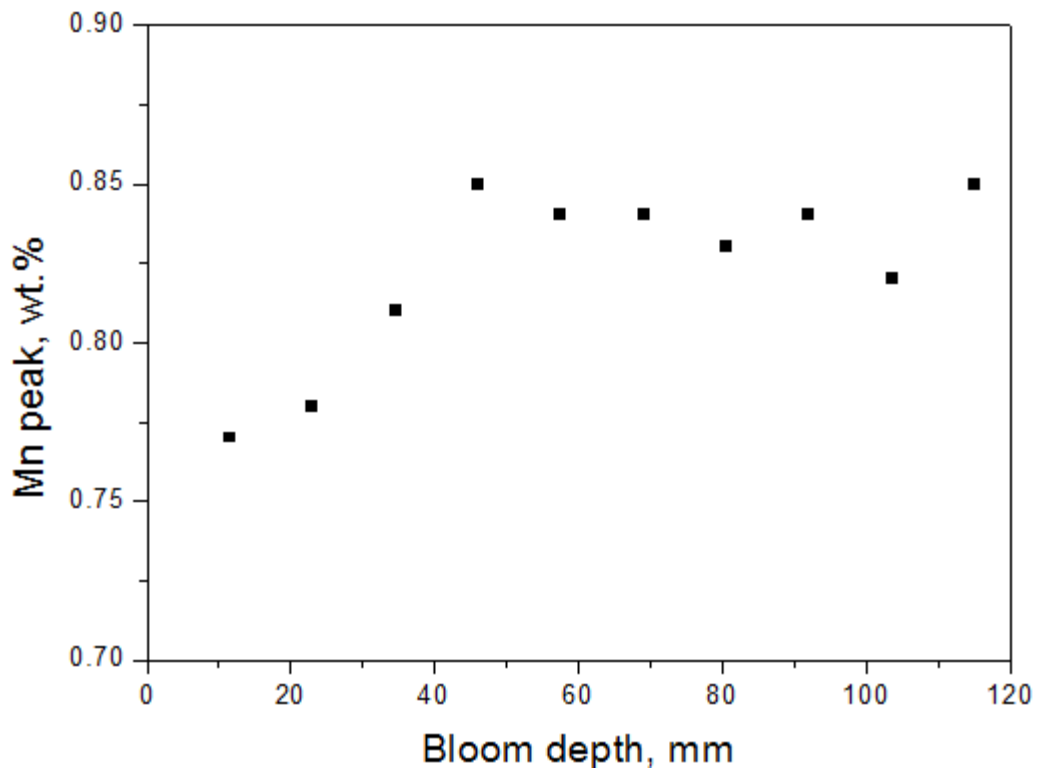
Figure 7-39: Mn peak profile at different depths of high carbon bloom steel
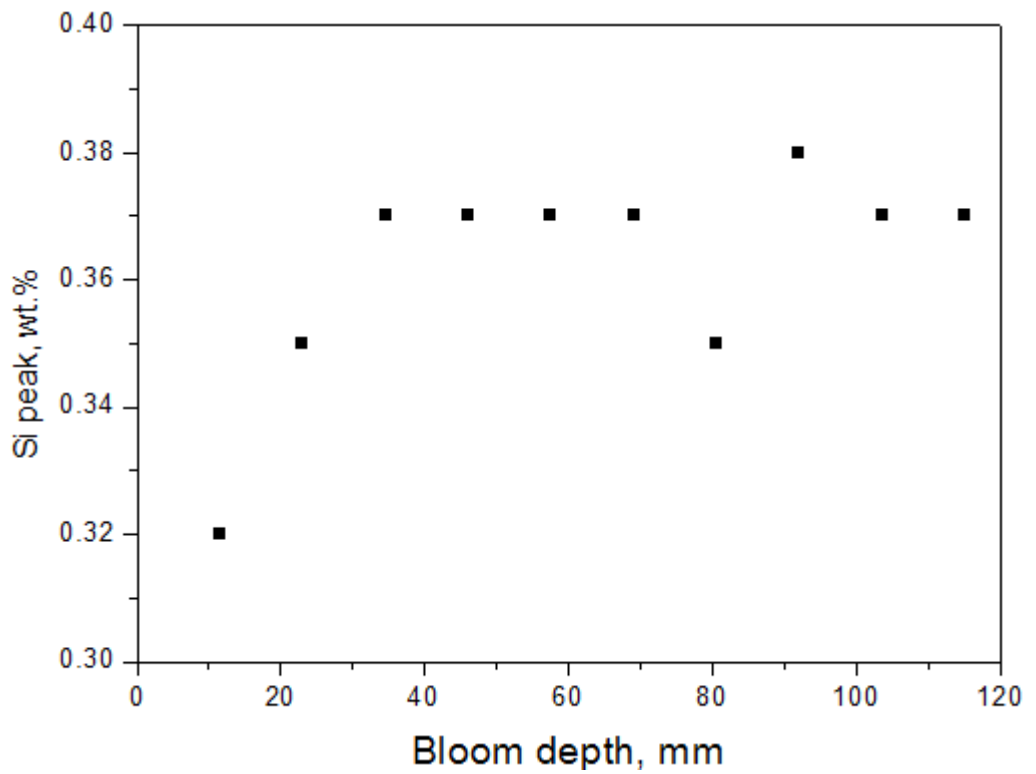
Figure 7-40: Si peak profile at different depths of high carbon bloom steel

Chapter 8: Micro-segregation Model

8.1 Micro-segregation models

There are some selected analytical non-equilibrium micro-segregation models as listed in table 8.1. These micro-segregation models with different assumptions and simplifications have been developed to predict solute redistribution. The Scheil model [99] assumes the state with complete diffusion in liquid phase and no diffusion in solid phase; this model does not adequately estimate the final solute concentration, because liquid solute becomes infinite at solid fraction equal to 1. The Brody-Flemings model [100] was the first to assume complete diffusion in liquid phase and incomplete "back diffusion" in the solid. These authors have introduced β as a back diffusion parameter, which has been modified by many researchers in different ways.

Micro-segregation equation description

Many micro-segregation models with different assumptions have been developed to predict solute element distribution during solidification. The present simple micro-segregation equation developed in this study is based on the Ohnaka model [102] for each solute element. The Ohnaka model considered an approximate solution of the diffusion for the plate like columnar dendrite, assuming a quadratic solute profile in the solid phase, from which he derived:

$$C_S = KC_0[1\text{-}(1\text{-}\beta K)f_S]^{(k\text{-}1)/(1\text{-}\beta k)} \qquad (8\text{-}1)$$

$$\beta_i = \frac{2\alpha_i}{1+2\alpha_i} \qquad (8\text{-}2)$$

where β_i is the back diffusion parameter developed similar to that by Brody-Flemings $2\alpha_i$ term, and α_i is a Fourier number for solute element i,

As mentioned in the literature survey, the original Brody-Flemings β_i was $2\alpha_i$, but this gave very poor prediction with high diffusivity.

$$\alpha_i = \frac{D_{s,i} t_f}{\lambda^2} \tag{8-3}$$

Effect of dendrite arm coarsening

During solidification, micro scale mechanisms in addition to the back diffusion parameter control the distribution of solute in both the liquid and solid phases, in particular the dendrite coarsening. Mortensen [72] showed that arm coarsening reduced the extent of micro-segregation, even avoiding the infinite result at $f_s = 1$ for zero solid diffusion (Scheil model). One limitation of Ohnaka's model is that the length scale of the microstructure is constant; in general, this assumption is not correct [76]. In order to satisfy this requirement, a new micro-segregation equation in proposed here that would account for the coarsening of the dendrite structure, measured by the secondary dendrite arm spacings, such that the equation 8-2 is rewritten, as follows:

$$\beta_i = \frac{2\alpha_i^+}{1 + 2\alpha_i^+} \tag{8-4}$$

The previous chapter (4), introduced the new secondary dendrite arm spacing model for multicomponent steels. The secondary dendrite arm spacing is a function of local solidification time which has a coarsening exponent of n =1/3 (a time $t_f^{1/3}$ dependence) [60], as follows:

$$\lambda_2 = B.M.t_f^{1/3} \tag{8-5}$$

In this study, we still considered the system to be of constant dendrite arm spacing of the final value (at solidus). In other models without the effect of coarsening, that leads to very high degree of segregation at the solidus. From theoretical arguments, Voller and Beckermann [76] argued that introducing an additional back diffusion term $\alpha^c = 0.1$ ($\alpha^+ = \alpha + \alpha^c$) approximates to the homogenising effect of coarsening which would lead to a reduced degree of segregation at the solidus. An alternative was adopted

of modifying the Fourier number to the back diffusion factor (see equation 8-4) in account with coarsening exponent of 1/3 (see equation 8-5), as follows:

$$\alpha_i^+ = \alpha^{1/3} \qquad\qquad (8\text{-}6)$$

Equation 8-6 is very important because the effect of dendrite coarsening can be included in our micro-segregation model which, just by replacing the Fourier number in the back diffusion parameter, accounts for the reduced the degree of micro-segregation expected from coarsening.

Solute profile across the solid

The models in Table 8-1 do not provide an estimate of the solute profile, but only the concentration at the solid/liquid interface, the new equation in this study also seeks a quick approach to calculation of solute profile across the solid. The solute profile must lie between the limit of the Scheil case and equilibrium (lever rule) case, and also satisfy the requirement to conserve solute [105].

In his quick micro-segregation model, Howe [106] proposed an equation to estimate the solute concentration at the dendrite core, in addition to the usual prediction of composition at the solid/liquid interface, as follows:

$$C_{core,i} = C_{0,i} * k_i^{(1-\beta_i)} \qquad\qquad (8\text{-}7)$$

where k_i is partition confident of element i and β_i is the back diffusion parameter ranging from 0 (Scheil) to 1 (lever Rule).

The solute profile that conserves solute was devised by Howe [106], for a power law:

$$C_{s,i} = C_{core,i} + \left(C_{peak,i} - C_{core,i}\right).f_s^n \qquad\qquad (8\text{-}8)$$

where $C_{peak,i}$ is maximum concentration of i at solidus, provided by the micro-segregation model.

and the exponent, n is given, as follow:

$$n = \frac{\frac{C_{peak,i}}{C_{0,i}} - 1}{1 - \frac{C_{core,i}}{C_{0,i}}} \qquad (8\text{-}9)$$

Table 8-1: Selected analytical microsegregation models

Model	Equation	Expression of back diffusion
Scheil	$C_S = KC_0(1-f_S)^{k-1}$	
Brody-Flemings	$C_S = KC_0[1-(1-\beta K)f_S]^{(k-1)/(1-\beta k)}$	$\beta = 2\alpha = 2D_st_f / (\lambda/2)^2$
Clyne-Kurz	$C_S = KC_0[1-(1-\beta K)f_S]^{(k-1)/(1-\beta k)}$	$\beta = 2\alpha[1-\exp(-1/\alpha)]-\exp(-1/2\alpha)$
Ohnaka 1 (linear)	$C_S = KC_0[1-(1-\beta K)f_S]^{(k-1)/(1-\beta k)}$	$\beta = 2\alpha/(1+2\alpha)$
Ohnaka 2 (Parabolic)	$C_S = KC_0[1-(1-\beta K)f_S]^{(k-1)/(1-\beta k)}$	$\beta = 4\alpha/(1+4\alpha)$
Won-Thomas	$C_S = KC_0[1-(1-\beta K)f_S]^{(k-1)/(1-\beta k)}$	$\beta = 2\alpha^+[1-\exp(-1/\alpha^+]-\exp(-1/2\alpha^+)$ Where $\alpha^+ = 2(\alpha + \alpha^c)$ And $\alpha^c = 0.1$ (effect of coarsening)
This study	$C_S = KC_0[1-(1-\beta K)f_S]^{(k-1)/(1-\beta k)}$	$\beta = 2\alpha^{1/3}/(1+2\alpha^{1/3})$

8.2 Effect of back diffusion factor

Table 8-2 shows the equilibrium partition coefficient and diffusion coefficient of γ-phase for calculations. For high carbon steel in this study, the solidification goes directly to the γ-phase during the solidification process. Complete mixing is assumed in each phase for carbon

Table 8-2: Mn and Si data for equilibrium partition coefficients, diffusion coefficients, and liquidus line slopes [2]

Element	$k^{\gamma/L}$(cm^2/s)	D^{γ}(cm^2/s)
Si	0.60	0.3*exp(-60100/RT)
Mn	0.78	0.055*exp(-59600/RT)

where R is the gas constant, 1.987 cal/mol K, and T is temperature in Kelvin

Table 8-3 shows the predicted results of back diffusion β for Mn and Si according to the micro-segregation models from table 8-1. The local solidification time is calculated from equation 6-1, and secondary dendrite arm spacing measurements are shown in table 5-2. The back diffusion β for Mn and Si is calculated from the top surface to centre, it shows that the back diffusion β for Mn and Si decreases with decreasing cooling rate in the columnar dendritic structure (from top surface to 34.5mm) for models of Brody-Flemings, Clyne Kurz, Ohnaka 1 and 2, and starts increasing toward the centre where the dendritic structure is fully equiaxed. The model of Brody-Flemings and Clyne Kurz predict the same value β for the same cooling rate, the Ohnaka 1 predicts slightly lower value of β compared to the Brody-Flemings and Clyne Kurz.

Won-Thomas' results of back diffusion differ because the Won-Thomas model applies the effect of dendritic coarsening during solidification by adding the value 0.1 into the back diffusion β. If the Won-Thomas model is not adding the value 0.1 into the back diffusion β, the back diffusion results are the same with the Brody-Fleming model. For this study, the predicted results of back diffusion for Mn and Si also slightly differ with the different cooling rate. Both this study and the Won-Thomas model show much higher back diffusion values compared to other models, so the effect of dendritic coarsening on solute diffusion appears to be strong during the solidification process.

Table 8-3: Calculated values of back diffusion β according to different models

Depth (mm)	t_f (s)	C_R (°C/s)	Brody-Flemings	Clyne-Kurz	Ohnaka 1	Ohnaka 2	Won-Thomas	This study
Silicon								
11.5	15.3	6.96	$1.38*10^{-2}$	$1.38*10^{-2}$	$1.36*10^{-2}$	$2.68*10^{-2}$	$4.24*10^{-1}$	$2.76*10^{-1}$
23	40.7	2.61	$6.69*10^{-3}$	$6.69*10^{-3}$	$6.65*10^{-3}$	$1.32*10^{-2}$	$4.10*10^{-1}$	$2.30*10^{-1}$
34.5	96.8	1.09	$4.95*10^{-3}$	$4.95*10^{-3}$	$4.93*10^{-3}$	$9.80*10^{-3}$	$4.07*10^{-1}$	$2.13*10^{-1}$
46	178.3	0.59	$7.79*10^{-3}$	$7.79*10^{-3}$	$7.73*10^{-3}$	$1.53*10^{-2}$	$3.22*10^{-1}$	$2.39*10^{-1}$
57.5	284.4	0.37	$9.40*10^{-3}$	$9.40*10^{-3}$	$9.31*10^{-3}$	$1.84*10^{-2}$	$4.15*10^{-1}$	$2.51*10^{-1}$
69	426.5	0.25	$1.49*10^{-2}$	$1.49*10^{-2}$	$1.46*10^{-2}$	$2.89*10^{-2}$	$4.26*10^{-1}$	$2.81*10^{-1}$
80.5	544.2	0.19	$1.55*10^{-2}$	$1.55*10^{-2}$	$1.52*10^{-2}$	$3.00*10^{-2}$	$4.27*10^{-1}$	$2.83*10^{-1}$
92	631.3	0.17	$1.81*10^{-2}$	$1.81*10^{-2}$	$1.78*10^{-2}$	$3.50*10^{-2}$	$4.42*10^{-1}$	$2.94*10^{-1}$
103.5	701.4	0.152	$1.75*10^{-2}$	$1.75*10^{-2}$	$1.72*10^{-2}$	$3.38*10^{-2}$	$4.31*10^{-1}$	$2.92*10^{-1}$
115	734	0.145	$2.85*10^{-2}$	$2.85*10^{-2}$	$2.77*10^{-2}$	$5.39*10^{-2}$	$4.52*10^{-1}$	$3.26*10^{-1}$
Manganese								
11.5	15.3	6.96	$2.95*10^{-3}$	$2.95*10^{-3}$	$2.94*10^{-3}$	$5.86*10^{-3}$	$3.18*10^{-1}$	$1.85*10^{-1}$
23	40.7	2.61	$1.43*10^{-3}$	$1.43*10^{-3}$	$1.43*10^{-3}$	$2.85*10^{-3}$	$4.00*10^{-1}$	$1.52*10^{-1}$
34.5	96.8	1.09	$1.06*10^{-3}$	$1.06*10^{-3}$	$1.06*10^{-3}$	$2.11*10^{-3}$	$4.00*10^{-1}$	$1.39*10^{-1}$
46	178.3	0.59	$1.66*10^{-3}$	$1.66*10^{-3}$	$1.66*10^{-3}$	$3.32*10^{-3}$	$3.17*10^{-1}$	$1.58*10^{-1}$
57.5	284.4	0.37	$2.00*10^{-3}$	$2.00*10^{-3}$	$2.00*10^{-3}$	$4.00*10^{-3}$	$4.01*10^{-1}$	$1.67*10^{-1}$
69	426.5	0.25	$3.18*10^{-3}$	$3.18*10^{-3}$	$3.17*10^{-3}$	$6.33*10^{-3}$	$4.04*10^{-1}$	$1.89*10^{-1}$
80.5	544.2	0.19	$3.30*10^{-3}$	$3.30*10^{-3}$	$3.29*10^{-3}$	$6.57*10^{-3}$	$4.03*10^{-1}$	$1.91*10^{-1}$
92	631.3	0.17	$3.87*10^{-3}$	$3.87*10^{-3}$	$3.86*10^{-3}$	$7.69*10^{-3}$	$4.05*10^{-1}$	$1.99*10^{-1}$
103.5	701.4	0.152	$3.74*10^{-3}$	$3.74*10^{-3}$	$3.72*10^{-3}$	$7.42*10^{-3}$	$4.04*10^{-1}$	$1.97*10^{-1}$
115	734	0.145	$6.14*10^{-3}$	$6.14*10^{-3}$	$6.11*10^{-3}$	$1.21*10^{-2}$	$4.09*10^{-1}$	$2.25*10^{-1}$
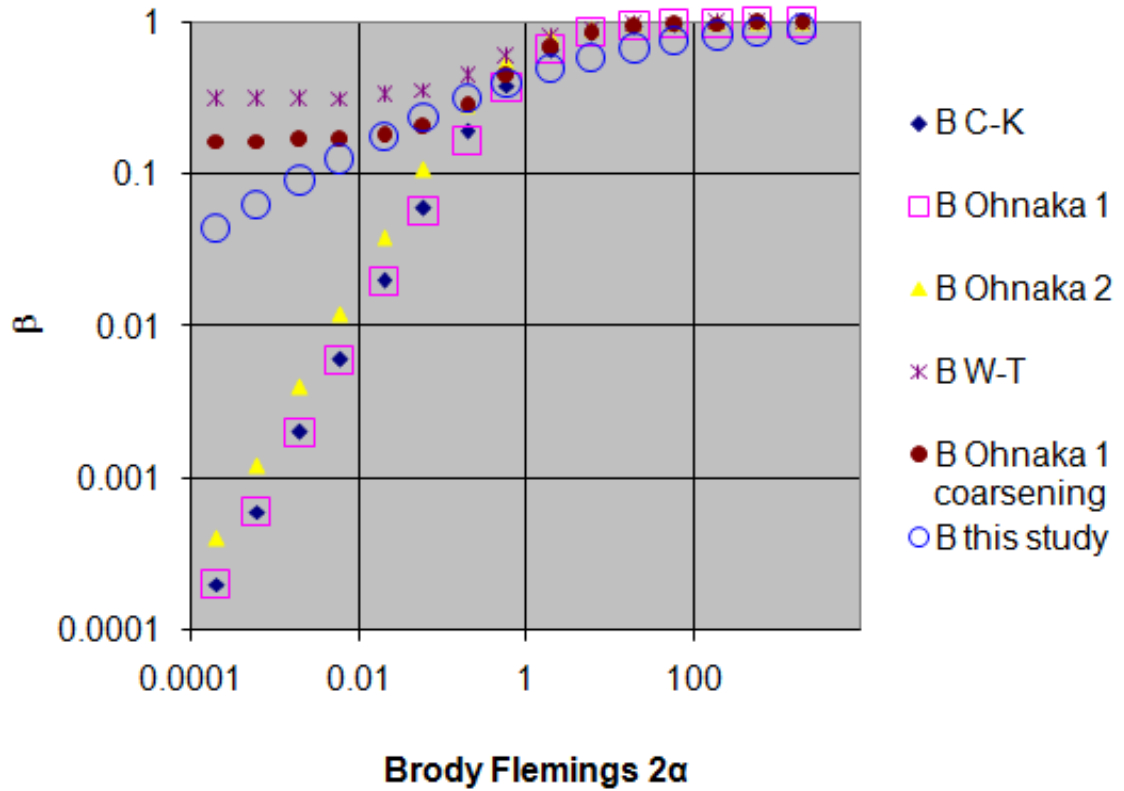
Figure 8-1: Comparison of back diffusion β parameters across a wide range of Brody-Flemings 2α for the different models.

Figure 8-1 shows the comparison of back diffusion β across a wide range of Brody-Flemings 2α values of 0.0001 to 2000. Increasing Brody-Flemings 2α is increasing the back diffusion, but it should stop at the equilibrium solution (β = 1). It shows that the Ohnaka 1 factor is almost identical to the Clyne-Kurz factor, the back diffusion β and Brody-Flemings 2α follow the ideal line from very low value of 0.0001 to around 0.01, then the back diffusion β gets limited to a maximum of 1 for a wide range of Brody-Flemings 2α values up to 2000. The Won-Thomas factor yields higher solute diffusivity compared to the Ohnaka 1&2, and Clyne-Kurz model, and also has the limitation to a maximum of 1. The coarsening factor $\alpha^c = 0.1$ leads to higher diffusivity compared to those models without dendritic coarsening. A good example is given by the Ohnaka 1 model normalised with the coarsening factor $\alpha^c = 0.1$ shown as equation 8-

10, the result shows much higher diffusivity for very low values of Brody-Flemings 2α, although not as much as by the Won-Thomas equation.

$$\beta = \frac{2(\alpha+0.1)}{1+2(\alpha+0.1)} \qquad (8\text{-}10)$$

This study with normalised dendritic coarsening shows much higher diffusivity compared to the Ohnaka 1&2, and Clyne-Kurz model, and shows the limitation to a maximum of 1 for a wide range of Brody-Flemings 2α values up to 2000. It is logical to expect a more complete micro-segregation model for multicomponent alloy solidification to include the effects of both coarsening secondary arm spacing and back diffusion [76].

Table 8-4: Predicted values of C max of Si and Mn when solid fraction $f_s = 1$

according to different models

Depth (mm)	t_f (s)	C_R (°C/s)	Brody-Flemings	Clyne-Kurz	Ohnaka 1	Ohnaka 2	Won-Thomas	This study
Silicon								
11.5	15.3	6.96	1.36	1.36	1.36	0.99	0.32	0.37
23	40.7	2.61	1.90	1.90	1.91	1.38	0.32	0.39
34.5	96.8	1.09	2.19	2.19	2.2	1.59	0.32	0.41
46	178.3	0.59	1.77	1.77	1.78	1.29	0.35	0.39
57.5	284.4	0.37	1.62	1.62	1.63	1.18	0.32	0.38
69	426.5	0.25	1.31	1.31	1.32	0.96	0.32	0.37
80.5	544.2	0.19	1.29	1.29	1.29	0.95	0.32	0.37
92	631.3	0.17	1.19	1.19	1.20	0.88	0.31	0.36
103.5	701.4	0.152	1.21	1.21	1.22	0.89	0.31	0.36
115	734	0.145	0.97	0.97	0.98	0.73	0.31	0.35
Manganese								
11.5	15.3	6.96	1.87	1.87	1.87	1.62	0.74	0.81
23	40.7	2.61	2.19	2.19	2.19	1.88	0.71	0.84
34.5	96.8	1.09	2.34	2.34	2.34	2.02	0.71	0.85
46	178.3	0.59	2.12	2.12	2.12	1.82	0.74	0.83
57.5	284.4	0.37	2.04	2.04	2.04	1.75	0.71	0.82
69	426.5	0.25	1.84	1.31	1.84	1.58	0.71	0.80
80.5	544.2	0.19	1.83	1.83	1.83	1.58	0.71	0.80
92	631.3	0.17	1.77	1.76	1.77	1.52	0.71	0.80
103.5	701.4	0.152	1.78	1.78	1.78	1.54	0.71	0.80
115	734	0.145	1.59	1.59	1.60	1.38	0.71	0.78

Table 8-4 shows the predicted results of Cmax of Si and Mn when solid fraction $f_s = 1$ according to the micro-segregation models from table 8-1. As expected severity of micro-segregation reflects the difference in β. The Cmax for Mn and Si are calculated from the top surface down to the centre. The models of Brody-Flemings and

Clyne Kurz predict the same value Cmax of Si and Mn for the same cooling rate, Ohnaka 1 predicts a slightly higher value of Cmax of Si and Mn compared to Brody-Flemings and Clyne Kurz. All micro-segregation models show the highest micro-segregation degree of Si and Mn at the depth of 34.5mm, and the predicted results show a higher micro-segregation degree at mid-way compared to the surface and centre, the predicted micro-segregation degree at the surface were found to be higher compared to the centre.

The predicted results of Cmax of Si and Mn for this study and Won-Thomas were much lower compared to other micro-segregation models; both models apply the effect of coarsening process on the course of solidification which is the reason for the reduced degree of micro-segregation. The Won-Thomas model prediction for Cmax, Si and Mn show almost the same values of micro-segregation except for the depth of 46mm. This is despite the solidification rate being much high at the surface and quickly decreasing at the centre. The predicted results of this study shows higher micro-segregation of Si and Mn compared to the Won-Thomas model.

Table 8-5: Predicted values of C core of Si and Mn when solid fraction $f_s = 1$ according to different models

Depth (mm)	t_f (s)	C_R (°C/s)	Brody-Flemings	Clyne-Kurz	Ohnaka 1	Ohnaka 2	Won-Thomas	This study
Silicon								
11.5	15.3	6.96	0.145	0.145	0.145	0.146	0.179	0.166
23	40.7	2.61	0.144	0.144	0.144	0.144	0.178	0.162
34.5	96.8	1.09	0.144	0.144	0.144	0.145	0.177	0.161
46	178.3	0.59	0.144	0.144	0.144	0.145	0.169	0.163
57.5	284.4	0.37	0.145	0.145	0.145	0.145	0.178	0.164
69	426.5	0.25	0.145	0.145	0.146	0.146	0.179	0.166
80.5	544.2	0.19	0.145	0.145	0.145	0.146	0.179	0.166
92	631.3	0.17	0.145	0.145	0.145	0.147	0.180	0.167
103.5	701.4	0.152	0.145	0.145	0.145	0.147	0.179	0.167
115	734	0.145	0.145	0.145	0.146	0.148	0.181	0.170
Manganese								
11.5	15.3	6.96	0.493	0.493	0.492	0.492	0.532	0.515
23	40.7	2.61	0.492	0.492	0.492	0.492	0.543	0.510
34.5	96.8	1.09	0.492	0.492	0.492	0.492	0.543	0.508
46	178.3	0.59	0.492	0.492	0.492	0.492	0.532	0.511
57.5	284.4	0.37	0.492	0.492	0.492	0.492	0.543	0.512
69	426.5	0.25	0.492	0.492	0.492	0.492	0.543	0.515
80.5	544.2	0.19	0.492	0.492	0.492	0.492	0.543	0.515
92	631.3	0.17	0.492	0.492	0.492	0.492	0.543	0.516
103.5	701.4	0.152	0.492	0.492	0.492	0.543	0.543	0.516
115	734	0.145	0.492	0.492	0.492	0.544	0.544	0.519

Table 8-5 shows the predicted results of C_{Core} concentration of Si and Mn based on Howe's solute core equation [106] (Equation 8-7) when solid fraction $f_s = 1$ according to the micro-segregation models from table 8-1. The C_{Core} concentrationd for Mn and Si are calculated from the top surface down to centre. The model of Brody-Flemings, Clyne-Kurz, and Ohnaka 1&2 predict the same value C_{core} of Si and Mn for the same cooling rate and different depths from the surface to centre. The explanation for the above results; Ohnaka' back diffusion factor is almost identical to the Clyne-Kurz' factor.

The predicted results of C_{Core} of Si and Mn for this study and Won-Thomas were higher compared to other micro-segregation models; both models apply the effect of the coarsening process on the course of solidification which is the reason for the decrease in the degree of micro-segregation. The Won-Thomas model predicts for Ccore Si and Mn are shown almost the same values of micro-segregation degree except for the depth at 46mm. Both models show lower predicted results of C_{Core} Si and Mn at the quarter thickness compared to the surface and centre, and the predicted results of C_{Core} of Si and Mn at the centre are higher compared to the surface. These differences must reflect the balance of solidification time and arm spacing.
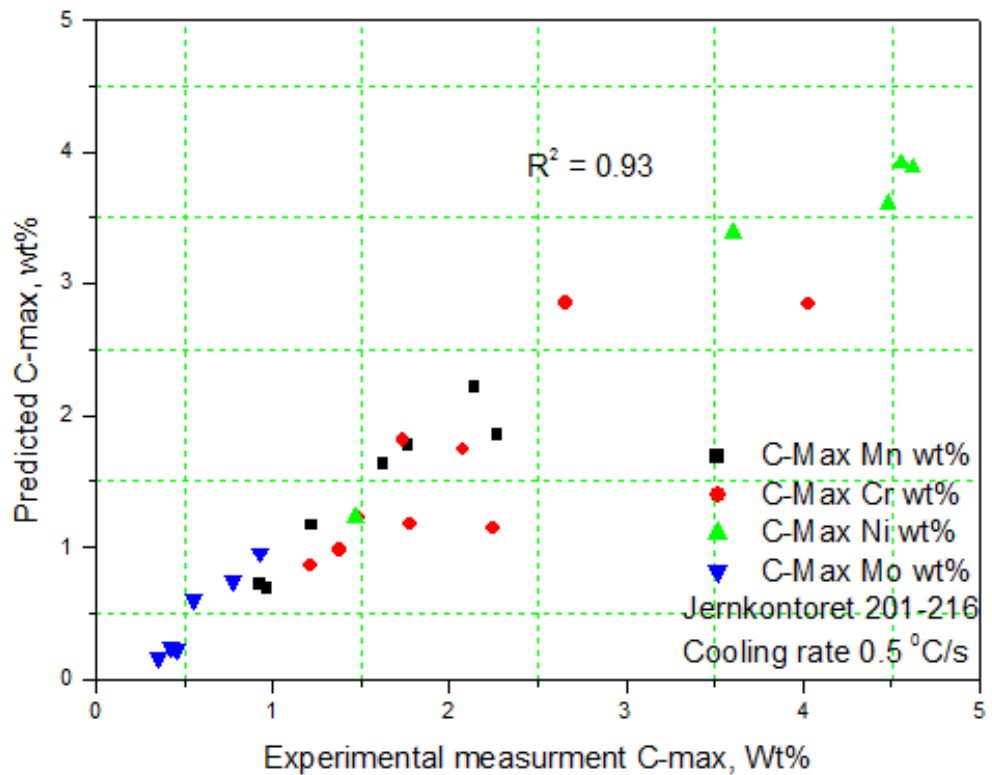
Figure 8-2: Comparison between predicted Cmax and measured Cmax from

Jernkontoret 201-216.

From figure 8-2 we can see that the predicted values follow closely the experimental values with high R-squared of 0.93. The two worst results are for chromium, which relate to the higher carbon steels. It is known from theory of solidification that increasing carbon leads to the reduction of the partition coefficient k of chromium which leads to increased degree of segregation as evident in figure 8-2 but this interaction is not included in the model. The new micro-segregation equation in this study appears to work better than would be expected for such an analytical model as compared with the Jernkontoret results [113]. It is difficult for an analytical model to show much better agreement with experimental results in view of the degree of experimental variability and error [105].

8.3 Comparison of the new equation with experimental results

This study adopts Howe' micro-segregation model [106] for the power-law profile in order to calculate silicon and manganese profiles across the secondary dendrite arms (see equation 8-8). The silicon and manganese peaks (final concentration at fraction solid = 1) are listed in table 8-4, which assume finite diffusivity in the solid phase and constant k values [105]. During solidification, at the solidus, the degree of micro-segregation across the depths depends on the accumulated modulus, Dt/λ^2 (for constant D and secondary dendrite arm spacing).

Table 8-6: DICTRA and QSP diffusion multiplier t_f/λ^2 predicted by given depths

Depth (mm)	Local time (s)	Measured SDAS (μm)	DICTRA diffusion multiplier	QSP diffusion multiplier
11.5	15.27	60.056	0.00466	0.00423
23	40.73	120.62	0.00308	0.0028
34.5	96.82	216.35	0.00243	0.00207
46	178.33	233.93	0.00388	0.00326
57.5	284.36	268.82	0.0047	0.00394
69	426.54	261.63	0.00721	0.00622
80.5	544.21	256.71	0.00951	0.00826
92	631.28	237.15	0.01277	0.01123
103.5	701.42	241.48	0.01358	0.01204
115	734	229.20	0.01558	0.01394

Table 8-6 show the calculated diffusion multiplier t_f/λ^2 (extracted from figure 6-7), it shows that the diffusion multiplier value at the depth 34.5mm is lowest compared to the surface and centre, the diffusion multiplier value at the surface is 2 times higher compared to the depth 34.5mm. The diffusion multiplier value at the

34.5mm is 3 times lower compared to the depth of 69mm, and 7 times lower compared to the centre.

Figures 8-3 to 4 show the comparison between experimental and predicted results for silicon and manganese profiles across secondary dendrite arms at the 11.5mm to 34.5mm depth. Manganese profiles show very good agreement with experimental results, it goes parallel with the EDS scatter and a little bit lower compared to experimental results, because there is some degree of diffusive homogenisation of the solute profile during the cooling below solidus, while predicted silicon profiles are lower in the core regions compared to experimental results. The core concentrations of silicon are lower than experimental results, and the core concentrations of manganese show good agreement with experimental results.

From the depth 34.5 toward 57.5mm, the predicted results of manganese profiles show good agreement with experimental results as shown in figures 8-5 to 9, it goes parallel with the EDS scatter and is lower compared to experimental results, because there is some degree of diffusive homogenisation of solute profile during the cooling below solidus. The strong evidence is listed in table 8-6, in these depths, the diffusion multipliers are lower compared to the surface, it means that manganese diffuses slower compared to the surface. Silicon profiles show agreement with experimental results but are lower at the quarter thickness regions.

From the depth of 80.5mm toward the centre, both silicon and manganese profile predictions show excellent agreement with experimental results. In these depths, the diffusion multipliers are much higher compared to the quarter thickness and surface as shown in table 8-6, it means that both silicon and manganese are strongly diffusing up to the end of the solidification process, however silicon concentration at the dendritic cores is a little lower than experimental results.

Overall, the new micro-segregation appears to work better than would be expected for the predicted Si and Mn peak concentrations. Indeed, the results show very good agreement with the experimental results, albeit without considering the effect of solid-state diffusive homogenisation below solidus.

Generally, Mn and Si are a bit less segregated in practice, and Si more segregated than Mn. Quantitatively, this is as expected from sub-solidus homogenisation.
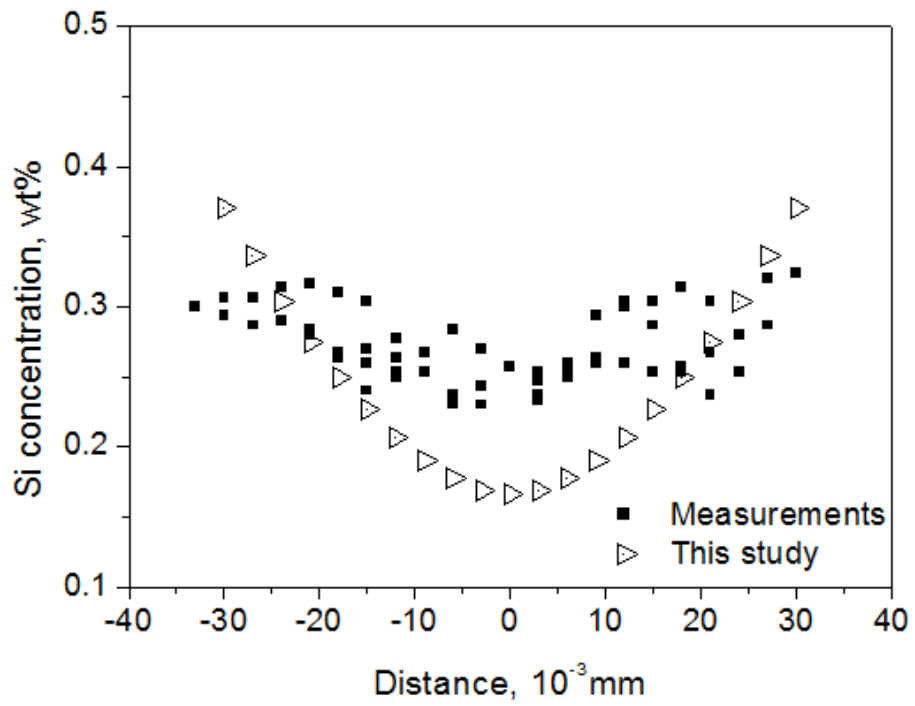
(a)
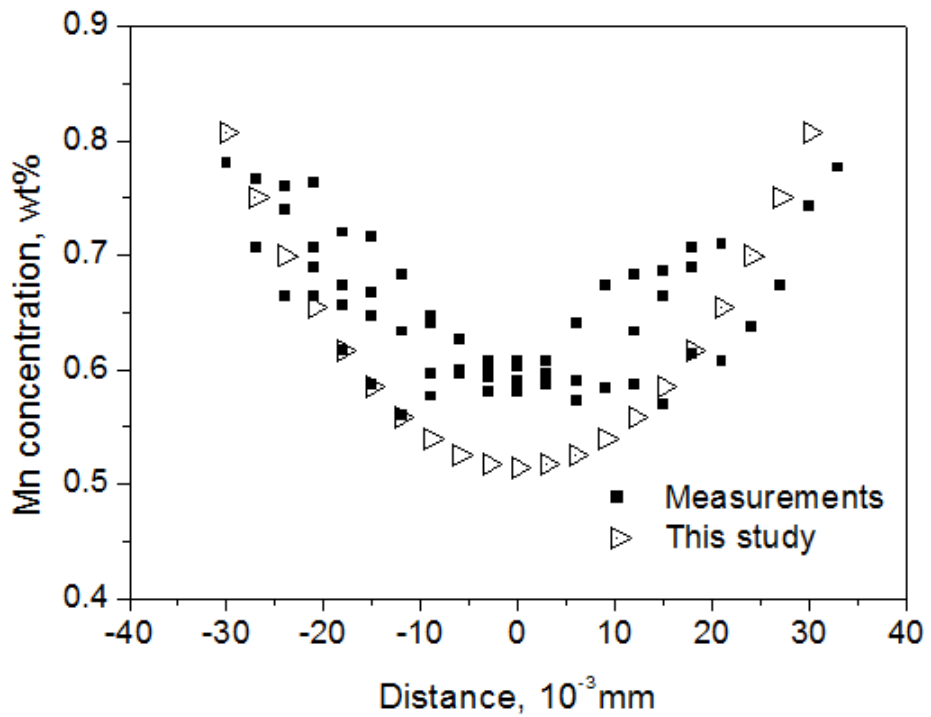
(b)

Figure 8-3: Experimental and predicted line profile compositions for high

carbon bloom steel across 60 μm secondary dendrite arms at the depth 11.5mm

for (a) silicon and (b) manganese
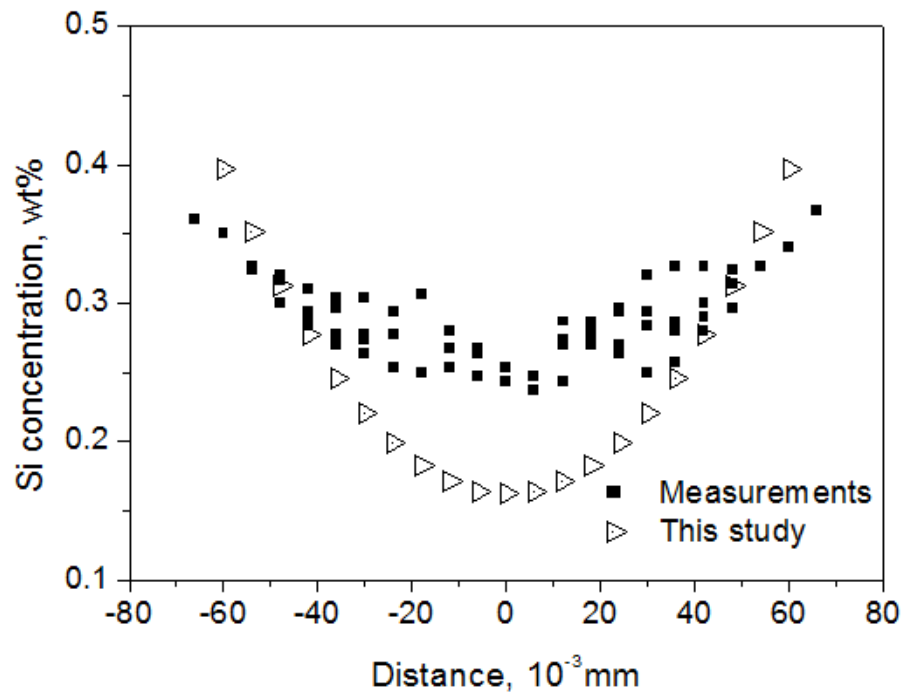
(a)
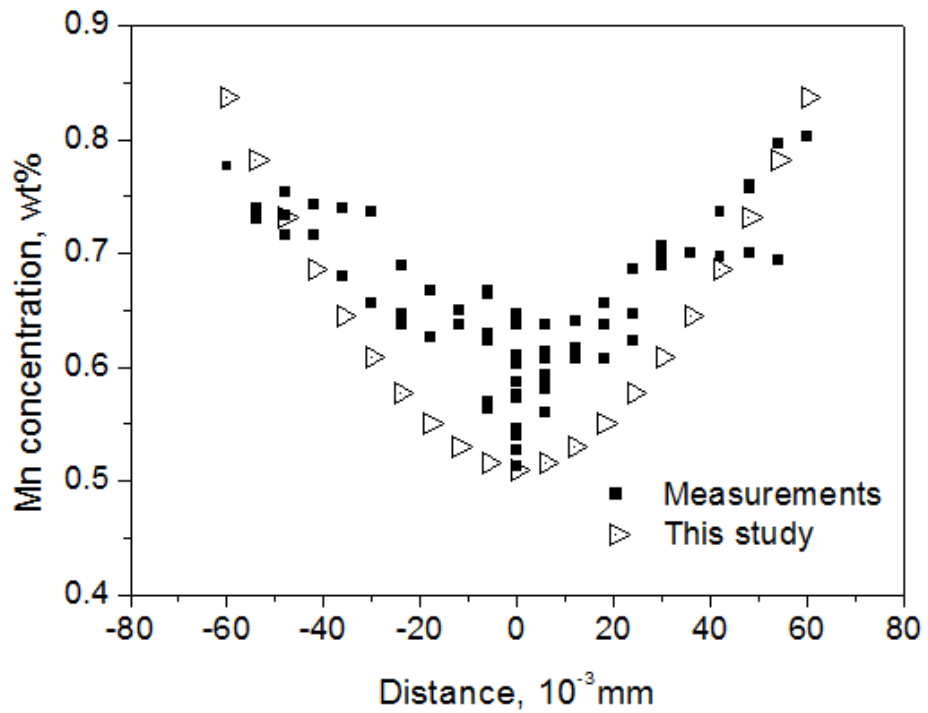
(b)

Figure 8-4: Experimental and predicted line profile compositions for high

carbon bloom steel across 120 μm secondary dendrite arms at the depth 23mm

for (a) silicon and (b) manganese
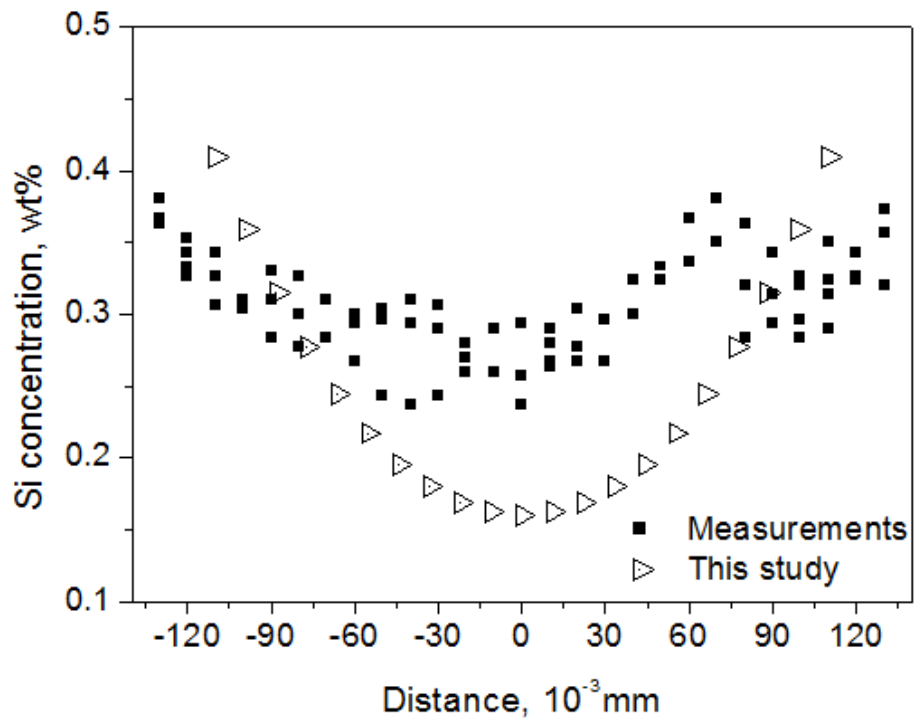
(a)
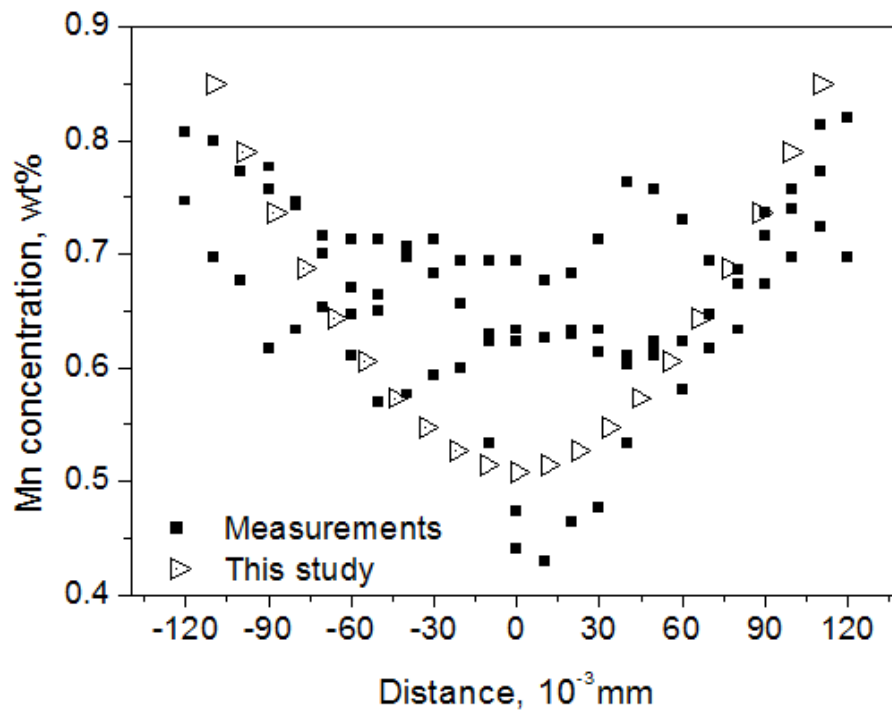
(b)

Figure 8-5: Experimental and predicted line profile compositions for high

carbon bloom steel across 216 μm secondary dendrite arms at the depth 34.5mm

for (a) silicon and (b) manganese

175
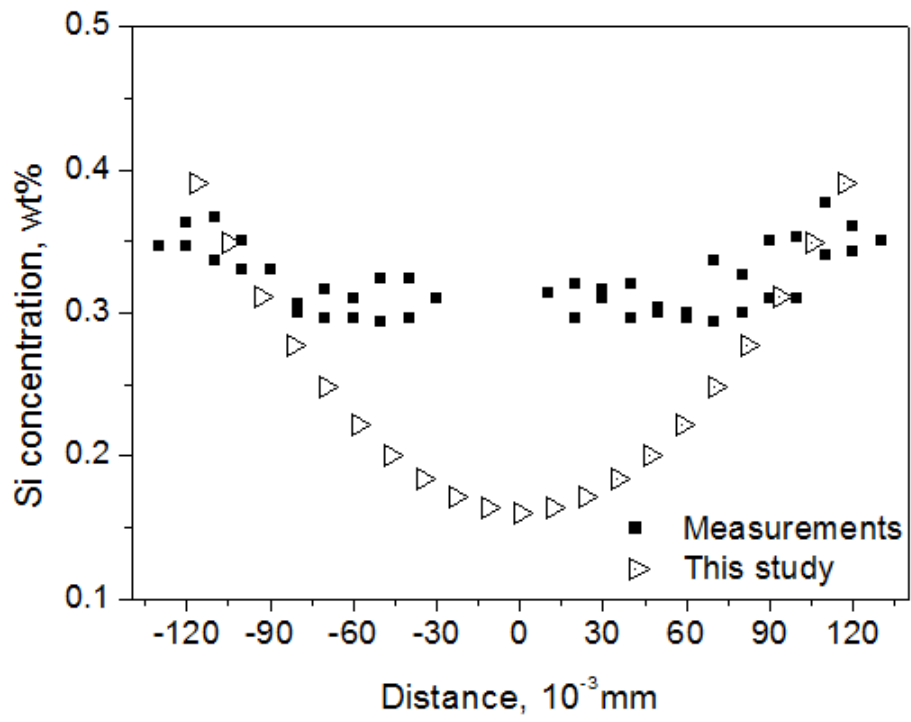
(a)
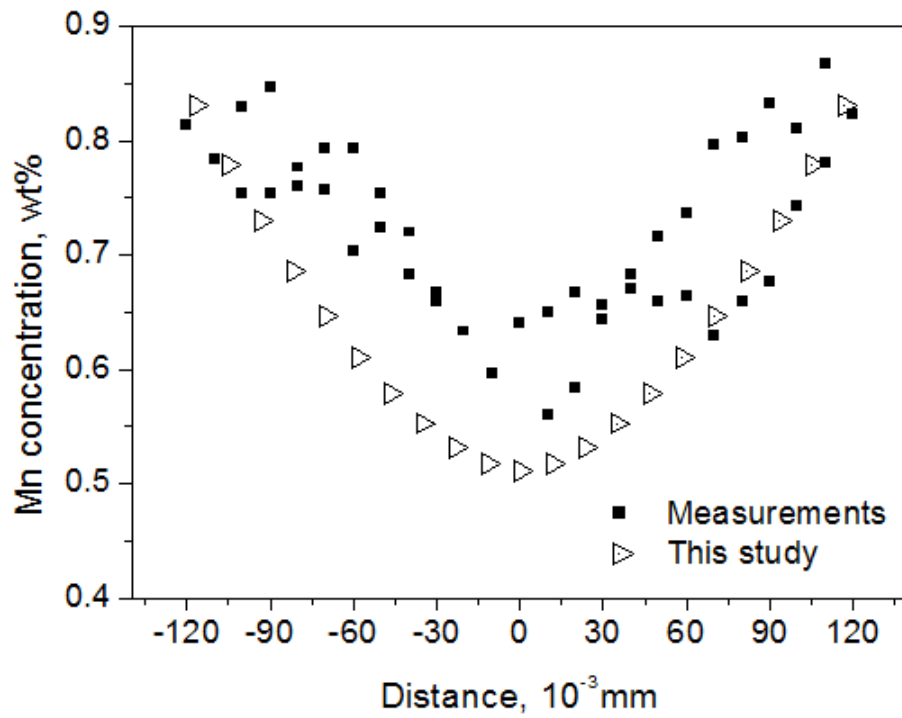
(b)

Figure 8-6: Experimental and predicted line profile compositions for high

carbon bloom steel across 234 μm secondary dendrite arms at the depth 46mm

for (a) silicon and (b) manganese
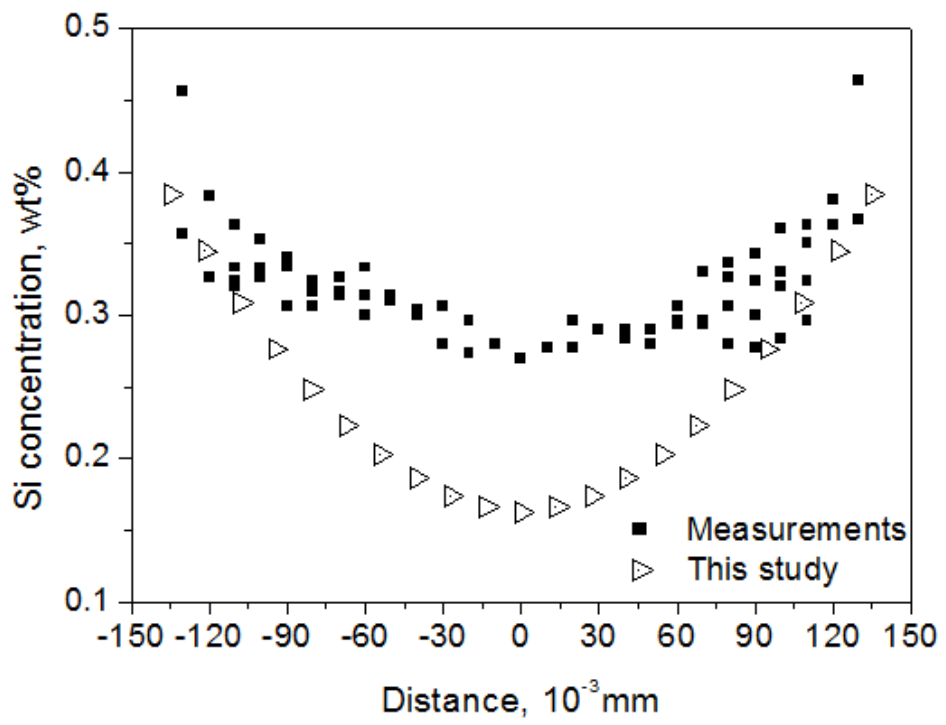
(a)
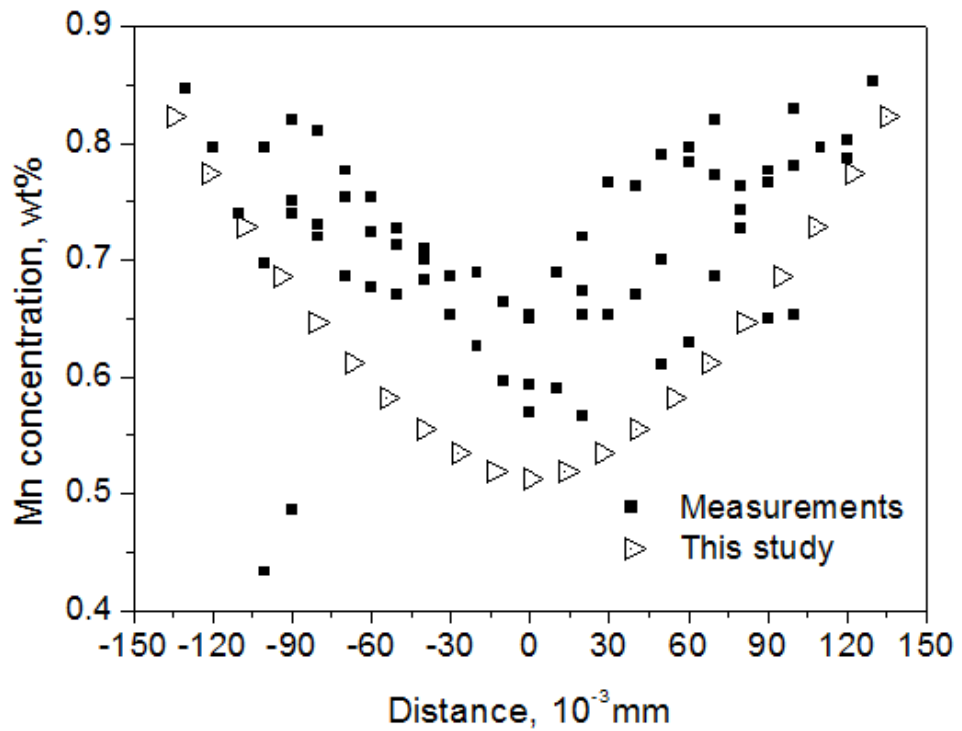
(b)

Figure 8-7: Experimental and predicted line profile compositions for high

carbon bloom steel across 269 μm secondary dendrite arms at the depth 57.5mm

for (a) silicon and (b) manganese

177
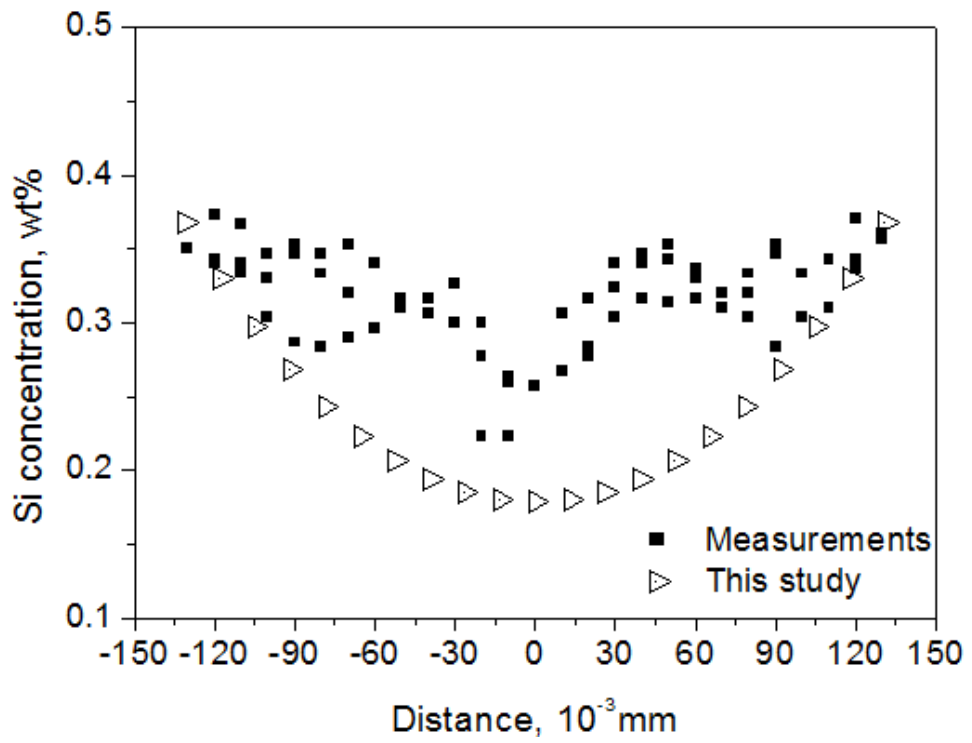
(a)
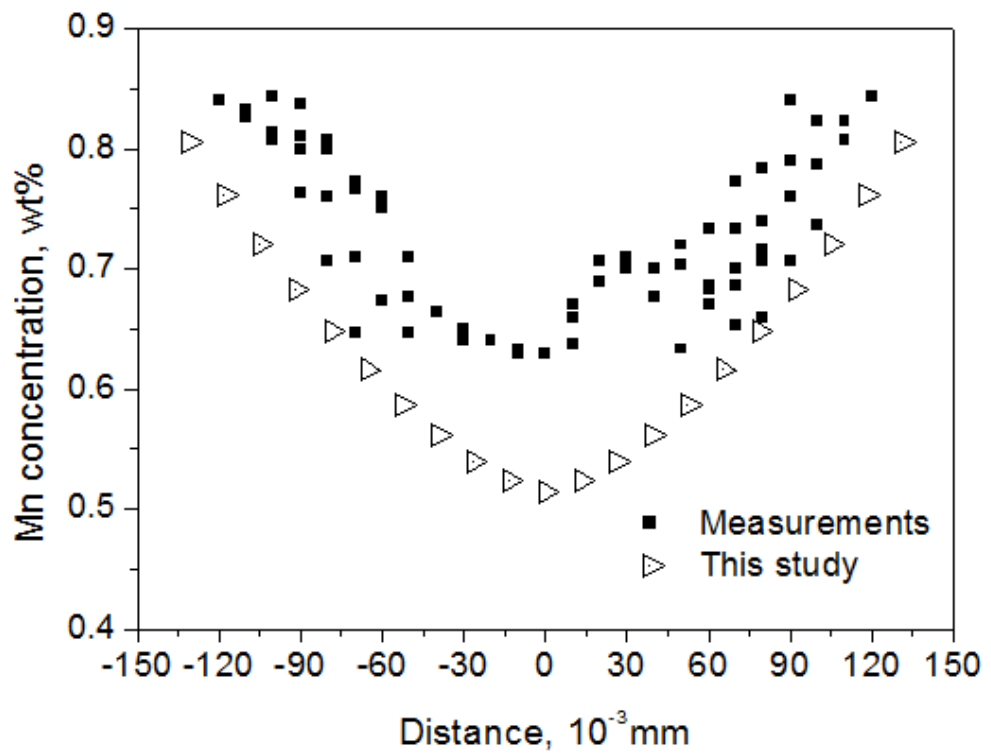
(b)

Figure 8-8: Experimental and predicted line profile compositions for high

carbon bloom steel across 262 μm secondary dendrite arms at the depth 69mm

for (a) silicon and (b) manganese
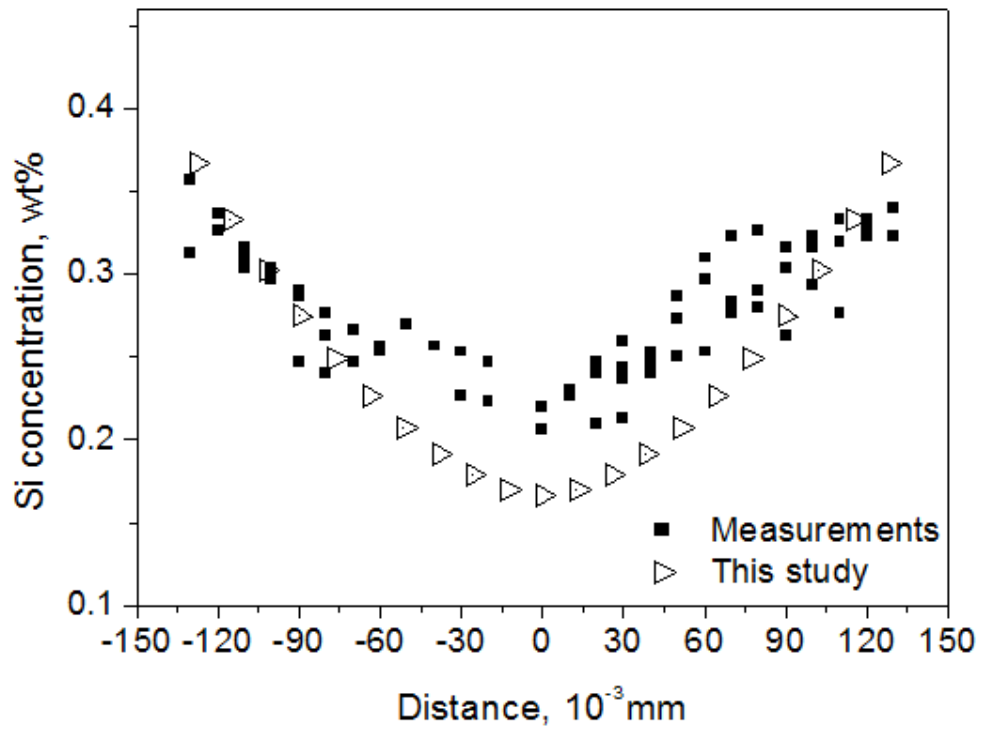
(a)
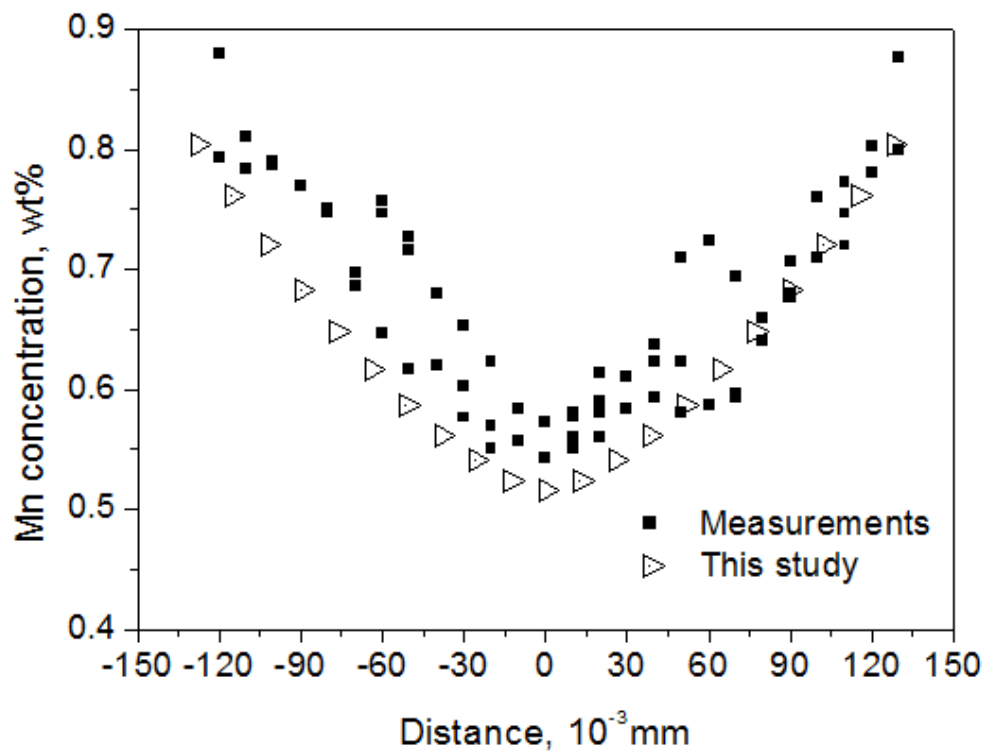
(b)

Figure 8-9: Experimental and predicted line profile compositions for high

carbon bloom steel across 257 μm secondary dendrite arms at the depth 80.5mm

for (a) silicon and (b) manganese
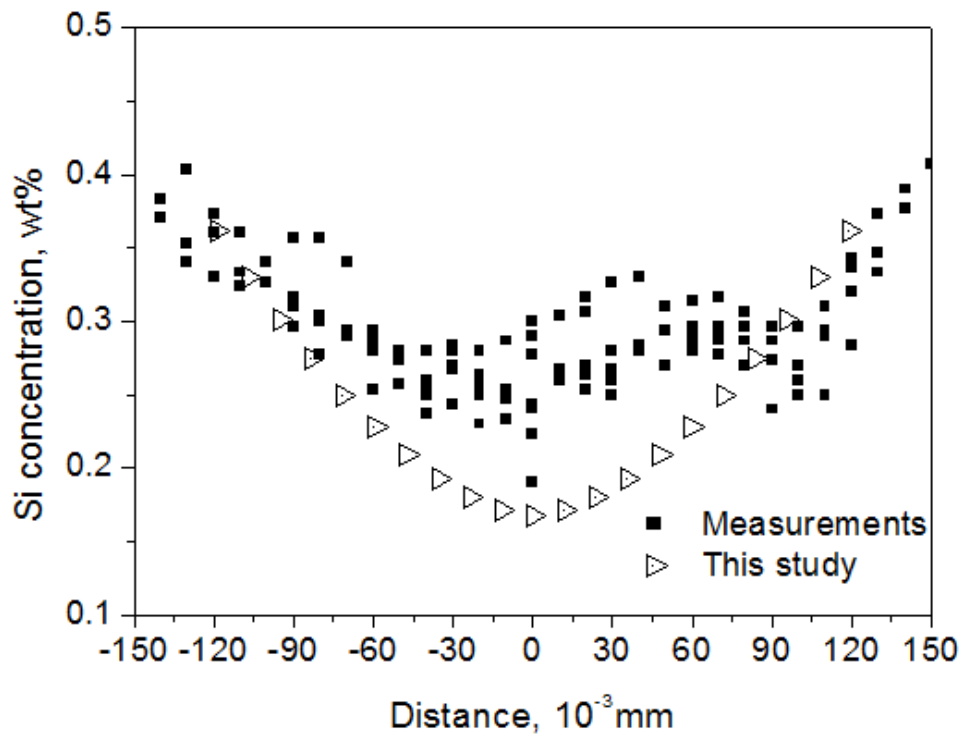
(a)
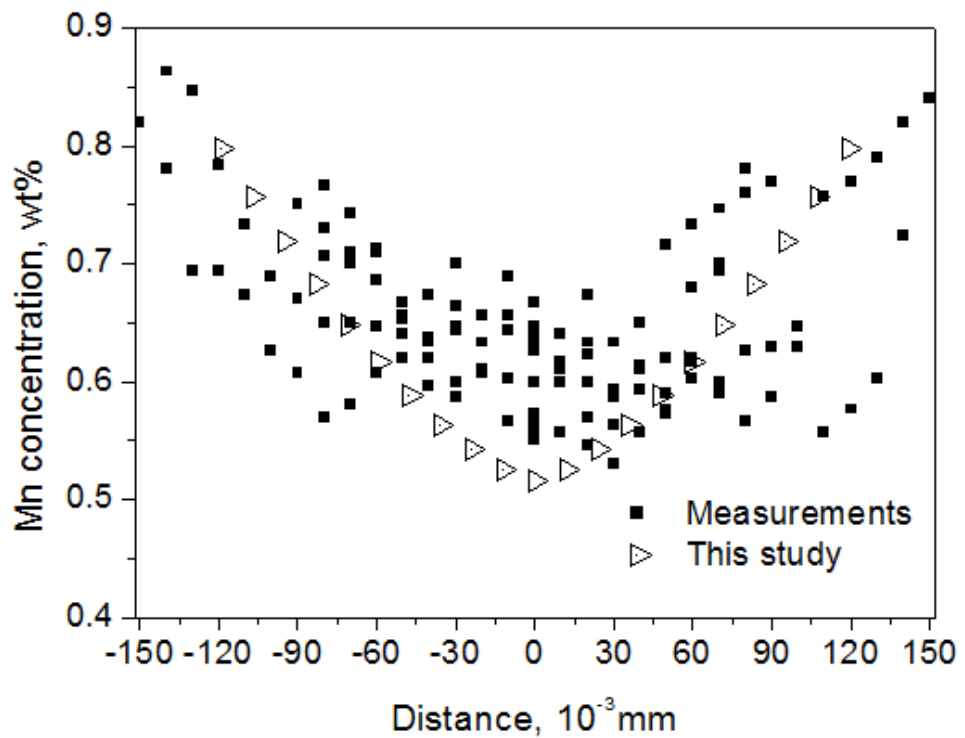
(b)

Figure 8-10: Experimental and predicted line profile compositions for high

carbon bloom steel across 237 μm secondary dendrite arms at the depth 92mm

for (a) silicon and (b) manganese
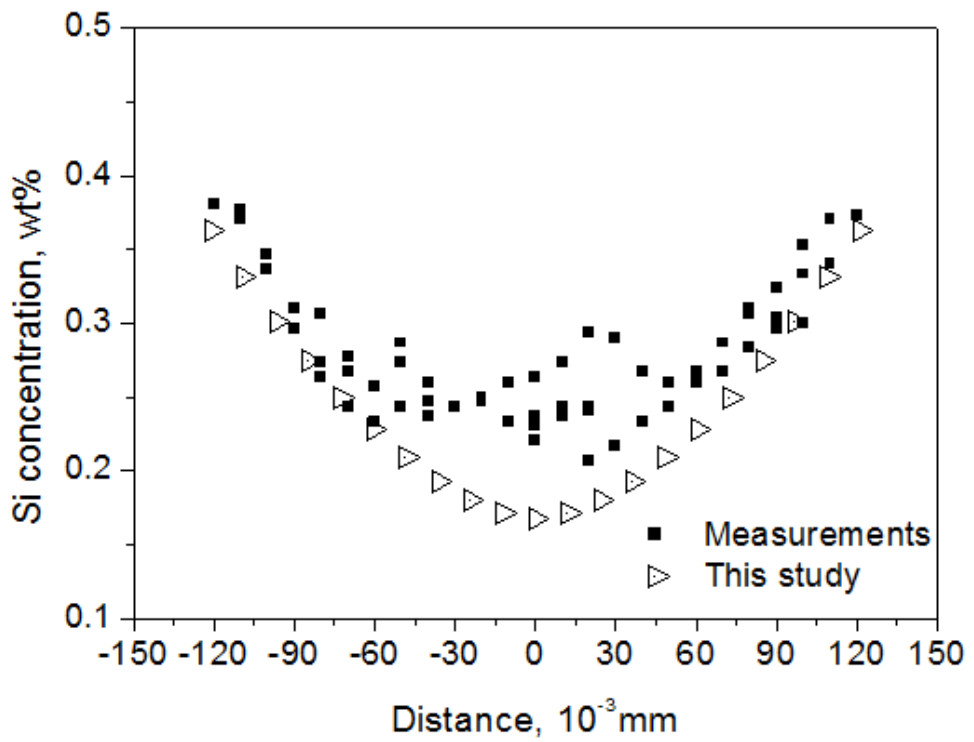
(a)
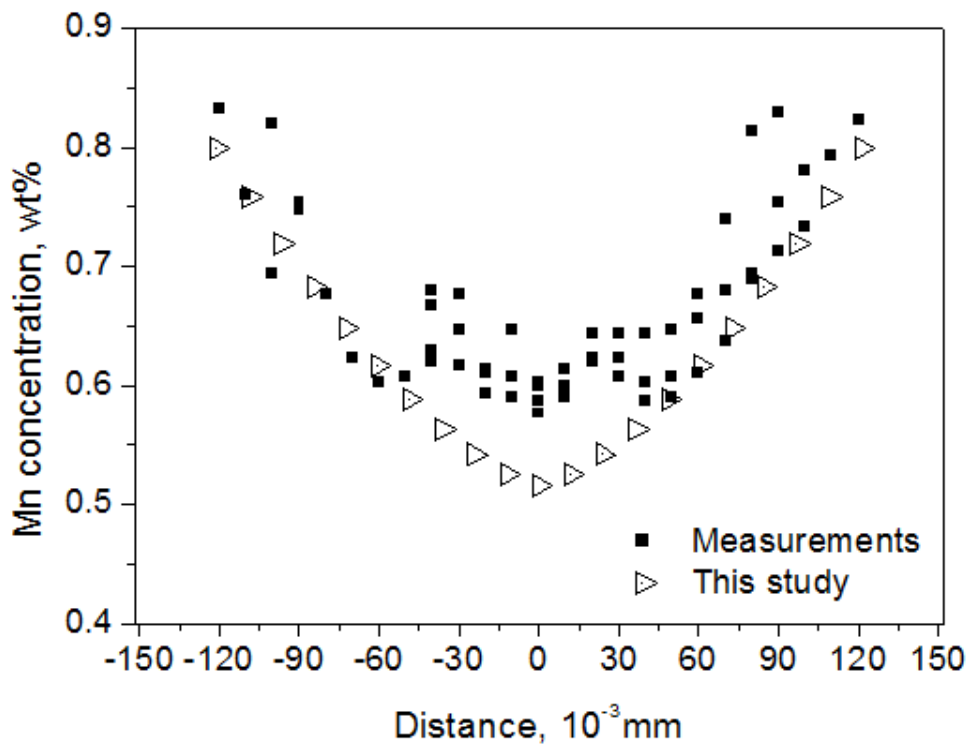
(b)

Figure 8-11: Experimental and predicted line profile compositions for high

carbon bloom steel across 242 μm secondary dendrite arms at the depth

103.5mm for (a) silicon and (b) manganese
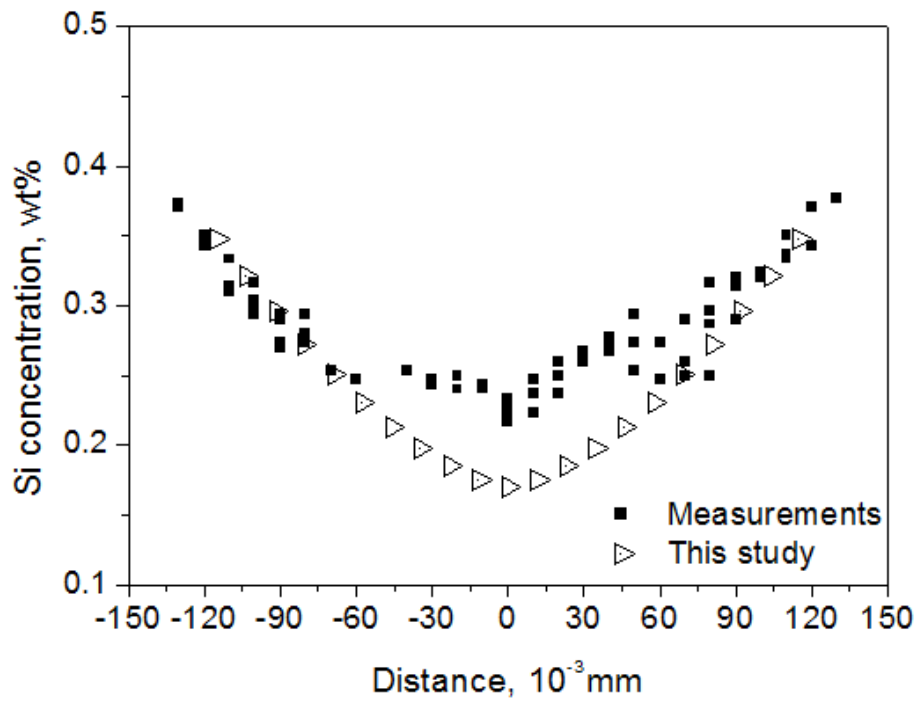
(a)
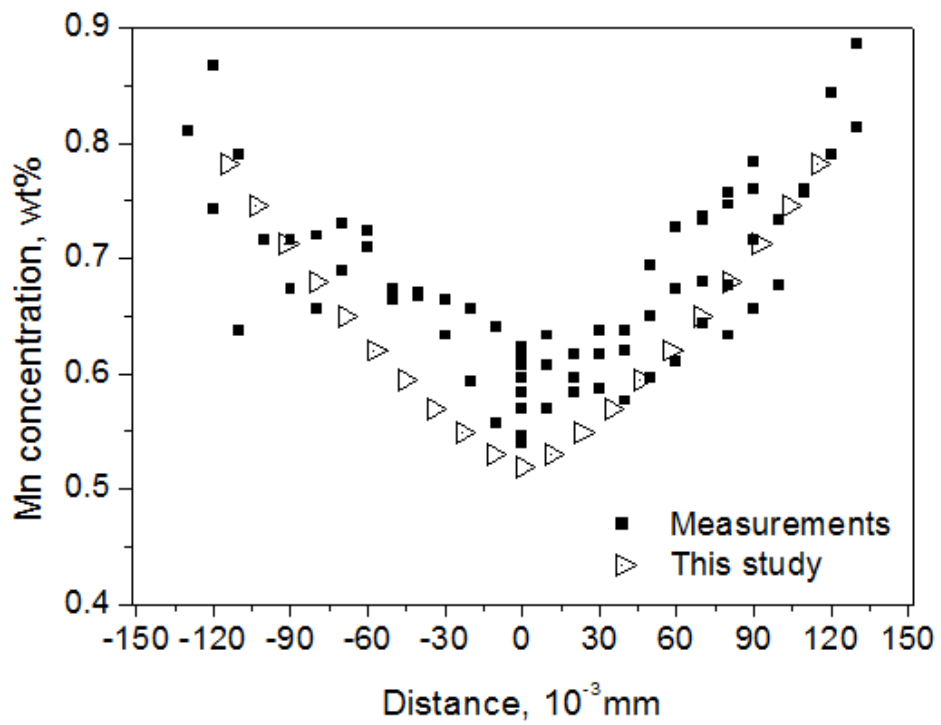
(b)

Figure 8-12: Experimental and predicted line profile compositions for high

carbon bloom steel across 229 µm secondary dendrite arms at the depth 115mm

for (a) silicon and (b) manganese

The rapid equation for the prediction of micro-segregation developed from the Ohnaka 1 model assumes finite diffusivity and coarsening. The prediction results show very good agreement with experimental results for high carbon bloom steel as-cast from the industrial scale; it also shows excellent agreement with Jernkontoret results for steels 201-216.

Chapter 9: Overall Summary Chapter

The effect of thermal history across a bloom, slab or billet during liquid–solid transformation and sub-solidus homogenisation was studied in this thesis. During the solidification process, the cooling rate varied from the surface to centre depending on the size of cast and casting speed. Increasing the casting speed leads to higher productivity and affects the quality of the product by introducing defects such as surface cracks, transverse cracks and internal cracks. However, higher speed also leads to increased micro-segregation and reduced secondary dendrite arm spacing (which in turn reduces the required diffusion distance for homogenisation during secondary cooling process).

9.1 Secondary dendrite arm spacing model

This model addresses a major question: How does the peritectic transformation affect secondary dendrite arm spacing? This research focused on two pathways; "peritectic equivalent" and "carbon equivalent". In the case of peritectic equivalent, the results show that similar results are obtained with slightly decreasing R-squared when the value of E_p is reduced from 1 to 0.9 allowing the use of $k_{\gamma/L}$ and $m_{\gamma/L}$. The geometric factor was found to vary with carbon content. The results also show that the coarsening dendrite parameter is strongly controlled by those elements with large values of the empirical factor A_i such as Si, Cr, Mo and N. Moreover, when the value of E_p was reduced from 1 to 0.9, there were no significant differences in the values of those elements with expanded austenite fields like C, Mn and Ni. A possible explanation for this finding is that when the temperature is below the peritectic temperature, the dendrite arms are formed and become stable. However, there were significant differences in the values of those elements with expended ferrite fields like Si, Cr and

Mo, which may be explained by the fact that the first ferrite formed at an earlier stage of solidification changes by the diffusion process or coarsening process.

When the term carbon content was changed to carbon equivalent, once the factors (k and m) were changed from ferritic to austenitic solidification at $C_p = 0.53$ (as in the Fe-C binary) rather than at $E_p = 1$. Not surprisingly, the results show slightly increasing R-squared of 0.941 (figure 4-5) compared with the use of E_p, where the R-squared value was 0.938 (figure 4-2).

9.2 Secondary dendrite arm spacing measurements

The results of the secondary dendrite arm spacing measurements indicated a typical variation of the average secondary dendrite arm spacing measurement and standard deviation from top surface to centre. Decreasing the cooling rate with the depth increased the secondary dendrite arm spacing, which can be explained by the fact that the surface has less solidification time in comparison to the centre.

Dendrite arm spacing measurement shows a half "seagull" λ_2 (µm) profile, with maximum values of dendrite arm measurement at the quarter-thickness. There are several possible explanations for this result. First, this finding corroborates the findings of Howe [120], who showed that an acceleration in the cooling rate at the centre of the bloom is induced by this seagull λ_2 profile. Second, t in the TTC model only assumes heat extraction transverse to the casting direction (the macro model does not include longitudinal heat extraction). Thus, the heat flow rate is steeper through the shell thickness than in the casting direction, and could reduce the local solidification time t_f (s) in the central region, resulting in a half "seagull" λ_2 profile.However, the dendrite arm spacing profile exhibits scatter beyond 40mm depth and a dip at the centre. Third,

Ganguly [5] provides another possible explanation for this result. In addition to the change in solidification rate, carbon enrichment of liquid and change in mobility of dendrites also have an impact on the dendrite size distribution in the equiaxed zone. From the observations beyond 40mm depth, the dendrite structure corresponds to the equiaxed zone.

In order to assess the analytical secondary dendrite arm spacing models (chapter 4), high carbon bloom steel was sectioned and the secondary dendrite arm spacing was measured. The results indicated that the SDAS predicted values were close to their actual values. However, the SDAS results continue to increase from surface and stop doing so from the quarter-thickness position whereas the SDAS predicted results continue to increase towards the centre. A possible explanation for the difference between the measured and predicted values is that most of the SDAS data used in this model are from the lab scale, which maintains a constant cooling rate, but in high carbon bloom steel production, which uses the thermal rate instead of the cooling rate. The thermal rate extracted from the macro model, which uses a 2D model (not a 3D model) and assumes heat extraction transverse to the casting direction.

9.3 Solidification and segregation modelling from QSP and DICTRA software

In order to study micro-segregation behaviour across the bloom thickness, QSP and DICTRA software were used to predict the solidus temperature across the thickness of the bloom. It was initially expected that the solidus decreases from the centre to surface, reflecting the increasing solidification rate. However the calculated solidus temperatures showed a typical difference of about 5K between them, exhibiting a solidus trough at

34.5 mm depth for QSP and 57.5 mm depth for DICTRA shown as figure 6-5. The QSP results show a stronger effect than the DICTRA ones.

Interestingly, the solidus temperature profile was found to be related to the SDAS measurement profile, the higher SDAS value at the quarter-thickness the lower the solidus temperature is. It is known that solidus temperature is related to the micro-segregation degree, with the lower solidus temperature being associated with a higher micro-segregation degree.

Sub-solidus homogenization was investigated in this research using QSP and DICTRA software. The micro-segregation of elements decreased as the temperature decreased during the continuous cooling process, with the size of decrease being dependent on the cooling conditions. For large cross sections of steel the sub-solidus homogenization is more complicated due to multicomponent and multiphase alloys. An example of micro-segregation of Si and Mn showed significant decrease after solidification.

QSP and DICTRA simulation of how Si and Mn solute profiles homogenise during the cooling process below the solidus temperature indicated that both Si and Mn solutes show significant decrease as the temperature decreases. However, both models indicated higher micro-segregation of Si and Mn at the 23 mm position, and homogenization sub-solidus toward the centre.

9.4 Si and Mn micro-segregation measurements

Si and Mn micro-segregation measurements were carried out using line scans with EDS-SEM technique. EDS-SEM line scans going through 2, 3 or 4 secondary dendrite arm spacings were selected. The 3 rolling averages technique was used on the Si and Mn concentration profiles in order to obtain some smoothing.

It was found that both Si and Mn concentration profiles were proportional, smooth and increased from the dendrite cores to the interdendritic position. However, in some cases, silicon and manganese solute peaks were not coincident. Instead, they exhibited peaks drifting between silicon and manganese profiles, where the manganese was not ideally aligned with the manganese and it is believed that the solute peaks slightly drifted apart as sub-solidus homogenization occurred. In another case, the manganese profile was smooth and exhibited a "saw-tooth". The silicon profile was not ideally aligned with the manganese and it was believed that the solute peaks slightly drifted apart after solidification.

The correlation between silicon and manganese followed the ideal line but showed large scatter at the surface toward the quarter-thickness. Toward the centre, a positive correlation was found between silicon and manganese which followed the ideal line with a high R-Squared value of 0.68. There are some possible reasons for this scatter;

- The faster cooling rate near the surface itself leads to more micro-segregation, and the tendency for precipitate formation could play a role
- When sub-solidus homogenization occurred during the cooling process,

The manganese concentration profile went around the average composition of 0.63 wt.% (with the exception of the depth of 69mm) and tended to segregate to the interdendritic region. At quarter-thickness, the minimum concentration of Si was generally higher than the average concentration of 0.24 wt.%. Further toward the centre, the minimum concentration of Mn was lower compared to the average concentration
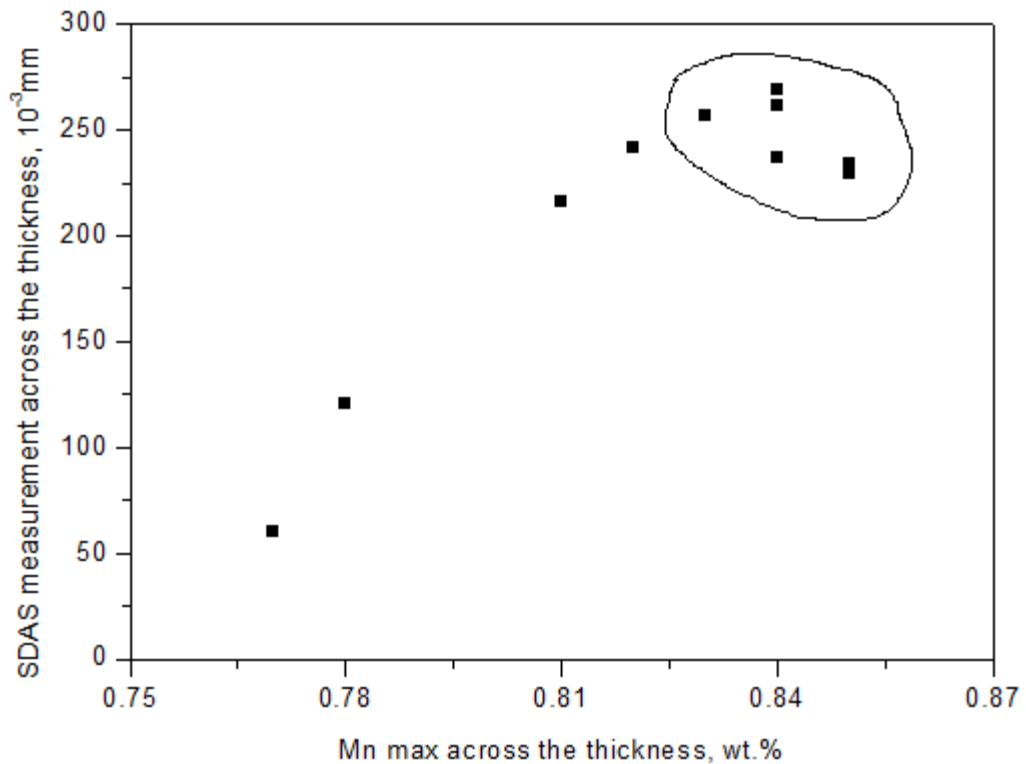
Figure 9-1: Correlation between Mn Max and SDAS measurement across the

thickness of bloom

Figure 9-1 shows the correlation between Mn max and SDAS measurement across the

thickness. It is clear that increasing the SDAS measurement resulted in an increase of

the Mn max concentration. However, at SDAS ranging between 230 and 270 μm, Mn

segregation (circled) was much higher. It was believed that manganese segregated more

at the quarter-thickness. From the solidification theory, the faster cooling rate near the

surface itself leads to more micro-segregation. However, they also lead to reduced

SDAS, which will reduce the required diffusion distance for homogenisation during

cooling in the solid state. This means that the SDAS value plays an important role in

terms of segregation compared with the cooling rate.
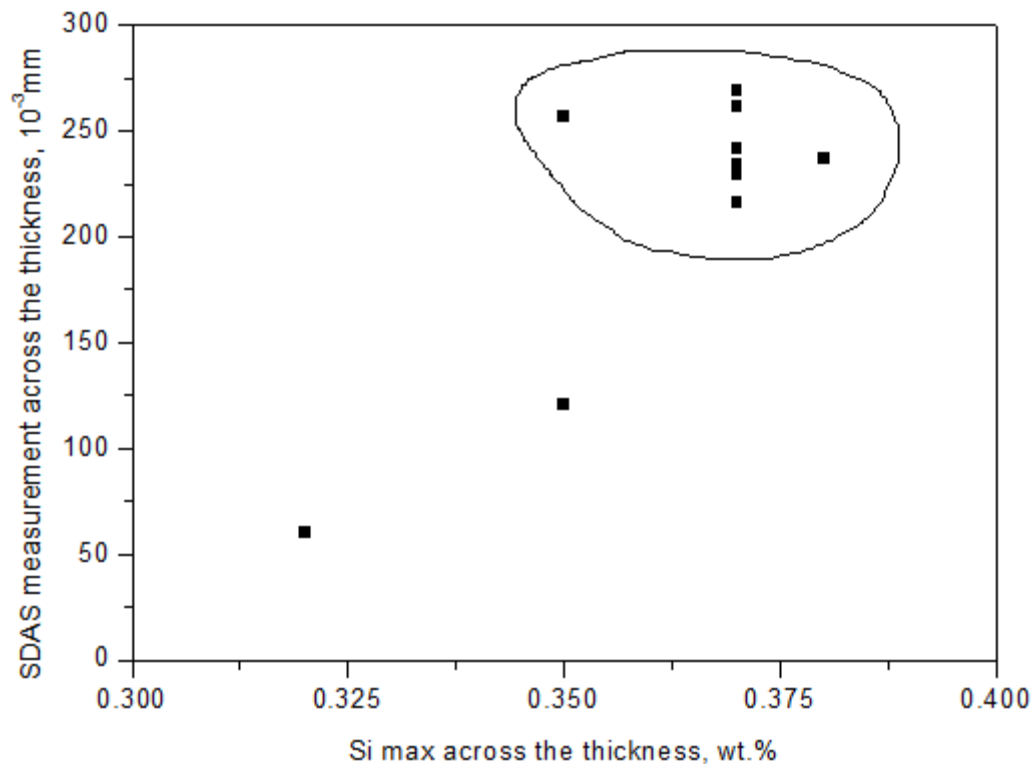
Figure 9-2: Correlation between Si Max and SDAS measurement across the

thickness of bloom

Figure 9-2 shows the correlation between Si max and SDAS measurement across the thickness. The correlation follows the ideal line, however, the points circled between 230 μm and 270 μm clearly shows that segregation is much higher in this region as compared to any of the other regions. Hence, we can conclude that silicon segregation was more concentrated at the quarter-thickness from the centre. This trend was found to be similar to manganese segregation previously shown in figure 9-1.

9.5 Micro-segregation model

The present simple micro-segregation model developed in this thesis is based on the Ohnaka model [102]. This model resolved the limitation of the Ohnaka model that the length scale of the microstructure is constant. This new micro-segregation model takes into account the coarsening of the dendrite structure, measured by the secondary

dendrite arm spacings. The advantage of this approach was an additional back diffusion term which leads to a reduced degree of segregation at the solidus.

The back diffusion β results of this model were compared to other models in table 8-1. In general, excellent agreement was obtained between the model of Brody-Flemings and Clyne Kurz for the value β with the same cooling rate. Both this study and the Won-Thomas model applied the effect of dendritic coarsening during solidification and they both showed much higher back diffusion β values compared to other models. The comparison of back diffusion β across a wide range of Brody-Flemings 2α of 0.0001 to 2000 for the different models was also studied in this thesis. The back diffusion β results agree well with theory, which suggests that it lies between the limit of the Scheil case of 0 and equilibrium (Lever rule) case of 1. The results obtained here, are therefore believed to be applicable to a more complete micro-segregation model for multicomponent alloys, which includes the effect of both dendritic coarsening and back diffusion.

The comparison between the predicted Si and Mn profiles and Si and Mn measured profiles across the depths was studied in this project. Manganese profiles showed very good agreement with measured results; it goes parallel with the EDS scatter. Silicon profiles also showed very good agreement with measured results, however, silicon concentration at the dendritic cores was a little lower than the measured results. It believed that there is some degree of diffusive homogenisation of solute profile during the cooling below the solidus.

Chapter 10: Conclusions

In this thesis studies have been carried out in four major areas:

(i) Development of an analytical secondary dendrite arm spacing model for multicomponent steels; effect of peritectic transformation from ferrite to austenitic during solidification, effect of carbon equivalent.

(ii) Secondary dendrite arm spacing measurements.

(iii) Solidification and micro-segregation modelling from QSP and DICTRA software; effect of heat extraction rate on micro-segregation level of silicon, manganese, including sub-solidus homogenization.

(iv) Si and Mn micro-segregation measurements

(v) Develop a new micro-segregation model; effect of back-diffusion (with an assumed simple geometry and ignoring the minor undercoolings associated with curvature) and coarsening on micro-segregation level of silicon and manganese.

10.1 Development of an analytical secondary dendrite arm spacing model for multicomponent steels; effect of peritectic transformation from ferrite to austenitic during solidification, effect of carbon equivalent.

1. A simple analytical dendrite arm spacing model has been developed using Matlab software which takes into account the peritectic transformation affecting SDAS. The study was successful as it was able to provide a simple model but adequate procedure for characterising a steel composition in relation to the peritectic, either through a "peritectic equivalent" or a "carbon equivalent". The predicted results show very good agreement with Jernkontoret results and other experimental results.

2. When the value of the peritectic equivalent E_p whereupon the calculation change from ferritic to austenitic data, is reduced from 1 to 0.97 and 0.9 respectively, it appears that even a temporary appearance of ferrite early on in solidification should not be ignored, and seems to control the secondary dendrite arm spacing.

3. In the case of the effect of multicomponent alloy elements, the results show that carbon is the only element affecting the geometric factor B in the proposed model; other elements are more strongly affecting the coarsening parameters A.

4. The new analytical SDAS model appears to work better than would be expected for the predicted SDAS. Indeed, the results show good agreement with the experimental results for Scunthorpe high carbon steel bloom. It also shows excellent agreement with Jernkontoret results for steels 201-216 and other previous SDAS studies.

10.2 Secondary dendrite arm spacing measurements.

1. The secondary dendrite arm spacing measurements show a typical variation from the top surface to the centre. It shows low values of dendrite arm spacing at the surface, increasing toward the centre; a maximum value was recorded at the quarter-thickness, and approximately constant (with much scatter), although indicating a slight decrease further toward the centre.

2. The SDAS measurements thus exhibit a "seagull profile". It would be expected that for a given steel, SDAS should increase with the local solidification time. The reason for this profile is suspected to be that t_f (s) actually decreases beyond the quarter-thickness position unlike in the TTC model which only assumes heat extraction transverse to the casting direction; the temperature gradient (and thus heat flow rate) will be much steeper through the shell thickness than down in the casting direction. But around the sump, heat flow

down in the casting direction could become significant, and could maybe reduce the local solidification t_f (s) in the central region (figure 9-1) which results in a "seagull profile".
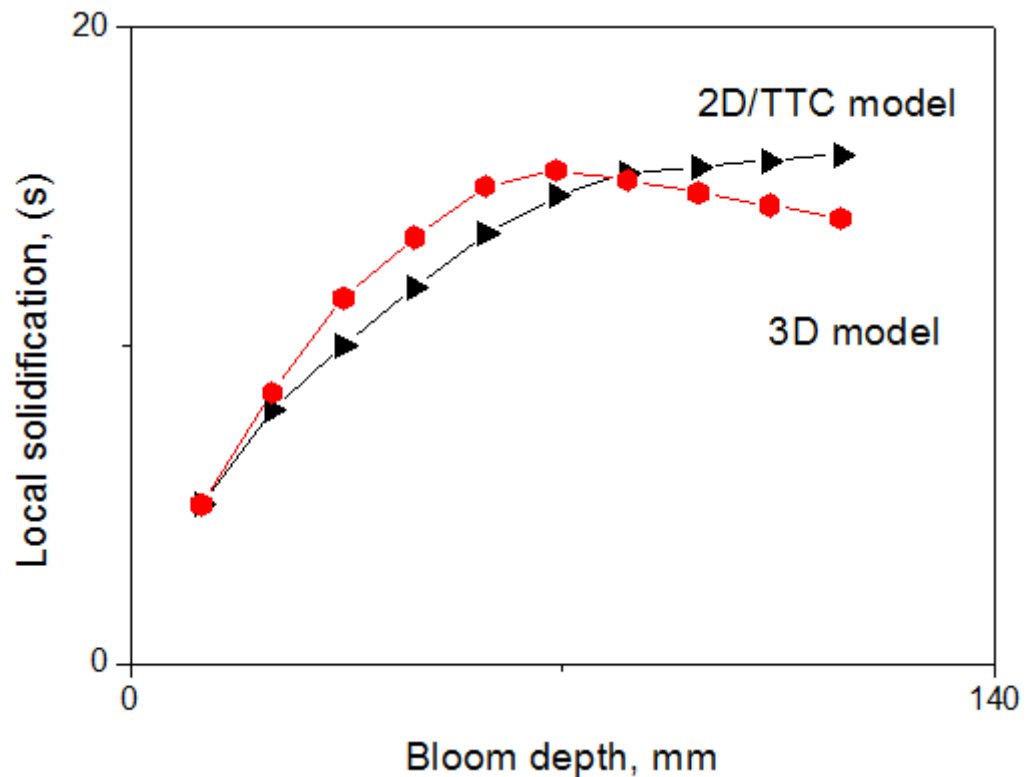
Figure 10-1: expectation between local solidification time (s) and bloom depth (mm) for 2D / TTC model and 3D model.

3. Another possible explanation for a SDAS "seagull profile" is that the submerged entry pouring configuration and the effect of argon on the flow pattern could move the liquidus isotherm relative to the macro model' prediction. It could be reduce the local solidification t_f (s) in the central region.

4. The analytical secondary dendrite arm spacing model agrees well with experimental results at the surface and centre. However, it shows big differences at the quarter-thickness. The reason for this is that it could involve limitations of the thermal model employed; the local solidification time beyond the quarter-

thickness might be lower compared to results from the TTC model, as shown schematically in figure 9-1.

10.3 Solidification and micro-segregation modelling from QSP and DICTRA software; effect of heat extraction rate on micro-segregation level of silicon, manganese including sub-solidus homogenization.

1. The solidus predictions across the thickness of the bloom are simulated by DICTRA and QSP: the calculated solidus temperatures showed a typical difference of only about 5k between them, the QSP results showing a stronger effect (solidus variation) than DICTRA. Unexpectedly, the results show solidus troughs (maximum micro-segregation at solidus) in the quarter-thickness of bloom, reflecting a balance of secondary dendrite arm spacing and local solidification time.

2. Both experimental results and model predictions show the quarter-thickness profiles are less homogeneous than the surface profiles, but the models showed highest micro-segregation at 23mm. QSP generally shows more silicon micro-segregation than DICTRA, manganese micro-segregation varies from rather similar (near surface) to very different (near centre).

10.4 Si and Mn micro-segregation measurements

1. Micro-segregation measurements show that from the depth of 57.5mm toward the centre, the Si and Mn concentration profiles are smooth and approximately proportional; the Si concentration profiles look smoother than back towards to the surface, both Si and Mn peaks are clearer.

2. The experimental results of the manganese peak profile increased from the surface to the depth of 46 mm. The silicon peak profile increased from surface to the depth of 35.5 mm, but scattered around that level to the centre. They compared very well to the measured SDAS than the DICTRA and QSP variations.

3. The experiments were successful as they were able to identify the Si and Mn micro-segregation degree from the surface, mid-way and toward the centre. The present results are significant in that at least they could identify the effect of cooling rate or heat extraction rate, solidification microstructure and solute diffusion on micro-segregation both during and after solidification, and support the queries regarding the macro-model thermal data.

10.5 Development of a new micro-segregation model; effect of back-diffusion (with an assumed simple geometry and ignoring the minor undercoolings associated with curvature) and coarsening on micro-segregation level of silicon and manganese.

1. The new micro-segregation equation with normalised dendritic coarsening shows much more diffusive homogenisation compared to the Ohnaka 1&2, and Clyne-Kurz models. All these models tend to the equilibrium limit (back-diffusion parameter equalling unity) for very high Brody-Flemings 2α values but the proposed model approaches this limit sooner.

2. The new micro-segregation equation shows that the predicted results of back diffusion for silicon and manganese slightly differ with cooling rate. Both this study and the Won-Thomas model which also accounts for SDAS coarsening, show much higher back diffusion values compared to other models, so the effect

of dendritic coarsening on solute diffusion is a very strong effect during the solidification process.

3. The new micro-segregation equation appears to work better than would be expected for the predicted peak concentration of silicon and manganese. Indeed, the results show very good agreement with the experimental results, albeit without considering the effect of solid-state diffusive homogenisation below the solidus. It also shows excellent agreement with Jernkontoret results for steels 201-216.

Chapter 11: Further Work

During the course of this research work, a number of areas were identified that required future work. This final chapter discusses these areas of possible future work which would help to develop a better understanding of the effect of cooling rate or heat extraction rate on the micro-segregation and SDAS for multicomponent steels.

1. Work is needed to obtain updated thermal input data from a 3D model, for the full 3D heat flow around the sump / solidus isotherm, and preferably also the effect of the liquid pouring streams on the position of the liquidus isotherm.

2. Micro-segregation measurements show some scatter around the dendrite cores, so further studies on the WDS-SEM are recommended in order to get even clearer Si and Mn micro-segregation profiles.

3. Further work may need in order to obtain information regarding the liquidus and solidus temperatures during and after the solidification processes across the thickness of typical slab, billet and bloom geometries. This information would be very helpful for SDAS and calculations of the degree of micro-segregation. Future work could also be carried out to develop a model which allows prediction of the liquidus and solidus temperature.

4. Further work could be carried out to develop a model which could predict the SDAS for stainless steels and other highly alloyed steels.

5. With a growing demand for new steel products with higher quality and optimum production rate, one area of future work could be in developing a model which allows prediction of crack formation during the continuous casting process.

6. Finally development of a micro-segregation model that would account for solute diffusion during and after solidification would increase our understanding in this important area.

References

[1]   M. R. Allazadeh, "The effect of cooling rate on the microstructure configuration of continuous cast steel slabs," Ph.D. thesis, University of Pittsburgh, 2009.

[2]   Y.-M. Won and B. Thomas, "Simple model of microsegregation during solidification of steels," *Metallurgical and Materials Transactions A,* vol. 32, pp. 1755-1767, 2001.

[3]   B. G. Thomas, "Continuous Casting," in *Encyclopedia of Materials: Science and Technology (Second Edition)*, ed: Elsevier, 2001, pp. 1595-1598.

[4]   S. Luo*, et al.*, "Numerical Simulation of Solidification Structure of High Carbon Steel in Continuous Casting Using Cellular Automaton Method," *ISIJ International,* vol. 52, pp. 823-830, 2012.

[5]   S. K. Choudhary and S. Ganguly, "Quantification of the Solidification Microstructure in Continuously-Cast High-Carbon Steel Billets," *Metallurgical and Materials Transactions B,* vol. 40, pp. 397-404, 2009.

[6]   G. E. Sellers, "First patent granted for continuous casting lead tubing," USA Patent, 1840.

[7]   J. Laing, US patent Patent No. 3023, 1843.

[8]   H. Bessemer, "On the manufacture of Continuous Sheets of Malleable Iron and Steel Direct from Fluid Metal," in *The Iron and Steel Institute Meeting*, 1891, pp. 1189-1191.

[9]   W. S. Association, "World steel in figures 2012," E. Basson, Ed., ed, 2012.

[10]   A. K. Bhattacharya and D. Sambasivam, "Optimization Of Oscillation Parameters In Continuous Casting Process Of Steel Manufacturing: Genetic Algorithms Versus Differential Evolution ", 2011.

[11]   G. J. D. Wet, "CFD Modelling and mathematical optimisation of a continuous caster submerged entry nozzle," Master thesis, University of Pretoria, 2005.

[12]   B. Kozak and J. Dzierzawski. Continuous Casting of Steel: Basic Principles [Online].

[13]   J. Sengupta*, et al.*, "Understanding the Role Water-cooling Plays during Continuous Casting of Steel and Aluminum Alloys," in *Materials Science and Technology Conference Proceedings*.

[14]   M. C. Flemings and T. Koseki, *Chapter 6 Solidification of steel, The Making, Shaping and Treating of Steel,* vol. 11th Edition Casting AISE Steel Foundation.

[15]   G. Lesoult, "Macrosegregation in steel strands and ingots: Characterisation, formation and consequences," *Materials Science and Engineering: A,* vol. 413–414, pp. 19-29, 2005.

[16]   A. A. Howe, "Development of a computer model of dendritic microsegregation for use with multicomponent steels," *Applied Scientific Research,* vol. 44, pp. 51-59, 1987.

[17]   A. Ghosh, "Segregation in cast products," *Sadhana,* vol. 26, pp. 5-24, 2001/02/01 2001.

[18]   A. A. Howe, "Micro-segregation in multicomponent steels involving the peritectic reaction," Ph.D. thesis, The University of Sheffield, Sheffield, 1993.

[19]   P. Tsakiropoulos, "Solidification lecture notes," ed: Sheffield University, 2010.

[20]   K. Hulka*, et al.*, "High Temperature Thermomechanical Processing of Pipe Steel – Technical Basis and Production Experience," in *Pipeline Technology*, Brügge, Belgium, 2000, pp. 291-306.

[21]   A. Turkeli and D. H. Kirkwood, "Microsegregation in manganese steels," in *Solidification Processing*, 1997.

[22]   A. A. Howe, "Micro-Segregation: Issues of Growth Rate and the Peritectic," *Materials Science Forum,* vol. 649, pp. 419-424, 2011.

[23]   A. A. Howe and D. H. Kirkwood, "Computer prediction of microsegregation in peritectic alloy systems," *Materials Science and Technology,* vol. 16, pp. 961-967, 2000.

[24]   C. Beckermann, "Modelling of macrosegregation: applications and future needs," *International Materials Reviews,* vol. 47, pp. 243-261, 2002.

[25]   C. Beckermann, "Macrosegregation," 2001.

[26]   M. Sadat*, et al.*, "The effects of casting speed on steel continuous casting process," *Heat and Mass Transfer,* vol. 47, pp. 1601-1609, 2011/12/01 2011.

[27]   J. W. Elmer*, et al.*, "Microstructural development during solidification of stainless steel alloys," *Metallurgical Transactions A,* vol. 20, pp. 2117-2131, 1989/10/01 1989.

[28]   J. W. Elmer, "The Influence of Cooling Rate on the Microstructure of Stainless Steel Alloys," PhD thesis, University of California, California, 1988.

[29]   A. B. Michael and M. B. Bever, *Transactions of the Metallurgical Society of AIME,,* vol. 200, pp. 47-56, 1954.

[30]   A. Kohn and J. Philibert, *Mem. Sci. Rev. Mét,* vol. 57, pp. 291-312, 1960.

[31]   O. Hammar and G. Grümbaum, *Scandinavian Journal of Metallurgy,* vol. 3, 1974.

[32]   R. D. Doherty and D. A. Melford, *Iron Steel Institute,* vol. 204, 1966.

[33]   Y. L. Liu and S. B. Kang, *Materials Science Technology,* vol. 13, 1997.

[34]   M. Martorano and J. Capocchi, "Effects of processing variables on the microsegregation of directionally cast samples," *Metallurgical and Materials Transactions A,* vol. 31, pp. 3137-3148, 2000.

[35]   T. A. Tran and a. R. P. Thackray, "Simulated and Experimental Study of Segregation in Continuously Cast High Carbon Bloom Steel," presented at the Association for Iron and Steel Technology 2012, Atlanta, USA, 2012.

[36]   M. Zuo*, et al.*, "Effect of rapid solidification on the microstructure and refining performance of an Al–Si–P master alloy," *Journal of Materials Processing Technology,* vol. 209, pp. 5504-5508, 2009.

[37]   T. Zhou, "Control of microstructure during solidification & homogenization of thin slab cast direct rolling (TSCDR) microalloyed steels," PhD thesis, McMaster University, 2010.

[38]   A. Howe, "Microsegregation and inclusion development during the casting of steel," presented at the Solidification processing, 2007.

[39]   J. Brimacomb and K. Sorimachi, "Crack formation in the continuous cast products," *Metallurgical Transactions B,* vol. 8, 1977.

[40]   J. K. Brimacombe, "Defect Problem in Continuous casting," in *33rd electric furnace conference*, texas, 1975.

[41]   J. K. Brimacombe*, et al.* (1984) Heat Flow, Solidification and Crack Formation.

[42]   S. Peľák*, et al.*, "Between the dendrite structure quality, the casting technology and defects in countinuously cast slabs," *Materials Engineering,* vol. 16, 2009.

[43]   *Continuous casting of steel 1985: A second study*. Brussels: International Iron and Steel Institute, Committee on Technology, 1986.

[44]   M. A. Shtremel, "Problems of the metallurgical quality of steel (nonmetallic inclusions)," *Metal Science and Heat Treatment,* vol. 22, pp. 539-544, 1980.

[45]   W. F. Pontius and C. R. Taylor, presented at the Proceedings of the Electric Furnace Conference, 1967.

[46]   R. Alberny*, et al.*, "Irisid process of magetorotative continuous casing for round and square products " *Revue De Metallurgie-Cahiers D Informations Techniques,* vol. 76, pp. 235-251, 1979.

[47] Poppmeie.W, *et al.*, "Alternating electromegnetic fields in continuous casing of steel," *Journal of Metals,* vol. 18, pp. 1109-&, 1966 1966.

[48] A. A. Tzavaras, "Stude of segregation phonomena in steel solidification strucutres grown under fluid flow," *Journal of Crystal Growth,* vol. 24, pp. 471-476, 1974.

[49] D. J. Hurtuk and A. A. Tzavaras, "Some effects of electromagnetically induced fluid-flow on macrosegregation in continuously cast steel," *Metallurgical Transactions B,* vol. 8, pp. 243-251, 1977.

[50] S. Mizoguchi, *et al.*, "Continuous casting of steel," *Annual Review of Materials Science,* vol. 11, pp. 151-169, 1981.

[51] A. S. Varde, *et al.*, "The QuenchMinerTM Expert System for Quenching and Distotion Control," presented at the Heat Treating and Surface Engineering-Chemistry of Quenching, Indiana, 2003.

[52] V. Stahleisen, "Casting and Solidification of Steel," Luxembourg, 1977.

[53] D. S. MacKenzie and D. Lambert, "Effect of Quenching Variables on Distortion and Residual Stresses," presented at the Heat Treating and Surface Engineering, Indiana, 2003.

[54] G. Thewlis, "Classification and quantification of microstructures in steels," *Materials Science and Technology,* vol. 20, pp. 143-160, 2004.

[55] D. R. Speich and R. L. Miller, "Hardenability of austenite after intercritical annealing of dual-phase steels," presented at the ASM Phase Transformations Committee, Pittsburgh, U.S.A, 1981.

[56] M. Yamazaki, *et al.*, "Numerical simulation of solidification structure formation during continuous casting in Fe-0.7mass%C alloy using cellular automaton method," *ISIJ International,* vol. 46, pp. 903-908, 2006.

[57] N. H. Pryds and X. Huang, "The effect of cooling rate on the microstructures formed during solidification of ferritic steel," *Metallurgical and Materials Transactions A,* vol. 31, pp. 3155-3166, 2000.

[58] M. Allizadeh, "Correlation between the continuous casting parameters and secondary dendrite arm spacing in the mold region," *Materials Letters,* vol. 91, pp. 146-149, 2013.

[59] M. Easton, *et al.*, "Effect of Alloy Composition on the Dendrite Arm Spacing of Multicomponent Aluminum Alloys," *Metallurgical and Materials Transactions A,* vol. 41, pp. 1528-1538, 2010.

[60] D. H. Kirkwood, "A simple model for dendrite arm coarsening during solidification," *Materials Science and Engineering,* vol. 73, pp. L1-L4, 1985.

[61] A. Roósz, *et al.*, "Numerical calculation of microsegregation in coarsened dendritic microstructures," *Materials Science and Technology,* vol. 2, pp. 1149-1155, 1986.

[62] R. Pierer and C. Bernhard, "On the influence of carbon on secondary dendrite arm spacing in steel," *Journal of Materials Science,* vol. 43, pp. 6938-6943, 2008.

[63] R. Mendoza, "Morphological and Topological Characterization of Coarsened Dendritic Microstructures," Ph.D thesis, Northwestern University, June 2004.

[64] R. C. Beaverstock, "Secondary dendrite arm coarsening and microsegregation in multicomponent alloys," in *Solidification Processing*, 1997, pp. 321-324.

[65] D. Kammer, "Three-Dimensional Analysis and Morphological Characterization of Coarsened Dendritic Microstructures," Ph.D thesis, Northwestern University 2006.

[66] T.Z. Kattamis, *et al.*, "Influence of coarsening on dendrite arm spacing of Al-Cu alloys," *Transactions of the Metallurgical Society of AIME,* pp. 1504–1511, 1967.

[67] M. Kahlweit, *Scripta Metallurgica et Materialia,* p. 251, 1968.

[68] S. C. Huang and M. E. Gliksman, *Acta Materialia,* p. 717, 1981.

[69] L. K. Aagesen, "Phase-Field Simulation of Solidication and Coarsening in Dendritic Microstructures," Ph.D. thesis, Royal Institute of Technology, 2010.

[70] T. F. Bower*, et al.*, "Measurements of Solute Redistribution in Dendritic Solidification," *Transactions of the Metallurgical Society of AIME,* vol. 236, p. 624, 1966.

[71] H. J. Diepers*, et al.*, "Simulation of convection and ripening in a binary alloy mush using the phase-field method," *Acta Materialia,* vol. 47, pp. 3663-3678, 1999.

[72] A. Mortensen, "On the rate of dendrite arm coarsening," *Metallurgical Transactions A,* vol. 22, pp. 569-574, 1991.

[73] Z. Fan, "Semisolid metal processing," *International Materials Reviews,* vol. 47, pp. 49-85, 2002.

[74] S. Terzi, *et al.*, "Coarsening mechanisms during isothermal holding of a dendritic Al-10wt%Cu alloy," *Transactions of the Indian Institute of Metals,* vol. 62, pp. 447-449, 2009/10/01 2009.

[75] M. C. Flemings. (1974). *Solidification Processing*.

[76] V. R. Voller and C. Beckermann, "A unified model of microsegregation and coarsening," *Metallurgical and Materials Transactions A,* vol. 30, pp. 2183-2189, 1999.

[77] R. Sasikumar*, et al.*, "Influence of the shape of the cooling curves on microsegregation," *Scripta Metallurgica et Materialia,* vol. 28, pp. 235-240, 1993.

[78] A. Howe, "Novel equations for use in rapid software for solidification " Corus RD&T Swinden Technology Centre.

[79] T. Z. Kattamis and M. C. Flemings, 1965.

[80] T.Z. Kattamis*, et al.*, "Influence of coarsening on dendrite arm spacing and grain size of magnesium-zinc alloys," *Journal of Institute of Metals,* pp. 343–347, 1967.

[81] M. Imagumbai, "Relationship between Primary- and Secondary-dendrite Arm Spacing of C-Mn Steel Uni-directionally Solidified in Steady State," *ISIJ International,* vol. 34, pp. 986-991, 1994.

[82] D. Ma*, et al.*, "On secondary dendrite arm coarsening in peritectic solidification," *Materials Science and Engineering: A,* vol. 390, pp. 52-62, 2005.

[83] V. R. Voller, "On a general back-diffusion parameter," *Journal of Crystal Growth,* vol. 226, pp. 562-568, 2001.

[84] C. Beckermann and R. Viskanta, "Mathematical Modeling of Transport Phenomena During Alloy Solidification," *Applied Mechanics Reviews,* vol. 46, pp. 1-27, 1993.

[85] H. Yoo and C.-J. Kim, "A solute diffusion model for micro-macroscopic analysis of columnar dendritic alloy solidification," *KSME International Journal,* vol. 11, pp. 319-330, 1997.

[86] A. Howe, "Implication for solidification models of Kobayashi's exact analytical solution," ed: Corus RD&T Swinden Technology Centre, 2001.

[87] M. Rappaz, "Modelling of microstructure formation in solidification processes," *International Materials Reviews,* vol. 34, pp. 93-124, 1989.

[88] J. A. Spittle and S. G. R. Brown, "Computer simulation of the effects of alloy variables on the grain structures of castings," *Acta Metallurgica,* vol. 37, pp. 1803-1810, 1989.

[89]   M. Rappaz and C. A. Gandin, "Probabilistic modelling of microstructure formation in solidification processes," *Acta Metallurgica et Materialia,* vol. 41, pp. 345-360, 1993.

[90]   W. Yang, *et al.*, "Monte carlo sampling for microsegregation measurements in cast structures," *Metallurgical and Materials Transactions A,* vol. 31, pp. 2569-2574, 2000.

[91]   Y. Sun and C. Beckermann, "Phase field simulation of solidification with density change," presented at the International Mechanical Engineering Congress and Exposition, 2004.

[92]   G. Caginalp and J. Jones, "A derivation of a phase field model with fluid properties," *Applied Mathematics Letters,* vol. 4, pp. 97-100, 1991.

[93]   K. Sakai, "Phase field model for phase transformations of multi-phase and multi-component alloys," *Journal of Crystal Growth,* vol. 237–239, Part 1, pp. 144-148, 2002.

[94]   C. Beckermann, *et al.*, "Modeling Melt Convection in Phase-Field Simulations of Solidification," *Journal of Computational Physics,* vol. 154, pp. 468-496, 1999.

[95]   S. Sundarraj and V. R. Voller, "Development of a microsegregation model for application in a micro-macro model," 1992, pp. 35-42.

[96]   C. Y. Wang and C. Beckermann, "A multiphase solute diffusion model for dendritic alloy solidification," *Metallurgical Transactions A,* vol. 24, pp. 2787-2802, 1993.

[97]   T. Battle and R. Pehlke, "Mathematical modeling of microsegregation in binary metallic alloys," *Metallurgical Transactions B,* vol. 21, pp. 357-375, 1990.

[98]   J. A. Sarreal and G. J. Abbaschian, "The effect of solidification rate on microsegregation," *Metallurgical Transactions A,* vol. 17, pp. 2063-2073, Nov 1986.

[99]   E. Scheil, *Zeitschrift fur Metallkunde,* vol. 34, pp. 70-72, 1942.

[100]   H. D. Brody and a. M. C. Flemings, "Solute redistribution in dendritic solidification," *Transactions of the Metallurgical Society of AIME, ,* vol. 263, 1966.

[101]   A. Howe, "Computatinal investigation of the effects of diffustion modelus and secondary dendrite arm coarsening parameters on micro-segregation in C-Mn steels," presented at the Solidification processing 1997.

[102]   I. Ohnaka, "Mathematical Analysis of Solute Redistribution Solidification with Diffusion in Solid Phase*," *Transactions of the Iron and Steel Institute of Japan,* vol. 26, 1986.

[103]   T. W. Clyne and W. Kurz, "Solute redistribution during solidification with rapid solid state diffusion," *Metallurgical Transactions A,* vol. 12, pp. 965-971, 1981.

[104]   S. Kobayashi, "Solute redistribution during solidification with diffusion in solid phase: A theoretical analysis," *Journal of Crystal Growth,* vol. 88, pp. 87-96, 1988.

[105]   A. Howe, "Rapid modelling of solidification and micro-segregation: The QuickSeg Peritectic V1 Software," ed: Corus RD&T, Swinden Technology Centre, private communication, 2007.

[106]   A. Howe, "Micro-Segregation: Issues of Growth Rate and the Peritectic," *Materials Science Forum,* vol. 649, 2010.

[107]   J. O. Andersson, *et al.*, "Thermo-Calc & DICTRA, computational tools for materials science," *Calphad,* vol. 26, pp. 273-312, 2002.

[108]   H. E. Lippard, *et al.*, "Microsegregation behavior during solidification and homogenization of AerMet100 steel," *Metallurgical and Materials Transactions B,* vol. 29, pp. 205-210, 1998.

[109] A. Engstrom, Division of Physical Metallurgy, Royal Institute of Technology, Stockholm, 1996.

[110] W. Löser, *et al.*, "Solidification modelling of microstructures in near-net-shape casting of steels," *Materials Science and Engineering: A,* vol. 173, pp. 323-326, 1993.

[111] U. Feurer and R. Wunderlin, Gesellschaft für Metallkunde, Oberursel 1977.

[112] R. C. Beaverstock, "Secondary dendrite arm coarsening and microsegregation in multicomponent alloys," in *Solidification Processing SP97*, Sheffield, 1997, pp. 321-324.

[113] S. Jernkontoret, "Guide to the solidification of steels," ed, 1977.

[114] H. Jacobi and K. Schwerdtfeger, "Dendrite morphology of steady state unidirectionally solidified steel," *Metallurgical and Materials Transactions A,* vol. 7, pp. 811-820, 1976.

[115] M. Taha, *et al.*, "Dendrite morphology of several steady state unidirectionally solidified iron base alloys," *Metallurgical and Materials Transactions A,* vol. 13, pp. 2131-2141, 1982.

[116] D. Stefanescu, "Peritectic solidification," in *Science and Engineering of Casting Solidification, Second Edition*, ed: Springer US, 2009, pp. 1-17.

[117] B. K. Dhindaw, *et al.*, "Characterization of the peritectic reaction in medium-alloy steel through microsegregation and heat-of-transformation studies," *Metallurgical and Materials Transactions A,* vol. 35, pp. 2869-2879, 2004.

[118] A. Howe, "Segregation and Phase Distribution During Solidification of Carbon, Alloy and Stainless Steels," in *European Communities* ed, 1991.

[119] J. Pavlovic-Krstic, "Impact of casting parameters and chemical composition on the solidification behaviour of Al-Si-Cu hypoeutectic alloy," Ph.D thesis, University of Magdeburg, 2009.

[120] A. A. Howe, Tata Steel research report2010.

[121] B. G. Thomas, "Chapter 15 in Modeling for Casting and Solidification Processing," 2003.

[122] A. J. W. Ogilvy, "PhD Thesis," Sheffield University, 1983.

[123] "DICTRA, version 24," ed. Stockholm: Royal Institute of Technology, 2004.

[124] "MOB2 mobility database," ed. Stockholm: Royal Institute of Technology, 2005.

[125] Jernkontoret, *A Guide to the Solidification of Steels*: Jernkontoret, 1977.

[126] J. Lacaze, *et al.*, "Some Issues Concerning Experiments and Models for Alloy Microsegregation," *Advanced Engineering Materials,* vol. 5, pp. 37-46, 2003.

[127] C. Selig and A. Lacaze, "Study of microsegregation buildup during solidification of spheroidal graphite cast iron," *Metallurgical and Materials Transactions B,* vol. 31, pp. 827-836, 2000.

[128] G. R. Purdy and J. S. Kirkaldy, "Homogenization by diffusion," *Metallurgical Transactions,* vol. 2, pp. 371-378, 1971.

[129] A. Howe, "Simple approaches for solidification and diffusive homogenisation," *Ironmaking & Steelmaking,* vol. 38, pp. 534-539, 2011.

Appendix: The Attached Compact Disc

The enclosed compact disc contains both Matlab codes and data as follows:

Appendix 1: Case 1: $k_{\delta/l}$ and $m_{\delta/l}$ for Ep < 1, and $k_{\gamma/l}$ and $m_{\gamma/l}$ for Ep $\geq$ 1

Appendix 2: Case 2: $k_{\delta/l}$ and $m_{\delta/l}$ for Ep < 0.97, and $k_{\gamma/l}$ and $m_{\gamma/l}$ for Ep $\geq$ 0.97

Appendix 3: Case 3: $k_{\delta/l}$ and $m_{\delta/l}$ for Ep < 0.9, and $k_{\gamma/l}$ and $m_{\gamma/l}$ for Ep $\geq$ 0.9

Appendix 4: Howe' carbon equivalent for carbon and low alloy steels with major Si and Mn contents

Appendix 5: Howe' carbon equivalent for carbon and low alloy steels with full multicomponent including Ni and Cr elements

Appendix 6: Peritectic equivalent

Appendix 7: Diffusivity data employed in this work